X-692-76-2
PREPRINT

NASA TM X- 71043

OBSERVATIONS OF THE INTERPLANETARY MAGNETIC FIELD BETWEEN 0.46 AND 1 A.U. BY THE MARINER 10 SPACECRAFT

(NASA-TM-X-71043) OBSERVATIONS OF THE INTERPLANETARY MAGNETIC FIELD BETWEEN 0.46 AND 1 A.U. BY THE MARINER 10 SPACECRAFT Ph.D. Thesis - Catholic Univ. of Am. (NASA) 234 p HC $8.00 CSCL 03B G3/92
N76-16994
Unclas
13248

KENNETH BEHANNON

JANUARY 1976

GSFC

GODDARD SPACE FLIGHT CENTER
GREENBELT, MARYLAND

ABSTRACT

Almost continuous measurement of the interplanetary magnetic field (IMF) at a sampling rate of 25 vectors/sec was performed by the Magnetic Field Experiment onboard the Mariner 10 spacecraft during the period November 3, 1973 to April 14, 1974, comprising approximately 5-2/3 solar rotations and extending in radial distance from the sun from 1 to 0.46 AU. A clearly discernible two-sector pattern of field polarity was observed during the last 3-1/2 months of the period, with the dominant polarity toward the sun below the solar equatorial plane. Two compound high-speed solar wind streams were also present during this period, one in each magnetic field sector. Though variable in time, the daily average radial component of the field was found through least squares fitting to a power law model to have an $r^{-1.95}$ dependence on heliocentric distance, while the azimuthal component was found to fall off with radial distance as $r^{-1.30}$. The field magnitude variation could be described equally well by an $r^{-1.65}$ dependence or by the Parker spiral model $(r^{-4} + r^{-2})^{1/2}$ dependence. Relative fluctuations of the field in magnitude and direction were found to have large time variations, but on average the relative magnitude fluctuations were approximately constant over the range of heliocentric distance covered while the relative directional fluctuations showed a slight decrease on average with increasing distance. The occurrence rate of directional discontinuities was also found to decrease with increasing radial distance from the sun. All types of fluctuations showed correlation with the high-speed stream structure in the medium, with highest fluctuation levels associated with the high-velocity regions of the streams. Highly coherent, polarized fluctuations were observed at frequencies between 0.01 and 10 Hz at all distances from the sun. These were generally plane-polarized fluctuations with wave normal vectors usually between 10° and 20° from the mean field direction. Both left-hand and right-hand polarizations were observed, with left-hand polarized waves more nearly circularly polarized. By use of estimated solar wind flow speed and density values, selected examples of these waves can be shown to be consistent with either the ion cyclotron mode or the electron whistler mode of wave propagation. The observed waves may be associated with temperature anisotropy-driven instabilities.

ACKNOWLEDGMENTS

I would like to express my appreciation to Dr. Y. C. Whang for his guidance and encouragement throughout the course of this research. A deep debt of gratitude is due to Dr. Norman F. Ness, my supervisor at the Goddard Space Flight Center, who made it possible for me to pursue my graduate studies through participation in the Goddard-Catholic University Three-Quarter Time Program, encouraged and advised me throughout my years of work and study at Goddard, and gave me the opportunity to analyze and interpret the interplanetary magnetic field measurements from the Mariner 10 spacecraft.

I particularly wish to thank those others who have been willing to discuss and advise me on many aspects of this research and who have made numerous helpful suggestions. These include Drs. M. H. Acuna, E. Barouch, J. W. Belcher, L. F. Burlaga, D. H. Fairfield, M. L. Goldstein, A. Klimas, R. P. Lepping, F. M. Neubauer, K. W. Ogilvie and J. D. Scudder.

A further debt of gratitude is owed to R. F. Thompson for his considerable advice on mathematical techniques and specific computer programming assistance on the curve-fitting portion of the analysis; to F. W. Ottens for programming support in the statistical computation and portions of the data plotting; to D. R. Howell for the Mariner 10 production processing software and frequent programming advice; and to P. Harrison for performance beyond the call of duty in cheerfully carrying out a multitude of tasks related to the production processing of the Mariner 10 data. A second vote of thanks is due to Dr. R. P. Lepping for his substantial assistance both in the calibration of Mariner 10 data and in the survey of directional discontinuities. Many thanks also to F. A. Hunsaker and J. R. Hodge for their drafting support and to P. Wilson for typing assistance during the writing of this thesis.

For their engineering support at Goddard, which helped to make the Magnetic Field Experiment on Mariner 10 an outstanding success, I wish to thank H. F. Burdick,

R. H. Hoffman, J. L. Scheifele and J. B. Seek. Special thanks are also due to the magnetometer instrument coordinator, J. H. Bruns of the Boeing Company and to the Mariner 10 project staff at the Jet Propulsion Laboratory under the able guidance of Project Manager W. E. Giberson and Project Scientist J. A. Dunne for their own considerable contributions to the successful conduct of this study.

I finally would like to thank my colleague at Goddard W. H. Mish for his continued data analysis advice and assistance and for helping me to keep my blood pressure down and my spirits up throughout this research by keeping me company during many hours of road running. For their constant moral support, many sacrifices and offloading from me many tasks at home during this endeavor, I am indebted more than I can find words to say to my wife, Betty and daughter Terry. And last but not least I would like to thank my mother, Mrs. Ruth Behannon, for starting me off in the right direction in the first place.

TABLE OF CONTENTS

CHAPTER Page

ABSTRACT iii

ACKNOWLEDGMENTS v

LIST OF TABLES ix

LIST OF ILLUSTRATIONS x

I. INTRODUCTION 1

1. The Mariner 10 Mission 1
2. The Solar Magnetic Field as Source of Interplanetary Field 6
3. Radial Variation of the Interplanetary Magnetic Field with Heliocentric Distance 11
4. Sector Structure of the IMF 14
5. Stream Structure of the Solar Wind 21
6. Variations of the IMF with Heliographic Latitude 27
7. Fluctuations of the IMF 30
8. Investigation Objectives 39
9. Supporting Measurements 40

II. MAGNETIC FIELD EXPERIMENT INSTRUMENTATION AND DATA ANALYSIS 43

1. General Instrument Description 43
2. Data Processing and Analysis 49

III. OBSERVATIONS OF THE LARGE-SCALE IMF 60

1. General Character of the IMF During the Mariner 10 Mission 60
2. Observed Radial Distance Dependence of the IMF 75
3. Observed Heliographic Latitude Effects 83
4. Observed High-Speed Stream Structure 88

Page

IV. OBSERVATIONS OF IMF FLUCTUATIONS 99

1. Characteristics of Relative Magnitude and Directional RMS Deviations 99

1.1 Solar Rotation Statistics of Fluctuation Parameters 99
1.2 Observed Radial Distance Dependence 106
1.3 Relation to Large-Scale Corotating Structure 114

2. Power Spectral Studies of IMF Fluctuations 127

2.1 Variation of Power Spectra with Radial Distance 128
2.2 Observations of Electromagnetic Waves in the IMF 135
2.3 Plausibility Arguments for Wave Mode Identification 156

V. SUMMARY OF RESULTS AND CONCLUSIONS 174

APPENDIX A. Least Squares Fits to Radial Distance Variation 183

APPENDIX B. Power Spectral Density and Polarization Analysis 188

LIST OF REFERENCES 200

TABLES 216

LIST OF TABLES

Table		Page
I	Summary of Hourly Average Field Magnitude F Distribution Data	216
II	Values of the Exponent C in the Power Law Model r^c for the Radial Distance Dependence of the Radial and Azimuthal Magnetic Field Components	217
III	Percentages of Observation Time in Each Sector Polarity During Each Solar Rotation	218
IV	Summary of Solar Rotation Statistics of Vector Field Fluctuations	219
V	Summary of Solar Rotation Statistics of Field Magnitude Fluctuations	220
VI	Error in Field Component Parallel to Magnetometer Boom Due to Boom Deflection	221

LIST OF ILLUSTRATIONS

Figure		Page
1	Mariner 10 Spacecraft in Flight Configuration	2
2	Ecliptic Plane Projection of Primary Mission Trajectory	4
3	Illustration of Restricted Time Period in Which Same Parcel of Plasma Observed at Mariner 10 and Earth	5
4	Mariner 10 Heliocentric Orbit with Respect to Earth-Sun Line	7
5	Theoretical Interplanetary Field (Parker Model)	12
6	Example of High Speed Stream Field and Plasma Parameter Profiles	23
7	Block Diagram of Magnetic Field Experiment	45
8	Prime Magnetometer Frequency Response	46
9	Typical Flight Sensor Noise Test Results	48
10	Typical Sensor Intrinsic Noise Spectrum	49
11	Dual Magnetometer Analysis Fundamentals	53
12	Solar Equatorial Coordinate System	56
13	IMP 8/HEOS Daily Average IMF Characteristics	62
14	Mariner 10 Daily Average IMF Characteristics	63
15	Mariner 10 Daily Average Vector Field in Rotating Solar Reference Frame	66
16	Hourly Average Field Magnitude Distribution, S.R. 1918-1920	68
17	Hourly Average Field Magnitude Distribution, S.R. 1921-1923	69
18	Hourly Average ϕ and θ Angle Distribution, S.R. 1918-1919	71

Figure Page

19 Hourly Average ϕ and θ Angle Distribution, S.R. 1920-1921 72

20 Hourly Average ϕ and θ Angle Distribution, S.R. 1922-1923 73

21 Comparison of M10 and IMP 8/HEOS ϕ Distribution, S.R. 1922-1923 74

22 Heliocentric Distance Variations in $|B_r|$ and B_t 76

23 Heliocentric Distance Variations in $|B_n|$ and $|B_\phi|$ 79

24 Heliocentric Distance Variations in Field Magnitude 82

25 Comparison of SR 1923 IMF Measurements with Photospheric Field Pattern 87

26 Geomagnetic Activity Index K_p During M10 Mission 90

27 IMP 8/HEOS Observation of Field in High Speed Stream in January 1974 92

28 Mariner 10 Observation of Same High-Speed Stream at 0.8-0.75 AU . 93

29 Superposition of M10 Observations of High-Speed Stream Field Magnitude Profile 96

30 Comparison of Relative Enhancement of Stream-Compressed Field at M10 and 1 AU 97

31 Hourly Average Relative Vector Field Fluctuation (σ_c /F) Distribution 104

32 Hourly Average Relative Field Magnitude Fluctuation (σ_F /F) Distribution 105

33 Heliocentric Distance Variations in σ_F/F and σ_c/F 106

34 Variation in Solar Rotation Average Fluctuation Parameters 110

Figure **Page**

35 Heliocentric Distance Variation in Directional Discontinuity Occurrence Rate. 113

36 Superposed Epoch Plot of IMP 8/HEOS Field Magnitude Daily Averages. 116

37 Superposed Epoch Plot of IMP 8/HEOS σ_c /F Daily Averages. 117

38 Superposed Epoch Plot of IMP 8/HEOS σ_F /F Daily Averages. 118

39 Discontinuity Occurrence Rate and σ_c /F Contours in Rotating Solar Reference Frame 121

40 Mariner 10 Field Magnitude and Component Measurements in Compound Stream 124

41 Field Component, Magnitude and Relative Fluctuations in the Stream . 125

42 Composite Radial Component Power Spectra at Three Heliocentric Distances. 130

43 Time and Distance Variations in Power Density at 10 Frequencies . . 133

44 Comparison of Power Spectra and Degree of Polarization Before and Within High-Speed Stream. 134

45 Examples of Transverse IMF Waves Observed at 0.99 and 0.46 AU . . 136

46 Examples of Waveform Variability Sometimes Seen in IMF 137

47 Summary of Mariner 10 Wave Observations 140

48 Distribution of Ellipticities of Observed Waves 143

49 Variation of Ellipticity with Sun-Wave Normal Angle 144

50 Observed Wave Frequency as Function of Ellipticity and Degree of Polarization. 146

Figure **Page**

51 Power Spectra and Wave Parameters for 0.3 Hz Wave Observed on March 9, 1974. 149

52 Power Spectra and Characteristics of 1 Hz Wave Observed on April 1, 1974 151

53 Power Spectra and Characteristics of 0.8 Hz Wave Observed on April 2, 1974 152

54 Power Spectra and Characteristics of 1.9 Hz Wave Observed on April 11, 1974 154

55 High Rate (25 Samples/sec) Field Component Data During April 11 Wave Observation. 155

56 Polarization Diagrams of April 11 Wave 157

57 Dispersion Relation, Wave Speeds and Doppler Shift for April 11 Wave 167

58 Dispersion Relation, Wave Speeds and Doppler Shift for January 29 10 Hz Wave 169

CHAPTER I

INTRODUCTION

1. The Mariner 10 Mission

The Mariner 10 spacecraft was launched on November 3, 1973 from Cape Canaveral, Florida. The primary objective of this mission was to perform the first close observations of the planet Mercury. It was also to be the first deep-space mission to use the gravity field of one planet to bend the spacecraft trajectory to produce an encounter with a second planet. Such a "gravity assist" from Venus was utilized to significantly reduce the launch vehicle energy required for Mariner 10 to reach Mercury and in the process made possible additional investigations of Venus.

The spacecraft and its complement of experiments is shown in Figure 1. In addition to these active experiments, the dual frequency spacecraft radio system was also used for planetary mass, radius, ionosphere and atmosphere measurements as well as interplanetary columnar electron content measurements. As can be seen in Figure 1, the Magnetic Field Experiment employed a dual magnetometer system on a long boom to remove spacecraft field contributions to the measurements. The experiment instrumentation is described in Chapter II. Successful observations of magnetic fields near Venus on February 5, 1974 and Mercury on

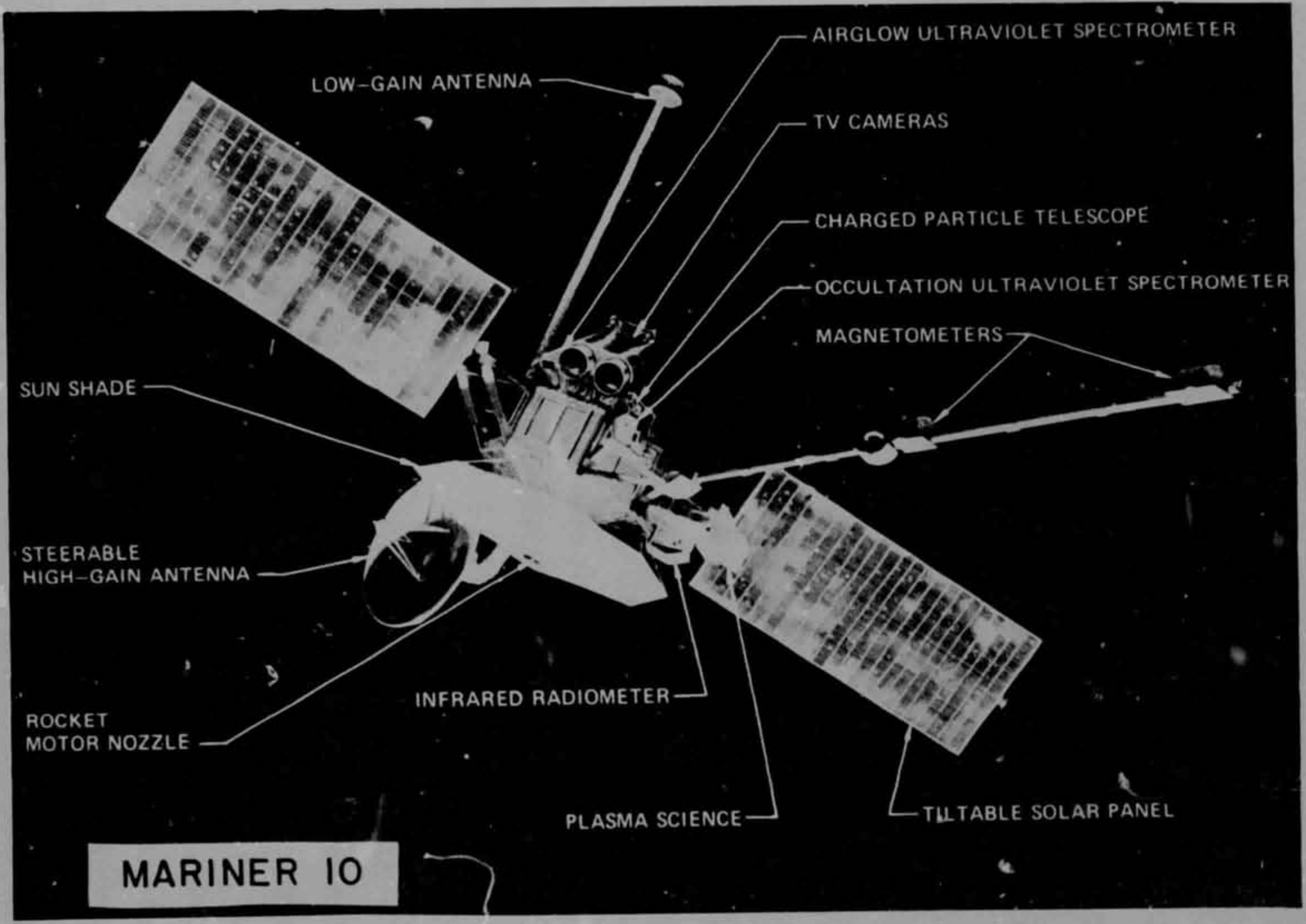

Figure 1. Artist's conception of the Mariner 10 spacecraft in flight. Active experiments and major spacecraft components are labeled.

March 29, 1974 have been described by Ness et al. (1974a, b). The unexpected magnetic field of Mercury discovered by this mission has been further described by Ness et al. (1975a). In addition, a second traverse through the near-planet downstream region on March 16, 1975 by the same spacecraft confirmed the discovery of Mercury's intrinsic magnetic field (Ness et al., 1975b).

Although the primary objectives of the mission concerned the planetary encounters, the unique trajectory afforded the opportunity for obtaining valuable measurements in the interplanetary medium during the cruise phases of the mission. To achieve the Mercury encounter, Mariner 10 made the nearest approach to the sun (0.46AU) by any spacecraft up to the Mercury I encounter date. The Mariner 10 trajectory relative to the orbits of Earth, Venus and Mercury is shown in Figure 2. The object of this present work is to describe the initial results from the interplanetary measurements performed by the Magnetic Field Experiment between launch on November 3, 1973 and April 14, 1974, a period that comprised approximately 5-2/3 solar rotations. The Bartels Solar Rotation numbers for this period are shown in Figure 2 along the associated portions of the earth's orbit and Mariner 10's trajectory.

Magnetic field measurements in the interplanetary medium by earth-orbiting spacecraft during the primary mission of Mariner 10 (launch to first Mercury encounter) provided the opportunity for comparative studies of large scale characteristics of the interplanetary magnetic field (IMF) at two different distances from the sun during this time. The experiments which performed these supporting measurements are described in Section I.9. The relative positions of Mariner 10 and the earth during the primary mission provided only very limited opportunity for measurements in the same parcel of solar wind plasma at two different heliocentric distances. This is illustrated by Figure 3, which shows

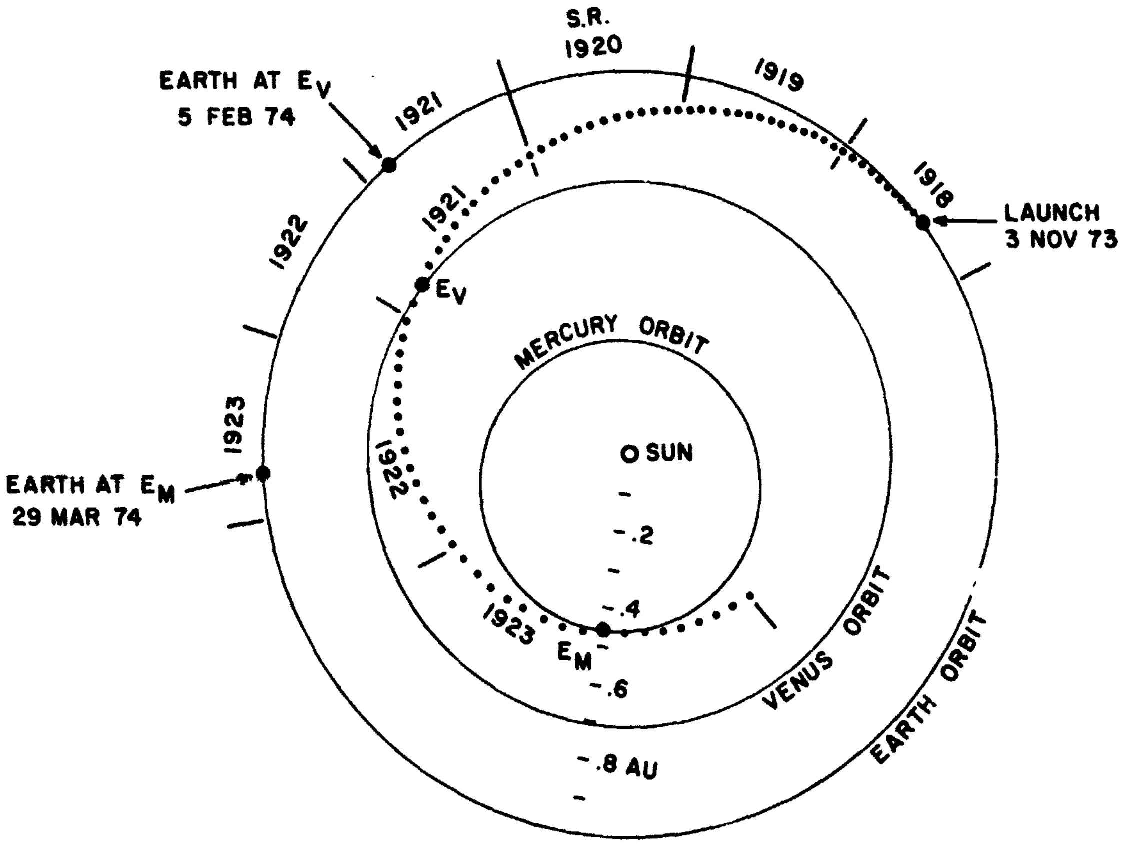

MARINER 10
ECLIPTIC PLANE PROJECTION

Figure 2. Ecliptic plane projection of the Mariner 10 primary mission trajectory. Each point on the trajectory represents two days of the mission. Also shown are the orbits of Earth, Venus and Mercury with the positions of the earth and planets at the times of encounters indicated as well as the numbers of solar rotations occurring during the indicated portions of the orbits.

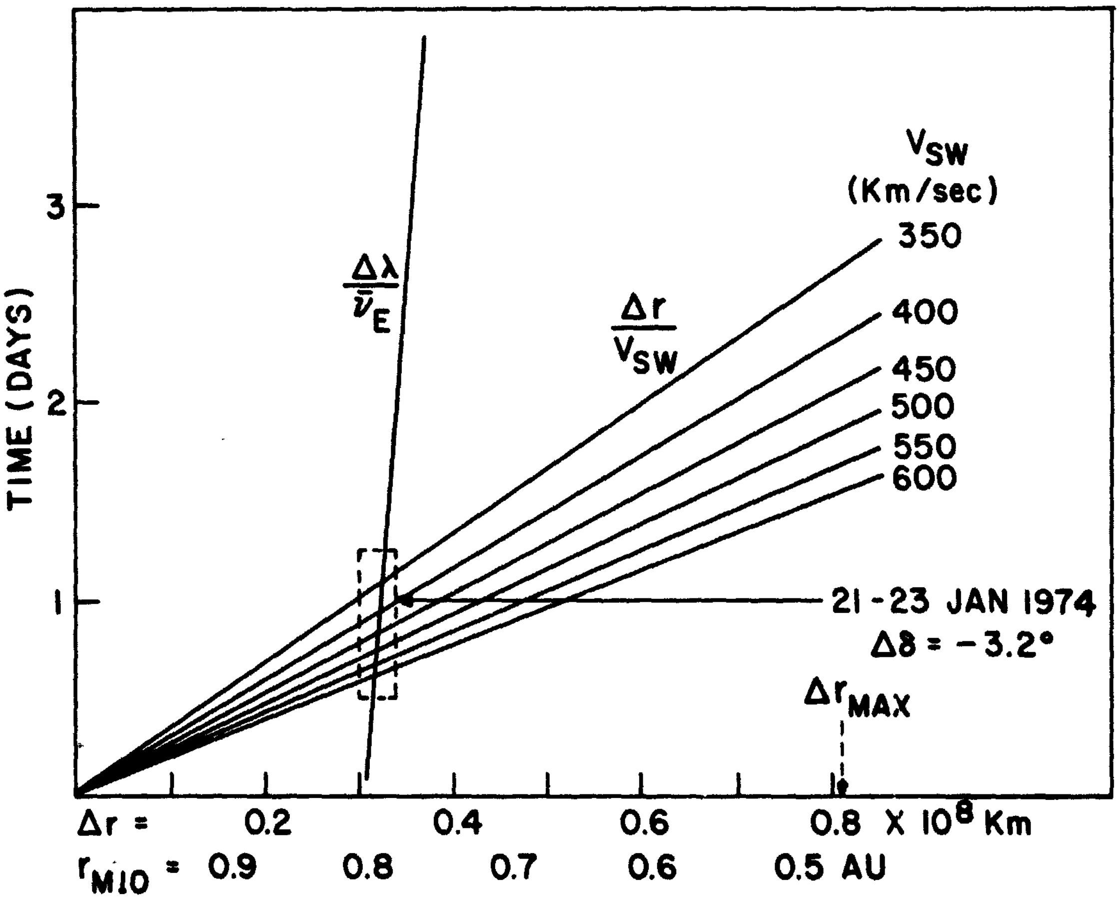

Figure 3. The only period during the mission when Mariner 10 and earth-orbiting spacecraft could have observed the same parcel of solar wind plasma was when the time required for the earth to move in its orbit to the point where a parcel of plasma passing Mariner 10 would intersect the orbit of earth was equal to the radial transit time between Mariner 10 and 1 AU. This could have occurred only during the period 21-23 January, depending on solar wind flow speed, when Mariner 10 was at a heliocentric distance of approximately 0.78 AU. (See text for parameter definitions.)

curves for the ratios $\Delta\lambda/\bar{\nu}_E$ and $\Delta r/V_{SW}$ plotted as functions of Δ r, where $\Delta\lambda = \lambda_M - \lambda_E$ = heliographic longitude separation of Mariner 10 and the Earth, $\bar{\nu}_E$ = average orbital angular speed of the earth = 0.986°/day, Δr = radial distance separation of Mariner 10 and the earth in km and V_{SW} is the solar wind bulk speed in m/sec. Only values of $\Delta\lambda/\bar{\nu}_E > 0$ are plotted, and $\Delta r/V_{SW}$ is shown for a range of solar wind speeds. Also shown along the abscissa is the distance of Mariner 10 from the sun in AU. One sees that there was only one brief period during the mission when the relative positions made observation of the same parcel of plasma possible, first at Mariner 10 and then at the earth approximately one day later during the period 21-23 January, 1974. However, as indicated, there was a heliographic latitude separation $\Delta\delta = \delta_M - \delta_E = -3.2°$ at that time, which would require that the coherent parcel of plasma extend on the order of at least 7×10^5 km (= 0.045 AU = 105 R_E, R_E = earth radius) in the direction perpendicular to the solar equatorial plane in order to be observed at both positions.

Figure 4 illustrates why this short period around January 22 was the only opportunity for observing the same plasma at two separated locations. A plot of the Mariner 10 trajectory to Mercury relative to the earth-sun line shows that from launch until January 20, the spacecraft actually lagged behind the earth in its orbit about the sun. Thus it was only after Mariner 10 began to lead the earth that such a favorable relative alignment was achieved. From that time on, however, the spacecraft-earth solar longitude separation continuously increased as Mariner 10 accelerated toward Mercury. The relative positions of Mariner 10 and the earth will be discussed further during the interpretation of the results.

2. The Sun as Source of Interplanetary Plasma and Magnetic Fields

It has long been known that the sun is responsible for transient variations in the geomagnetic field observed at the surface of the earth. A relationship

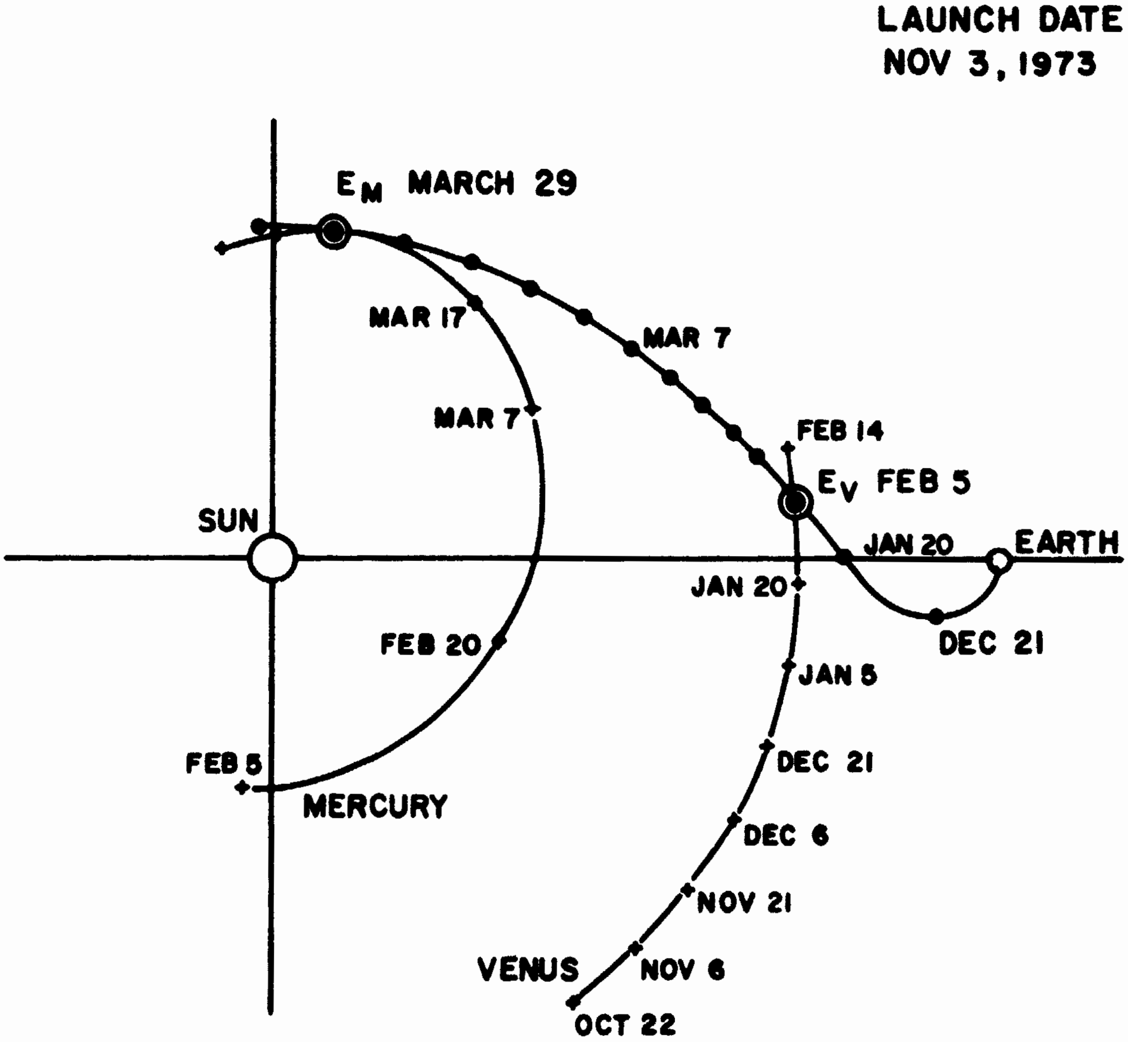

Figure 4. A plot of the Mariner 10 trajectory relative to the earth-sun line shows that Mariner 10 was at inferior conjunction with the earth on 20 January. After that date, when Mariner 10 began to lead the earth in its orbit, the same plasma flowing past Mariner 10 could be observed near earth approximately one day later as shown in Fig. 3.

between solar flares and geomagnetic storms was first suggested by Carrington, an astronomer at Greenwich Observatory in 1859, after noting that a magnetic storm occurred approximately one day after observing a flare in white light. He did not suggest a mechanism. A corpuscular theory of magnetic storms and auroras was first proposed in 1896 by Birkeland, who suggested that both phenomena were caused by streams of fast electrons emitted by the sun. Otherwise, interplanetary space was assumed to be a void. This theory was further elaborated on by Chapman and Ferraro, who postulated the transient ejection of solar plasma as the source of geomagnetic storms (reviewed by Chapman, 1963).

Following the early suggestion of Biermann (1951) for a continuous and substantial solar corpuscular flux to explain the observed characteristics of type I comet tails, Parker (1958, 1963) developed the theory of the solar wind and thus concluded that a continuous confinement of the geomagnetic field would exist. Such a confinement was suggested by early measurements on Pioneers 1 and 5 by Sonett (1960), Sonett et al. (1960a, b), Coleman et al. (1960) and Coleman (1964), and was confirmed by measurements by Explorer 10 (Bonetti et al., 1963, Heppner et al., 1963).

The curvature of a stream of particles, continuously emitted radially, owing to the sun's rotation, was first discussed by Chapman and Bartels (1940). Chapman (1963) further expanded the concept, considering the lateral extent and expansion of such a stream and how it could effect the whole earth almost simultaneously. Dessler (1958) pointed out that since interplanetary gas is compressible, a disturbance would propagate with the velocity of compression or as longitudinal waves in the presence of a magnetic field. Ferraro (1960) described the way in which a stream of particles would act as a piston, compressing the gas ahead of it and inducing a shock wave.

It was known by this time that the sun had a magnetic field and that this field was extended into interplanetary space by the outflowing solar plasma. The first observations of magnetic fields in cosmical bodies was of the Zeeman effect in the spectra of sunspots by Hale (1908). Early spectroscopic investigations by Hale et al. (1913, 1918) showed that during 1913-1914 the sun was like a uniform magnetized sphere with magnetic axis slightly inclined to the axis of rotation and with a polarity of the same sense as that of the earth's magnetic field. The first attempt to measure the weak field of the sun by photoelectric means was by Kiepenheuer (1953). He found fine structure in the field, far outside of sunspots. Babcock and Babcock (1955), with the aid of a photoelectric magnetograph developed by Babcock (1953), were able to reveal a general field on the order of one Gauss in the polar regions. They observed a polarity reversal of this magnetic field in 1957-58.

The relationship between the weak general magnetic field of the photosphere observed by the Babcocks and the strong fields of sunspots is still not completely understood. The number of active regions on the surface of the sun has been found to vary with a period of about 11 years; the most recent maxima occurred in 1957-58 and 1968-69, with a minimum in 1964-65. Magnetically the period is 22 years, because the magnetic polarity of a given hemisphere reverses from one 11-year half-cycle to the next. Babcock (1960) proposed a model in which the solar field gets "wrapped-up" within the sun as it rotates, leading up to a maximum of solar activity followed by a main dipolar field reversal. This topological model, based on a mechanism discussed by Cowling (1953), accounted for some of the most characteristic qualitative features of the solar cycle. The Babcock model has been further developed by Leighton (1969) using a kinematic model based on field amplification by the solar differential rotation. Solution of the model equations showed the existence of oscillatory modes for the subsurface fields. A characteristic feature of the Babcock-Leighton model is the conversion of a poloidal magnetic field to a toroidal field and back again to a poloidal field of opposite polarity.

A number of authors from Babcock (1959) to Severny (1971) have discussed the various complexities of the general solar magnetic field in detail. The polarities of the fields observed on the solar surface are not generally consistent with a dipole field. At times both poles have the same polarity, and the variation of the mean field strength with latitude is inconsistent with that expected of a dipole. The solar field is, at times, more consistent with a magnetic quadrupole. In a broad band of solar latitudes centered on the equator, the solar field is dominated by localized areas of enhanced field strength called active regions, or bipolar magnetic regions (BMR's) (Babcock, 1960). These regions exist as localized areas for periods of weeks to months, after which they spread their field lines over progressively larger areas of the sun. The fields of order 1 gauss observed at the rotation poles are postulated to be the relics of old active regions, transported from low to high solar latitudes by a random walk diffusion along supergranule peripheries (Leighton, 1964).

New magnetic flux arrives at the surface of the sun from below at the birth of an active region. There is no evidence that magnetic fields come to the surface of the sun in any other manner (Howard, 1972). According to theory (Leighton, 1969), dipole magnetic field lines or flux tubes beneath the photosphere are distorted by differential rotation and amplified in field strength. When a sufficiently large field strength is reached, the flux tube becomes buoyant (Parker, 1955, 1975; Schatten, 1973) and breaks through the photosphere as a BMR. Large unipolar magnetic regions (UMR's) are also observed in maps of the photospheric field. These surface fields which are organized into patterns of dominant magnetic polarity extend into the overlying corona. The high electrical conductivity of the solar wind plasma means that some of the solar magnetic field lines will be "frozen" into this streaming plasma (Alfven, 1950) and stretched out radially away from the sun. Parker (1958) pointed out that the combination of a radial solar wind velocity plus the solar rotation will cause the IMF field lines to be stretched out into Archimedean spirals. The first experimental demonstration of this predicted spiral structure was obtained by McCracken (1959, 1962) using solar flare cosmic ray data obtained at the earth's surface, which showed that the observed particles were steered to the earth from the sun along a spiral field which at 1 AU was oriented at an angle of 50° to the earth-sun line. The first direct measurements of the magnetized solar plasma were performed by Pioneer 5 (Coleman et al., 1960, 1961). Extensive reviews of the source of the IMF in the solar photosphere and corona have been given by Dessler (1967), Wilcox (1968), Newkirk (1972), Schatten (1972) and others. Dynamo theories of the sun's main magnetic field have been reviewed recently by Gubbins (1974). The results of recent detailed observations of solar magnetic fields have been reported by Howard (1974a, b, c).

3. Radial Variation of the IMF with Heliocentric Distance

Figure 5 shows the variation with distance from the sun, in the solar equatorial plane, of the theoretical spiral angle magnetic field magnitude and radial and azimuthal components. This model of the IMF (Parker, 1963) predicts an inverse power law dependence of the field on radial distance from the sun, with the total field magnitude and radial component falling off more rapidly with distance than the azimuthal component. Exponents of -2 and -1 are predicted, respectively, for the radial and azimuthal components. According to this model the angle between the magnetic field and the radial solar wind flow direction, the "spiral angle" of the field, is about 45° (or 225°) at 1 AU and decreases toward the sun while increasing for $r > 1$ AU.

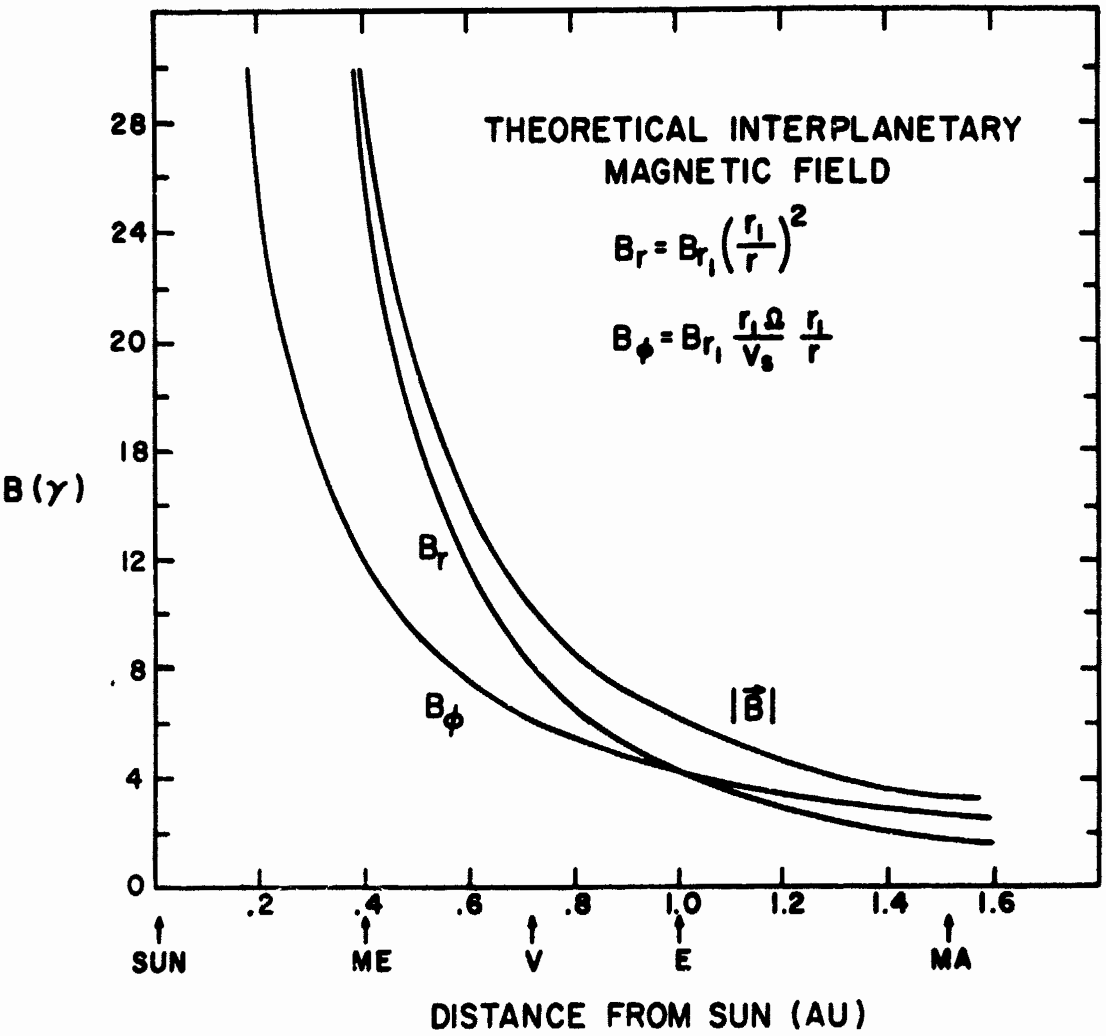

Figure 5. Variation of the theoretical spiral magnetic field magnitude and components with heliocentric distance in the solar equatorial plane.

Observations by both Pioneer 6 (Burlaga and Ness, 1968), which had a radial distance variation of 0.17 AU, and Mariner 5 (Coleman and Rosenberg, 1968, 1971; Rosenberg, 1970; Rosenberg and Coleman, 1973), which traversed the region between 1 AU and the orbit of Venus at 0.71 AU, showed gross consistency with the Parker model for B_r. Neugebauer (1975a) combined these measurements with those by Mariner 4, enroute to Mars encounter, and by Pioneer 10 (Smith, 1974), which has observed the IMF out to the orbit of Jupiter and beyond, and showed that the total data set can be reasonably well represented by an inverse-square law variation. However, Coleman et al. (1969) found an $r^{-1.46}$ dependence for the Mariner 4 data alone. The Pioneer 10 observations, which had the advantage of covering a greater range of heliocentric distance, providing a larger % change in the field relative to 1 AU, also were separately demonstrated to be consistent with the inverse-square law. The preliminary analyses of the Pioneer 6 (Burlaga and Ness, 1968) and Pioneer 10 (Smith, 1974) radial distance variations did not include the rigorous fitting of power-law curves to the data. Villante and Mariani (1975) have updated the Pioneer 6 analysis, and a more extensive analysis of Pioneer 10 radial variations has been performed (Rosenberg et al., 1975).

In contrast with the results for the radial component, showing generally good agreement with the Parker model, Neugebauer found that the various measurements are consistent in suggesting that the azimuthal component radial dependence is much steeper than the r^{-1} dependence predicted by the Parker spiral model. The Pioneer 10 observations, said to be consistent with a dependence of $\sim r^{-1}$ (Smith, 1974) have more recently been shown to vary as $r^{-1.29}$ (Rosenberg et al., 1975). For Mariner 4, an average dependence of $r^{-1.83}$ was obtained (Rosenberg, 1970; Coleman et al., 1969), and a best fit of $r^{-1.85}$ for Mariner 5 was calculated

(Rosenberg and Coleman, 1973). In addition, Villante and Mariani (1975) reported an $r^{-2.5}$ dependence from Pioneer 6. Mechanisms possibly contributing to the variability in the azimuthal component of the IMF will be discussed in Section I.5.

Pioneer 10 solar rotation most probable values of field magnitude have also been shown to be roughly consistent with the radial dependence predicted by Parker's theory $|\vec{F}| \propto (r^{-4} + r^{-2})^{1/2}$ (Smith, 1974). The largest departures from the theoretical dependence were at the ends of the distance range, the observations being high near 1 AU and low near 4 AU.

4. Sector Structure of the IMF

The complexities of the photospheric magnetic field are not apparent in the solar wind because the high harmonics of the photospheric field are not present at heights in the corona where the field pattern is frozen into the solar wind (Schatten et al., 1969). That the photosphere was the source of the IMF was established in the mid-1960's by Ness and Wilcox using measurements made by the IMP 1 spacecraft. They demonstrated that the IMF had the 27-day rotation rate of the sun, and they also delineated the sector structure of the field (Ness and Wilcox, 1964; Wilcox and Ness, 1965). This was shown to be on an average a quasi-stationary pattern of alternating regions of dominant field polarity, either toward or away from the sun along the spiral direction.

Above the photosphere the plasma energy density diminishes very rapidly with only moderate decreases in the magnetic energy density (Schatten et al., 1969). This results in a region between the plasma domination near the sun and that further out in the corona. In this intermediate region the magnetic energy density is greater than the plasma energy density and hence controls the configuration. The magnetic field existing on the boundary between this and the exterior region is oriented approximately in the radial direction and serves as a source for the IMF. Since the highest closed arches in eclipse data have been observed to have a mean height of

0.6 $R_{\odot}$ above the limb, this height was used for the "source surface" of a model of the large scale magnetic field structure, which used a Green's function solution to Maxwell's equations. The large scale IMF sector pattern was shown to be related to the field pattern at this source surface (Schatten, 1968; Schatten et al., 1969). At the height of the source surface roughly one third of the photospheric magnetic field lines reach the source surface. Results of cross-correlating the fields calculated on the source surface with the radial component of the IMF as a function of time indicated that new magnetic fields reaching the photosphere require roughly one solar rotation before their effects become present in the interplanetary medium.

Magnetic field measurements performed by the Mariner 2 spacecraft during the period August-November 1962 showed that the IMF had a well-defined two-sector pattern that remained stable for the three solar rotations of observation (Coleman et al., 1966). During the IMP-1 period of observation, November 1963-February 1964, four stable sectors were observed during three solar rotations. During two solar rotations in the latter half of 1964, IMP-2 observed the four sector pattern observed by IMP-1, although some changes in the sizes of individual sectors were noted (Fairfield and Ness, 1967). During the first four solar rotations in 1965, Mariner 4 observed the pattern to change considerably from the four-sector pattern seen earlier (Coleman et al., 1967). Considerable evolution was observed from one solar rotation to the next, and often, for periods of days, the polarity was so variable that none was assigned. Observations of the IMF in the latter half of 1965 by IMP-3, when new 11-year sunspot cycle activity was becoming prominent on the sun, showed a rapidly evolving pattern, with new sectors appearing and expanding (Ness and Wilcox, 1967). Sectors with field directed toward the sun were predominant, but the young away sectors had the highest correlation with geomagnetic activity (Schatten and Wilcox, 1967). A stable recurring away sector associated with a sequence of recurring geomagnetic storms had persisted from 1962 to the beginning of 1965 (Wilcox and Ness, 1965). That sector contained a stream of protons of a few MeV energy.

During the rising portion of the sunspot cycle in 1966 and 1967, measurements by Explorers 33 and 35 continued to reveal a variable sector polarity structure that would often remain quasi-stationary for a few rotations, followed by appreciable change (Wilcox and Colburn, 1969). A persistent two-sector pattern began to emerge, however, and was observed during 1968 and 1969, through solar maximum, with occasional short-lived smaller sectors (Wilcox and Colburn, 1970, 1972). Using data from Explorers 35, 41, 43 and 47, Fairfield and Ness (1974) extended the previous observations, showing that the basic two-sector pattern continued through 1970. 1971 was characterized by four unequal sectors dominated by a large toward sector dating back to at least 1968. The pattern became more complex in the first half of 1972. Six sectors were present near the middle of 1972, for a single rotation, but a shift in the structure and merging of sectors took place, coinciding with the very large solar flares of August 1972 and resulting in a four sector pattern through the remainder of 1972.

Knowledge of the IMF sector polarity has been extended back in time beyond the era of direct space measurements through use of a technique involving polar geomagnetic observations (Svalgaard, 1968, 1972, 1973; Friis-Christensen et al., 1972; Wilcox and Scherrer, 1972; Svalgaard and Wilcox, 1975). The IMF has been found to govern the interaction between the solar wind and the geomagnetic field. Direct connection of IMF lines and the terrestrial field provides for transfer of solar wind kinetic energy to the stretched out geomagnetic tail. The geomagnetospheric configuration is dependent on the direction of the IMF. Different configurations have different magnetic signatures as measured on the ground in the terrestrial polar caps, and permit the determination of the sign of the azimuthal B component in the ecliptic plane.

Through use of this technique, Svalgaard (1972) inferred the sector polarity back to 1926 and suggested that the sector pattern time evolution follows similar patterns in each cycle. A two-sector pattern is characteristic of the approach to solar maximum, while a four-sector pattern has a high probability of occurrence during the approach to solar minimum. During most of the solar cycle a four-sector structure with a recurrence period near 27 days is apparent. Near sunspot maximum a superposed structure having polarity into the sun and a recurrence period of 28-29 days can be observed (Svalgaard and Wilcox, 1975). At this time it may be more difficult to discern the four-sector structure clearly, and therefore the observed structure appears to be composed of only two sectors. Sometime after solar maximum the four sector pattern becomes prominent again as the cycle progresses toward sunspot minimum. The reason for this behavior is not generally understood.

Altschuler et al. (1974) have analyzed the large scale photospheric magnetic field in terms of surface harmonics $P_n^m(\theta)\cos m\phi$ and $P_n^m(\theta)\sin m\phi$ for the years 1959 through 1972. They have found that for most of the time between 1959 and 1962, the dominant harmonic was a dipole lying in the plane of the equator ($n = m = 1$). This corresponds to one hemisphere of positive polarity and the other of negative polarity. There was also a significant zonal harmonic ($n = 2$, $m = 0$) in which both solar poles had the same magnetic polarity, opposite to that at the equator. At the end of 1962 and lasting through 1964, the structure ($n = m = 2$) with 4 sectors often became the dominant harmonic, largely because the dipole harmonic ($n = m = 1$) decreased in importance. In 1965 and 1966 in the post-minimum part of the solar cycle, the north-south dipole component ($n = 1$, $m = 0$) became significant. From the end of 1967 to 1970, the equatorial component ($n = m = 1$) was most often the dominant harmonic, particularly during the latter part of 1969. During this period a quadupole structure ($n = m = 2$) was also occasionally found. Rarely was there any significant zonal structure. The harmonic analysis of 1969-1972 gave similar results to that of 1959 to 1962, a solar cycle earlier. Early in 1972 the $n = m = 5$ harmonic became dominant and remained so through the August 1972 flares. Rapid changes in global harmonics suggested to these authors that either the global field is not very deep or that very strong fluid flows couple the photosphere with deeper layers.

The analyses of Ness and Wilcox (1966) and Wilcox and Ness (1967) in comparing IMP 1 IMF observations and photospheric magnetic fields showed a high degree of correlation between these fields and suggested that the interplanetary field provided a continuous mapping of the photospheric field within the heliographic latitudes of 10° and 20° north. Winters et al. (1969) made a similar comparison using Mariner 4 data. As already indicated, the field structure was relatively unstable during the flight of Mariner 4, and all auto and cross correlation coefficients were considerably less than those obtained from IMP 1. The results indicated that during this time interval the IMF was not a simple extension of the photospheric field at any solar latitude and suggested that the nozzle hypothesis of Davis (1965) may be more appropriate during times of unstable field structure. According to this hypothesis, the IMF is characteristic of the properties of a few localized regions in the lower corona.

Various efforts have been made to relate sector boundaries with other solar features. It was demonstrated that the regions of sector boundaries were relatively free of plages (Wilcox and Ness, 1967; Wilcox, 1968). Correlating sector data with radio observations of solar coronal active centers and condensations in the metric wavelengths, Martres et al., (1970) showed that sector boundaries are always located west of a coronal condensation, and active centers have the effect of systematically displacing a boundary to the east. Observed rigidly rotating patterns of green line emission (Fe XIV at 5303A) from the corona (Sykora, 1971; Antonucci and Svalgaard, 1974) have been associated with emission from plasma condensation trapped on closed field lines across the rigidly rotating solar sector boundaries (Wilcox and Howard, 1968). Wilcox and Svalgaard (1974) have found that the persistent large scale coronal magnetic structure associated with a sector boundary consists of a magnetic arcade loop structure extending from one solar polar region to the other in approximately a north-south direction.

Hansen et al. (1974) discovered a correlation between patterns of paired coronal streamers in opposite hemispheres and the IMF sector boundaries. This work was extended by Howard and Koomen (1974), who observed the alternation of northern and southern hemisphere streamers, frequently separated by equatorial fans, on the east limb of the sun. They concluded that for most of 1972 there was a stable four-sectored coronal structure produced by two northern hemisphere streamers 180° apart in longitude and a similar pair of southern streamers. Toward the end of 1972 this pattern evolved into a two-sectored structure with a single northern and a single southern streamer, separated by 180° in longitude. This structure was observed to remain stable during most of 1973. Howard and Koomen further found that the transition from northern to southern streamer corresponded to a -/+ or toward/away sector boundary passage, and the southern to northern streamer transition was similarly associated with a +/- sector boundary passage.

Svalgaard et al. (1974) developed a phenomenological model combining the large scale polar field and solar sector structure which suggests that sector boundaries form between regions of opposite polarity resulting from the superposition of three large scale field patterns. Between regions with oppositely directed open field lines, neutral or current sheets must occur, and it is these neutral sheets that constitute the sector boundaries (the intersection of these sheets with the ecliptic plane are observed by spacecraft as sector boundaries

(Wilcox, 1968)). Schulz (1973) proposed a similar model based on theoretical considerations. In this interpretation of the sector structure, the solar wind extends the heliomagnetic equator into a warped annular neutral surface which intersects the ecliptic along corotating arcs which the observer interprets as sector boundaries. An inclination of the solar magnetic axis to the rotation axis would cause the neutral surface to wobble, creating a two-sector pattern. A quadrupole contribution is required to account for four sectors.

Among other recent theoretical work on sector structure is that of Wolff (1974) who in a mostly qualitative theory considers long period oscillations that involve the entire mass of the sun and rotate like rigid bodies. These oscillations drive convection flows of global scale which then organize photospheric and coronal magnetic fields into patterns which rotate rigidly. The rising convection creates the magnetic arcade structures in the corona and unipolar photospheric regions on each side by dynamo action. These regions are then the sources of the sector structure. Stix (1974) has studied solutions of the kinematic dynamo theory that predict longitude-dependent modes. He concludes that while the axially symmetric dipole-type field will generally dominate solar magnetism, non-linear coupling of modes will be present. The same agents which maintain the axisymmetric mean field, namely non-uniform rotation and cyclonic turbulence, also generate non-axisymmetric large scale fields. The non-axisymmetric fields are rigid structures drifting in longitude. These are assumed to represent magnetic sectors. Stix also suggests that an alternative explanation is that the sector structure might be a consequence of an Alfvén wave modified by rotation (Roberts and Stix, 1972) such as has been suggested to be the cause of the westward drift of the geomagnetic field (Hide, 1966). Suess (1975) has also considered magnetic sectors as slow hydromagnetic waves controlled by solar rotation, toroidal magnetic fields and by stratification within the solar convection zone.

Whatever the mechanism that produces the IMF sector pattern, it remains that the sector pattern is the dominant large-scale magnetic feature of the interplanetary medium throughout the region that has been explored by spacecraft. Fisk and VanHollebeke (1972) have inferred from cosmic ray electron observations that the interplanetary sector pattern persists out to ~30 AU. Other large scale variations of the magnetic field within certain sectors have been observed by numerous investigators and correlated with high-speed plasma streams in the solar wind. These features will be discussed in the following section.

5. Stream Structure of the Solar Wind

As described in Section I.2, the existence of streams of particles from the sun in interplanetary space was inferred to account for geomagnetic disturbance variations observed at the surface of the earth. The concept of long-lived, recurrent streams developed as a result of the so-called 27-day recurrence tendency noted in geomagnetic records. Pioneering investigations of this tendency consisted of time pattern studies by Mauder (1904, 1905, 1916) and Bartels (1932, 1934) and superposed epoch studies by Chree (1912, 1913) and Chree and Stagg (1927). Bartels (1945, 1951, 1958) assumed that the disturbances which showed the 27-day recurrence tendency were produced by enhanced radiation emitted from regions on the sun that he called M-regions. Some geomagnetic disturbances were associated with solar flare activity, and delay time calculations gave velocities for stream particles between 400 and 1000 km/sec, with the higher velocities associated with major geomagnetic storms (Mustel, 1961). Chapman (1963) discussed numerous characteristics of such a stream, including its lateral extent.

High-speed plasma streams were first identified in situ in the Mariner 2 data of 1962 (Neugebauer and Snyder, 1966). Various correlations of the plasma and magnetic field measurements on IMP 1 (Wilcox and Ness, 1965), Vela 3 (Ness et al., 1971a) and Mariner 2 (Coleman et al., 1966) have shown that each high speed stream has a predominant magnetic polarity, with one or more streams occurring within a single magnetic sector. Not every magnetic sector contains a high-speed stream, however. The magnetic field magnitude is found to be enhanced in the leading part of a stream, which is the high velocity, high density (compression) region, and reduced in the trailing part, which is the low velocity, low density (rarefaction) region. These features have been predicted in models by Sakurai (1971), Matsuda and Sakurai (1972), Urch (1972) and Nakagawa and Wellck (1973).

Hundhausen (1972) has reviewed the properties of high-speed streams, stream-stream interaction and the association of these properties with recurrent structural features of IMF sectors. Burlaga (1974, 1975) has studied the structure of corotating streams and has identified characteristic regions in the structure. The "interaction" region consists generally of the rising part of the speed profile, extending from a point ahead of the onset of increasing velocity to somewhat behind the velocity maximum. In this region density, temperature and magnetic field strength reach relatively high values. The region of enhanced density (compressed region) is displaced ahead of the region of enhanced temperature (hot spot). The interaction region is generated in the collision that results when a faster stream of plasma overtakes a slower one. At 1 AU the compressed region and the hot spot are separated by a thin boundary called "the stream interface". Ahead of the interface, swept up ambient material is deflected to the west while stream material behind the interface slips to the east. In the region behind V_{max} the density and temperature are relatively low. This is referred to as the "rarefaction" region.

Figure 6, which is taken from Siscoe (1972) and is based on Pioneer 6 hourly average data, shows some of these features. This figure has been included because a clear understanding of the plasma and field variations through a typical stream will facilitate the correct interpretation of the magnetic field observations that are

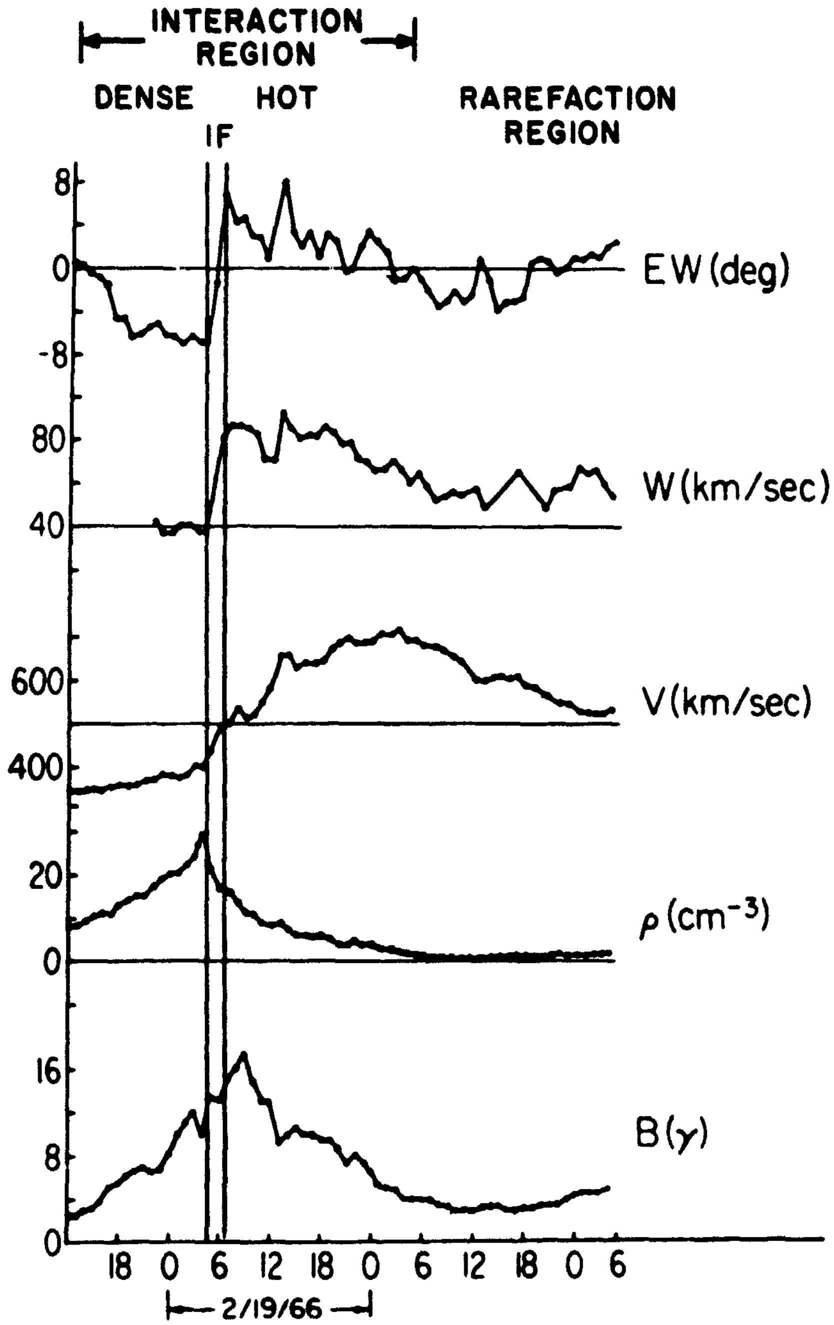

Figure 6. Illustration of the characteristic field and plasma variations through a simple corotating interplanetary stream. The stream interface (IF) separates the high density and high temperature portions of the interaction region ahead of the high velocity stream (Pioneer 6 observations – Siscoe, 1972).

the subject of this study, although in reality many streams are more complex in structure and display atypical properties. One sees in Figure 6 that the peak in the magnetic field intensity follows the peak in the density by a few hours, falling roughly in the region of highest temperature, which is represented in Figure 6 by the proton thermal speed $W = 4 \sqrt{T}$, with T in units of kilo degrees Kelvin. The magnetic field intensity is high because of the compression in this region, but the peak in B does not coincide with the peak in density ρ, as expected on a purely kinematic basis, for reasons not yet completely understood. This part of the interaction region, where the flow speed V is rising to its peak value, can be seen then to be the region where elevated pressure $P = B^2/8\pi + nkT$ is concentrated. It is also usually found that the magnetic field direction fluctuates considerably in the interaction region (Davis et al., 1966; Coleman, 1968; Burlaga et al., 1971). Finally, Figure 6 also shows the westward deflection ahead of the stream interface, represented by the double vertical lines, and one seen that in the region of declining V, the density ρ falls to very low values, below the prestream values; this is the rarefaction region mentioned above.

The search for the source of high-speed solar wind streams has now centered on the study of coronal holes. These regions of the sun are seen as open features at soft x-ray wavelengths, devoid of x-ray emission and bounded by apparently divergent coronal loop structure (Vaiana et al., 1973a). The long term development of the corona has been studied using synoptic charts formed from images of the solar corona from an x-ray experiment on the Apollo telescope mount, using a filter of bandpass 3-32A, 44-54A (Variana et al., 1973b; Timothy et al., 1975). The topology of photospheric magnetic fields associated with these features suggests that holes are formed when the remnants of active region fields, emerging in both hemispheres over a period of several solar rotations, combine to form a large area of essentially unipolar field (Timothy et al., 1975). Remnants of opposite polarity fields surround these features, resulting in a divergent magnetic configuration at the hole boundaries. Holes are seen to form and evolve as long as this large-scale divergent field pattern is reinforced and to close when other large-scale remnants occur which tend to disrupt the general field pattern.

Coronal holes are not only regions devoid of soft x-ray emission, but are also seen as areas of reduced electron density in K-coronameter data (Altschuler et al., 1972) and metric radio scans (Dulk and Sheridan, 1974) and reduced emission in certain extreme ultraviolet (EUV) lines (Munro and Withbroe, 1972; Neupert and Pizzo, 1974) and in the D_3 (5876A) line and 10830A line of Helium I (Harvey et al., 1974). Analysis of the physical characteristics of a hole have shown it to have a reduced emission scale height, approximately one-half that of other coronal structures. Holes have been shown to be cool compared with the large-scale closed structure surrounding them (Timothy et al., 1975).

A correlation of coronal holes with solar wind velocity observations at 1 AU by IMP 7 (Krieger et al., 1975) during 150 days in 1973 found two recurrent streams associated with coronal holes and two originating in the high corona ($20\text{-}50R_\odot$) over faint x-ray emission areas. Such areas were also found without associated high-speed streams, however. Nolte et al. (1975) have studied the association of high-speed streams with coronal holes during the Skylab period, including data through the end of 1974, and have found that there are no large equatorial holes without an associated high-speed stream. Furthermore, the area of the equatorial region of coronal holes is highly correlated with the maximum velocity observed in the associated streams near 1 AU.

The study of high-speed streams and stream interactions in the interplanetary medium is of great importance not only to solar physics and for a complete understanding of interplanetary dynamical processes, but also because the factors that most influence geomagnetic activity are probably related to streams and determined by the dynamics of streams (Burlaga, 1974). The importance of both a southward magnetic field component (Dungey, 1961; Fairfield and Cahill, 1966; Kane, 1974; Hirshberg and Colburn, 1969) and magnetic field fluctuations (Coleman et al., 1966; Garrett, 1973; Jones et al., 1974) have been recognized, and interplanetary shock signatures play a fairly well understood role with respect to storm sudden commencement (SSC) events (Colburn and Sonett, 1966; Taylor, 1969; Burlaga and Ogilvie, 1969).

The significance to geomagnetic activity of other solar wind parameters is still debated. Bobrov (1973) has suggested that geomagnetic activity is high during the passage of the interaction regions of both corotating and flare-associated streams because both negative B_z and the fluctuations in $\vec{B}$ are high in the interaction region. He notes that recurrent geomagnetic storms do not terminate with the return of IMF intensity to quiet levels but continue for several days. He shows that continued high values observed in the 3-hour geomagnetic activity index K_p in the trailing part of corotating streams is due to the presence of large fluctuations in $\vec{B}$ in that region of the stream.

A study of the dynamics of streams is also of importance to the determination of the radial variation of the IMF with distance from the sun. At least some of the variability among the various measurements of the radial distance dependence of the IMF azimuthal component can be attributed to the variability in the characteristics of corotating plasma streams of different velocities and to the complex structuring of the interplanetary medium that results from the collisions between such streams (Rosenberg, 1970). Streams not only interact to produce changes in the state of the medium, but also carry variations in the source out into the medium. Burlaga and Barouch (1975) have shown that variations in the initial value of the azimuthal angle of the magnetic field near the sun can also contribute to the lack of consistency among measurements at greater distances from the sun.

6. Variations of the IMF with Heliographic Latitude

Measurements of the IMF to date have been limited to the region within ± 7-1/4° of the solar equatorial plane because those are the limits of the earth's excursion above and below that plane as it orbits the sun. Even with the region of observation so severly restricted, two major variations of the IMF with heliographic latitude have been detected. These are the "dominant polarity" effect and the "north-south component" effect.

Rosenberg and Coleman (1969) found evidence for the dominant polarity effect in an analysis of magnetic field measurements by Mariners 2, 4 and 5 and OGO 5 between 0.7 and 1.5 AU during the period from 1962 to 1969. The dominant sector polarity was found to be inward toward the sun (negative polarity) above the solar equatorial (SEQ) plane and outwards (positive polarity) below this plane. It was noted that the general dipolar field of the sun had been toward the sun over the northern solar hemisphere since the last previous maximum in solar activity (1958) and outward over the southern hemisphere during this period. This suggested that the dominant polarity of the IMF in the northern and southern hemispheres of interplanetary space is simply that of the sun's dipolar field over the same hemisphere of the photosphere.

This work was extended by Fairfield and Ness (1974). They found that observations during 1971, 1972 did not confirm the same pattern found by Rosenberg and Coleman, but rather were consistent with a reversal of the sun's dipole field in 1971. Such a reversal was observed in 1971 by Howard (1972). King (1975) has studied a composite data set and has established the following sequence of events.

During 1965-1967 negative polarity was found to dominate at both northerly and equatorial latitudes, with positive polarity dominant at southerly latitudes, in agreement with the results of Rosenberg and Coleman. The negative polarity dominance at northern latitudes was found to be stronger than the positive polarity dominance at southern latitudes. During the solar maximum period 1968-1969, negative polarity was dominant at all latitudes. In the next two year interval, 1970-1971, the positive polarity dominance was reasserted at southern latitudes, but neither polarity was dominant in the northern hemisphere. Negative polarity was anomalously dominant during the quarters of passage of the earth from negative to positive latitudes, however. During the period 1972-1974, approaching solar minimum, the dominant polarity effect was found by King to have reversed from its pre-solar maximum pattern. The new pattern was more symmetric, with the negative polarity dominance at southerly latitudes and the positive polarity dominance at northerly latitudes approximately equal in terms of percent of total observations, while at equatorial latitudes neither was found to dominate.

An independent confirmation of this latitude dependence of the interplanetary field polarity was obtained studying the semiannual variation of geomagnetic activity (Russell and McPherron, 1973). Observations by the HEOS satellites (Hedgecock, 1975c) also independently confirmed the change to positive polarity dominance above the solar equatorial plane during 1971, and Rosenberg (1975) has confirmed the 1972-73 dominant polarity configuration using Pioneer 10 data.

The north-south component effect has been studied by Coleman et al. (1960), Ness and Wilcox (1964), Davis et al. (1966), Coleman and Rosenberg (1971), Rosenberg et al. (1971, 1973) and Hedgecock (1975c) and discussed by Davis (1972). The characteristics of this effect are summarized as follows (Coleman and Rosenberg, 1971). Given the IMF relative to a spherical, polar coordinate system with polar axis along the sun's axis of rotation (i.e., $\vec{B} = B_r \hat{r} + B_\theta \hat{\theta} + B_\phi \hat{\phi}$), for a field of outward (positive) sector polarity, the mean value of B_θ is less than zero northward of the heliographic equator and is greater than zero southward of the equator. For inward (negative) sector polarity, the sign of mean B_θ is reversed. Since spherical coordinates were used for the analysis, the result means a skewing of the IMF relative to a radius vector from the sun to the point of observation. The sense of the observed mean B_θ implied that the lines of force above and below the equatorial plane deviated from the radial direction by increasingly bending away from the equatorial plane with increasing heliocentric distance. The analysis indicated that a mean value of 0.2-0.4 γ at ± 7.5° and 1 AU may be typical for $|B_\theta|$.

Possible causes for the behavior of B_θ include (a) disturbance in the interplanetary medium, (b) the nonradial flow forces in steady state models for propagation of the solar wind, and (c) the effect of the greater activity and pressure from a solar hemisphere's midlatitude region in bending the interplanetary field lines near the solar equatorial plane (Coleman and Rosenberg, 1971; Rosenberg et al., 1973). Rosenberg et al. (1971, 1973) noted that while the effect was strong during the period of low to moderate solar activity (1965-1966), as solar maximum was approached (1967-1968) the effect became less pronounced. It was suggested that this could be due to the disruptive influence of midlatitude streams in the opposite hemisphere.

Hedgecock (1975c) has examined a composite Explorer data set as well as Heos data in the period June 1965 to March 1970 and September 1970 to December 1973. He concludes that a correlation of B_θ with heliographic latitude in the same sense as Rosenberg's result was probable in 1965 and late 1966-1967. However, no statistically significant correlation could be found for the 1969-1974 period. King (private communication) has also studied the effect using the larger composite data set contained in the NSSDC IMF Data Book (King, 1975b) and has found the skewing effect in 1966-1968 data, a possible effect in the southern hemisphere but confused in the northern hemisphere in 1969-1971 and no significant effect in 1972-1974. This essentially confirms the results of Hedgecock using a larger body of data, as well as the earlier work of Rosenberg and co-workers.

Mariani et al. (1974) have looked for a latitude effect in the magnetic field magnitude using data from a variety of spacecraft near earth, normalized to standard conditions. No clear trend was found. King (1975) also found no latitude dependence for the long time-averaged field magnitudes, but found that yearly-averaged magnitudes of separated positive and negative polarity field vectors show separate solar cycle variation, while the same averages of the combined set of vectors show virtually no solar cycle variation. Hedgecock (1975c) has found that the mean field strength and the amplitude of the directional fluctuation of the IMF showed no significant variation with heliographic latitude, although significant differences between hemispheres may have existed in 1969.

7. Fluctuations of the IMF

In addition to the large scale structure of the interplanetary magnetic field, there has been considerable interest in and study of interplanetary mesoscale and microscale field phenomena. To a degree such phenomena are related to the large scale structure in the sense that undoubtedly the colliding plasma streams in interplanetary space provide the source for at least some of the observed microscale features. As introduced by Burlaga, the term microscale includes events and/or structures with an observed duration or period of ≤ one hour. This includes directional discontinuities and shock waves, and hydromagnetic and electromagnetic waves with periods less than one hour ($f \geq 2.8 \times 10^{-4}$ Hz). Mesoscale phenomena include long period ($\tau \sim$ one hour to one day) Alfvén waves as observed initially in the Mariner 2 data (Unti and Neugebauer, 1968; Coleman, 1967, 1968), and analyzed extensively by Belcher et al. (1969) and Belcher and Davis (1971). In addition to these studies, other extensive discussions and reviews of various microscale and mesoscale magnetic field phenomena include Coleman (1968), Burlaga (1968, 1969, 1971a, b), Scarf (1970), Võlk and Alpers (1973), Barnes and Hollweg (1974), Hollweg (1974, 1975), Burlaga and Ness (1969), Burlaga and Turner (1974), Lee and Lerche (1975), and Võlk (1975).

The term fluctuation has been used to describe almost every type of variation of the magnetic field relative to an average background field. As discussed by Coleman (1968), Burlaga (1972), Smith (1974) and others, the total field time series usually contains stream-stream interactions, shocks, directional discontinuities, hydromagnetic waves and higher frequency phenomena, although the power spectrum may be dominated by one particular type of structural variation at a given time with the dominant type changing with time. One method that has been utilized to study long period magnetic field fluctuations has been the computation of variances or standard deviations of the field magnitude and the field components (both combined, as in the Pythagorean mean, and separately). Additional techniques which have been employed are power spectrum analysis, which gives the frequency dependence of the fluctuations, and the correlation of changes in the field with changes in solar wind velocity. The latter approach has been used in attempts to identify Alfvén waves in the interplanetary medium (Coleman, 1966; Belcher et al., 1969; Belcher and Davis, 1971; Belcher and Burchsted, 1974; Burlaga and Turner, 1974).

Time variations with periods of a few hours or less appear to be dominated by waves and discontinuities, while those with periods of 24 hours or longer seem to be dominated by stream interaction effects (Coleman, 1968; Goldstein and Siscoe, 1972). Thus the choice of time scale in the computation of variances (or standard deviations) from magnetic field measurements permits a limited degree of separation of contributing phenomena. A study of the changes in these field parameters with heliocentric distance can indicate whether or not the interplanetary field is becoming more or less irregular on a given time (or, equivalently, length) scale with increasing radial distance (Smith, 1974).

IMF fluctuations are of importance in cosmic ray propagation theory. It is believed that they play the role of scattering centers for the particles, producing a spatial gradient in cosmic ray intensities as well as a modulation with solar activity. Fisk and Sari (1973) argue that two correlation lengths for IMF fluctuations must be considered. For particles with gyroradii large enough to encounter and be scattered by large-scale tangential discontinuities in the field (particles of energy $\geq$ several GeV/nucleon), the appropriate correlation length is simply the mean spatial separation between discontinuities $L \simeq 2 \times 10^{11}$ cm (Burlaga, 1969). This is the correlation length that is inferred from the total power observed in field fluctuations (Jokipii and Coleman, 1968). Low energy particles ($E \leq 100$ MeV/nucleon), however, appear to be unaffected by large-scale tangential discontinuities (Sari, 1972, 1975). They respond only to smaller scale fluctuations between the tangential discontinuities that are mainly propagating wave disturbances and rotational discontinuities. These fluctuations have a correlation length of $L \simeq 2 \times 10^{10}$ cm, inferred from the shape of the power spectrum. For $V_{sw} =$ 350 km/sec, $B = 5\gamma$, and $f_c \simeq 3 \times 10^{-5}$ Hz (f_c = the frequency where the observed power spectrum shows a break from a flat spectrum to a fairly steep inverse power law dependence on frequency), $L = 2 \times 10^{11}$ cm is roughly equal to the gyroradius of a 3 GeV particle and $L = 2 \times 10^{10}$ cm is comparable to the gyroradius of a 50 MeV proton. Jokipii (1966) has also argued that scattering is due to irregularities with scale sizes equal to the cyclotron radius of a particle.

There has been considerable interest, both theoretical and experimental, in the character of IMF fluctuations at various heliocentric distances. Parker (1965) and Dessler (1967) predicted that relative magnetic field magnitude fluctuations $\Delta B/B$ for undamped waves would increase with distance from the sun up to a shock-limited ratio of $\Delta B/B = 1$, which Coleman et al. (1969) suggested could occur at about 4.3 AU. Such an increase could occur for transverse Alfvén waves as well as for compressional fast mode waves. For the case of the limit (particle pressure ignored relative to magnetic pressure), $\Delta B/B \propto r$. Thus $\Delta B/B$ would essentially double between the orbits of Mercury and Earth. Whang (1973) constructed a model for the propagation of microscale Alfvén waves in a spiral field in which a attenuation of the waves has been included. This model predicts that the relative amplitude of Alfvénic fluctuations has a maximum near 1 AU, with a variation of only a few percent between 0.4 and 5 AU.

Linear hydromagnetic theory predicts three types of waves: fast, slow and Alfvén waves (Burlaga, 1972; Völk, 1975). It is possible that all three are present at one time or another in the solar wind, as well as larger amplitude waves. There have been only a few visual identifications of the signatures of these types of waves reported in the literature (Burlaga, 1968, 1971b; Unti and Neugebauer, 1968). The observed waves are very seldom periodic and are almost always nonlinear, and they are probably coupled with one another.

Coleman (1966, 1967) noted a high value for the coherence he obtained from the cross spectrum for interplanetary V and $\vec{B}$ data, and he noted that the phase difference at a particular frequency obtained from these cross spectra was $\sim 180°$ when $\vec{B}$ was away from the sun and $\sim 0°$ when $\vec{B}$ was toward the sun. He concluded that fast waves or Alfvén waves (or both) were present but could not distinguish between the two. Belcher et al. (1969) found in the Mariner 5 data that the bulk speed and radial component of the magnetic field were strongly correlated 30% of the time, and argued that the fluctuations during these times were primarily Alfvén waves. The study of such waves with "periods" of two to three hours and less has been extended by Belcher and Davis (1971), Belcher (1971), Martin et al. (1973), Belcher (1974) and Belcher and Solodyna (1974). The only study of the radial dependence of this type of fluctuation available in the literature to date is the work of Belcher and Burchsted (1974), who used plasma and field data from Mariners 4 and 5 between 0.7 and 1.6 AU. They concluded that their results were consistent with no damping or local generation of Alfvén waves over this range of heliocentric distance, and that local sources or sinks for these waves produce at most only relatively small perturbations on the ambient level of Alfvénic fluctuations.

There have been other efforts to measure the radial distance dependence of IMF fluctuations using standard deviations or variances of the field components and magnitude. Neugebauer (1975a) has combined the results from Mariners 4 and 5 and Pioneer 10 for $\sigma^2(B)$ and $\sigma^2(B_r)$ and has shown that the data from the three spacecraft are in rough agreement with each other despite different methods of calculation. The combined data for the variances of both B and B_r were found to be roughly consistent with r^{-4} radial distance dependences, primarily because of the strong domination of Pioneer 10 data. Taken separately, the Mariner 4 data set in particular exhibits a less steep decrease with increasing heliocentric distance.

The fact that the Pioneer 10 observations of $\sigma^2(B_r)$ follow an r^{-4} dependence on radial distance (Smith, 1974), when taken with the observed r^{-2} dependence for B_r, implies that $\Delta B_r/B_r$ is roughly independent of distance from the sun for the ranges studied. In contrast, the Mariner 4 observations of a more rapid fall off in field intensity ($B \propto r^{-1.25}$) than in fluctuations ($\sigma_x \propto r^{-0.54}$) suggested that $\Delta B/B$ increases in proportion to $r^{0.7}$ between 1 and 1.5 AU (Coleman et al., 1969) for fluctuations with periods shorter than one day. It was from this rate of increase that the estimate was made for achieving a value of $\Delta B/B = 1$ at a distance of $r \simeq 4.3$ AU. Since σ_x is actually a measure of the power in fluctuations parallel to the mean field, the Mariner 4 results suggested that there is relative growth of the compressional fluctuations and a weaker relative decrease in fluctuations transverse to the mean field with increasing heliocentric distance. This suggests that the compressive mode tends to become dominant and the Alfvén mode less significant as one moves away from the sun beyond 1 AU. The most recent Pioneer 10 analysis suggests that $\Delta B/B = 1$ will be reached at $r = 10.7$ AU, with a growing compressional mode at a frequency of one cycle per solar rotation (Rosenberg et al., 1975).

At all radial distances sampled, fluctuations in field direction were found to be more important than fluctuations in field magnitude. All three spacecraft found roughly equal power in the fluctuations along the three components B_r, B_ϕ and B_θ, and this power in component fluctuations was a factor of 2 to 10 greater than the power in the magnitude variations.

The application of power spectrum analysis to the study of magnetic field fluctuations yields not only the power in fluctuations along various directions in space and in the total field but also the variation of that power with frequency. Such an analysis can be further augmented to provide coherence and phase information concerning the fluctuations and hence can be a valuable tool in the identification of wave modes in the data. Published power spectral studies of the IMF include work by Coleman (1966, 1967, 1968), Ness et al. (1966), Siscoe et al. (1968), Sari and Ness (1969), Coleman et al. (1969), Russell et al. (1971), Sari (1972, 1975) and Blake and Belcher (1973). A discussion of the instrumental problems and other interpretational difficulties associated with such studies has been presented by Russell (1972).

The first IMF power spectra that were computed that show the variation in field fluctuation power with radial distance utilized Mariner 2 data (Coleman, 1968). A general increase in power across the spectrum (from 4×10^{-6} to 10^{-2} Hz) with decreasing radial distance from 1 to 0.87 AU was found for the total field, and increased power at the lowest frequencies for the radial component. The total power in the field magnitude increased by almost a factor of 2. Also spectra in the frequency range 10^{-6} to 10^{-2} Hz were computed from Mariner 4 measurements taken between 1 and 1.43 AU (Coleman et al., 1969). For both the total field and the radial component a decrease in power with increasing radial distance at almost every spectral estimate was found. However, a greater decrease in integrated power was found for the B_r component than for the total field. In addition, decreases by more than a factor of two in integrated power were found for the B_θ and B_ϕ components.

Blake and Belcher (1973) have computed power spectral densities for IMF fluctuations with frequencies between 1.16×10^{-5} Hz and 2.96×10^{-3} Hz using Mariners 4 and 5 168.75 second averages, with eight days of data per spectrum. Once again except for a general decrease in the overall power level with increasing distance from the sun, these spectra show no striking dependence on heliocentric distance between 0.7 and 1.6 AU. The total power in components (trace of the power spectral matrix) was found to be usually an order of magnitude greater than that in field strength at all frequencies, and the power in the direction of maximum variation a factor of two to three greater than in the minimum fluctuation direction. Most of the total component spectra show a distinct break at a frequency of about 10^{-4} Hz (Jokipii and Coleman, 1968), with the fall off of the total power in components above that frequency roughly as $f^{-1.6}$ or slightly faster and below that frequency as $f^{-1.2}$ or slightly faster.

Waves previously observed in the interplanetary medium in the frequency range 0.01 - 10 Hz have been either identified as associated with the earth's bow shock (Holzer et al., 1966; Heppner, et al., 1967; Fairfield, 1969, 1974; Greenstadt et al., 1970; Childers and Russell, 1972) or with interplanetary shocks (Fairfield, 1974), and were observed in association with the wake of the moon in the solar wind (Ness and Schatten, 1969; Krall and Tidman, 1969; Whang and Ness, 1970). They also have recently been observed near Mercury's bow shock (Fairfield and Behannon, 1975).

Unti et al. (1973) and Neugebauer (1974, 1975b) have presented power spectra of proton flux density nv for the frequency range 0.1 to 10 Hz from observations of OGO 5. These spectra occasionally show a distinct hump or shoulder in the range 0.1 to 1 Hz. These humps indicate enhanced levels of density fluctuation at small spatial scales of the order of the proton cyclotron radius. These observations include cases when OGO 5 was not connected to the bow shock by the IMF. Thus these fluctuations may be the signature of one or more solar wind plasma instabilities (Hollweg, 1975). They may be due to heat flux instabilities (Volk, 1975). These plasma fluctuation observations have not been extended to cover a range of heliocentric distance, but Unti et al. (1973) point out that these spectral features bear a strong resemblance to the spectrum predicted from radio scintillation observations by Matheson and Little (1971).

Belcher and Davis (1971) and Ness et al. (1971) have suggested that the properties of the interplanetary microstructure are correlated with the large-scale solar wind stream structure. The latter study bases the association on the observations by Burlaga et al. (1969) that magnetic field fluctuations with periods in the range 1 min. to 1 hour are related to the proton beta, together with observations of a rise in proton beta with rising flow speed. This leads to the expectation of quiet fields at low flow speeds and disturbed fields at high speeds. As discussed in Section 5, Bobrov (1973) has inferred high fluctuation levels in both the interaction region and the trailing part of corotating streams from studies of geomagnetic activity.

Discontinuities in the IMF have been studied and described in varying degrees of detail by Ness et al. (1966), Colburn and Sonett (1966), Burlaga and Ness (1968, 1969), Siscoe et al. (1968), Belcher and Solodyna (1974), Burlaga (1969, 1971a, b) Turner and Siscoe (1971), Smith (1973a, b), and others. These studies have shown that these discontinuities pass a spacecraft at the rate of approximately one per hour at 1 AU. From studies of Pioneer 6 data, using the definition that the field direction must change by more than 30° in less than 30 seconds, Burlaga concluded that most of the directional discontinuities found in that study were tangential (Burlaga, 1971a) rather than rotational discontinuities. He further concluded that the Pioneer 6 field and plasma data were not consistent with directional discontinuities originating primarily in the collision of fast streams with slower plasma, since their occurrence rate was only slightly higher in regions of increasing bulk speed than elsewhere. Demonstrating a possible radial gradient in the occurrence rate, he found 0.7 discontinuities/hour at 0.82 AU, 0.8 at 0.91 AU and 1.1 at 0.98 AU. He cautioned, however, that the higher rate nearer 1 AU could be in part or entirely due to better and more continuous data at 1 AU.

From an analysis of Pioneer 8 data, Mariani et al. (1973) reported an inverse relation between radial distance and the occurrence rate of discontinuities. The linear best fit to the observations suggests a rather steep gradient over the small range of 0.05 AU that was covered by the measurements. An alternative explanation in terms of a variation with heliographic latitude was suggested.

8. Investigation Objectives

The primary objective of this investigation was to perform the first comprehensive survey of the Mariner 10 IMF measurements during the initial traverse of the interplanetary medium between 1 and 0.46 AU. The Magnetic Field Experiment instrumentation and data analysis are briefly described in Chapter II. Of major interest in this work was the radial heliocentric distance dependence of the magnetic field, both magnitude and components, and its magnitude and total vector fluctuations, and of the occurrence rate of directional discontinuities. In addition, solar rotation statistical distributions were computed for the field magnitude, orientation angles and fluctuation parameters. The relationship of magnetic field characteristics to the large-scale plasma stream structure of the medium has been considered in the interpretation of the observations, as well as heliographic latitude effects. Both the results of the part of this investigation that concerns the large-scale properties of the IMF and a comparison of the results with previous results are presented in Chapter III.

The basic vector sampling rate of the Mariner 10 magnetometers was 25/sec. In the prime data mode, which was used almost exclusively during the primary mission, except for a period of approximately 5 days in early January, 1974, a full readout of this high rate was available. Thus with a Nyquist frequency of 12.5 Hz and a digitization noise level during IMF measurements of $6 \times 10^{-6}\ \gamma^2/\text{Hz}$, it has been possible to extend spectral studies in radial distance to 0.46 AU from the sun and to higher frequencies than previously achieved on deep-space probes with DC magnetometers. Because of this, the major interest in this first survey of the data was concentrated at frequencies above 0.01 Hz, since considerable spectral analysis of the IMF fluctuations at lower frequencies has already been performed in previous studies. The existence of sinusoidal, highly coherent fluctuations transverse to the magnetic field have been found by this study in this higher frequency range at all distances between 1 and 0.46 AU. The results of spectral and polarization analysis of these waves are presented in Chapter IV, along with the results on the variation of fluctuations with heliocentric distance and the relationship between the occurrence of fluctuations and the stream structure of the interplanetary medium.

A summary of the major results of this survey study is given in Chapter V, as well as a brief discussion of outstanding problems remaining concerning the temporal and spatial characteristics of the IMF.

9. Supporting Measurements

To facilitate the separation of time and space variations in the interpretation of the Mariner 10 IMF observations as well as to augment the Mariner 10 data in studies of the corotating structure of the interplanetary medium, measurements during the same time period by spacecraft in earth-orbit have been included in the analysis.

The primary source of comparative data has been the IMP 8 (Explorer 50) spacecraft, launched October 26, 1973. It was intended that the orbit be nearly circular, but the initial orbital characteristics were a perigee of 24.4 R_E, apogee of 44.5 R_E and period of 12.4 days. In early 1975 the orbit had a perigee of 23.2 R_E, apogee of 46.2 R_E and a period of 11.8 days. The IMP 8 Magnetic Field Experiments (Principal Investigator N. F. Ness) consists of a triaxial fluxgate magnetometer with reorientation flipper for zero level calibration and onboard data processing consisting of digital spin demodulation and 2-bit adaptive delta-modulation (Moyer, 1968). IMP 8 is a spin-stabilized spacecraft, and the magnetometer sensors are located on a rigid boom 4 m from the spin axis. The sampling rate of the experiment is 25/sec in the primary data mode, which was the mode used during the period of interest. The experiment operating ranges are $\pm$ 12γ, $\pm$ 36γ and $\pm$ 108γ with associated sensitivities of $\pm$ 0.05γ, $\pm$ 0.14γ and $\pm$ 0.42γ, respectively. The intrinsic sensor noise level is 0.025γ rms, and the accuracy of the IMF measurements is estimated to be ± 0.1 γ. The IMP 8 spacecraft nominally spends approximately 8 days out of its ~12 day period in the interplanetary medium (64% of the orbital period). For more detail on the IMP 8 experiment see Scearce et al. (1975).

To fill in the gaps when IMP 8 was not in the interplanetary medium, data from the HEOS spacecraft magnetic field experiment (Principal Investigator P. C. Hedgecock) were obtained from the National Space Science Data Center. HEOS 2 was launched January 31, 1972 into a highly eccentric orbit with the orbital plane nearly perpendicular to the earth's equatorial plane. The apogee was 37.6 R_E and the initial perigee height was 350 km (or 0.05 R_E), increasing to 5400 km (0.85 R_E) in mid 1973. The orbital period was 5.2 days, and the time spent in interplanetary space ranged between 50 - 75% of the orbital period. The spacecraft reentered the earth's atmosphere on August 2, 1974. Heos 1 started measurements on December 5, 1968, with a lower inclination orbit than Heos 2. It had a similar magnetometer to that on Heos 2 and was still in operation during the Mariner 10 flight. The data set available in the NSSDC is a combined set of Heos 1 and 2 observations. The Heos magnetometers have ranges of ± 16γ and ± 144γ with corresponding sensitivities of ± 0.25γ and ± 2 γ, respectively. The sampling rate is one vector/32 sec, with occasional higher rates on a limited duty cycle when core buffer storage is used. Additional details may be found in Hedgecock (1975a, b).

For a thorough analysis of the magnetized plasma in interplanetary space, both magnetic field and plasma measurements are necessary. The sunward facing plasma analyzer on Mariner 10 was designed to accept both electrons and positive ions, but unfortunately provided no data during the mission due to an unexplained electrical or mechanical failure. The rearward-looking analyzer, which accepts electrons in the energy range 13 to 715 eV, did provide measurements throughout the mission (Bridge et al., 1974; Ogilvie et al., 1974; Scudder, 1975). The IMF electron data analysis was in progress during this study of the magnetic field, so that only limited information concerning the gross character of the solar wind during the mission was available (Ogilvie and Scudder, private communication). Averaged plasma parameters for the first three months of the mission from measurements by the MIT experiments on IMP's 7 and 8 at 1 AU were made available to assist the interpretation (Lazarus, private communication).

Synoptic charts of photospheric magnetic fields for the Mariner 10 period were provided by the Hale Observatories, Pasadena, California. X-ray synoptic charts and coronal hole and high-speed stream correlation charts and tables were kindly provided by Dr. Jerome Nolte of American Science and Engineering Inc. in advance of publication for use as background for interpreting the IMP 8 and Mariner 10 observations.

CHAPTER II

MAGNETIC FIELD EXPERIMENT INSTRUMENTATION AND DATA ANALYSIS

1. General Instrument Description

The Magnetic Field Experiment on the Mariner 10 spacecraft consisted of two identical fluxgate magnetometer sensors which measured the magnetic field intensity along three mutually orthogonal axes simultaneously. The operating principle of fluxgate magnetometer sensors has been described in numerous publications (see Ness, 1970 for technical details and applications in space research of various types of magnetometers). Briefly, the fluxgate sensors used on Mariner 10 are saturable magnetic cores which are cyclically driven at a rate of approximately 10 kHz from positive to negative saturation by a solenoidal drive coil The presence of an external magnetic field results in an imbalance in core flux and generates even harmonics of the drive frequency in a secondary winding on the solenoid. The second harmonic content (at approximately 20 kHz). which is proportional to the ambient magnetic field, is detected to yield a magnetic field component parallel to each axis of each sensor. The ambient field components sensed by the three fluxgate sensors of a triaxial magnetometer can then be combined in the analysis to yield a measurement of the vector magnetic field. The three axes are sampled, digitized and buffer-stored in less than 15 ms within the instrument. The magnetometer sensors and drive electronics were manufactured by the Schonstedt Instrument Company of Reston, Virginia.

The two fluxgate magnetometers of the dual magnetometer system were located on a 5.8 m boom with the primary magnetometer at the end of the boom and the secondary sensor set positioned 2.3 m inboard of the primary. Location of the sensors at a distance from the main spacecraft structure reduced the level of spacecraft field detectable at the sensors. The dual system permitted analytic separation of the ambient field in space from the still significant and sometimes variable spacecraft field (Ness et al., 1971b; Neubauer, 1975). See section II.2 for further discussion. The outboard triaxial sensor set was equipped with a heat-initiated mechanical reorientation device or "flipper" to permit sensor zero offset calibration (McCarthy, 1970). This procedure will also be further described in II.2.

The magnetometer electronics provided a dual range capability that consisted of full scale equal to either ± 16γ (low range, high sensitivity) or ± 128γ (high range, low sensitivity). The range was selected either automatically or by ground command. Digitization of the analog sensor signals with ten-bit precision yielded quantization step sizes of 0.030γ and 0.26γ in the low and high ranges, respectively. A bias field switching capability was provided which permitted either the automatic or manual adding or subtracting of a known and fixed incremental magnetic field to extend the range of measurement while maintaining a uniform high sensitivity. A total of ± 255 bias steps using a factor of 12γ/step permitted a maximum extended range of ± 3188γ .

Figure 7 shows a block diagram of the experiment electronics. The major constituents are the analog sensor drive electronics and flipper and thermal control electronics, analog-to-digital converters, digital data processor and buffering

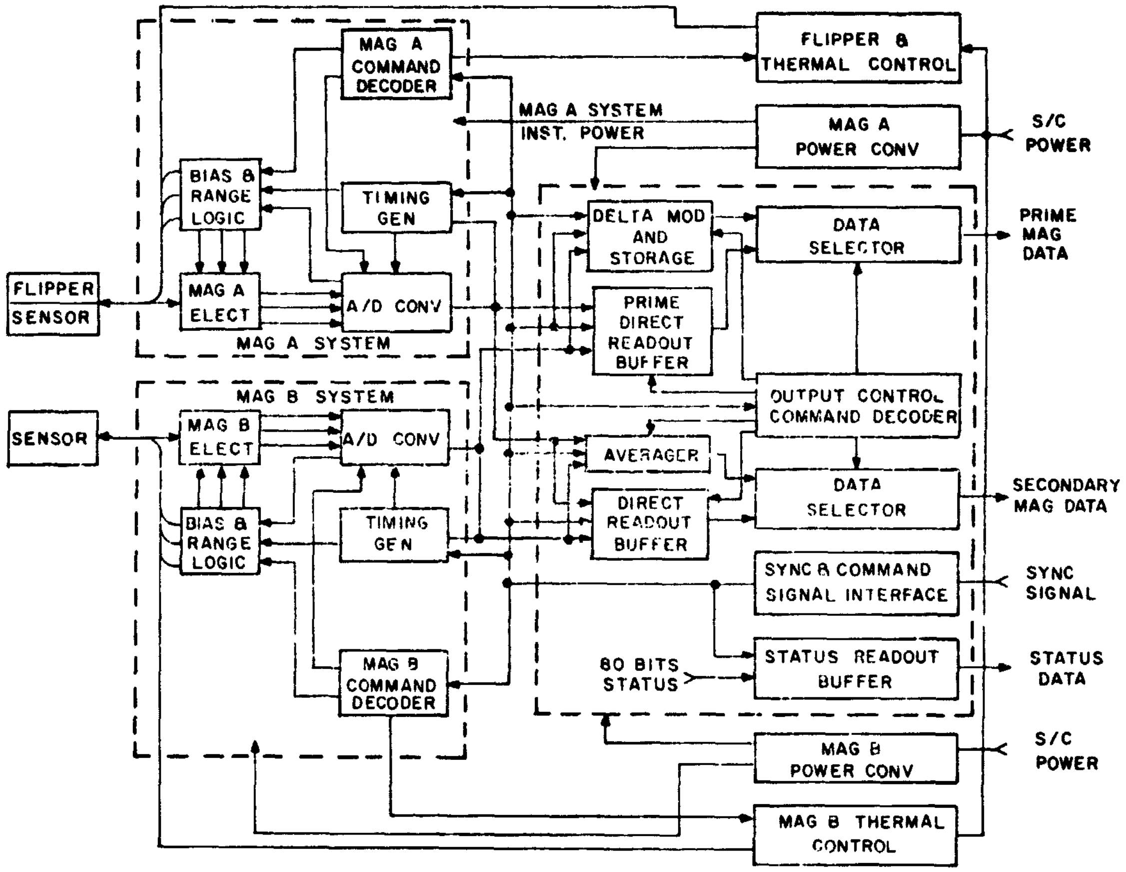

Figure 7. Block diagram of Mariner 10 Magnetic Field Experiment showing dual sensor and electronics systems. Each magnetometer was powered separately and had a separate data line to the spacecraft Flight Data Subsystem, but they were both controlled through a common sync and command interface point.

subsystems, housekeeping logic, command decoders and separate power converter and power input lines for each system. The experiment was designed to operate in either of two spacecraft data modes. The spacecraft Flight Data Subsystem operated in the primary or high-rate mode for 97% of the data telemetered to earth during the primary mission. Only high-rate mode data (1052 BPS for the Magnetic Field Experiment) are discussed in this study. In that mode the full 25 vector samples/sec data from the outboard magnetometer were sent directly to ground, while data from the inboard (spacecraft field monitor) magnetometer, also sampled at 25/sec, were summed over three successive samples on the spacecraft and the sums transmitted to ground with 12-bit resolution. Averages were subsequently computed from these sums in the ground data processing system. The data were then used to estimate the spacecraft magnetic field at the outer magnetometer position and subtracted from the total field measured at that position (Ness et al., 1971). The data analysis will be described in the following section.

In Figure 8 are shown frequency response characteristics of the Mariner 10 primary magnetometer sensors in the most sensitive range. Similar characteristics were also measured for the secondary (inboard) magnetometer. The uppermost curve (at low frequencies) gives the variation of the relative amplitudes (RA) of detected fluctuating magnetic fields with increasing frequency. It can be seen that the response of the sensors is essentially flat to approximately 0.5 Hz, with the

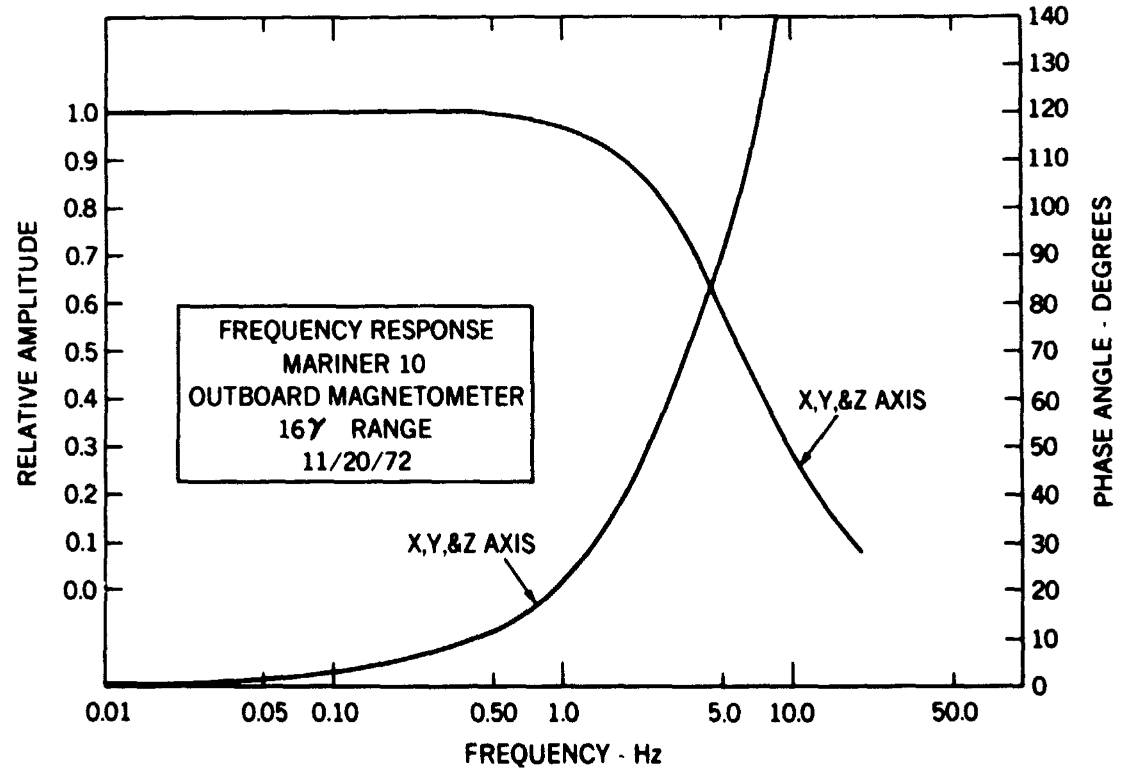

Figure 8. Measured transfer function characteristics of the prime magnetometer sensors in the most sensitive (± 16γ) range. Since the characteristics were almost identical for each sensor of the triaxial system, only single curves are shown.

3db point (RA = 0.707) occurring between 4 and 5 Hz. The lower curve (at low frequencies) shows the phase angle variation with increasing frequency for detected field fluctuations. A phase shift of 11° at 0.5 Hz is seen, increasing to 21° at 1 Hz and 90° at the 3db point.

Figure 9 illustrates the result of a typical intrinsic noise test for one of the flight sensors. The top panels shows the output of the sensor in gammas in a shielded environment at room temperature with no input. The fluctuations observed during the 41 sec run were due to intrinsic sensor noise. The distribution of 1024 measurements during the test period is shown in the large panel. The root mean square (rms) noise level of that particular sensor was determined to be 0.040γ. Individual flight sensor intrinsic noise levels ranged between 0.030 and 0.069γ.

In Figure 10 is shown the spectrum of the data displayed in Figure 9. The spectral shape is primarily due to the noise characteristics of the sensor and sensor electronics. The sensor noise spectrum is approximately proportional to f^{-1}, where f is the frequency. The attenuation due to the rolloff of the instrument also contributes to a lesser degree to the spectrum shown in Figure 10. The spectral density equivalent of an rms noise level of 0.040γ is $1.28 \times 10^{-4}\ \gamma^2/\mathrm{Hz}$. This can be compared with the digitization or quantization noise levels for each range, which are computed from (Russell, 1972; Beudat and Piersol, 1971)

$$P_{DN} = \frac{\Delta^2}{12 \times \text{bandwidth}}, \tag{II-1}$$

where $\Delta = 32/1024$ for the $\pm 16\gamma$ range and 256/1024 for the $\pm 128\gamma$ range, and bandwidth = 12.5 Hz. Values of $6.5 \times 10^{-6}\ \gamma^2/\mathrm{Hz}$ and $4.2 \times 10^{-4}\ \gamma^2/\mathrm{Hz}$ are obtained for the low and high ranges, respectively. These characteristics of the instrument will be considered further in Chapter IV in relation to interpretation of power spectra of IMF fluctuations. Additional technical details concerning the Mariner 10 magnetometer instrumentation may be found in a report by Seek et al. (1975).

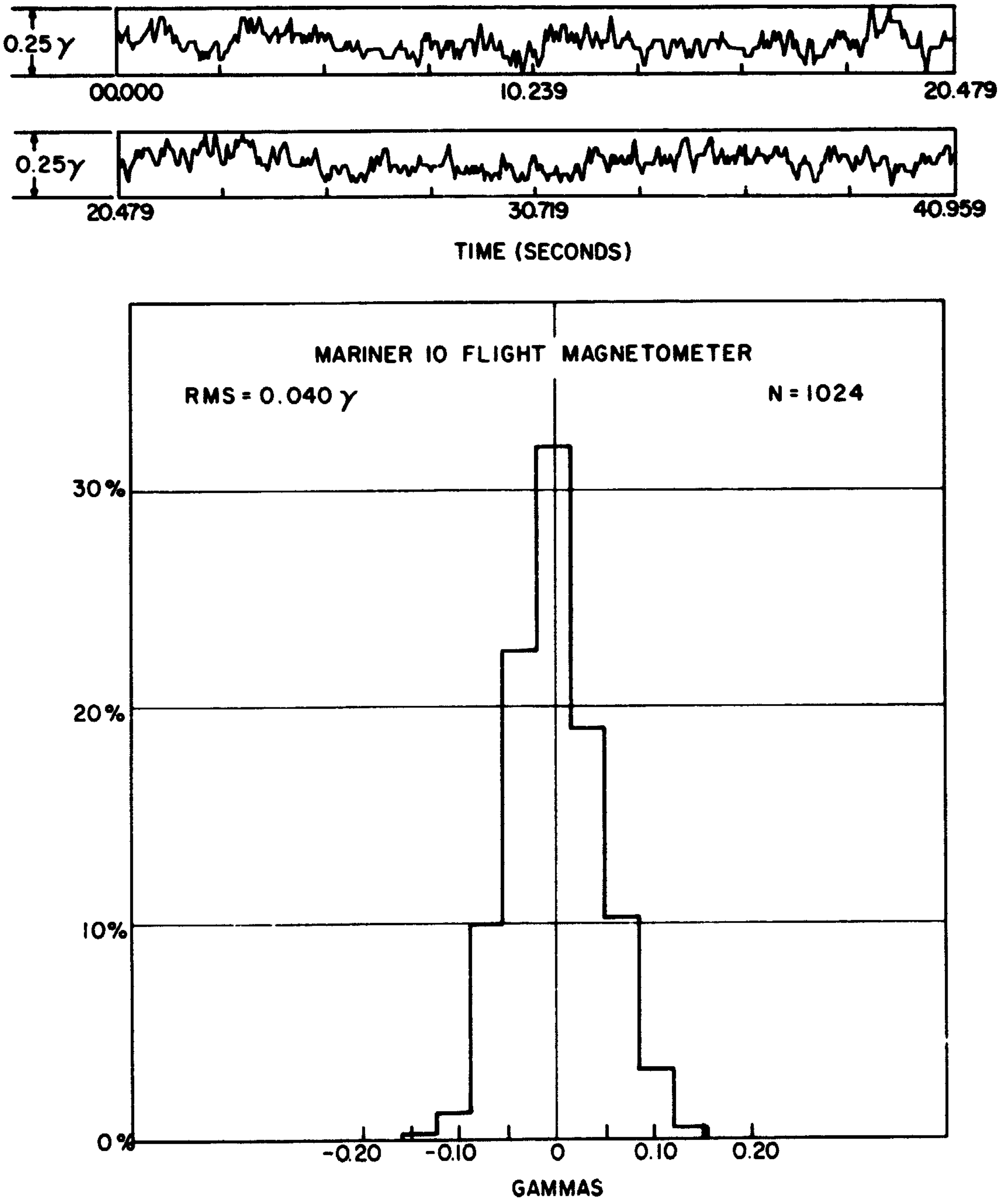

Figure 9. Typical flight sensor noise test result showing 41 sec run of output data from sensor in constant external field (upper small panels) and distribution of the 1024 points in the digital output signals (lower large panel).

2. Data Processing and Analysis

Production processing of the Mariner 10 Magnetic Field Experiment data was carried out on the IBM 360/75 and 91 computers at the Goddard Space Flight Center. The scientific analyses described in this report utilized both the GSFC IBM 360/75 computer and the IBM 1800 computer in the Laboratory for Extraterrestrial Physics at GSFC.

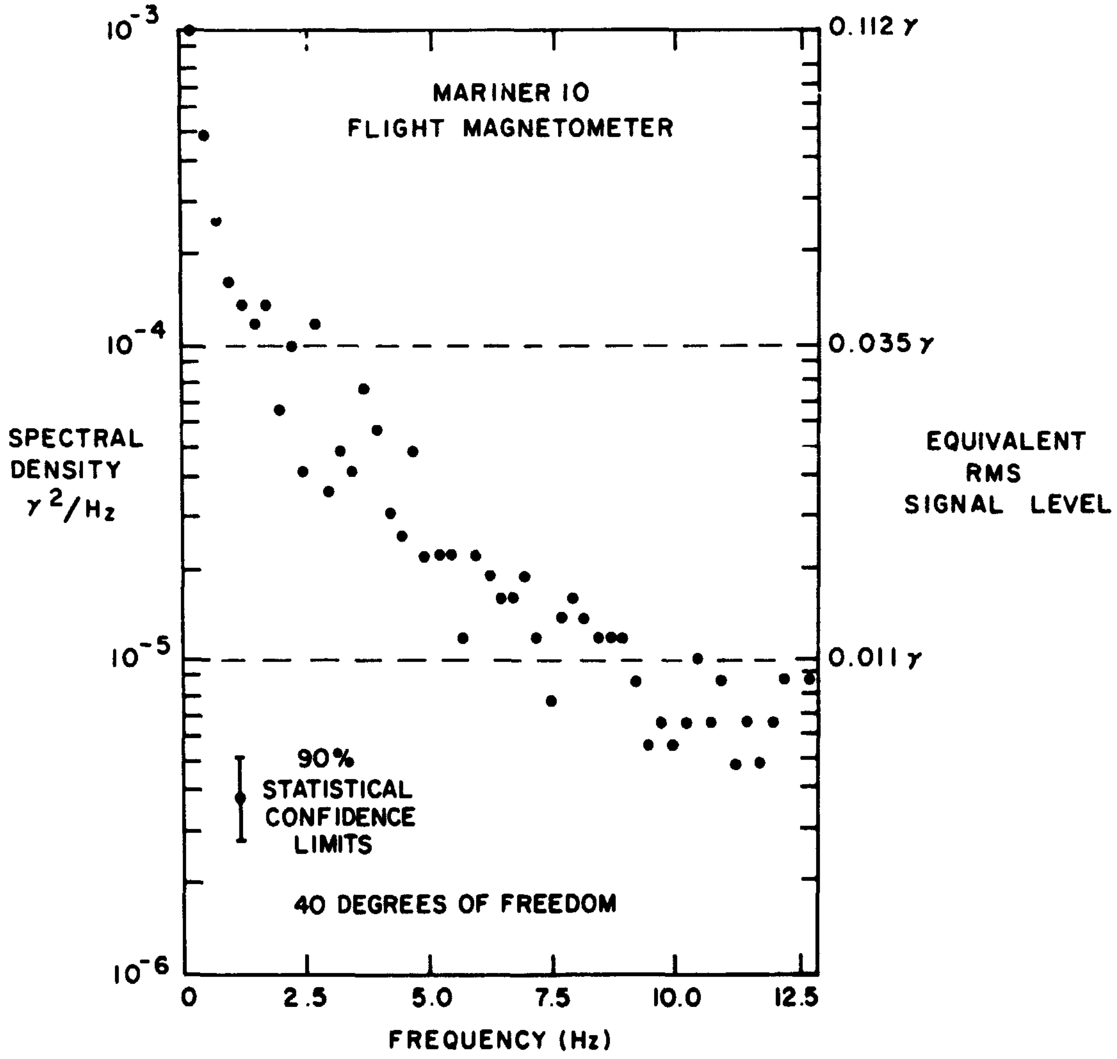

Figure 10. Power spectrum of noise test data. Power density decrease with increasing frequency results from instrument frequency response characteristics (see Fig. 8 and section IV.2.1).

The first stage of production processing consisted of a series of separate programs used to extract calibration information from the raw data. This information consisted basically of zero offset and sensitivity data for the magnetometer sensors. Inflight sensitivity values were found to be consistent with pre-flight values. Thus, most of the effort centered around extracting the best possible effective zero offsets, which included contributions from the spacecraft field. A great deal of effort went into this portion of the data processing due to the fact that the Mariner 10 sensors proved to have less stable zeros than similar fluxgate sensors used on previous space missions. This was primarily due to the more stringent Mariner 10 power and weight design specifications.

For both the calibration analysis and subsequent scientific analyses, the raw sensor data were referenced to a payload or spacecraft-centered coordinate system. This orthogonal coordinate set was defined such that the Z_p axis was the spacecraft roll axis, positive in the sunward direction, except during occasional off-axis trajectory correction maneuvers; the Y_p axis was anti-parallel to the magnetometer boom, i.e., the boom extended in the $-Y_p$ direction; and the X_p axis, chosen such as to complete the right-handed set of coordinates, was parallel to the axis of the solar panels (spacecraft pitch axis). The magnetometer sensors were aligned approximately parallel to these payload coordinate axes. The small misalignment angles of each individual sensor relative to the payload axes were very accurately measured pre-flight using a combination of magnetic and optical measurements and were incorporated into the matrices used to transform from the sensor system to payload coordinates.

The outboard magnetometer was equipped with a "flipper" mechanism which used a heat-driven toggle actuator with over-center spring to rotate the X_p and Z_p axis sensors through an angle of 180° about the Y_p or boom axis. This rotation relative to the ambient IMF plus spacecraft field permitted a unique determination of sensor zero offsets for two of the three outboard magnetometer sensors.

This flip exercise was used in conjunction with Roll Calibration Maneuvers (RCM), during which the spacecraft was put through a series of rolls about the Z_p axis. On a spin-stabilized spacecraft, the relatively rapid and continuous rotation of the spacecraft effectively permits continuous monitoring of the zero offsets for the two sensors perpendicular to the spin axis. Mariner 10 was an attitude-stabilized spacecraft, and hence the periodic RCM was necessary. This exercise permitted a determination of the effective offsets (zero level plus spacecraft field) for the sensors parallel to the X_p and Y_p axes for both magnetometers (Lepping et al., 1975). Because of the very slow roll rate (33 1/3 min/roll), a series of 8 contiguous rolls was implemented in each case to permit a statistical determination of the offsets since stationarity of the external field during any single roll was usually not a good assumption. It was originally planned that an RCM would be conducted every other week during the primary mission, which would have given a total of 15 RCM's. Because of serious attitude control difficulties during the mission, only four RCM's were permitted: RCM 1 on 6 November 1973, RCM 3 on 7 December, RCM 4 on 19 December and RCM 7 on 28 January 1974. Thus all of these maneuvers were conducted prior to the Venus encounter on 5 February 1974.

The pre-flight and in-flight maneuver calibration data yielded calibration curves which were extrapolated in time and then used throughout the primary mission in the production processing to convert the data from engineering units (E.U.) to gammas (γ) according to

$$B_i(\gamma) = (B_i(\text{E.U.}) - ZO_i)\, S_i, \qquad i = x,\ y,\ z, \tag{II-2}$$

where ZO = zero offset and S = sensitivity in γ/E.U. The converted and calibrated primary magnetometer detailed data and secondary magnetometer averaged data were then used to derive estimates of the ambient magnetic field through application of the dual magnetometer analysis (Ness et al., 1971b). The dual magnetometer analysis is summarized briefly in Figure 11. In the way in which the method was applied for Mariner 10 data processing it assumes that the spacecraft field at the positions of the magnetometer sensors is to a good approximation a spacecraft-centered dipole field. Pre-flight static magnetic mapping of the spacecraft and dynamic mapping of the solar panels plus preliminary analysis in-flight of spacecraft field variations indicated that such an assumption is generally valid for Mariner 10. Under such an assumption, then, there is a coupling coefficient $\alpha = (r_1/r_2)^3$ relating the spacecraft field along a given direction at one magnetometer with the spacecraft field along the same direction at another magnetometer located along the same radial line from the spacecraft magnetic center, where r_1 is the distance from the center of the spacecraft to the innermost sensor and r_2 is the distance to the outermost sensor as shown in Figure 11.

In the Mariner 10 application of this concept, the primary (outbound) magnetometer data are averaged over each three consecutive samples to provide time compatibility with the secondary (inboard) magnetometer data. The formulation for $\vec{B}_{SC}^{EST}(r_2)$ is used to produce three-second averages of the estimated spacecraft field at the primary magnetometer. These average values for each field component are then subtracted from the detailed (25 samples/sec) data from the outer sensor position to yield an estimate of the instantaneous ambient magnetic field according to

$$\vec{B}_{AMB}^{EST} = \vec{B}_{OBS}(r_2) - \left\langle \vec{B}_{SC}^{EST}(r_2) \right\rangle . \qquad \text{(II-3)}$$

where zero offset correction has been previously performed.

Because all of the RCM's occurred during the first half of the primary mission, and only four maneuvers were permitted in all, the output data from the first

DUAL MAGNETOMETER FUNDAMENTALS

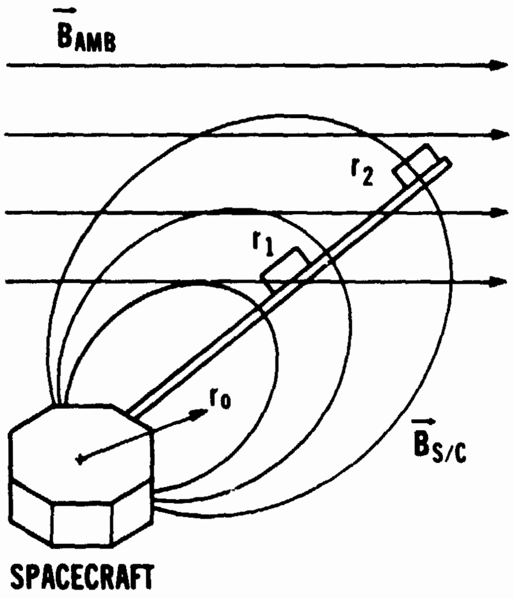

ASSUME $\vec{B}_{SC} = \vec{B}_0 \left(\frac{r_0}{r}\right)^3, r >> r_0$

THEN $\vec{B}_{SC}(r_2) = \left(\frac{r_1}{r_2}\right)^3 \vec{B}_{SC}(r_1)$

NOW $\vec{B}_{OBS}(r_i) = \vec{B}_{AMB} + \vec{B}_{SC}(r_i) + \vec{B}_{ZO}(r_i)$

$\therefore$ CAN SOLVE THESE KNOWING r_1, r_2

$$\vec{B}^{EST}_{SC}(r_1) = \frac{\vec{B}_{OBS}(r_1) - \vec{B}_{OBS}(r_2)}{1-a}$$

$$\vec{B}^{EST}_{AMB} = \frac{\vec{B}_{OBS}(r_2) - a\,\vec{B}_{OBS}(r_1)}{1-a}$$

WHERE $a = \left(\frac{r_1}{r_2}\right)^3$

Figure 11. Dual magnetometer analysis for case of spacecraft field which varies as a dipole field at $r \geq r_1$. Components of field observed at r_1 and r_2 are then related by scalar coupling coefficient a and the spacecraft and ambient fields can be separately determined from the measured fields as shown.

production processing pass were further analyzed using the so-called variances method of spacecraft field determination (Davis and Smith, 1968; Belcher, 1973; Hedgecock, 1975b) in an effort to identify and remove from the data any remaining residual error field contribution. Since any significant time variations occurring in the spacecraft field had already been removed, it was assumed that the requirement of a steady spacecraft field during the interval of application of the minimum variance method (as long as several days) was satisfied by the residual error field. The method as applied uses symmetries in the statistical properties of certain types of discontinuities in the IMF to determine the combined error due to the spacecraft field and zero offset errors. Smooth curves were derived for the error field for each component of the ambient field during the primary mission by spline fitting the variance data, and these were used to correct the first-pass ambient field estimates.

To identify the directional discontinuities used in the variance analysis, the selection criteria established by Burlaga (1969) and also described in detail by Sari (1972) were employed, except that 42 sec data points rather than 30 sec points were used for the analysis. Thus the fundamental criterion was that a directional discontinuity was defined by a $\geq 30°$ change in magnetic field direction in ≤ 42 sec. The data in the vicinity of such a change had to be continuous, the field both before and after the discontinuity had to be relatively undisturbed, and the change had to be relatively linear. An additional constraint that was imposed was that $|F_1 - F_2|/F_{max} < 0.35$, where F_1 and F_2 are the field magnitudes on the two sides of the discontinuity and F_{max} is the larger of F_1 and F_2. This requirement insured the use of directional discontinuities for which the magnetic field change was predominantly a change in direction.

The results of applying the discontinuity variance method to the Mariner 10 data produced corrected estimates of the components of the ambient IMF which to a 95% confidence level are accurate to within ±0.25 γ during the first four months of the primary mission and to within ±0.60 γ during the last 1.5 months of the analysis period, when the largest fields were encountered. Near the end of the period the percent or relative error was actually slightly less, however, than it was during the early portion of the mission since the field was generally near 20 γ during the final month. It is possible that some of the increase in the absolute uncertainty near the end of the primary mission was due to the use of calibration curves in the initial processing of the data from the latter part of the mission that were extrapolations that did not accurately describe the zero level variations during those later months, resulting in larger error fields in those data. For a more detailed description of the Mariner 10 zero level analysis, see Lepping et al. (1975).

For this initial survey of the Mariner 10 primary mission IMF measurements, the ambient field data were transformed to a Solar Equatorial Coordinate System (SEQ) and the spacecraft position throughout the period of interest was determined relative to that sun-fixed reference frame. The SEQ system shown schematically in Figure 12, is defined as follows: X_{SEQ} lies along the intersection of the 0° SEQ meridian plane and the solar equatorial plane, with the 0° meridian defined for this study as that meridian which was at the center of the solar disk for earth observers at 0000 UT 25 October 1973 (beginning of Bartels Solar Rotation No. 1918 (Lincoln, 1974a)); Z_{SEQ} is parallel to the sun's rotation axis, positive northward; and Y_{SEQ}, also lying in the solar equatorial plane, completes the right-handed set. The Bartels Solar Rotation numbering system used by geomagneticians is related in this case to the Carrington Solar Rotation system used by solar observers such that BSR No. 1918/0° = CSR No. 1607/231°, where the CSR longitude is the solar longitude used in synoptic charts of photospheric fields. In the SEQ system, δ_{SEQ} and λ_{SEQ} are the latitude and longitude angles, respectively, with $0° \leq \lambda_{SEQ} \leq 360°$ increasing counterclockwise when viewed from north of the solar equatorial plane and

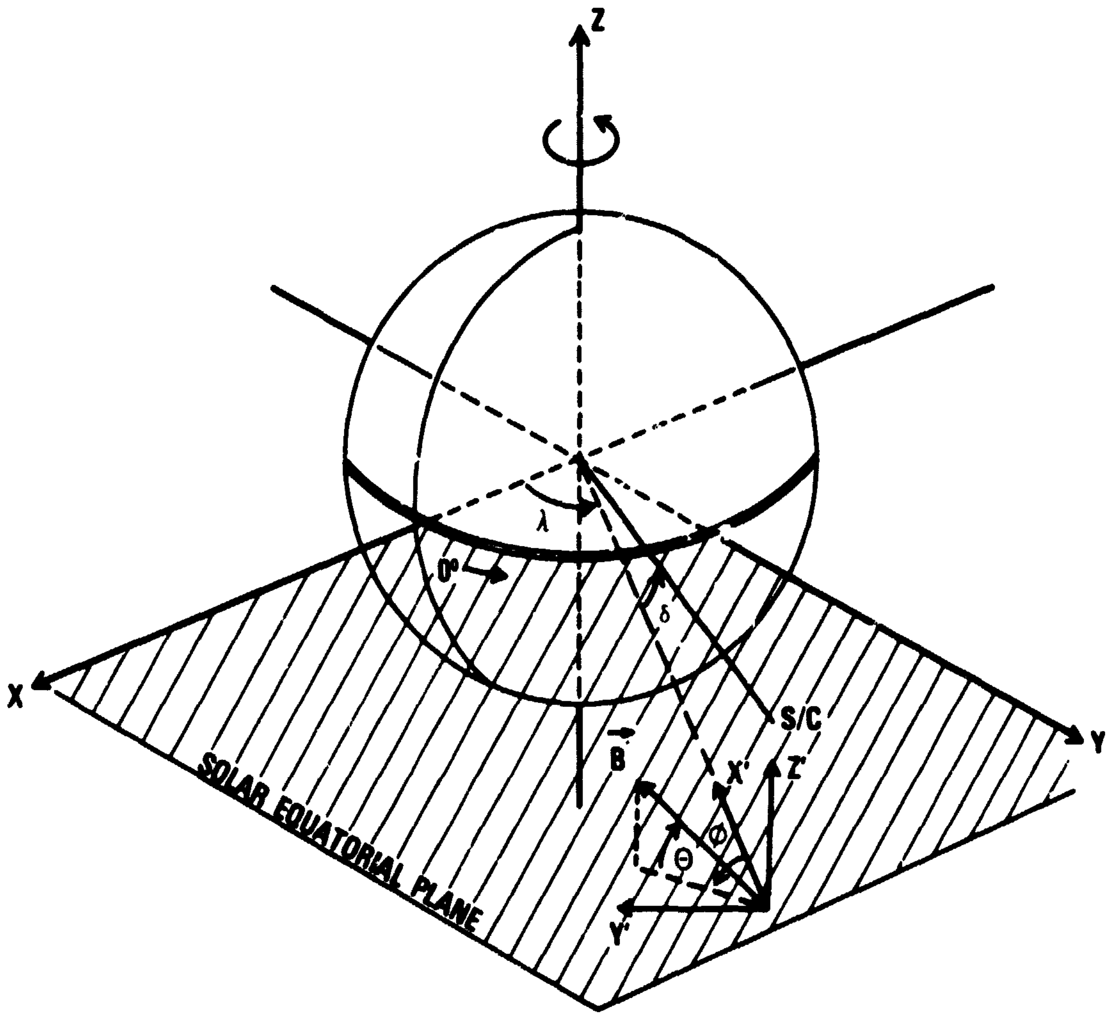

Figure 12. Geometry of solar equatorial coordinate system. Spacecraft position is referenced to x, y, z axes rotating with the sun. The measured magnetic field vector B at the spacecraft position is referenced to the x', y', z' coordinate axes (see text).

$-90° \leq \delta_{SEQ} \leq +90°$ relative to the solar equatorial plane. This is the rotating frame of reference to which spacecraft position is referenced.

SEQ data coordinates are as follows (see Figure 12). We define BX_{SEQ} along X', parallel to the solar equatorial plane projection of the spacecraft-sun vector, positive toward the sun; BZ_{SEQ} along Z', parallel to and of the same sense as the Z_{SEQ} axis; and BY_{SEQ} along Y', also lying in the solar equatorial plane and completing the right-handed set. Field vector orientation angles are also computed. The azimuthal angle in the solar equatorial plane, ϕ_{SEQ}, is defined by

$$\phi_{SEQ} = \tan^{-1}\left(\frac{BY_{SEQ}}{BX_{SEQ}}\right). \qquad \text{(II-4)}$$

$\phi_{SEQ} = 0°$ in the sunward direction and increases in the sense of counterclockwise rotation when viewed from north ($+Z_{SEQ}$ direction) of the solar equatorial plane. The altitude angle, θ_{SEQ}, between the field vector and the solar equatorial plane is defined by

$$\theta_{SEQ} = \tan^{-1}\left(\frac{BZ_{SEQ}}{\sqrt{BX^2_{SEQ} + BY^2_{SEQ}}}\right). \qquad \text{(II-5)}$$

θ_{SEQ} is positive north of the solar equatorial plane and negative south of that plane (same sense as BZ_{SEQ}). The field magnitude is simply

$$F = \sqrt{BX^2 + BY^2 + BZ^2}, \qquad \text{(II-6)}$$

invariant in any system of coordinates.

For Mariner 10 data the telemetry frame length was 42 sec. In the Magnetic Field Experiment data processing, 1.2, 6 and 42 sec averages are computed.

Averages over one hour are also computed at a later stage. For each type of average that is computed for either the total field or field components, the corresponding root-mean-square (rms) deviation is also computed, using the average and the N data values that produced the average, according to the relation

$$\sigma = \mathrm{BRMS} = \sqrt{\frac{1}{N}\sum_{i=1}^{N} (B_i - \langle B \rangle)^2} \qquad \text{(II-7)}$$

These rms deviations are measures of the fluctuations of the field. The field magnitude fluctuations will be labeled by σ_F, and the vector field fluctuation or field directional fluctuation by σ_C, which is computed from the individual component rms deviations according to

$$\sigma_C = \sqrt{\sigma_X^2 + \sigma_Y^2 + \sigma_Z^2}. \qquad \text{(II-8)}$$

In the case of the hourly averages, relative quantities σ_F/F and σ_C/F are also computed, in which the respective field magnitude and vector field rms deviations over the hour are normalized by the hourly average field magnitude.

Additional techniques utilized in the analyses performed in this study are described in the appendices. For the investigation of the variation of various properties of the IMF with heliocentric distance, daily averages were computed from the hourly averages, and a least squares fit of the data to the nonlinear model

$$\langle f \rangle = A r^C \qquad \text{(II-9)}$$

was performed. In each case f was the property whose radial variation was being studied, r was the radial distance from the sun in AU (i.e., $r = R/R_0$ = the distance from the sun relative to the mean distance R_0 of the earth from the sun), and A and C were the characteristic parameters of the power law variation to be determined by the procedure. This data fitting technique and the associated error analysis are described in Appendix A. In the study of fluctuations of the magnetic field magnitude and components, power spectral density and polarization characteristics were computed. In Appendix B the techniques which were used are described and quantities which were derived are defined.

Measurements of the IMF during the Mariner 10 primary mission by earth-orbiting spacecraft are also included in Chapter III to facilitate the interpretation of time variations of the IMF during that period. Those hourly average data were available in solar ecliptic coordinates, in which the reference plane is that of the Earth's orbit about the sun (see Ness et al., 1964 for a detailed definition of the SE coordinate system). For this initial survey, those comparative data were not further transformed to the SEQ system. See Section III.1 for further discussion.

CHAPTER III

OBSERVATIONS OF THE LARGE-SCALE IMF

1. General Character of the IMF during the MIO Mission

The sun can be characterized as relatively inactive during the Mariner 10 primary mission. Sunspot cycle 20 began in October, 1964. As of February 1975 the start of sunspot cycle 21 could not yet be identified (NOAA, 1975). Thus the Mariner 10 mission took place during the approach to sunspot minimum. The last sunspot maximum was in November 1968, with a Zurich smoothed sunspot number of 110.6 (the sunspot number is an index based on the number of sunspot groups as well as the total number of distinct spots; see NOAA (1975) for the rigorous definition). The sunspot number is typically 10 or less at sunspot minimum. Values during the Mariner 10 mission ranged from 32.7 in November 1973 to 31.6 in April 1974.

Figure 13 shows daily average IMF data from IMP-8/HEOS in earth orbit during the November 1973-April 1974 time period. The top panel shows the variation of δ_{SEQ} , the heliographic latitude, for the earth. The second panel shows the magnetic field magnitude $\bar{F}$ in gammas (one gamma = 10^{-5} gauss). Beneath the field magnitude panel is given the Bartels solar rotation number. The third panel displays the azimuthal angle ϕ of the magnetic field vector in the solar ecliptic (SE) plane. Superimposed on the ϕ angle plot is the solar equatorial longitude angle λ_{SEQ} (dashed curve) which was defined in Section II.2. The coordinate systems to which the magnetic field direction is referenced in this and all other figures throughout this study are also defined in II.2, as well as the parameters used to characterize the fluctuation of the field. In panel four is shown the elevation angle θ of the field vector above or below the ecliptic plane. Panels five and six show the relative field magnitude and relative vector field fluctuation parameters σ_F/F and σ_C/F, respectively. Included in the seventh (bottom) panel is the daily sum of the planetary magnetic activity index, Kp, for this time period (Lincoln, 1974a, b, 1975). (See NOAA (1975) for the definition of K_p).

One sees from the ϕ angle that although the field polarity pattern was somewhat irregular during November and December 1973, during the next four months a clearly discernable, regular two-sector pattern was observed. As discussed in Section I.4, the two-sector pattern has been found in association with the approach to maximum of the solar activity cycle, while a four-sector pattern has been found to be generally predominant, especially during the declining portion of the cycle (Svalgaard, 1972; Svalgaard and Wilcox, 1975; Ness and Wilcox, 1 and others). A four-sector pattern was observed during 1972 (Fairfield and Nes. 1974), but Hedgecock (1975) has reported that a two-sector pattern existed throughout most of the period between December 1968 and August 1974, with occasional 2 to 3 month periods in which four sectors appeared. These recent results suggest that this most recent approach to solar minimum is atypical with respect to the sectoring of the IMF.

Although the Mariner 10 period was considered to be relatively quiet in terms of solar activity, Figure 13 shows that the IMF at 1 AU was moderately variable during that period. A comparison of the field magnitude variations with the solar

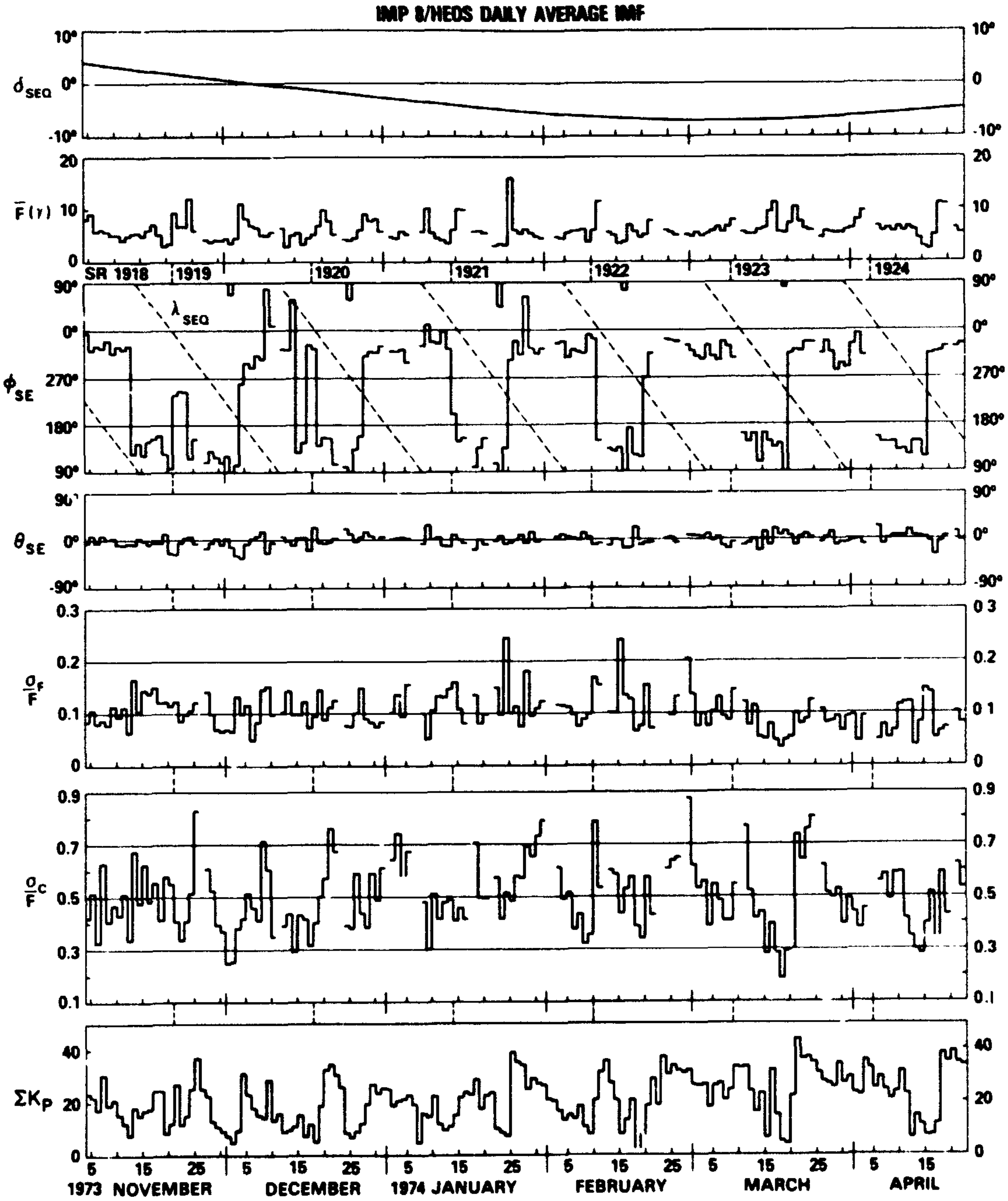

Figure 1 Combined IMP 8 and HEOS daily average interplanetary magnetic field (IMF) and fluctuation parameters measured at 1 AU during the Mariner 10 mission, in solar ecliptic coordinates. Also shown are the solar equatorial latitude and longitude of earth and the daily sum of the planetary index K_p during the period.

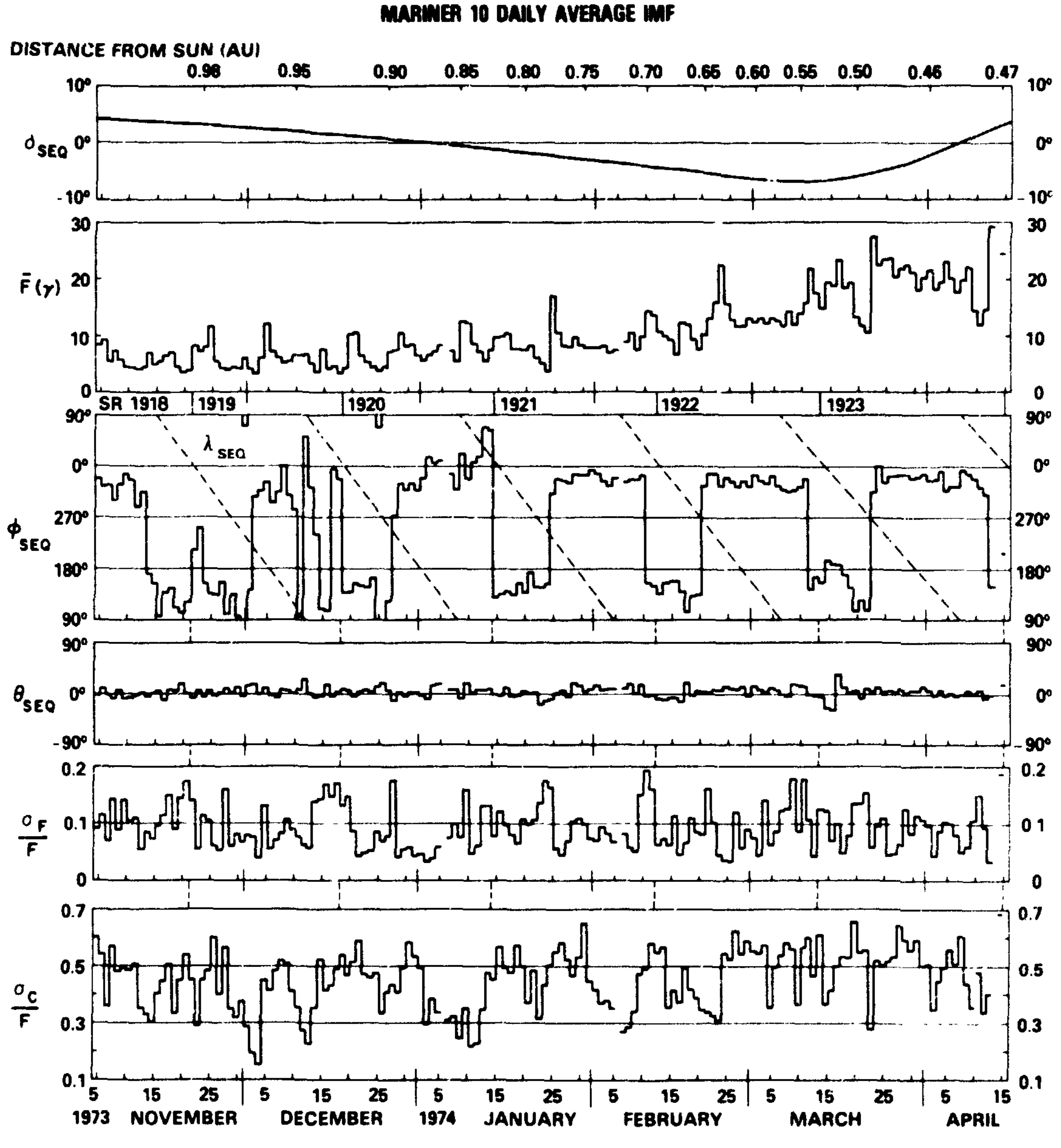

Figure 14. Mariner 10 daily average IMF and fluctuation parameters during the primary mission, in solar equatorial coordinates. The solar equatorial latitude and longitude of the spacecraft during the mission are also shown.

longitude curve and the sector polarity pattern strongly suggests the presence of recurrent disturbances in the medium during the 5-1/2 month interval covered by the figure. This is supported by the plot of K_p which shows a definite recurrence tendency in geomagnetic activity. A correlation can be seen between K and the relative vector field fluctuation parameter σ_C /F. As was briefly discussed in Chapter I, the correlation between geomagnetic activity and recurrent structure in the interplanetary medium has been long known and studied by many workers. Also a high correlation between IMF fluctuations and geomagnetic activity has been found and discussed by Ballif et al. (1967, 1969), Hirshberg and Colburn (1969), Garrett (1973, 1974), Bobrov (1973), Burlaga (1975) and others. This topic will be pursued further in Section III.4. Sudden commencement variations of the geomagnetic field were observed to begin on 11/24; 12/19, 30; 01/01, 15, 24, 25; 02/20, 22, 24; 03/09, 16, 19 and 04/03, 05 and 18 (NOAA, 1974). Only those beginning on 01/24, 03/19 and 04/03 were followed by significant geomagnetic storms. Relative fluctuations in the magnetic field magnitude, represented by σ_F/F, which are found on average to have amplitudes which are only 25% or less of the amplitudes of the relative vector field fluctuations, do not reveal such a clear correspondence with recurrent structure in the medium.

Figure 14 shows the corresponding Mariner 10 data in the same format. In this case the magnetic field orientation angles ϕ and θ are given relative to the SEQ coordinate system. The small angular differences between the SE and SEQ systems are not significant for the gross comparison being given here, however (the sun's rotation axis is inclined 7.25° to the ecliptic plane). One sees similar characteristics in the data, in particular the tendency for the sector polarity pattern to become more well-defined during solar rotation 1920 is again clearly apparent. The fact that this change in character took place at approximately the same time as the solar equatorial plane was crossed, as indicated by δ_{SEQ} , suggests a possible association. This will be pursued further in Section III.3. The most notable difference in the two sets of data is seen in the field magnitude, which generally increases at Mariner 10 with decreasing heliocentric distance (given across the top of the figure). The dependence of the large-scale IMF on radial distance from the sun will be discussed in the following section. One also notes differences in the daily average relative fluctuations observed by the different spacecraft, such as a larger peak-to-peak variation of σ_C/F at IMP 8/HEOS. The fluctuation of the IMF will be considered in detail in Chapter IV. The effect of the increasing Mariner 10 azimuthal velocity relative to corotating IMF structure during the last three months of the mission can be seen in the λ_{SEQ} curve and the solar rotation number scale, as well as in the lengthening sector duration in the angle plot.

Another way of presenting a summary of the daily average magnetic field is in terms of a projection of the field vectors on the equatorial plane in a frame of reference rotating with the sun. In that system of coordinates Mariner 10 appears to spiral in toward the sun while the earth revolves around the outer rim of the field of observation. Thus a mapping of the corotating IMF is produced that shows variations both in space and time. Figure 15 is such a presentation for Mariner 10 and IMP 8/HEOS data for most of the mission. This demonstrates more dramatically the spiral nature of the field as well as the increase in field intensity with decreasing radial distance. The two sector boundaries have been sketched in as smooth spiral curves in approximately the correct locations. The spirals were generated using the formula $\tan\alpha = \Omega_r/V_{SW}$, where $\Omega = 14.18°/\text{day}$ is the equatorial rotation rate of the sun, r is the radial distance and V_{SW} was obtained from the solar wind velocity variation with radial distance predicted by Whang and Chang (1965). Figure 15 illustrates the relative stability of the sector pattern in time during most of the Mariner 10 primary mission.

IMF SECTOR STRUCTURE DECEMBER '73 - APRIL '74

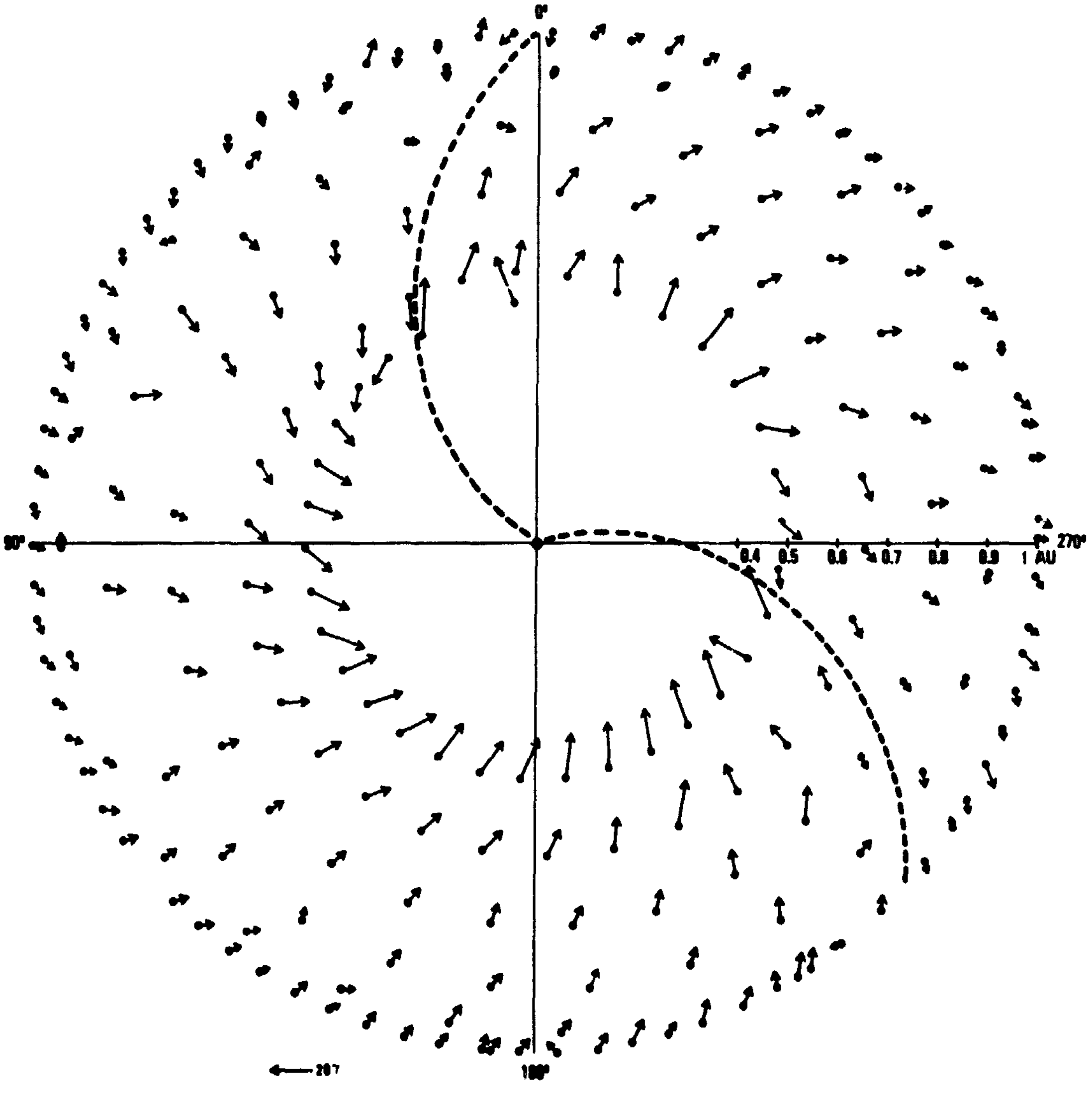

Figure 15. Daily average field vectors observed by Mariner 10 projected on solar equatorial plane and shown in rotating reference frame of the sun. The two-sector structure with toward (or negative) field polarity dominant is clearly apparent for most of the mission.

A more quantitative way of illustrating the gross characteristics of the IMF during the Mariner 10 mission, and the variations of those characteristics with time and space, is to use statistical distributions. Distributions of hourly average values of field magnitude, SEQ orientation angles ϕ and θ, and fluctuation parameters σ_C /F and σ_F /F have been computed for each solar rotation included in the time interval of this investigation. Similar distributions have been computed for the IMP 8/HEOS data for comparison. The σ_C /F and σ_F /F distributions will be discussed in Chapter IV.

Figure 16 shows a comparison of Mariner 10 field magnitude distributions with those from IMP 8/HEOS for solar rotations 1918-1920, and Figure 17 continues the comparison through SR 1923. It should be pointed out that SR 1918 was in progress when Mariner 10 was launched on November 3, 1973, so that all of the different distributions computed for both Mariner 10 and IMP 8/HEOS for SR 1918 only included data from approximately 2/3 of that solar rotation. Another point to notice is that for solar rotations 1918-1920, the associated dates were the same at both Mariner 10 and the earth, while during SR's 1921-1923, an increasing shift in the dates occurred for Mariner 10 since it moved increasingly further ahead of the earth in orbiting the sun. (See Figure 2 for relation of solar rotation periods to Mariner 10 trajectory and earth orbit positions.)

One sees in Figures 16 and 17 that initially the distributions were quite similar, especially those for SR 1919, the first complete solar rotation, where identical means and most probable values were found. One sees no systematic variation in the IMP 8/HEOS distribution throughout this time period, such as might be produced by a heliographic latitude variation. As shown in Table I, which summarizes the field magnitude statistics, the average mean magnitude at 1 AU during the period was 6.00γ, with an average solar rotation standard deviation of field magnitude of 2.45γ. The only major effect visible in these distributions is that due to the decreasing heliocentric distance at Mariner 10, reflected

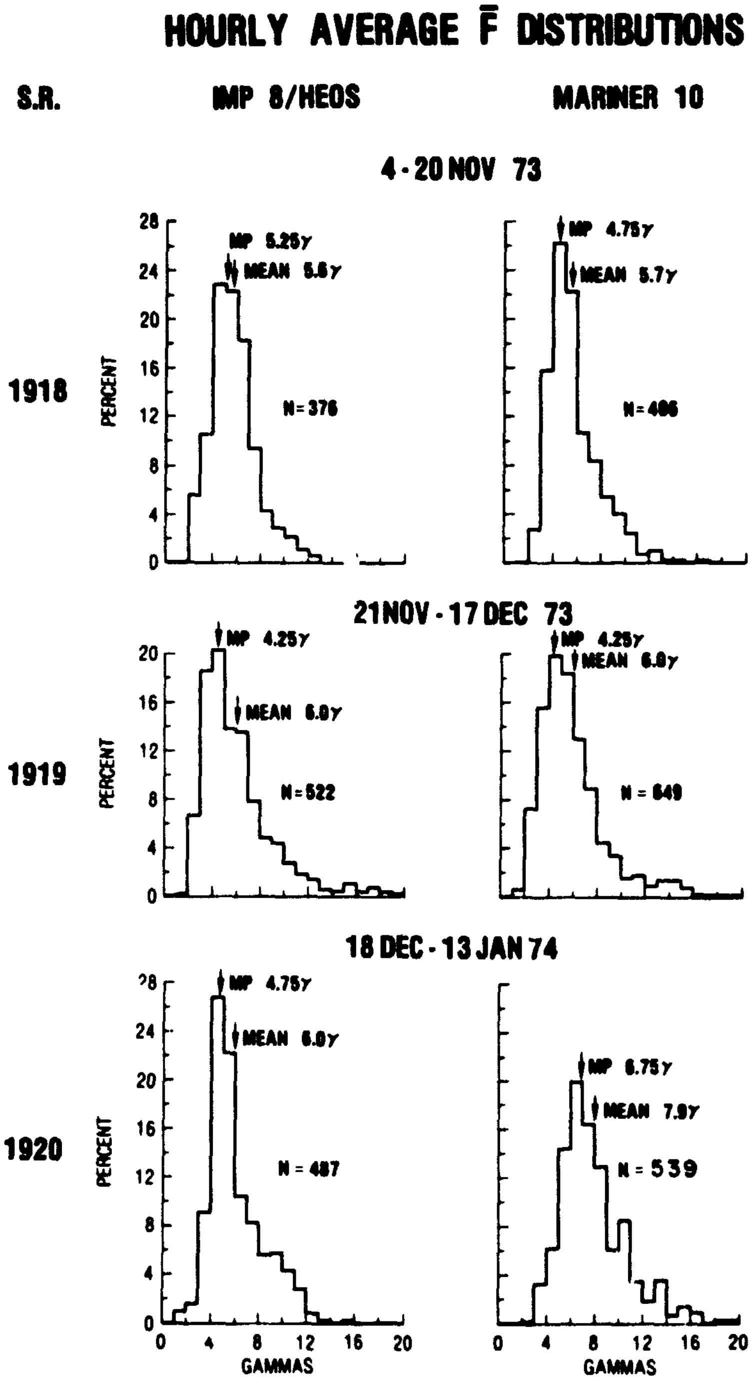

Figure 16. Comparison of Mariner 10 and IMP 8/HEOS hourly average magnetic field magnitude distributions during solar rotations 1918-1920.

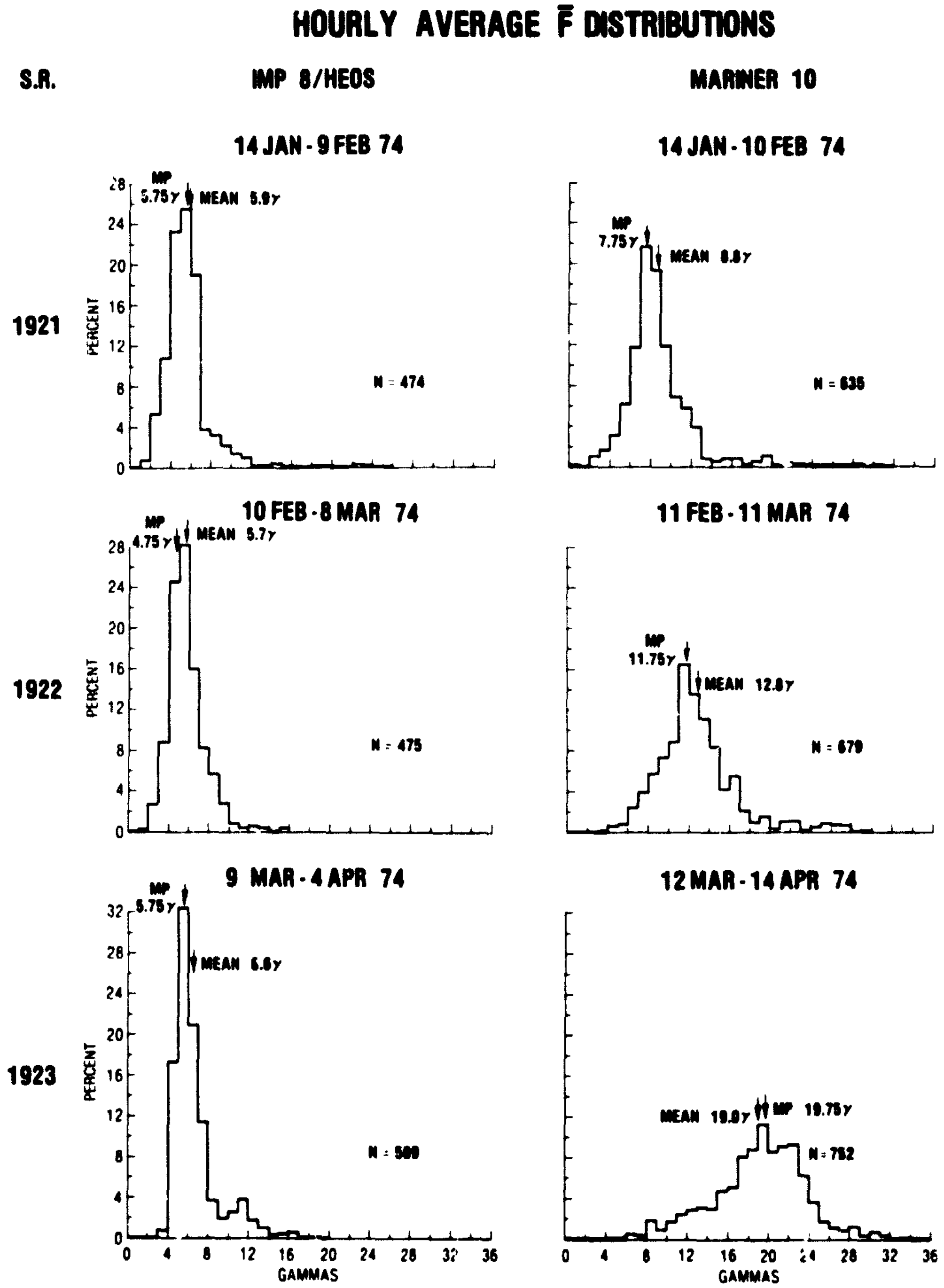

Figure 17. Comparison of Mariner 10 and IMP 8/HEOS hourly average field magnitude distributions during solar rotation 1921-1923. A progressive change in the shape of the Mariner 10 distribution that is primarily attributable to the variation with heliocentric distance is seen.

both in the steadily increasing mean and most probable value (from SR 1919 onward) and in the progressive change of shape of the Mariner 10 distribution to a less peaked, less skewed (more nearly Gaussian) distribution. Table I also shows the IMP 8/HEOS data separated by sector polarity. No significant differences were found between the average magnitude and magnitude deviations in the two different polarity categories during this period of 5-2/3 solar rotations.

Figures 18 through 20 give the distribution of the solar equatorial ϕ and θ angles by solar rotation for Mariner 10. Again the SR 1918 distributions were computed from an incomplete data set, but the ϕ distributions for the first several solar rotations support previous observations of the average spiral angle field at 1 AU, with most probable values of 140°/320° for both of rotations 1918 and 1919. One sees the effect of the decreasing radial distance from the sun throughout the analysis period in the rotation of the field vector toward the radial direction (sun - 180° line). The most probable values of ϕ for both of SR's 1922 and 1923 were 160°/340°. To demonstrate that the field was not also becoming more radial with time at 1 AU during this period, Figure 21 compares the Mariner 10 ϕ distributions for SR's 1922 and 1923 with the IMP 8/HEOS ecliptic plane distribution for those rotations. Again the differences due to differences between coordinate systems are small compared with the observed differences of 20° between most probable values for Mariner 10 and IMP 8/HEOS for both of the solar rotations. Figures 18-21 one also sees a tendency for the ϕ distribution to become more peaked with decreasing heliocentric distance. The results of an analysis to determine the dependence of the magnetic field magnitude and its components on radial distance from the sun will be presented in Section III.2.

The distributions of the SEQ field elevation angle θ shown in Figures 18-20 have been separated by sector polarity. This results in a small reduction in the number of values included in the distribution because those which correspond to

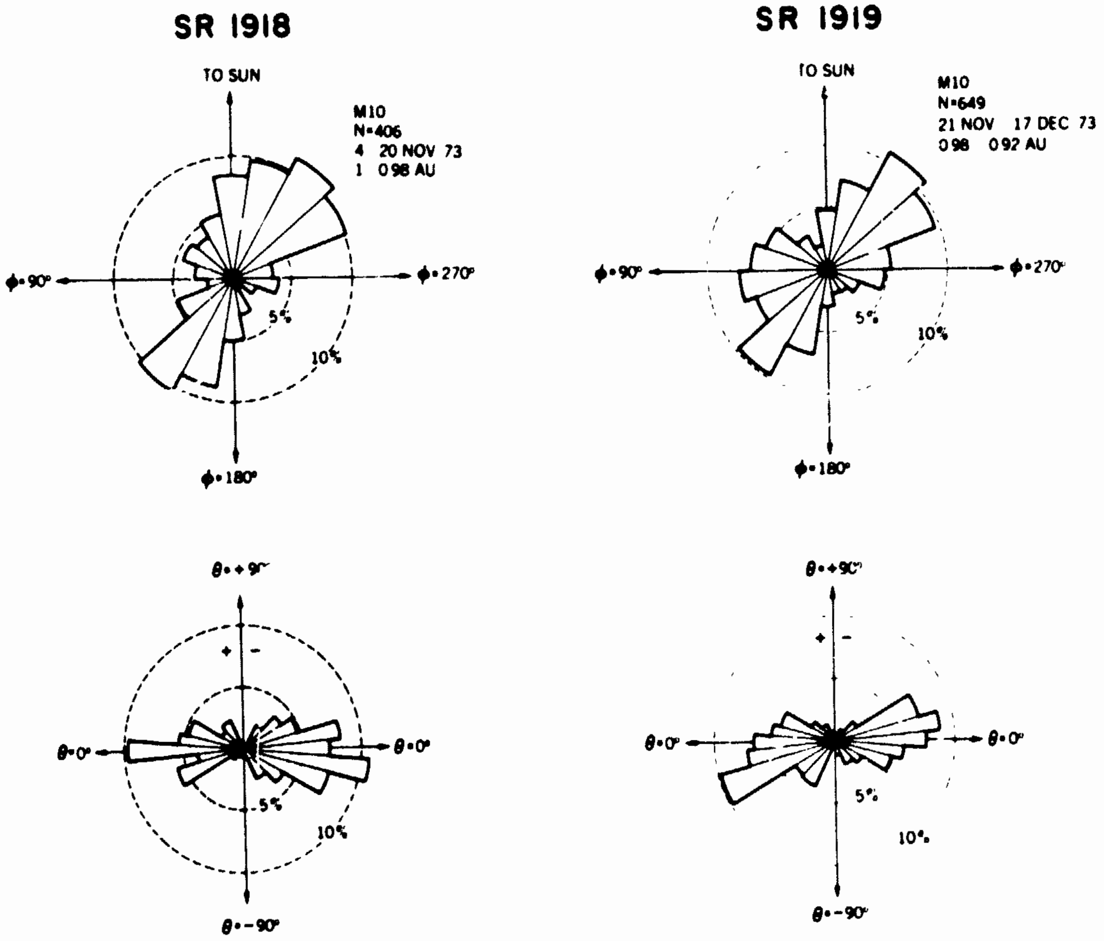

Figure 18. Distributions of hourly solar equatorial field direction angles φ and θ observed by Mariner 10 during solar rotations 1918-1919.

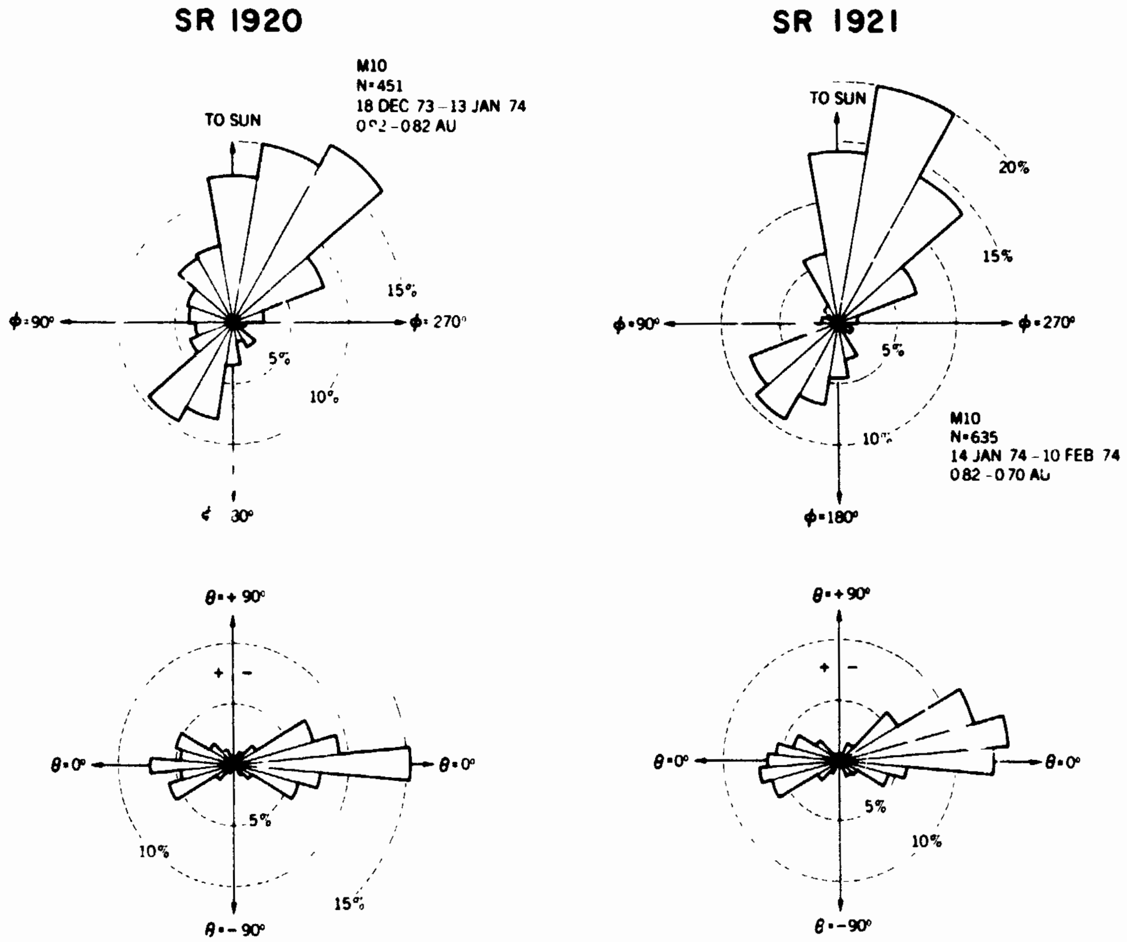

Figure 19. Mariner 10 ϕ and θ distributions for solar rotations 1920-1921.

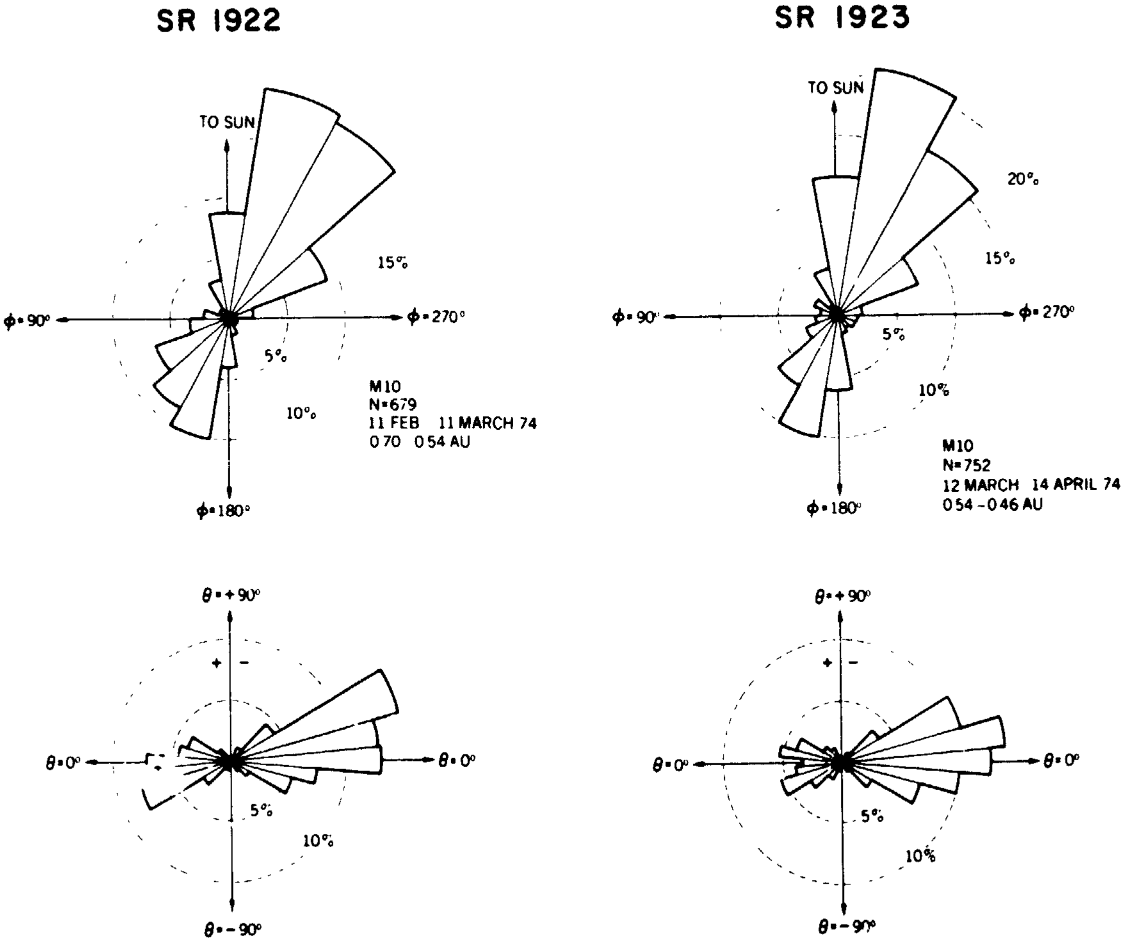

Figure 20. Mariner 10 ϕ and θ distributions for solar rotations 1922-1923. Note that the ϕ distribution has become more peaked and shows the rotation of the field "spiral angle" toward nearly more radial ($\phi = 0°$ or $180°$) alignment.

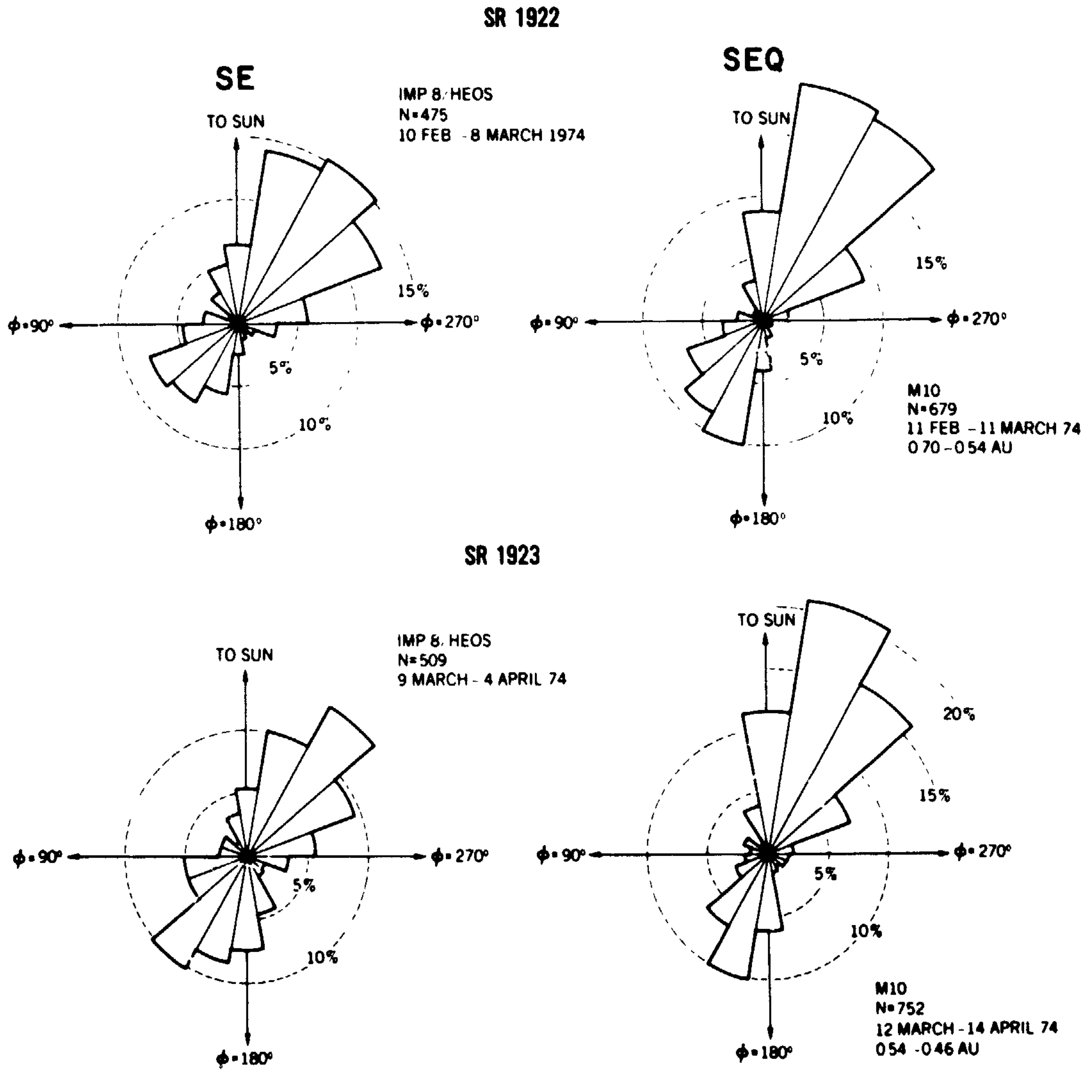

Figure 21. Comparison of Mariner 10 and IMP 8/HEOS φ distributions for solar rotation 1922 and 1923 showing that the tendency for the field to become more radial at Mariner 10 at the time of the observation is clearly a spatial rather than a temporal effect.

times when the hourly average field was roughly perpendicular to the spiral direction (and thus having neither sector polarity) have been excluded. Values have been excluded from the θ distribution (and the sector statistics in Table I) if the hourly average values of ϕ was within a range of ±20° about the perpendicular to the mean spiral direction for each solar rotation. The resulting Mariner 10 θ distributions show that the most probable value of θ was zero for both polarities of the field only for SR 1920 when Mariner 10 crossed the heliographic equatorial plane. Deviations from zero during the other solar rotations will be discussed in Section III.3.

2. Observed Radial Distance Dependence of the IMF

As described in Chapter I, Parker's idealized model of the variation of the IMF with distance from the sun in the solar equatorial plane predicts a $1/r^2$ dependence for the radial component of the field and a $1/r$ dependence for the azimuthal component. Figure 5 showed the field component variations with heliocentric distance according to the Parker model, as well as the variation in field magnitude with radial distance that corresponds to the given component distance dependences. It was also pointed out that previous analyses to determine these dependences experimentally have shown generally good agreement with the Parker model for the radial component and a generally steeper variation with distance than $1/r$ for the azimuthal component, with some differences among the various results.

To investigate the radial distance dependences of the components of the field and its magnitude observed by Mariner 10 between 1 and 0.46 AU, daily averages of those quantities were used. Figure 22 shows the results of performing a least squares fit using the nonlinear model $\langle f \rangle = Ar^C$, where f was the daily average data of interest, r was the heliocentric radial distance of AU (i.e., in reality this was the relative distance R/R_0, where the reference distance R_0 is the mean distance from the sun to the earth), and A and C were the characteristic parameters

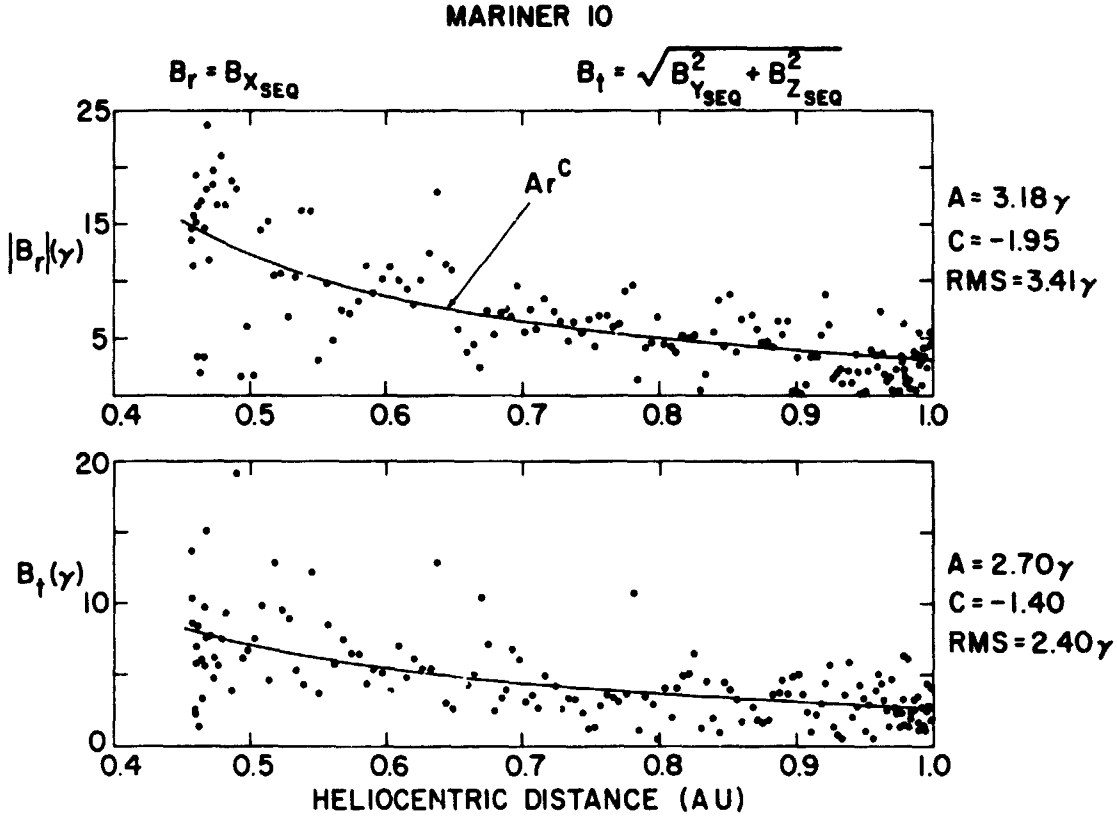

Figure 22. Daily averages of the magnitudes of the radial component, B_r, and of the component perpendicular to the radius vector, B_t, measured by Mariner 10 during the primary mission. Superimposed on the data are the nonlinear least squares best fits of power law variations to the data. The parameters of the best fits are also shown.

of the power law variation to be determined by the fitting procedure. The fitting procedure and the associated error analysis are described in Appendix A.

Figure 22 includes plots of the daily average radial component B_r and tangential component B_t data, as functions of the heliocentric distance r. The "best fit" curves are superimposed on the data, and the "best fit" values of the parameters A and C are given at the right of the figure, along with the rms of the fit. Note that the fit is made to the absolute value of the radial component to remove sector reversal variations from the data. Also the tangential component B_t includes the component normal to the equatorial plane as well as the azimuthal component in the plane, i.e.,

$$B_t = \sqrt{B_\phi^2 + B_n^2} = \sqrt{B_{y_{SEQ}}^2 + B_{z_{SEQ}}^2} .$$

Note the large variability of even the daily averages about the best fit curves.

Of primary interest in this analysis are the components C for $|B_r|$ and B_t. The value of -1.95 for the exponent of the $|B_r|$ dependence shows excellent agreement with the inverse square dependence predicted by theory and with a combined data set consisting of all previous measurements (Neugebauer, 1975a). The value of -1.40 for the B_t exponent is consistent with a steeper gradient than predicted by theory for the azimuthal component. There is not complete agreement between the various experimental values obtained for the azimuthal component distance dependence, however. Table II summarizes the various experimental results for the variation of the magnetic field components with distance from the sun.

It should be noted that the results are not all strictly comparable in that the Mariner 4 and 5 data used in the analysis were overlapping 27-day averages (Coleman et al., 1969), the Pioneer 6 data were solar rotation averages, the Pioneer 10 data were solar rotation most probable values in one case and polarity-weighted solar rotation averages in the other, and the Mariner 10 data were daily averages. Further, for the azimuthal component B_ϕ, in addition to Mariner 4 and 5 data being averages of the magnitude of B_ϕ and Pioneer 10 data being most probable value of $|B_\phi|$, the Pioneer 6 data were averages of $B_t = \sqrt{B_y^2 + B_z^2}$. The Mariner 10 data shown in the lower panel of Figure 22 were also values of the tangential component B_t. A separate fit was made as well to each of $|B_n|$ and $|B_\phi|$ for Mariner 10, as shown in Figure 23, and the results for the exponent in each case were similar to that obtained for B_t. These results are also tabulated in Table II. One sees that the B_ϕ dependence of $r^{-1.30}$ for Mariner 10 is in close agreement with the $r^{-1.29}$ dependence found for Pioneer 10 and for Mariner 4 (when all the data were used in the fit). The Mariner 4 data gave a result closer to a 1/r variation when only "quiet" data were used (the data were subdivided into sets corresponding to low and moderate levels of geomagnetic activity, with appropriate time shift, and the analysis was run on these subsets as well as on the combined set (Coleman, et al., 1969)).

Comparison with Mariner 5 and Pioneer 6 results shows that the Mariner 5 result is even further from the theoretical 1/r dependence and the Pioneer 6 result of Villante and Mariani represents an even steeper gradient than an inverse square dependence and is significantly different from all the other results.

To explain the deviation of the Mariner 4 observations from spiral field behavior, Coleman et al. (1969) suggested that possibly either the solar wind velocity was higher when Mariner 4 was at 1.4 AU than when it was at 1 AU or that the IMF had broken up into magnetic loops at that time. They favored the latter possibility on the basis of the observed instability of the IMF polarity pattern during the period of observation (November 28, 1964 to July 14, 1965). The effects of variable average solar wind velocity from one solar rotation to the next are cited by Villante and Mariani (1975) as being the most probable reason for the large

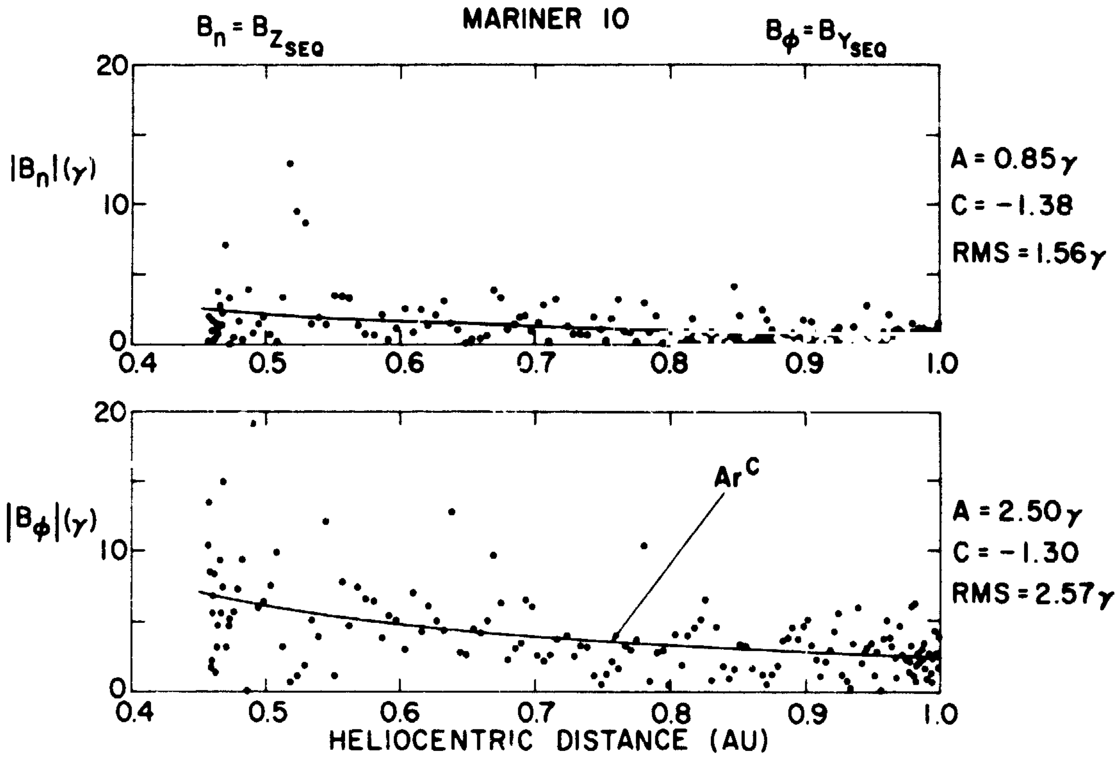

Figure 23. Daily averages of the magnitudes of the individual components of B_t. B_n is the component normal to the solar equatorial plane and B_ϕ is the azimuthal component lying in the plane. Best fit power law curves and fitting parameter values are also given.

deviation from the spiral model of the Pioneer 6 result on the radial distance dependence of the B_ϕ component.

The Pioneer 10 solar rotation most probable field azimuthal angles showed significant variability from rotation to rotation, producing considerable scatter about the superimposed theoretical spiral angle (Smith, 1974). Burlaga and Barouch (1975) have used the kinematic approximation $dV/dt = 0$ (i.e., V = constant for any given volume element) to study the effects of the radial velocity profile in corotating solar wind streams on the magnetic fields between 20 $R_\odot$ and 1 AU, considering the streams to begin as speed variations at the inner boundary. The kinematic approximation is valid for typical streams of moderate amplitude. As we have previously mentioned, interplanetary streams interact to produce changes in the state of the medium and in addition carry variations in the source out into the medium. Burlaga and Barouch have found by averaging over a typical stream that while the B_r variation is well-described by the inverse-square dependence, B_ϕ does not vary in a simple way. Their model suggests that measured values of B_ϕ will depend on the initial value of the azimuthal angle Φ_0 of the field near the sun and on its fluctuations, as well as on the stream parameters.

Using data from Mariners 2, 4 and 5, Rosenberg (1970) has shown that the tangent of the observed spiral angle, $\tan \alpha_B = -B_\phi / B_r$, has a dependence on solar wind stream flow speed. When "slow" streams dominate the flow, $\tan \alpha_B < \tan \alpha_p$, and when fast streams dominate, $\tan \alpha_B > \tan \alpha_p$, where $\tan \alpha_p = \Omega r \sin \theta / V_r$ from the Parker model (Ω = sun's angular velocity and r = spacecraft - sun distance). That report discusses the possible contribution of a non-zero, average B_θ (north-south) component, to deviations from the spiral field model. Coleman and Rosenberg (1971) suggested that the nonzero average values of B_θ (indicating that the IMF is skewed relative to the radial direction) could be produced by Alfvén shock waves (rotational discontinuities) which essentially are "links" propagating outwardly along the field at the Alfvén speed. Alfvén shocks have the same form as linear oscillatory Alfvén waves, so that $B_\theta = -P(4\pi\rho)^{1/2}\ v_\theta$, where θ is measured from the sun's rotation axis and P = 1 for an outward field and -1 for an inward field. Coleman and Rosenberg further suggest that plasma velocity can be skewed from the radial by plasma stream latitude differences. Evidence for Alfvén shocks in the solar wind has been presented by Belcher and Davis (1971).

While it is now clear that the radial dependence of B_ϕ is steeper than r^{-1}, it is not clear what the exact mechanism is that produces the more rapid decrease. In particular it is not clear that the time variations in B_ϕ can result in a modification of the distance dependence. There is also the possibility that a more rapid fall off of B_ϕ with increasing heliocentric distance than that predicted by the spiral model can be accommodated within the framework of steady flow, three-dimensional solar wind theory by considering the effects of meridional flow (Nerny and Suess, 1975). However, the meridional flow theory also predicts a more rapid falloff in B_r than is observed.

As discussed in Chapter I, the Pioneer 10 solar rotation magnetic field magnitude data were found to be consistent with a curve having the radial dependence predicted by Parker's theory (Smith, 1974). The Mariner 4 analysis resulted in a radial dependence of the measured field strength that was close to that of the idealized spiral model during the periods of relatively low geomagnetic activity, even though there were significant discrepancies between the best-fit results for $|B_r|$ and $|B_\phi|$ taken individually and the model field component radial distance dependences (Coleman et al. 1969). Figure 24 shows the Mariner 10 daily average field magnitude data with a best fit power law curve superposed. In this case a best fit exponent of -1.67 was found. For $0.46 \leq r \leq 1$ AU, an almost identical curve can be fit to the data for approximately the same quality of fit (RMS = 2.91) using the form of the Parker model, though it gives a higher field strength at greater distances (0.8γ vs 0.4γ, at 5 AU).

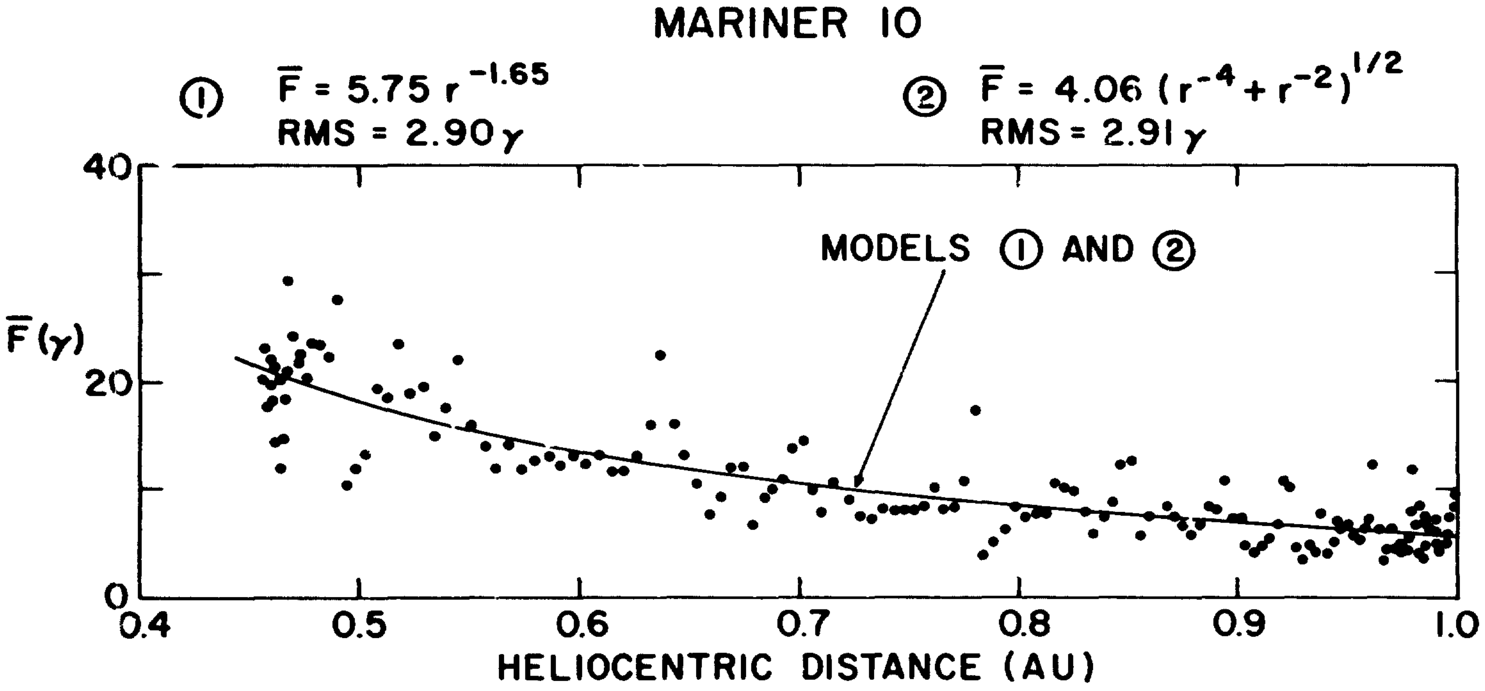

Figure 24. Daily averages of Mariner 10 measurements of total magnetic field magnitude. The nonlinear least squares fits of power law model A and spiral model B to the data produce best fit curves which are essentially indistinguishable over the radial distance range 0.46 to 1 AU. However, the spiral model rises more steeply nearer the sun and decreases more slowly at greater distances.

It is also possible that some dissipation mechanism produces the observed dependence. Jokipii (1975) has recently suggested that the steeper than r^{-1} dependence for the azimuthal component can be accounted for at least in part by considering the influence of solar wind fluctuations which do not influence B_r. Careful observations of $\langle \delta B_\phi \delta V \rangle$ as a function of r are required to establish whether this effect is important (Jokipii, 1975).

3. Observed Heliographic Latitude Effects

No attempt was made in this general survey study to conduct a detailed analysis for possible latitude effects in the Mariner 10 data. However, one finds evidence for such effects in examining the statistics of hourly average measurements as well as plots of hourly and daily average data. One sees immediately from these various data displays that the dominant polarity of the IMF during the Mariner 10 mission was negative, or toward the sun, at southerly latitudes.

The actual percentages of total hours of observations in each solar rotation spent in each sector polarity are given in Table III. The values given for SR 1918 should be interpreted with caution since Mariner 10 was in space fo[illegible] [illegible] approximately 2/3 of that rotation. SR 1919 data show approximately equ[illegible] [illegible] between the two sector polarities with a small bias in favor of negative pola[illegible], and [illegible] SR's 1920-1923 the data demonstrate the dominance of negative polarity [illegible] during SR 1920, when the equatorial plane was crossed, a dominance of [illegible] polarity was found. The gap in the Mariner 10 data during the period of negative sector polarity in early January (see Chapter II) means that in reality a stronger dominance of negative polarity than 60% should have been observed in that rotation. For SR 1923, when the equatorial plane was crossed from south to north, a dominance of negative over positive polarity of 67% was found. The corresponding data from IMP 8/HEOS are also given in Table III. Those data are also biased by the presence of data gaps, in this case due to periods when none of the contributing spacecraft were in the solar wind. This may account for some of the differences between the results from the earth-orbiting spacecraft and those from Mariner 10, in addition to possible effects due to the latitude differences.

The dominance of negative polarity at southerly latitudes during the primary mission of Mariner 10 is consistent with the results of Fairfield and Ness (1974), Hedgecock (1975c) and King (1975) and with the dominant polarity predicted from the long-term statistics of Wilcox and Sherrer (1972). Since little of the time during the mission was spent at northerly heliographic latitudes, it is not possible to comment on the relative symmetry of polarity dominance between the hemispheres. The fact that negative dominance was observed during both equatorial plane crossings could be due to the "magnetic equator" of the large-scale solar field being north of the heliographic equator. The almost equal split in polarities observed during SR 1919 above the solar equatorial plane tends to support that possibility.

An additional heliographic latitude effect that was described in Chapter I is the north-south component (B_θ) effect. A search for that effect requires careful analysis of data in spherical coordinates, using data from a multi-spacecraft data set if possible. Such an analysis was not included in this investigation. However, once again one sees in the solar rotation statistical distributions (Figures 18-20) some evidence for a latitude dependence effect. The θ_{SEQ} distribution for SR 1920, during which the spacecraft crossed the solar equatorial plane, showed most probable θ angles of 0° for both sector polarities. Subsequent rotation distributions were found to be peaked at positive values of θ for negative sector polarity and at negative values of θ for positive sector polarity. Looking at the negative sector distribution, one sees a most probable value of +10° for SR 1921, +22.5° for SR 1922 and a return to +10° for SR 1923, roughly correlating with the heliographic latitude variation of the spacecraft during that time. One sees a similar pattern of variation for the positive sector distribution. One can also see this sector polarity - related periodicity in the daily average plots for both Mariner 10 and IMP 8/HEOS (Figures 13 and 14).

Although the most probable values of for the negative polarity distribution suggest that perhaps the north-south component effect was observed, average values of were found to be closer to zero. For SR 1922, for example, an average value of $\langle {}_{SEQ} \rangle$ = +6.0° was obtained for negative polarity and $\langle {}_{SEQ} \rangle$ = -5.5° was found for positive polarity. In the first case the heliographic latitude was on average $\langle {}_{SEQ} \rangle$ = 6.3° and in the latter case $\langle {}_{SEQ} \rangle$ = 5.0°. Since these average latitudes are of the same order as the average solar equatorial angles, one can only conclude that on average during this period the solar meridian plane component of the field was roughly along the radial direction. This agrees with the findings of King (private communication), who used a multi-spacecraft data set and found no evidence for the north-south component effect during 1972-1974. It should also be noted that the distributions in Figure 18 for SR 1919 when Mariner 10 was above the heliographic equator are not consistent with a reversal in the sense of the ${}_{SEQ}$ angles to be expected above the equatorial plane for either radial or skewed meridional fields, whereas the distributions for the partial solar rotation 1918 do show a peak at negative angles as expected for fields above the heliographic equator of negative sector polarity, but a most probable value of = 0° for positive polarity fields.

One final possible effect related to heliographic latitude was the change in the observed sector pattern to a well-defined pattern when Mariner 10 crossed the solar equatorial plane into the southern hemisphere. An examination of photospheric magnetic field synoptic charts for the period October 15, 1973 to April 22, 1974 (Carrington solar rotations 1607 to 1614) has shown that throughout this interval photospheric magnetic structure above the 5 Gauss level (> + 5G, < -5G) was concentrated in the southern hemisphere of the sun.

Figure 25 shows a comparison between the Mariner 10 hourly average magnetic field magnitude and direction angles in SEQ coordinates for Bartels SR 1923 and the corresponding photospheric synoptic data from Hale Observatories for Carrington SR's 1612 and 1613. As already seen, it was during SR 1923 that Mariner 10 made its closest approach to the sun (r = 0.46 AU). In Figure 25 the Mariner 10 data have been shifted 2 days toward earlier time relative to the solar data. That shift removes a lag corresponding to a mean propagation speed of 400 km/sec. Enclosed regions of the synoptic chart correspond to fields above the 5 Gauss level, with light regions corresponding to fields out of the sun and dark regions indicating fields into the sun. Although there were changes in the photospheric field pattern from rotation to rotation during the mission, the synoptic charts show that the distribution of photospheric fields shown in Figure 25 is roughly typical of the entire period, with the large photospheric magnetic features tending to be clustered in southern latitudes between heliographic longitudes of 140° and 210° during CSR 1607, growing somewhat in size and expanding in longitude to an extent of 110° to 240° by CSR 1614, which was beyond the time interval of interest. The observed growth and expansion of photospheric features may also have contributed to the observed change in character of the observed IMF sector structure. As discussed in Chapter I, it was possible to obtain a relatively good mapping between photospheric fields and interplanetary fields at 1 AU near the solar minimum of 1964 - 1965 (Ness and Wilcox, 1967; Wilcox and Ness, 1967; Schatten, 1968; Schatten et al., 1969). One sees in Figure 25 that an association can be made between the photospheric magnetic features with outward polarity and the small positive interplanetary sector at 0.5 AU. The adjoining photospheric features with inward polarity roughly correspond to the leading portion of the large negative sector.

To confirm that the sector structure was not well-defined north of the solar equatorial plane will require a longer period of analysis, in particular a study of

C.2

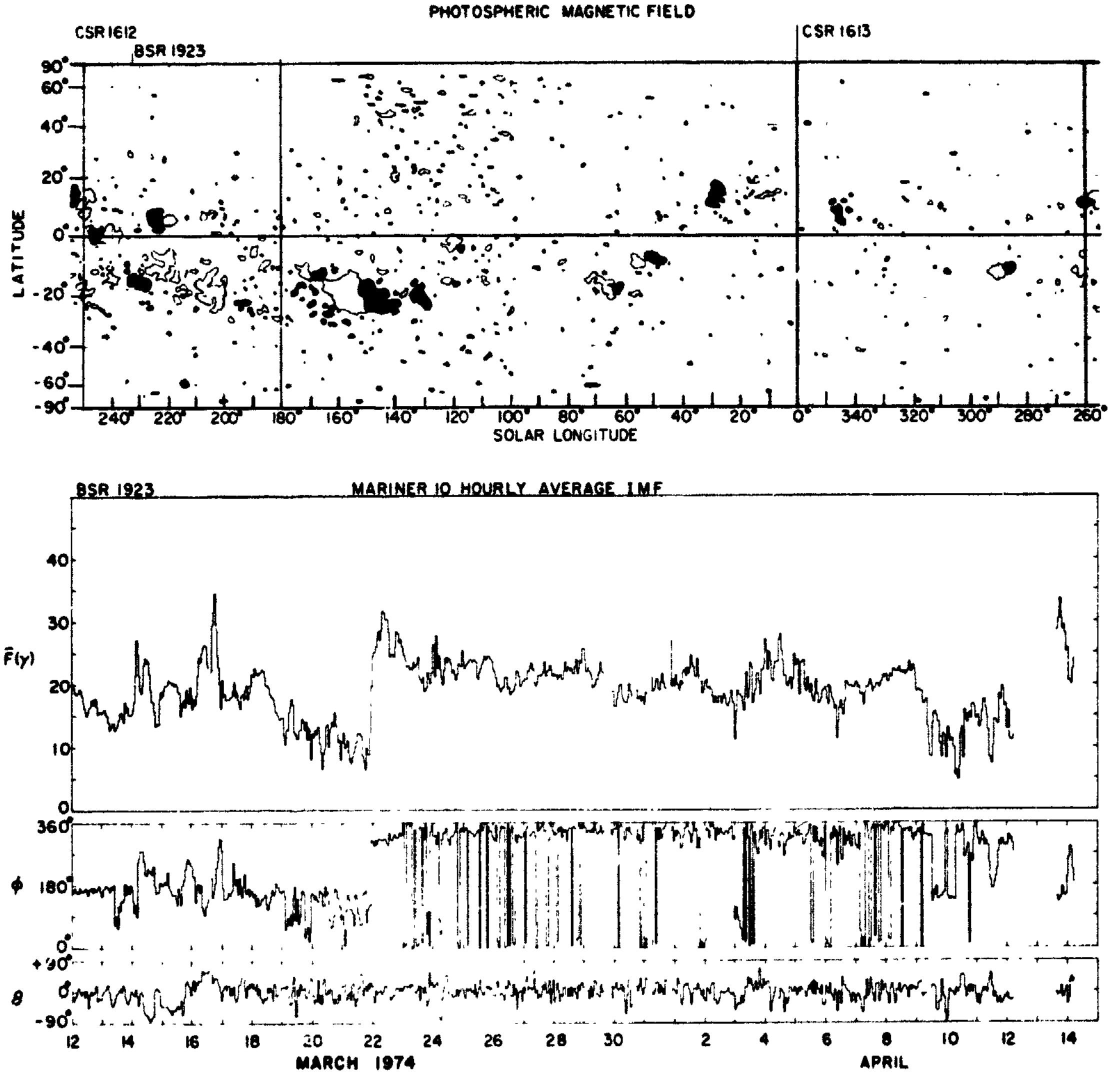

Figure 25. Comparison of Mariner 10 hourly average IMF measurements during Bartels solar rotation 1923 near 0.46 AU with a synoptic chart of photospheric fields above 5 gauss. Shaded regions in upper panel represent fields into the sun, while unshaded regions represent fields out of the sun. The M10 data have been shifted to allow for propagation time. Apparent ϕ angle changes of nearly 360° are merely indicative of scale folding, i.e., changes through $\phi = 0°$.

the Mariner 10 extended mission data. Although past observations have suggested that sector boundaries extend roughly between heliographic latitudes of 40°N and 40°S (Wilcox and Howard, 1968; Schatten et al. 1969), it is possible that they are more restricted in latitudinal extent when photospheric source fields are not symmetrically distributed relative to the heliographic equator. Latitude studies between earth and Mariner 5 have shown that the solar wind velocity structure can be distinctly different in the two hemispheres (Rhodes and Smith, 1975).

4. Observed High-Speed Stream Structure

As discussed in Section I.5, it is now recognized that high-speed plasma streams in the solar wind are a major contributor to dynamical processes in the interplanetary medium, and that the factors that most influence geomagnetic activity are probably related to streams and are determined by the dynamics of streams. Magnetic field experiments in the IMF can contribute to the study of the structure, dynamical processes and evolution in both space and time of high-speed streams through studies of the magnetic signatures or profiles of such streams, which for typical simple fast streams are related to the plasma characteristics of the stream as shown in Figure 6.

Many high-speed streams are observed to exist only during a single rotation of the sun. Another class of streams recur for two or more solar rotations. During the Mariner 10 primary mission, two major high-speed streams were observed by the MIT Plasma Experiments on IMP's 7 and 8 at 1 AU to persist at least through SR's 1918-1921 (Lazarus, private communication). At the time of this study SR 1921 was the latest rotation for which the plasma data were available. The two recurrent streams that are seen in the solar wind measurements are the streams designated as B and D by Krieger et al. (1975) and associated by them with coronal holes. Stream B had persisted through at least seven solar rotations at the time of the Mariner 10 launch, while stream D was on its second rotation at that time. The coronal hole associated with B was observed by Krieger et al. to migrate in heliographic longitude from 60° to 80° -90° during Carrington solar rotations 1601 to 1607. During CSR's 1606-1608 the coronal hole associated with stream D migrated from 210° to 230° longitude.

The plasma data showed stream B to be generally of higher peak velocity and greater extent in longitude than stream D. Stream B was contained within the large negative sector observed by Mariner 10, and by virtue of its recurrent magnetic signature it was found to persist at least into BSR 1923. Stream D was found to be associated with the small positive sector. Although a recurrent stream magnetic signature is seen each solar rotation during the period of study in association with the positive sector, the effects of stream D on geomagnetic activity generally were less pronounced than for stream B and more variable in character, suggesting significant evolutionary changes in the properties of that stream during the Mariner 10 mission.

The geomagnetic variations observed on earth during the period of study due to the effects of these streams are shown in Figure 26, which shows the variations of the three-hour planetary magnetic index K_p as a function of time within each successive solar rotation. During solar rotations 1918 - 1921 the effects of two weaker streams A and E are also seen. Stream E was found to be near a coronal hole that developed near heliographic longitude 300° on Carrington rotations 1607 and 1608 (during BSR's 1918-1919). The effects of stream E may also be visible in SR 1922, but the structure becomes more complex during rotations 1922-1924, with a more continuous high level of geomagnetic activity throughout the negative sector region perhaps indicating an expansion and coalescing of streams or the appearance of other new streams.

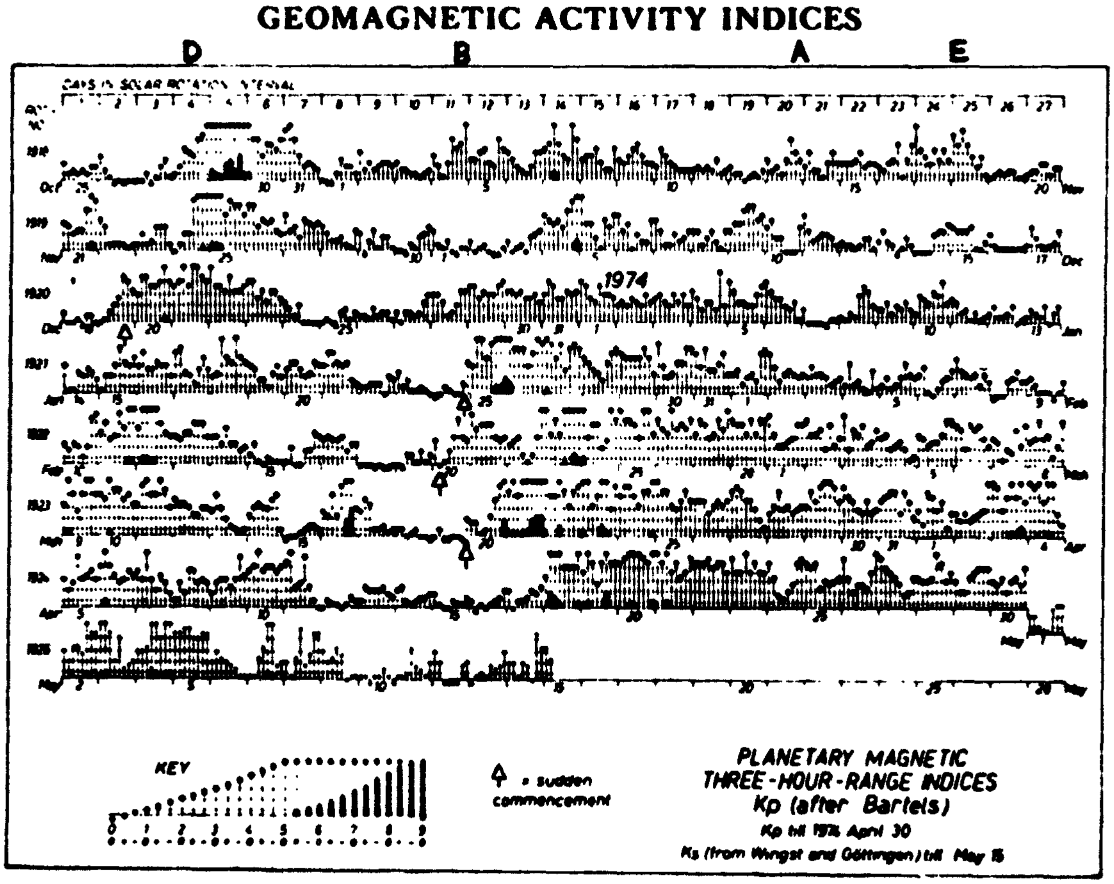

Figure 26. A Bartels "musical diagram" of 3-hour K_p values during the Mariner 10 mission. The signature of the high-speed stream structure of the solar wind is seen in the time variation of the geomagnetic activity index during the mission (see text).

Geomagnetic disturbances associated with stream D began on November 24, December 19 (SC at 1642-1645 UT), January 15 and February 10-11 (NOAA, 1974). A more complex pattern of disturbances was seen during March 1974. A disturbance beginning on 8-9 March preceded the passing of the positive sector leading boundary, and a storm beginning on 16 March occurred later in the positive sector than had previously been observed for stream D. One sees in Figure 26 a tendency for stream D to drift such that it advances in time relative to the 27-day recurrence period, while stream B tends generally to drift to later times. Stream B produced geomagnetic sudden commencement storms (SSC events) beginning at 2259 UT on January 24 at 2204 UT on March 19. A sudden commencement was observed at 0156 UT on February 20, followed by several days of geomagnetic disturbance not officially classified as an SSC event. Other lesser disturbances produced by stream B began on November 4-5, December 4, and April 18.

Figures 27 and 28 show the magnetic profile of stream B in hourly average field magnitude and direction angles as seen by both IMP 8/HEOS at 1 AU and by Mariner 10 at 0.78 AU during BSR 1921. It was pointed out in Chapter I that perhaps the same parcel of solar wind plasma that was seen at Mariner 10 during approximately 19-21 January was also observed at Earth with ≤ 1 day propagation time. From the IMP 8 plasma observation (Lazarus, private communication) we have indicated on Figure 27 the location in time of the density and temperature peaks as well as the extent of the region of velocity greater than 750 km/sec. This stream is seen to be similar in magnetic characteristics to the classical example shown in Figure 6. In addition, it was found to have an extended magnetic field fluctuation region associated with it. This aspect of the stream's magnetic signature will be illustrated and discussed in Chapter IV.

The hourly average magnetic field magnitude is seen in Figure 27 to fall to 1γ for several hours just before the relatively steep increase in magnitude to a

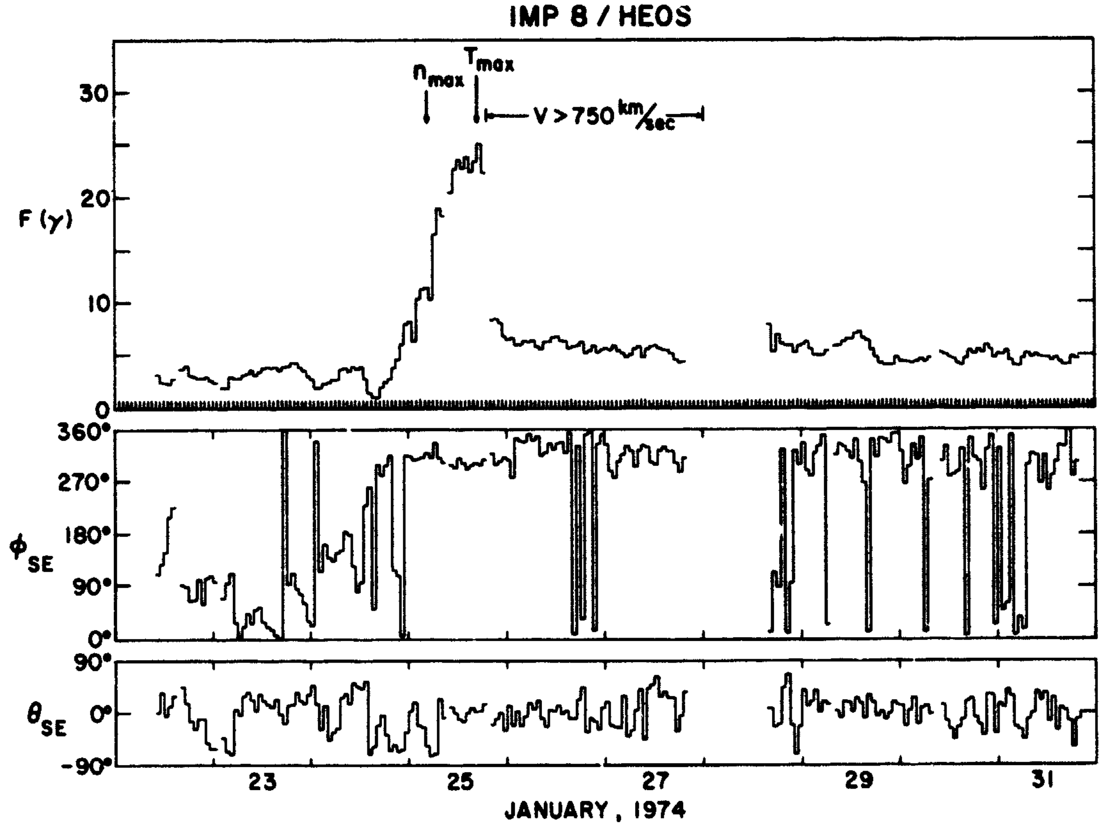

Figure 27. Hourly average magnetic field magnitude and direction angles ϕ and θ observed during the passage of a corotating high-speed stream at 1 AU by the IMP 8/HEOS spacecraft. Positions of maximum solar wind density, temperature and bulk speed observed by the IMP 8 Plasma Analyzer are also indicated.

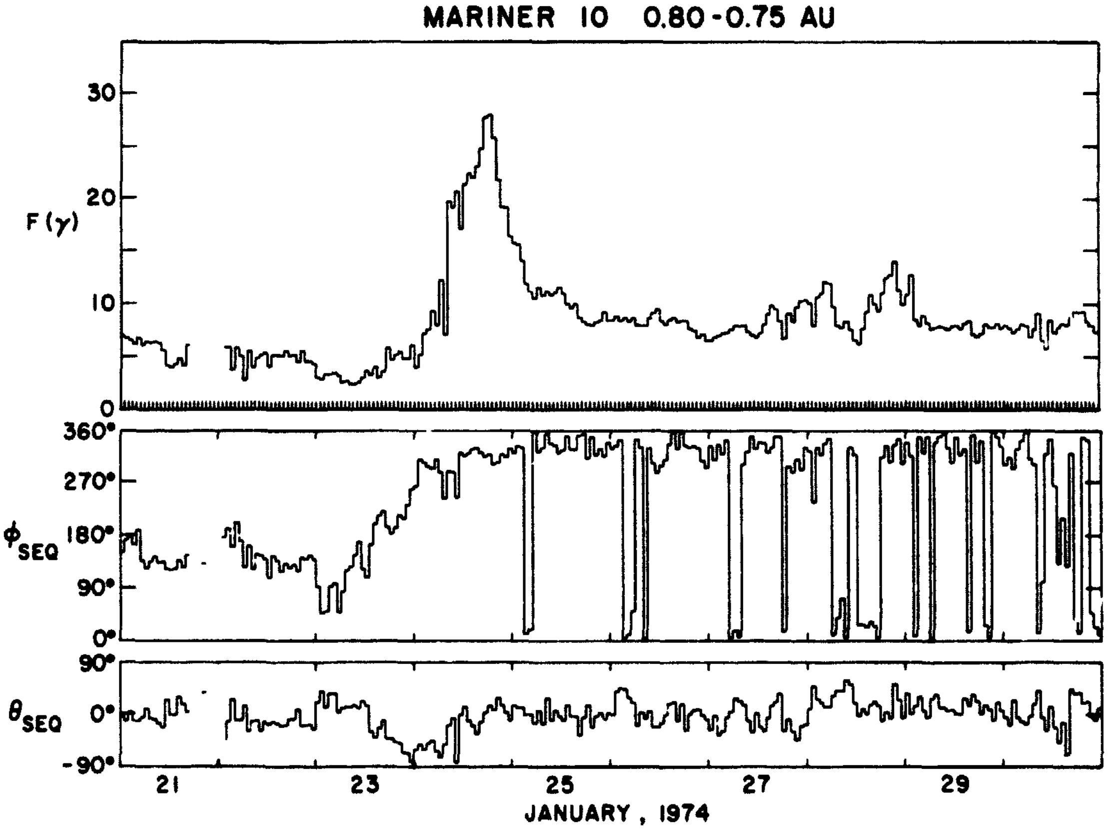

Figure 28. Mariner 10 hourly average magnetic field measurements during the passage of the same stream shown in Fig. 27 at 1 AU. Mariner 10 ranged in heliocentric distance from 0.8 – 0.75 AU during this 9-day period.

maximum of 25γ in the field compression region, which, as discussed in Chapter I, is seen to lag in time behind the density maximum (in this case) by ~12 hours. The field magnitude at Mariner 10 is seen in Figure 28 to be reduced to 2.4γ somewhat further in advance of the maximum field region. The maximum magnitude at Mariner 10 was 28γ, so that a reduction in peak field in the stream of only 10% took place between 0.78 and 1 AU. This stream closely follows the sector boundary which is relatively broad if defined in terms of the field reversal region, which takes approximately one entire day to pass the spacecraft at both locations. Once again we are comparing SE data at 1 AU with Mariner 10 SEQ data, but the small difference in coordinate system orientation should not influence a qualitative comparison of large-scale characteristics.

A southward component of B has been found to be an important factor in geomagnetic disturbances (Dungey, 1961; Fairfield and Cahill, 1966; Kane, 1972, 1974; Hirshberg and Colburn, 1969 and others). A negative B_z enables the merging of IMF and geomagnetic fields. A large negative B_z enhances the rate at which disturbance energy in the solar wind can be coupled into the magnetosphere. Bobrov (1973) has suggested that a large negative B_z component is a feature of the interaction region of both corotating and flare associated streams that produce magnetic storms. One sees that both IMP 8/HEOS and Mariner 10 observed large negative B_z values in the portion of the interaction region ahead of the stream interface. The period of negative B_z has a time duration in this case of 16-20 hours.

One final large-scale feature of note that can be seen in comparing Figures 27 and 28 is that, while the maximum field magnitude in the field compression region is only reduced by approximately 10% from 0.78 AU to 1 AU, the post-stream field intensity has a larger reduction over that radial distance. Although there may still be stream-related effects in the field measurements 5-6 days after the passage of the interaction region, if one takes the average magnitude level there as an "undisturbed" field intensity, then comparison in this case shows a reduction from 0.78 to 1 AU of approximately 40%. The observed difference is consistent with the heliocentric distance dependence of the magnitude of the average magnetic field, as shown in Figure 24.

This effect can also be seen in Mariner 10 measurements taken at different radial distances from the sun. In Figure 29 we have superimposed the field magnitude signatures of stream B observed by Mariner 10 on three successive solar rotation at heliocentric distances of 0.78, 0.64 and 0.48 AU, giving a radial distance variation of 0.14 AU between SR's 1921 and 1922 and 0.16 AU between 1922 and 1923. One sees that the peak values of the magnitude enhancements are not very different. The differences between the interaction region maxima are considerably less than the differences between the average field intensities on later days. Thus with the post-stream field magnitude decreasing with radial distance from the sun according to the radial distance dependence of the undisturbed solar wind while the maximum magnitude in the field compression region of the stream shows only a small variation with distance, the maximum magnitude must increase with distance relative to the undisturbed field intensity.

The previously described kinematic model of Burlaga and Barouch (1975) predicts an increase in the magnitude enhancement of the field in the leading portion of a typical stream with increasing heliocentric distance. Their ecliptic plane contour map of field magnitude enhancements relative to the values that would be measured in the absence of a high-speed stream predicts that between 0.5 AU and 1 AU an increase in the field in the leading part of a typical stream of almost a factor of two could be expected. Figure 30 shows once again hourly average data for the two solar rotations 1921 and 1923. In this figure the observations have been normalized by the average post-stream field magnitude levels to give magnitude enhancement values for both the Mariner 10 and IMP 8/HEOS

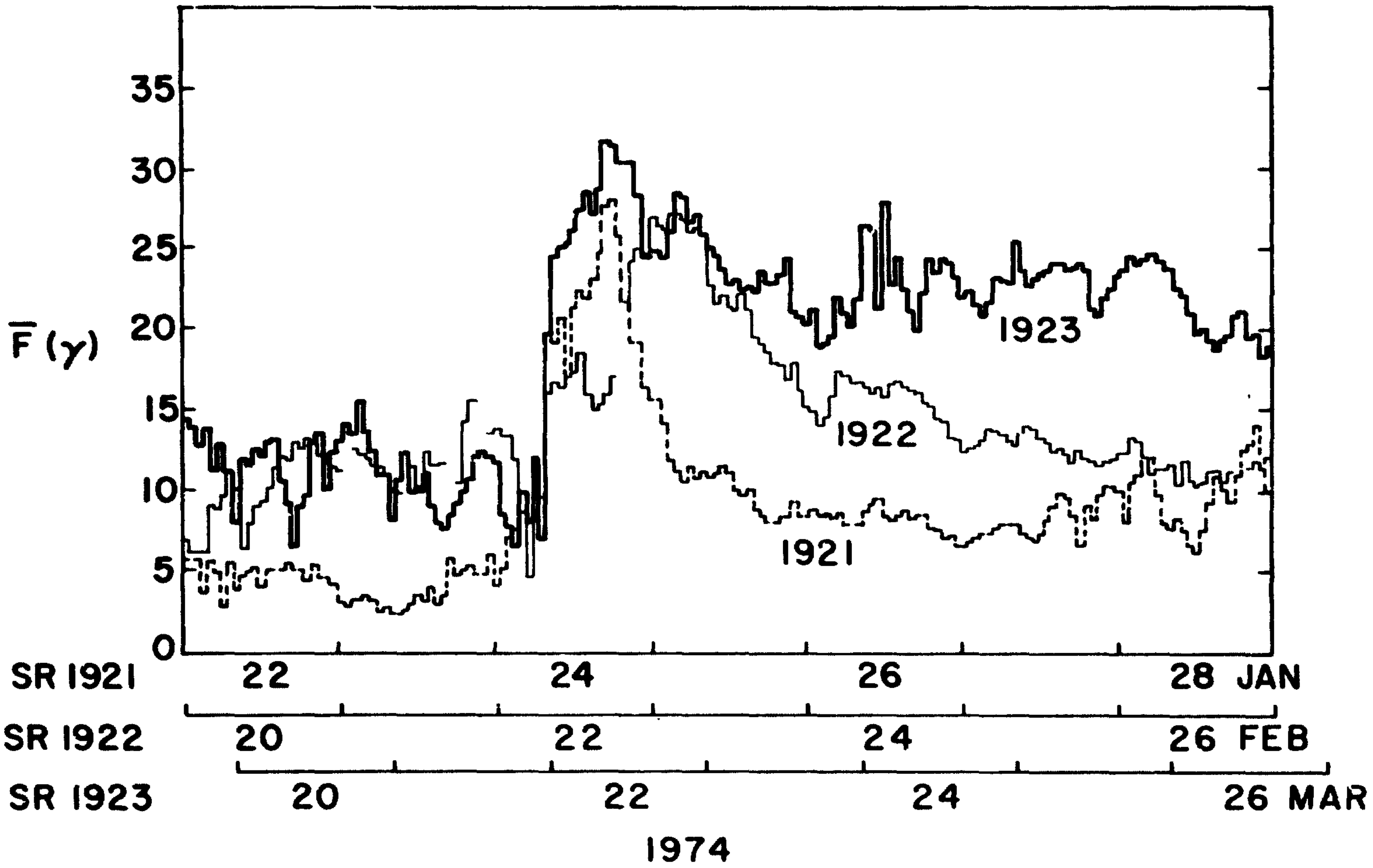

Figure 29. Superimposed field magnitude high-speed stream profiles observed by Mariner 10 during three successive passages of the same corotating stream. Heliocentric distance of M10 ranged from 0.78 to 0.48 AU during the three solar rotations. Note the relatively small differences between peak values of F.

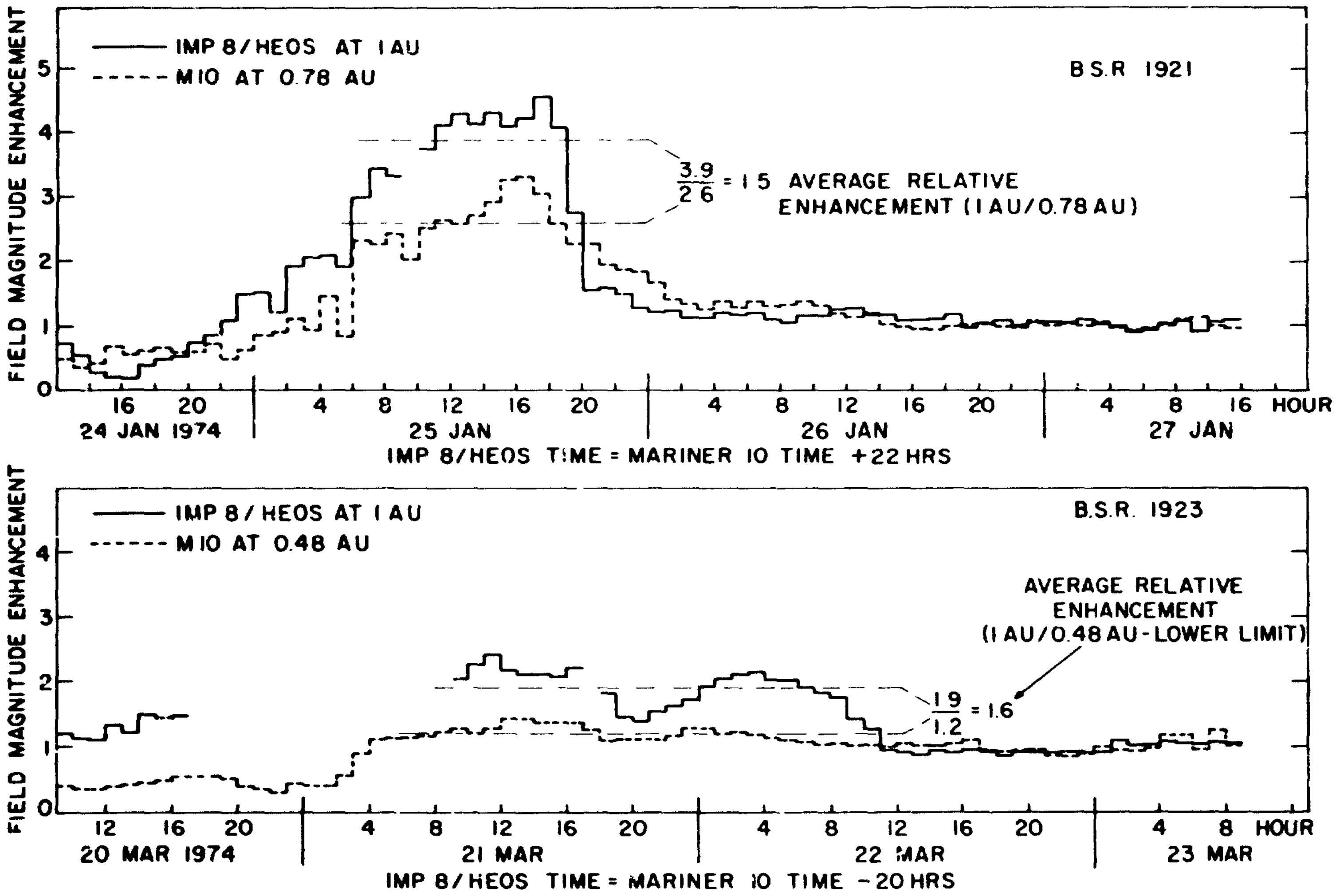

Figure 30. Observation of the field magnitude enhancement in a recurring stream at two heliocentric distances by Mariner 10 and the same stream profile at 1 AU by IMP 8/HEOS. Enhancements are computed in each case relative to the average of a 12-hour post-stream interval (last 12 hours on each data plot). Mariner 10 data have been time-shifted as indicated below each panel.

data, which are shown superimposed for comparison. Data from the leading portion of the enchancement region were not obtained at 1 AU during SR 1923, so that the relative enchancement determined for that rotation is a lower limit. For the two cases shown, an increase in field magnitude enhancement with increasing distance is found, with the relative enhancement being at least 1.5 in both cases.

In addition to that feature, Figure 30 also shows both a weakening and a broadening of the enhancement region between SR's 1921 and 1923. If the relative enhancement value obtained for SR 1923 is approximately correct, then it took a greater distance to build up to the same relative enhancement that developed in SR 1921 over a shorter radial distance.

The theory of Burlaga and Barouch (1974) also predicts that characteristic variations of plasma and field parameters through typical streams should be more gradual closer to the sun, with a steepening of these features taking place with increasing radial distance from the sun. The Mariner 10 data may be too limited at this time to use as a basis for generalization, but the stream-associated variations observed during SR 1923 tend to be steep abrupt features. This can best be seen in Figure 25. In particular the leading edge of the field compression region has a steeper gradient than was observed during any previous observation of the stream. Since that portion of the stream was not observed at 1 AU, it is not possible to say whether the steeper character observed at 0.48 AU was simply a result of the temporal evolution of the stream or was truly a feature of the IMF nearer to the sun.

CHAPTER 4

OBSERVATIONS OF IMF FLUCTUATIONS

1. Characteristics of Relative Magnitude and Directional RMS Deviations

Figures 13 and 14 showed daily average values of the field magnitude and vector field relative fluctuation parameters σ_F/F and σ_C/F, respectively, at both Mariner 10 and near earth throughout the mission. In Figure 14 one sees the suggestion of an increasing trend in σ_C/F with decreasing radial distance from the sun, while σ_F/F shows no clear radial distance dependence. The heliocentric distance related characteristics of the data will be discussed in Section IV 1.1.

1.1 Solar Rotation Statistics of Fluctuation Parameters

In comparing the variations in σ_C/F at Mariner 10 with those at 1 AU during this period, one sees larger amplitude excursions in the IMP 8/HEOS data than in the Mariner 10 data. Means and standard deviations of σ_C/F were computed for each solar rotation for both IMP 8/HEOS and Mariner 10, and for every solar rotation both the mean and the standard deviation were higher for IMP 8/HEOS than for Mariner 10. The mean was on average 12% higher and the standard deviation 30% higher on average. Since there is no indication in the Mariner 10 data that either the mean or the standard deviation of σ_C/F decreased with decreasing heliocentric distance, a closer examination of the source data was conducted.

Upon inspecting the IMP 8/HEOS data in detail it was found that there were 22 daily average σ_C/F values greater than the largest σ_C/F value from Mariner 10. All of the data from those days were from the HEOS spacecraft. When statistics are computed for only the IMP 8 data by solar rotation, the results are more nearly comparable to the Mariner 10 results (the means differ by 1.6% on average and the standard deviation by 7%). Table IV includes the comparative statistics for each solar rotation as well as for the combined IMP 8/HEOS data set. An inspection of the σ_C data from both IMP 8 and HEOS when both spacecraft were in the interplanetary medium during a single complete period of HEOS IMF observations shows that the HEOS σ_C values are usually, though not always, higher than the IMP 8 values throughout the entire period.

Statistics taken over the lifetime of the HEOS spacecraft show an average value for σ_C of 3.0γ for 18,500 hourly averages (King NSSDC, private communication). For a combined set of 46,000 hours from eight IMP spacecraft an average of $2.5\,\gamma$ with standard deviation of 0.14γ was obtained. Thus the HEOS mean value of σ_C was found to be greater than for the series of IMP spacecraft, from IMP 1 through IMP 8, by 3σ. These results suggest either (1) that the HEOS IMF data include some contamination from magnetosheath observations or (2) that the different way in which σ_C is computed for HEOS data relative to the method used for IMP data provides a biased result. Assuming that sufficient care has been taken in (1) and because of the fact that the observed offset appears to occur throughout the entire HEOS IMF period, we must conclude that (2) is the source of the observed difference. That this is so has been confirmed by Hedgecock (Private communication).

The computational differences are as follows. While the IMP spacecraft and Mariner 10 analyses use the definition

$$\sigma_C = (\sigma^2_{B_X} + \sigma^2_{B_Y} + \sigma^2_{B_Z})^{1/2}, \qquad \text{(IV-1)}$$

the definition

$$\sigma_C = (\sigma_F^2 + F^2\sigma_\theta^2 + F^2 \cos^2 \theta\sigma_\phi^2)^{1/2} \qquad \text{(IV-2)}$$

is used for the HEOS data, since the HEOS data tapes include only the means and rms deviations of the field magnitude F and the θ, ϕ direction angles rather than the rectangular component means and rms deviations. Equation (IV-2) is derived by taking differentials of the components

$$B_j = f_j(F, \theta, \phi), \quad j = 1, 2, 3$$

and then simply squaring and adding terms. Application with a discrete time series then requires replacing the differentials with rms deviations of the magnitude and the two direction angles. The resulting expression is not in exact mathematical equivalence with the first expression given above for σ_C.

As one can see from Figure 13, the correlation between ΣK_p and σ_C/F suggests that almost all of the large geomagnetic variations coincidentally occurred when HEOS was the only spacecraft measuring the IMF. Although higher values of σ_C/F is expected at those times, it is probable that the equivalence between equations (IV-1) and (IV-2) is poorer at times of larger angular fluctuations, resulting in a poorer (and generally higher) estimate of σ_C. At any rate, whatever the source, the larger variation seen in σ_C/F in the 1 AU data will be considered to be an artifact of the data analysis rather than due to any physical processes. Referring again to Table IV, we see that the only SR during which the Mariner 10 mean value of σ_C/F is significantly greater than that observed by IMP 8 was SR 1923. The standard deviation of the daily averages over the rotation show that the level of fluctuation was more variable from day to day at 1 AU than at Mariner 10 at 0.46 - 0.52 AU. Also, one still sees a tendency in the IMP 8 data alone for the solar rotation mean value of σ_C/F to be more variable from one solar rotation to the next than that for Mariner 10, but since the IMP 8 data set alone only contains from 12 to 15 days of data per solar rotation, caution should be employed in interpretating the comparative values. These data are plotted in Figure 34 and will be discussed further in the next section.

In comparing the Mariner 10 daily average σ_F/F values with those from IMP 8/HEOS in Figures 13 and 14, one sees larger variations in that quantity at Mariner 10 than in the 1 AU data. Since there are no differences in this case in the way σ_F/F is computed for the various spacecraft, the results from each should be equivalent. The only differences here are the differences in the time resolution of the fine time scale data used to compute the hourly averages. Table V is a comparison of solar rotation means and standard deviations for σ_F/F for each of the three spacecraft separately as well as for the combined IMP 8/HEOS data set. One sees in Table V that the IMP 8/HEOS means were greater than those for Mariner 10 except for SR 1923. Taken separately, the solar rotation means for IMP 8 were on average 9% greater than for Mariner 10 and those for HEOS were 17% greater on average. The averages of solar rotation standard deviations of the daily σ_F/F values, on the other hand, were lower for IMP 8 and HEOS than for Mariner 10. Note that for SR's 1918 and 1919 the means were identical for Mariner 10 and HEOS, while more variability from day to day was observed by Mariner 10 even during those early solar rotations, although the difference during SR 1918 when Mariner 10 was near 1 AU is probably not significant. As in the case of the σ_C/F solar rotation statistics, these data will be discussed further in relation to the radial distance variations of fluctuations in the following section.

The statistical distributions of hourly average σ_C/F and σ_F/F values by solar rotation during the period of study are shown in Figures 31 and 32, respectively. The IMP 8/HEOS distributions have been included in each case for comparison. For the σ_C/F distribution shown in Figure 31, the IMP 8/HEOS distribution must be interpreted with caution because of the computation problem already discussed.

The IMP 8/HEOS distributions exhibit structures that are quite similar to the Mariner 10 distributions for at least the first two solar rotations, and even to some extent for later rotations. The general tendency at 1 AU is for the σ_C/F distribution to be peaked at low values of relative amplitude but with a substantial tail of high relative amplitude values, so that the probability is high that σ_C/F will be moderately low (0.3 - 0.4 on average), but large values ($\sigma_C/F \approx 1$) can also be observed. The trend that can be seen in the Mariner 10 distribution relative to the IMP 8/HEOS distribution is a gradual shift toward a more symmetric distribution with decreasing heliocentric distance. This means fewer cases of relative amplitude lower than the mean value and more cases of relative amplitude higher than the mean, while the mean itself did not change significantly. A similar tendency was at times seen in the 1 AU data as well, as during SR 1922 for example, so that it cannot be concluded that such a variation in the σ_C/F distribution is strictly a radial distance effect. It is likely that such variation in the fluctuation characteristics of the IMF are intimately coupled with the corotating stream structure of the interplanetary medium and with changes in stream characteristics with radial distance from the sun.

Figure 32 compares the σ_F/F solar rotation distributions for Mariner 10 with those from IMP 8/HEOS during the mission. The Mariner 10 distributions, especially for the later solar rotations, tend to be more sharply peaked than the IMP 8/HEOS distributions, with a more nearly constant most probable value. The mean values are not significantly different for the two sets of distributions, which means that there also must be a greater number of large relative amplitude cases at Mariner 10, as indicated by the higher percentage of cases of RA > 0.25. This difference is seen throughout most of the period of interest, with the tendency toward a lower most probable value at Mariner 10 even during the earliest solar rotations, though the differences during SR 1918 may not be significant.

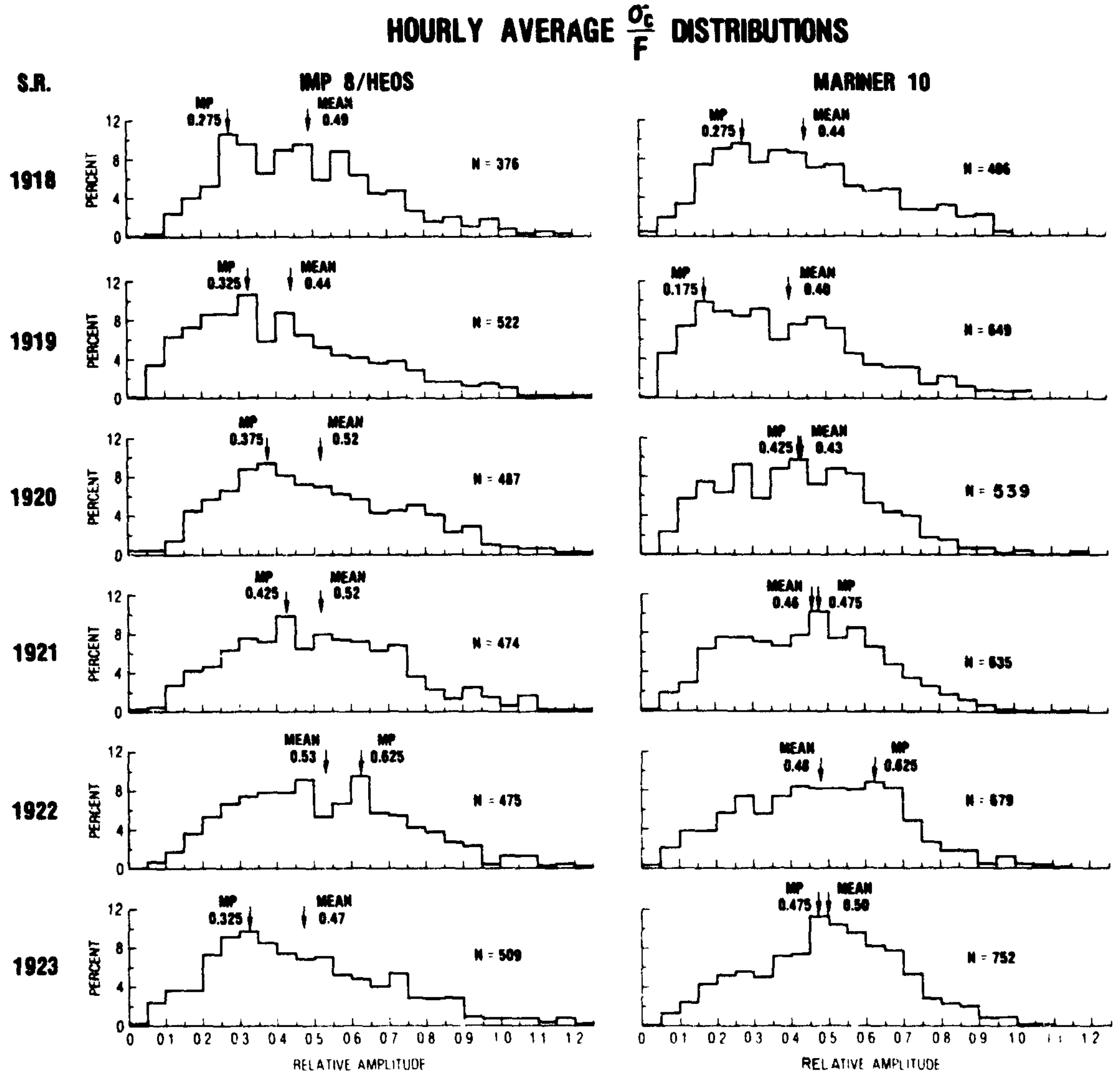

Figure 31. Comparison of hourly average relative vector field fluctuation distribution at Mariner 10 and IMP 8/HEOS for each solar rotation during the mission.

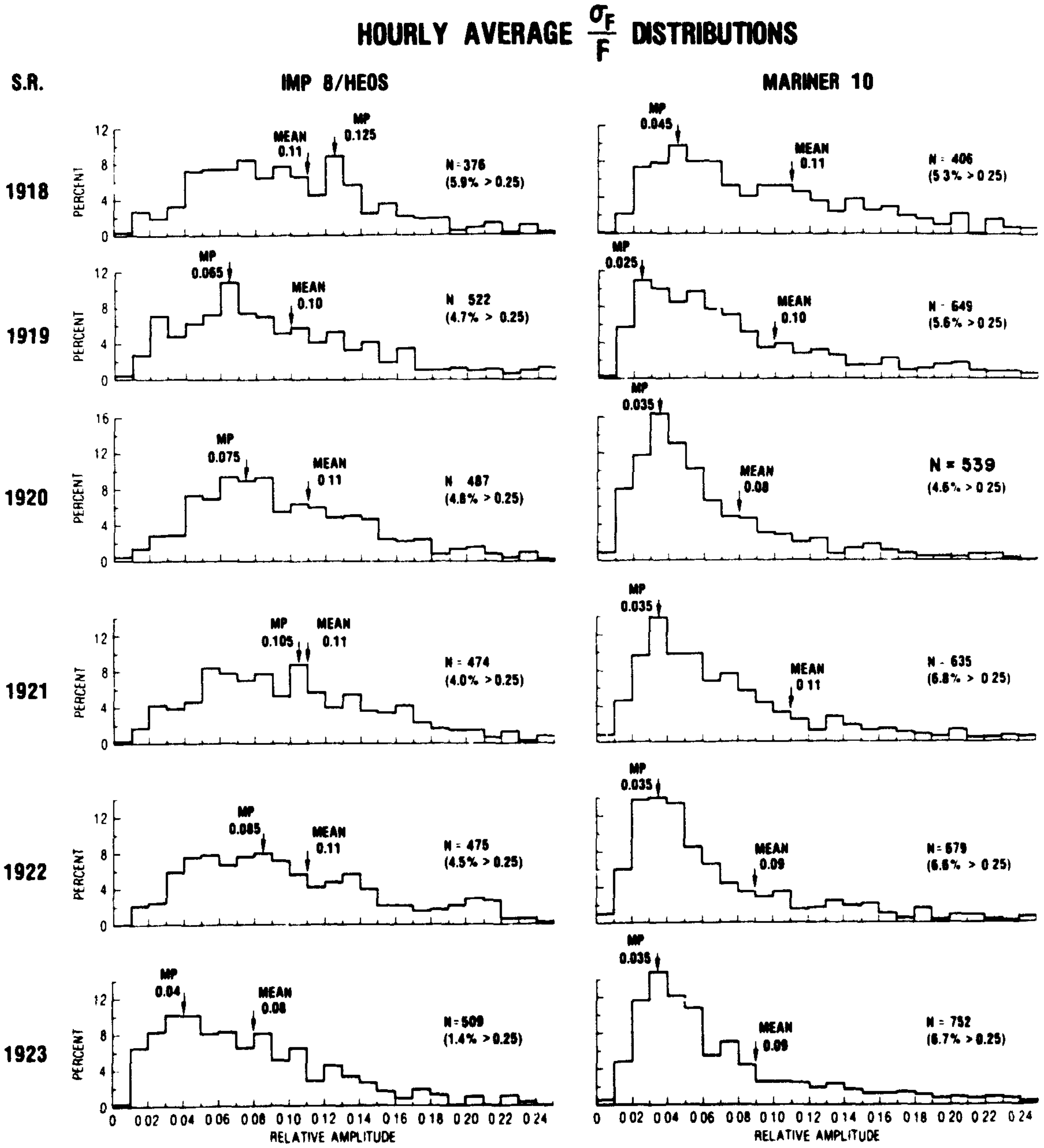

Figure 32. Comparison of hourly average relative magnitude fluctuation distribution at Mariner 10 and IMP 8/HEOS for each solar rotation during the mission.

1.2 Observed Radial Distance Dependence

The daily average values of σ_F/F and σ_C/F are plotted in the upper and lower panels, respectively, of Figure 33. These are the daily averages of the hourly relative fluctuation data, which were computed from the one-hour averages and rms deviations of the 42 sec total field and field component rms deviations as described in section II.2. Also shown are the least-squares best-fit power law curves for each of the parameters (see Appendix A).

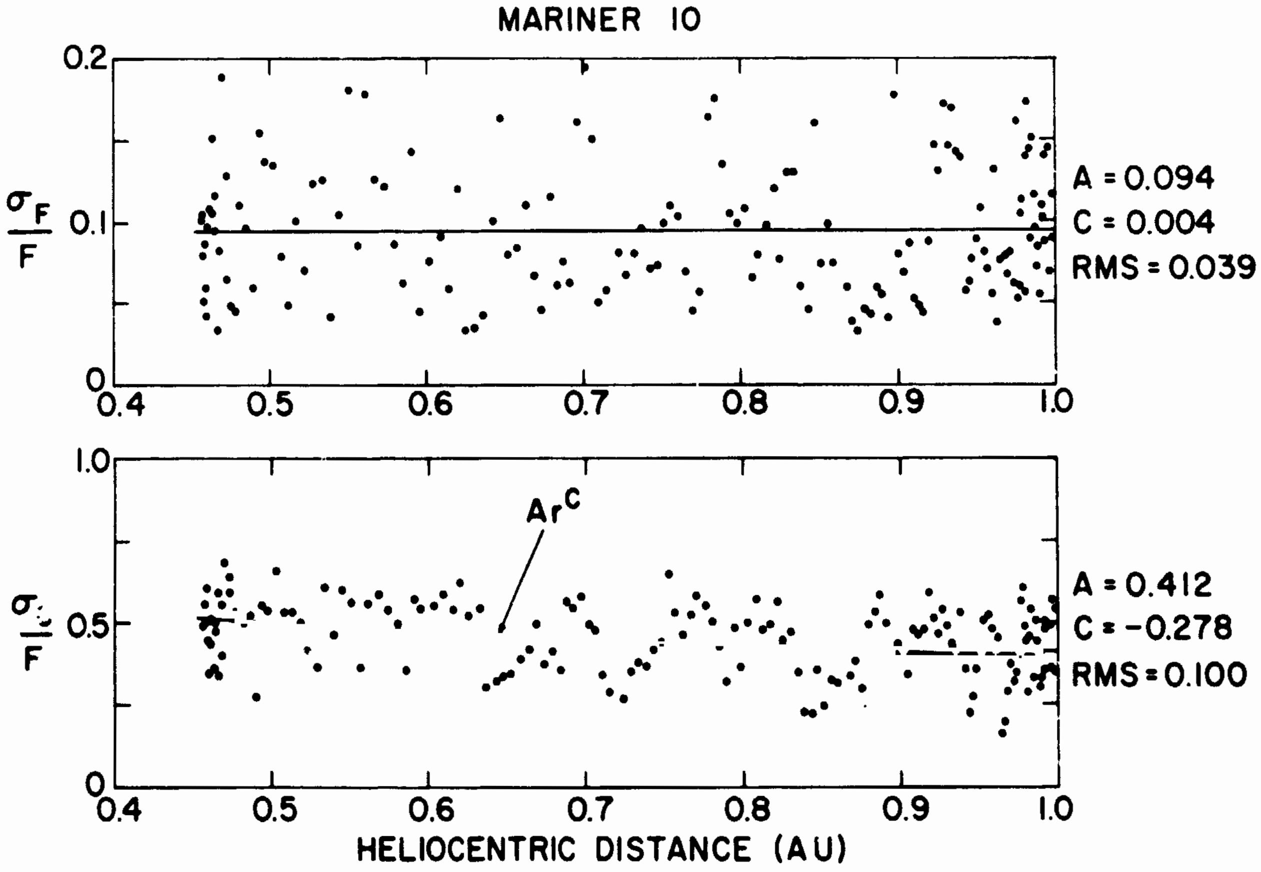

Figure 33. Mariner 10 daily average relative magnitude rms deviation values (upper panel) and relative vector field rms deviation values (lower panel) as functions of heliocentric distance. The best fit power law curves show little if any variation with distance of σ_F/F and a weak decrease with increasing distance of σ_C/F.

Considerable scatter is seen in the σ_F/F data, but even with the relatively sensitive scale employed in Figure 33, the power law fit suggests that on average the relative fluctuations in the magnetic field magnitude remained approximately constant over the range of heliocentric distance covered by Mariner 10. The power law dependence was found to be

$$\frac{\sigma_F}{F} = (0.094 \pm 0.010)\, r^{+0.004 \pm 0.249}.$$

This dependence is not consistent with the increasing gradient observed by Mariner 4 (Coleman et al., 1969) but is consistent with the lack of strong variation one infers for the relative magnitude variation observed by Pioneer 10 (Smith, 1974).

The Mariner 10 and Mariner 4 data were analyzed in quite different ways. The Mariner 4 distance dependence with exponent 0.71 was computed by dividing the distance dependence of the rms deviation of 50.4 sec field magnitude values over 27-day intervals by the distance dependence of 27-day average field magnitudes, where the analysis was carried out for 68 overlapping 27-day intervals with three-day centers. Further, this result was based on a data set which had been edited to correspond to a low level of solar-terrestrial activity. A radial distance dependence $r^{0.50}$ was obtained when the full data set was used.

The Mariner 4 analysis also included rms deviations taken over periods of one day and three hours, respectively. These were again averaged over each of the 68 overlapping 27-day intervals in an attempt to smooth out temporal variations. The three-hour values should be the most directly comparable to the Mariner 10 results which were averages of one-hour rms values. The difference still remains that the Mariner 10 analysis included the normalization of the one-hour rms's by the one-hour average magnitude of the field, and these quantities were further averaged over one-day periods and then subjected to curve fitting. In contrast, the three-hour rms's for Mariner 4 were averaged, smoothed and curve-fitted, and the resulting distance dependence normalized by the distance dependence of the smoothed 27-day average field magnitude. For those data the Mariner 4 analysis yielded distance dependences of $r^{0.38}$ for the "quiet" data and $r^{0.56}$ for the total data set. The "quiet" data result is the most nearly comparable to the Mariner 10 result, but still falls outside the error limits on the exponent of the Mariner 10 distance dependence. The differences in the results are significant, and must be due to a combination of factors, including the differences in the methods used to derive the fluctuation parameters as well as the differences in the times of the investigations and in the regions of interplanetary space being studied ($1.0 < r < 1.5$ AU for Mariner 4). The fluctuation state of the IMF during the Mariner 4 mission may have been different from that during Mariner 10. Mariner 4 observed a much more unstable IMF in terms of sector polarity. Coleman et al. (1967) reported that the polarity was often so variable that no polarity could be assigned. The degree to which the characteristics of the medium were evolving in time could have influenced the Mariner 4 results. It was from the distance dependence $r^{0.7}$ that it was estimated that relative fluctuations could reach a value $\Delta B/B = 1$ at a heliocentric distance of $r \simeq 4.3$ AU (Coleman et al., 1969). This prediction is contrary to the Pioneer 10 observations (Rosenberg et al., 1975) which suggest a more gradual increase in relative magnitude fluctuations with increasing distance.

Referring to the lower panel of Figure 33, we see that the best fit to the daily average values of σ_C/F from Mariner 10 suggests a gradual decrease in relative vector field fluctuations with increasing radial distance from the sun. The radial distance dependence for that relative fluctuation parameter, which is derived from field component rms deviations, was found to be

$$\frac{\sigma_C}{F} = (0.412 \pm 0.238)\, r^{-0.278 \pm 0.129}$$

This parameter is a measure of the fluctuations in the vector field and thus includes transverse wave modes as well as other types of directional fluctuation. The

Mariner 4 parameter which is closest to this in definition is $\sigma_S(b_H)/\langle B\rangle$, where $\sigma_S^2(b_H) = \sigma_S^2(b_y) + \sigma_S^2(b_z)$ is a measure of fluctuation transverse to the mean field direction, which defines the X-direction in the coordinate system used for the analysis. $\sigma_S(b_i)$ is the rms deviation of the ith component over each of the overlapping 27-day periods. The best-fit to the resulting smoothed relative fluctuation data gave a radial distance dependence of $r^{-0.07}$ for the "quiet" data set and a dependence of $r^{0.02}$ for the combined data set (Coleman et al., 1969). The Mariner 10 result is in agreement with the "quiet" data fit from Mariner 4 in that the latter also suggests a decrease in relative vector field fluctuation with radial distance, although the gradient computed from the Mariner 4 data is more gradual than that found for Mariner 10. The total set of Mariner 4 data suggests an even more gradual increase with increasing distance.

The sclar rotation most probable values of the Pioneer 10 daily and hourly field component variances were all found to be proportional to the square of the most probable value of the field magnitude (Smith, 1974). This was interpreted as implying that relative fluctuations were approximately constant with distance. The combined Mariner 4, Mariner 10 and Pioneer 10 support the conclusion that there is only a weak gradient, if any, in the relative directional fluctuation of the IMF between 0.46 and 4 AU. Mariner 5 measurements between 1 and 0.7 AU were not included in this comparison because no results concerning the radial dependence of IMF fluctuations as observed by that spacecraft have as yet been published.

Figure 34 displays the data of Tables IV and V in graphical form. In the top section of Figure 34a we see that the solar rotation mean values of σ_C/F indicate considerable variability from one solar rotation to the next, although, as indicated previously, some of the scatter in the data is probably due to the incomplete coverage of the IMF by the earth-orbiting spacecraft. One sees again that the values computed from HEOS data alone, and hence also for the combined data set,

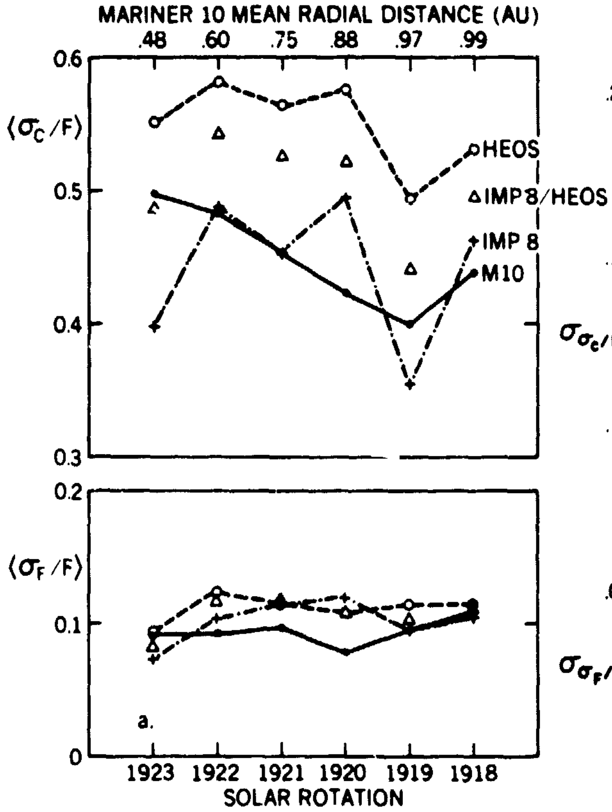

Figure 34a. Solar rotation averages of relative vector field (top panel) and field magnitude (lower panel) rms deviations during the mission for Mariner 10, combined IMP 8/HEOS and separately for IMP 8 and HEOS, with symbols plotted at the mean radial distance of Mariner 10 during each solar rotation. IMP 8 and HEOS data at 1 AU are included to show time variations (see text for discussion of differences between IMP 8 and HEOS values).

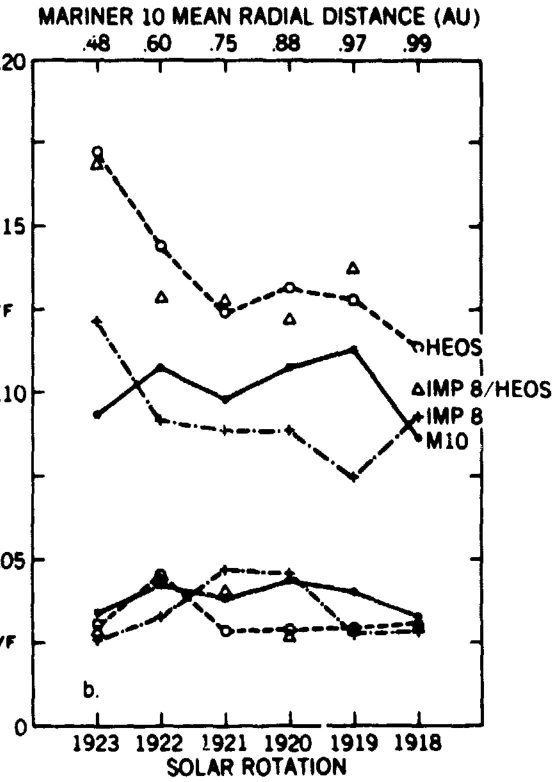

Figure 34b. Standard deviations of relative fluctuation parameters associated with solar rotation mean values plotted in (a). These data indicate variability of fluctuations levels throughout the mission both at 1 AU (IMP 8/HEOS) and over the range 1 to 0.46 AU (M10).

are higher than for IMP 8 and Mariner 10 due both to computational differences and the fact that HEOS IMF observing periods coincided with most of the periods of highest disturbance activity in the interplanetary medium during the 5-2/3 solar rotations under investigation. One does see, however, the same variational tendencies at both HEOS and IMP 8. This suggests that one can at least interpret the trends in the solar rotation data as real time variations, even though the absolute values of the data and the amplitudes of the variations are subject to question.

The HEOS data suggest that there may have been an overall general increase in $\langle {}_C/F \rangle$ with time at 1 AU during the period of the investigation, so that at least some of the increase with decreasing heliocentric distance observed by Mariner 10 could also have been a time variation. However, the tendency for a decrease in $\langle {}_C/F \rangle$ at 1 AU between SR's 1922 and 1923 as seen by both HEOS and IMP 8, while the monotonically increasing trend at Mariner 10 continued, suggest that there was a genuinely higher level (greater relative amplitude) of directional fluctuation near 0.46 AU than at 1 AU during SR 1923. The top portion of Figure 34b, which is a plot of the ${}_D$ values in Table IV, shows that there was apparently an increase in the day-to-day variability of ${}_C/F$ at 1 AU between solar rotations 1918 and 1923, while no significant overall change was seen at Mariner 10.

The lower portion of Figure 34a supports the view that relatively little change in ${}_F/F$, representative of compressional fluctuations, was observed either with decreasing radial distance by Mariner 10 or with time during this period by earth-orbiting spacecraft. In fact, these data show that the very slight decreasing trend with decreasing heliocentric distance found by fitting the Mariner 10 daily averages could be totally accounted for by a small gradual decrease in time during the period of study. No significant overall variation in day-to-day variability of ${}_F/F$ was observed by Mariner 10 or at 1 AU during this period, as can be seen in the lower part of Figure 34b, though slightly greater variability in the middle of the period is suggested by both the Mariner 10 and the IMP 8 data.

It is possible that some portion of the changes seen in IMF fluctuation either in time or with changing radial distance could also be due to changing heliographic latitude. There is insufficient data available to this investigation, especially from spacecraft at significantly different latitudes, to separate such effects from the other possible types of variation.

One final point should be mentioned concerning the Mariner 10 result for the radial distance dependence of the vector field directional fluctuations. Using data from Pioneer 6, Burlaga and Ness (1969) and Burlaga (1971a) showed that the directional discontinuities occurring during an eight-day period were primarily tangential. For the same period, Sari and Ness (1969, 1970) demonstrated that these discontinuities are a major contributor to the overall level of microscale fluctuations as measured by the power spectra. Such discontinuities were not excluded from the rms deviation averages used in this initial survey of the variation of σ_c/F with radial distance.

The results of an initial survey of the occurrence rate of directional discontinuities observed by Mariner 10 during the primary mission are shown in Figure 35. The occurrence rate is given in daily average number/hour and is plotted as a function of heliocentric distance in AU. Even though there is considerable scatter in the data, a clear increasing trend with decreasing heliocentric distance is seen. If a linear best fit were extrapolated out to greater distances the fall off rate would imply that few discontinuities would be seen beyond about 1.5 AU, which is disproved by observations. However, one can see from the trend of the data that the distance dependence is not linear, and, as shown, a nonlinear best fit results in a power law dependence of $r^{-1.28}$. Considerable structure can be seen in the occurrence rate data. Reference to the magnetic sector polarity pattern included across the top of the figure suggests strongly that at least some of the structure in the occurrence rate is related to the large-scale structure of the interplanetary medium during this time (this will be discussed further in the next section).

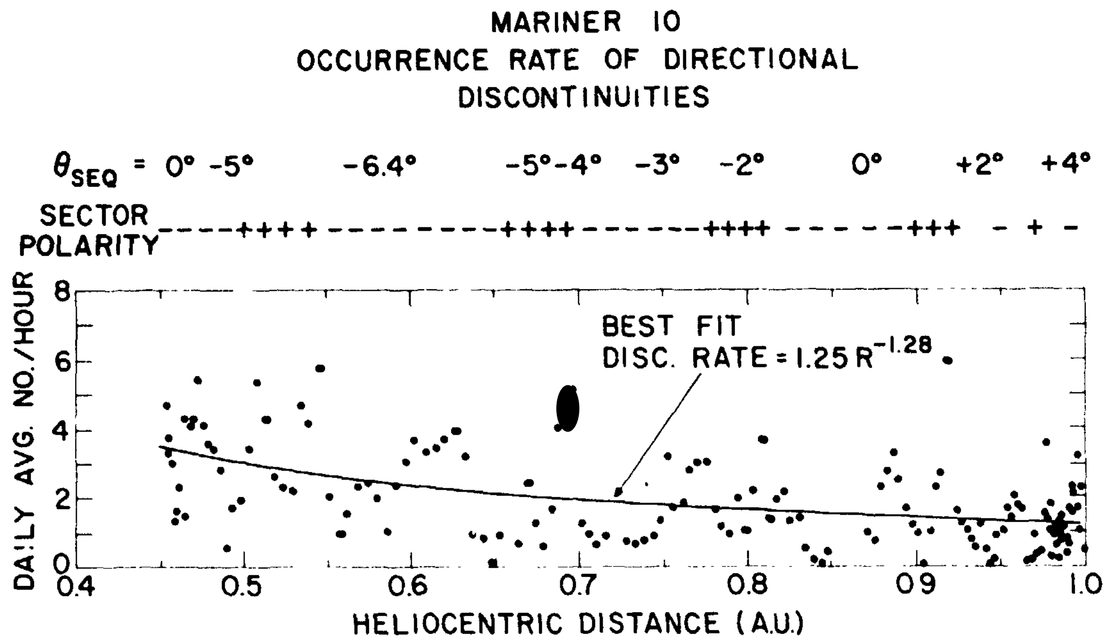

Figure 35. Mariner 10 observation of the variation with radial distance from the sun in the daily average occurrence rate of directional discontinuities. The nonlinear least-squares best fit curve is superimposed on the data. Also shown is the solar equatorial latitude of the spacecraft and the IMF sector polarity pattern.

Also shown at the top of Figure 35 are the heliographic latitudes of the spacecraft during this mission. As in the case of Mariani's result, one could also argue in this case that the variation is one with latitude rather than distance. We feel, however, that it is less likely that the rate would have continuously increased so systematically in going from northern to southern latitudes. The fact that an inverse power law dependence stronger than that found for σ_c/F was found for the rate of occurrence of directional discontinuities suggests that caution should be employed in interpreting the σ_c/F result in terms of simply a variation with distance of fluctuation energy due to transverse wave modes.

A similar dependence of the directional discontinuity occurrence rate on radial distance from the sun has been found by Tsurutani and Smith (1975) using Pioneer 10 and 11 data. They indicate that a decrease by roughly a factor of three in the occurrence rate between 1 and 5 AU was found using Pioneer 11 data, while a change by a factor of ~2 was seen by Pioneer 10. Higher rates were observed to follow high field regions in the IMF. They found evidence that discontinuities are "thicker" by a factor of 5 to 10 at 5 AU compared to 1 AU. This could account for at least part of the apparent occurrence rate decrease with increasing radial distance because of the increasing tendency for individual discontinuities to fall outside the limits of the fixed automatic selection criteria. A search for evidence of this directional discontinuity "thickness" variation with radial distance in the discontinuities observed by Mariner 10 has not yet been performed.

1.3 Relation to Large-Scale, Corotating Structure

We have seen that there is considerable variation in the large-scale IMF and in its fluctuation characteristics on a daily average time scale and even from one solar rotation to the next. This is due to the dynamic nature both of the sun as source of the interplanetary fields and plasmas and of the interplanetary medium itself. Even near the minimum of solar activity, the physical processes associated with interaction between different solar wind streams are continuously modifying the detailed characteristics of the IMF. These variations on a detailed or micro-scale level manifest themselves as perturbations of the large-scale properties of the field, and, along with variations in plasma streams and fields introduced at the source, contribute to the difficulties commonly encountered in attempts to separate space and time variations in the IMF.

In order to understand the interactive processes for purposes of assessing their detailed contributions to geomagnetic activity as well as to modification of the large-scale properties of the medium, a more complete understanding of the distribution of IMF fluctuations in both space and time relative to high-speed stream structure is needed. Only by fully understanding the magnetic field variations in high speed streams can one hope to make the most meaningful separation of IMF data into sets which contain the appropriately isolated characteristics of the relatively steady background IMF on the one hand and the disturbance field, which is almost always superimposed on it to some degree, on the other. Even when that is carefully done, at least some of the properties of the "background" IMF will be found to be different from one measuring period to the next since the source field on the sun is constantly evolving.

Since the magnitude enhancement in the interaction region of high-speed streams is a relatively well-known feature of simply structured high-speed streams, it can be used as a point of reference in the study of the magnetic structure of such streams. This compression effect on the field has already been described and discussed to some extent in Chapters I and III. Figure 36 is a superposed epoch plot of the IMP 8/HEOS daily average magnitude of the IMF at 1 AU by solar rotation during the four rotations 1920-1923. The individual daily values are plotted as points according to sector polarity, and the superimposed histogram denotes the average of these points. One sees the effects of the two major high speed streams (B and D) discussed in Chapter III. The smaller enhanced features may be related to weaker stream structures. The broad feature from days 23 to 26 is located in the same position in time as stream E identified in Figure 26. The feature at days 8 and 9 in the solar rotation roughly occupies the position at which stream A was observed during at least 6 solar rotation prior to the Mariner 10 launch, suggesting that there is at least a remnant of that stream also tending to recur during this time. A suggestion of this can also be seen in the K_p data of Figure 26 for SR's 1921-1923.

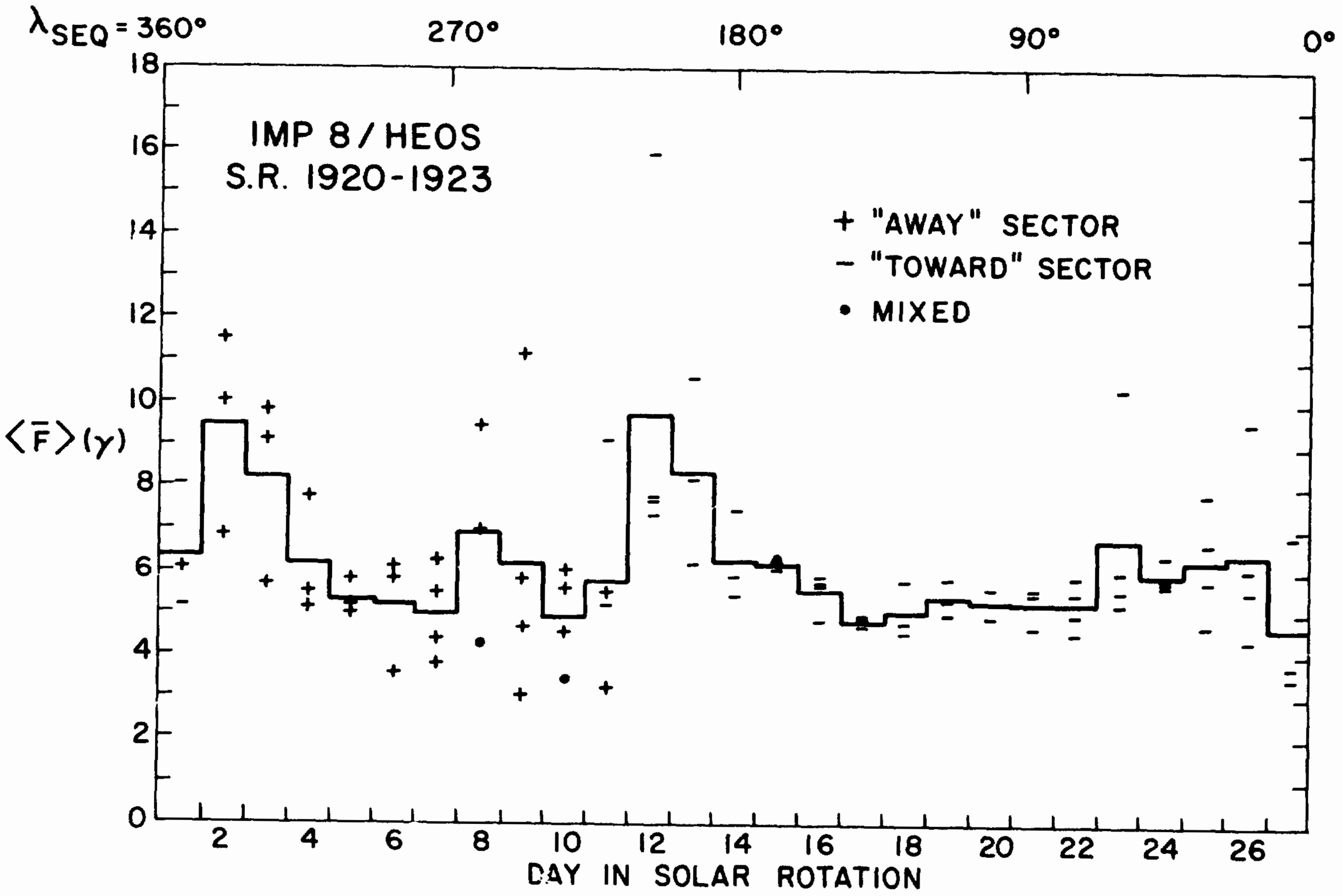

Figure 36. Superposed epoch plot of daily average IMP 8/HEOS field magnitude values for four solar rotations. Symbols plotted indicate average magnetic field sector polarity for a given day. In the case of mixed polarity ⟨φ⟩ was within ±20° of the perpendicular to the spiral direction. Solar equatorial longitude of earth is shown at top of figures. Histogram curve denotes averages of points for each day.

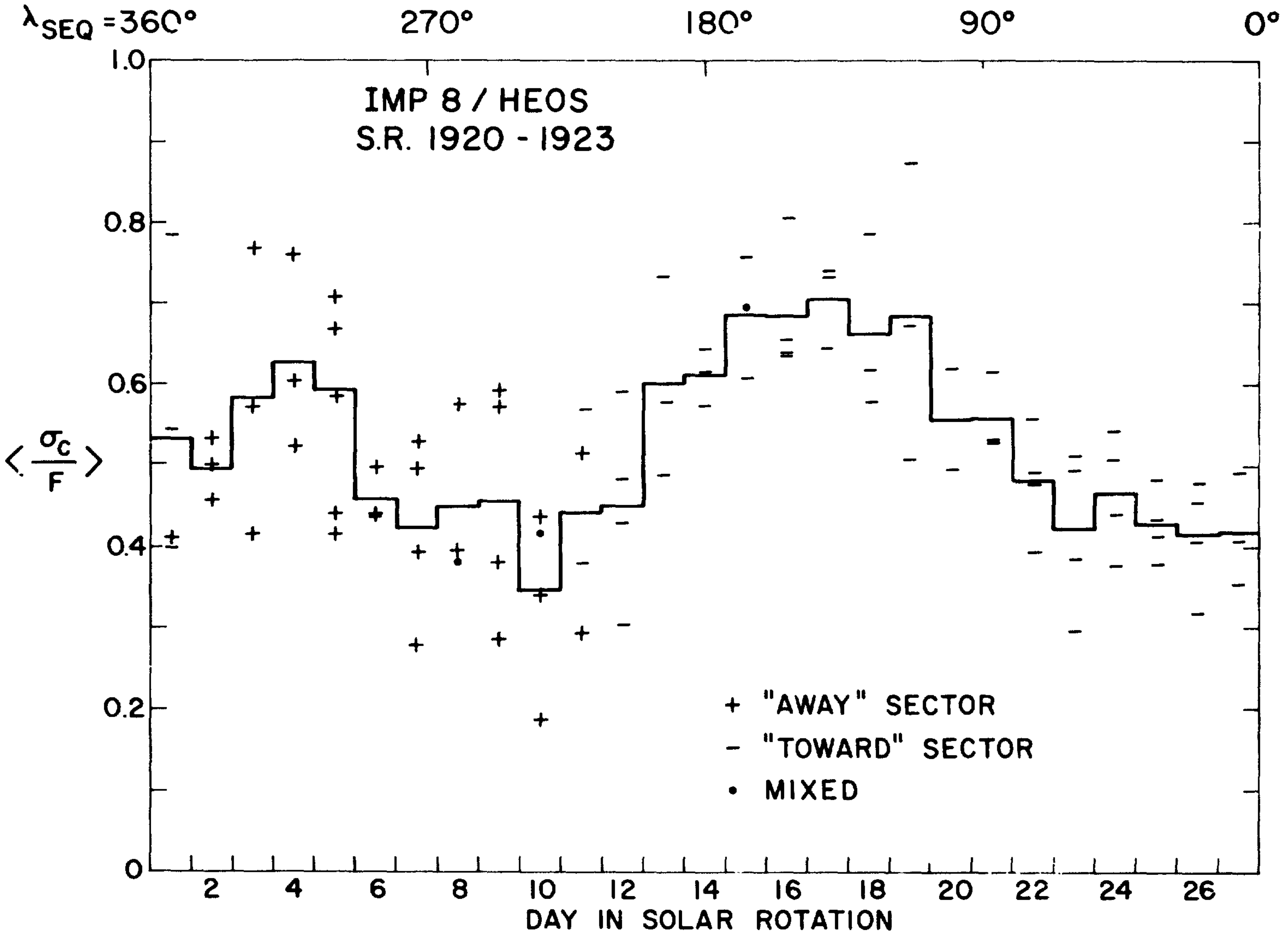

Figure 37. Superposed epoch plot of IMP 8/HEOS daily average relative vector field rms deviation values in same format as Fig. 36. Note position in solar rotation of enhanced fluctuation regions relative to positions of magnitude enhancements.

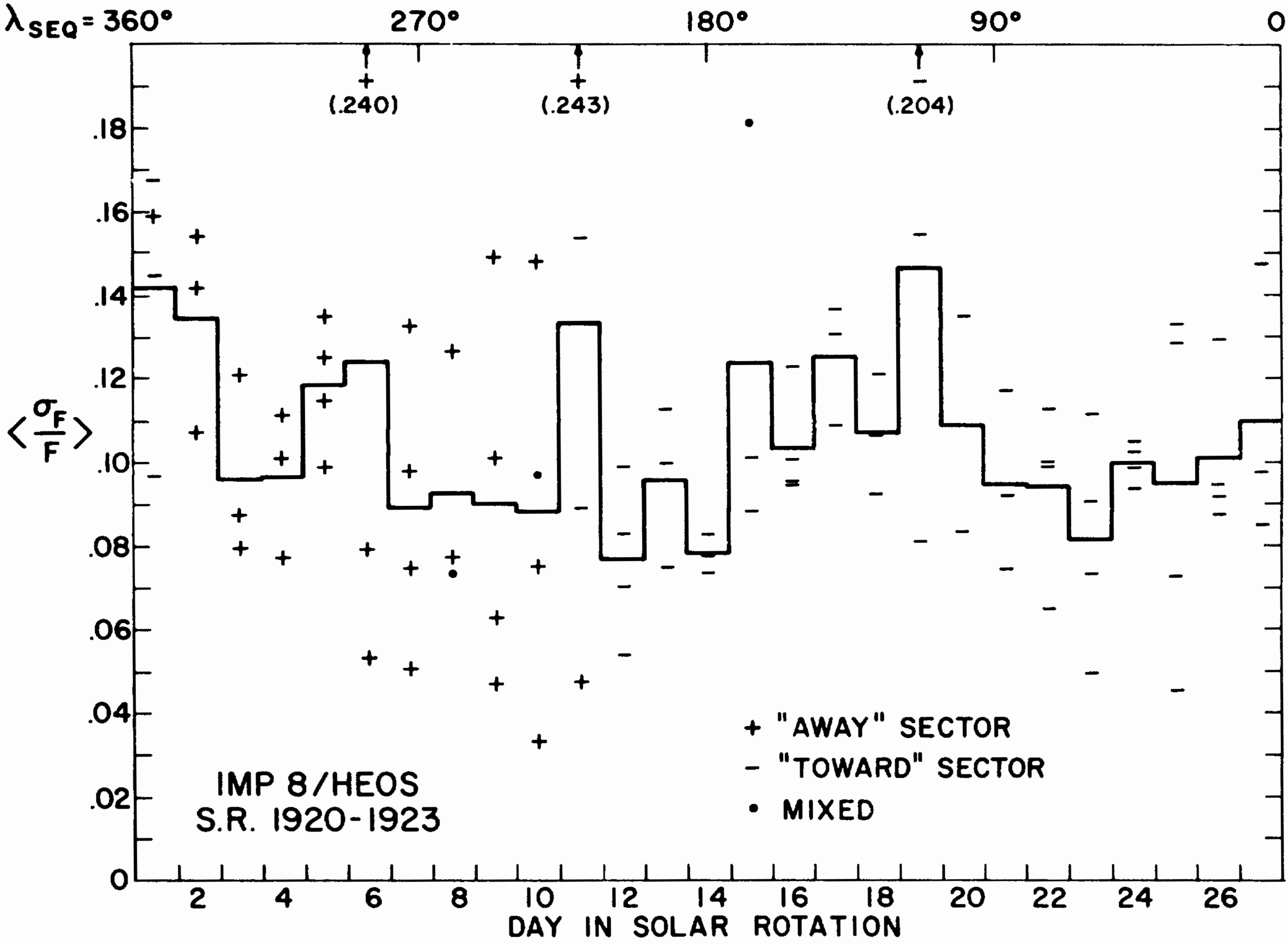

Figure 38. Superposed epoch plot of IMP 8/HEOS daily average relative field magnitude rms deviation values in same format as Fig. 36. Much less regularity in the variation of the average value is seen, but largest average values tend to be seen both near sector boundaries and again in high σ_C/F region of streams though with peak values tending to occur later in time than σ_C/F peaks.

Figure 37 is a superposed epoch plot of daily average σ_c/F at 1 AU by solar rotation during the same four rotations and in the same format as in Figure 36. Since a portion of the data shown is calculated from HEOS measurements the absolute values of the points, especially those near the maxima, should not be taken as anything more than suggestive of the character of the stream-associated features seen. However, the contribution from stream B during SR 1921 was observed by IMP-8, and follows the general pattern clearly to be seen in the data from the other rotations.

The features of most significance in Figure 37 are the regions of enhanced daily average σ_c/F that occur in association with the major high-speed streams. The magnitude enhancement for stream D occurred on days 2 and 3 in each solar rotation. Enhanced $\langle \sigma_c/F \rangle$ is seen on days 3-5. The minimum in $\langle \sigma_c/F \rangle$ just preceded the sector boundary passage. Enhanced $\langle \overline{F} \rangle$ for stream B was seen on days 12 and 13, while a large region of enhanced $\langle \sigma_c/F \rangle$ extended from day 13 to 22. This corresponded roughly to the period of high and variable K_p in Figure 26. During SR 1921 the IMP 8 plasma experiment observed a region of enhanced temperature in stream B extending from the initial peak on day 12 in the solar rotation to day 22, with maximum values on days 15-18 (Lazarus, private communication). An extended density rarefaction region roughly coincided with this high temperature region, with minimum values on days 18-19. There is a complex structure to the plasma data during the SR 1921 passage of stream B, in that there is a second significant increase in temperature and density on day 15 following the region of highest bulk speed, shown in Figure 27. This was followed by several lesser maxima in bulk speed extending through the rarefaction and high temperature region. Similar though smaller regions of high temperature, low density and variable bulk speed were seen in association with stream D during days 3-8. This extended structure will be discussed further later.

Figure 38 is a superposed epoch plot of daily average σ_F/F in the same format as Figures 34-35. We see immediately that there is a less organized pattern for this field magnitude fluctuation parameter, indicating that there was much more variation from one solar rotation to the next. There is, however, a suggestion of a region of enhanced though variable $\langle\sigma_F/F\rangle$ during days 15-20. Figure 38 shows another, narrower enhancement during the "toward" to "away" sector boundary passage, when $\bar{F}$ tended to be low, and extending into the compression region. One sees a tendency for the daily average σ_F/F points to be increasingly scattered late in each sector.

The set of Figures 36-38 represent an averaging in time over four solar rotations and at least where $\langle\bar{F}\rangle$ and $\langle\sigma_C/F\rangle$ are concerned support earlier comments concerning the relatively high degree of stationarity of the corotating structure during this period. Those figures show the time history of the structure at 1 AU. It would be instructive to construct similar plots from the Mariner 10 observations, but the apparent lengthening in time of successive solar rotations due to Mariner 10's relative motion, as well as the effects of radial variation of the relevant properties of the IMF, make such an approach more complicated. A rough assessment of the changes in both space and time of relative fluctuation patterns in the corotating structure can be made, however, by mapping these relative fluctuations, normalized by the solar rotation averages, in the corotating frame of reference. This has been done in Figure 39 both for daily average σ_C/F, which demonstrated a relatively stationary pattern at 1 AU, and for the daily occurrence rate of directional discontinuities. Contours have been sketched in connecting equal levels of fractional increase and decrease relative to the solar rotation average, which is represented by a contour level of 1 in each case. The sector boundaries from Figure 15 also have been sketched in for reference.

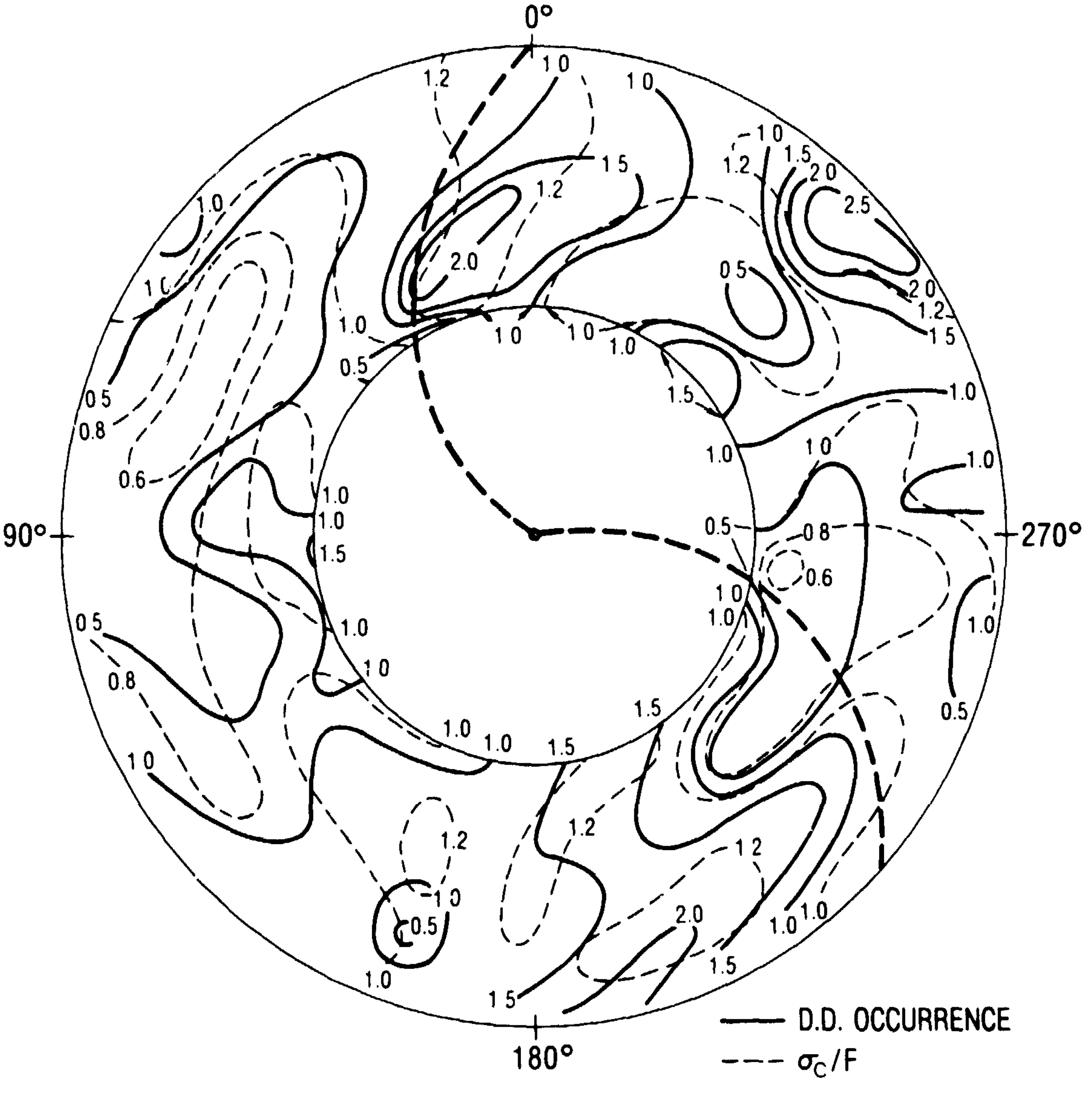

Figure 39. Contours of equal daily average directional discontinuity occurrence rate (solid) and σ_C/F (dashed) as observed by Mariner 10 between 1 and 0.46 AU in frame of reference rotating with the sun. Values in each solar rotation were normalized by solar rotation averages. Section boundaries from Fig. 15 are sketched in.

As expected, one sees the strong correlation between directional discontinuity occurrence rate and σ_c/F. Behind the leading edge of the large negative sector (at ~ 225°) the region of maximum fluctuation associated with stream B can be seen, with some distortion of the contours due to relative shifts in time from one rotation to the next. Except for a small valley in the discontinuity rate which is localized in time to two successive rotations, the rather broad region in which these fluctuations exceed the rotation averages extends to approximately 135°, with an additional tongue of higher relative fluctuation extending to beyond 90° on the later solar rotations. The region of below average fluctuation levels extends roughly from 90° to the leading edge of the positive sector. Again the high fluctuation region associated with stream D is seen in the leading portion of the sector and actually extends ahead of the sector boundary on later solar rotations. This time evolution was discussed in Chapter III. A more complex pattern of structural changes in time are seen in the positive sector, with a region of high fluctuation centered near 315° onthe early solar rotations being replaced by lower than average fluctuation on later rotations. The low fluctuation region that precedes the leading edge of the negative sector extends across that sector boundary on solar rotation 1923, marking a shift in the position of stream B relative to the boundary.

The picture which emerges from these plots is that there is an apparent association between the spatial pattern of occurrence of magnetic field fluctuations, particularly directional fluctuations, and stream structure. In cases in which there are extended regions of hot-plasma flow following major streams, such as with stream B, above average levels of fluctuations, including directional discontinuities, extend throughout those regions and, as has been recognized by Bobrov (1973) and others, contribute to the observed extended periods of geomagnetic disturbance. It is clear that in these observations we are not dealing with simple narrow high-speed streams which have an effect only over a 2-3 days period, such as the case illustrated by Figure 6. Though the duration of "simple" streams may be anywhere from 2-7 days, they are characterized by monotonic bulk speed increases and decreases (Burlaga, 1975). In the cases of both streams B and D, at least two additional significant bulk speed increases were seen during the period of declining bulk speed following the initial speed maximum (Lazarus, private communication). These then correspond to what Burlaga (1975) calls "compound" streams which appear to be the result of faster streams overtaking slower streams and are presumably due to successive (adjacent) perturbations near the sun.

Additional insight into the nature of the magnetic field variations through such a region of compound stream activity is provided by looking at the field components and their fluctuations during the period of stream passage. Figure 40 shows once again the hourly average field data during the passing of stream B during SR 921. In this case, in addition to the field magnitude, the three rectangular SEQ components have been plotted. Figure 41 shows the corresponding one-hour rms deviations (of 42 sec data points) for each of the three field components and for the magnitude $\overline{F}$. Also shown are the two field fluctuation parameters σ_C and σ_F, as well as the two relative parameters σ_C/F and σ_F/F. Finally, at the bottom of Figure 41 is plotted the daily occurrence rate of directional discontinuities during this period.

One sees again in Figure 40 the strongly southward field (large negative BZ) just preceding the compression of the field by the stream. Since the magnetic field does not change in any characteristic way across the stream interface (Burlaga, 1974), it is notpossible to locate the interface in the magnetic field data alone. As pointed out in connection with Figures 27 and 28, however, this stream appears to have the classic profile at 1 AU, at least in the portion of the stream up to the first bulk speed maximum, and hence the interface must be located roughly in the 12-hour region between hour 7 and 19 in these plots (between the first BZ value $< -10\,\gamma$ and the maximum $\overline{F}$ value) on January 24.

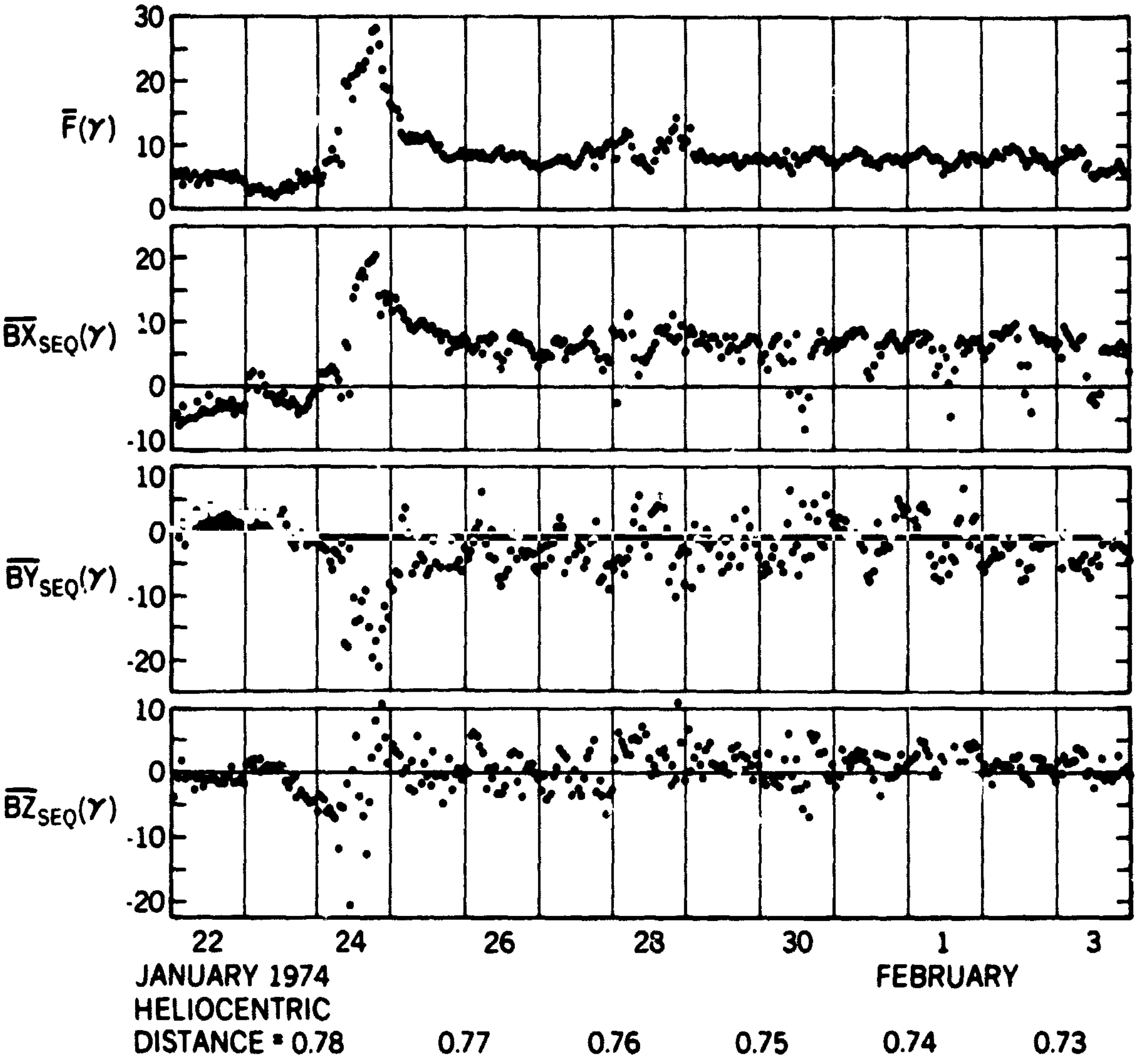

Figure 40. Mariner 10 hourly average field magnitude and component variation during passage of corotating, compound high-speed stream (same event illustrated by Fig. 38). A sustained period of fluctuation, particularly in direction, as a result of compound stream effects is seen.

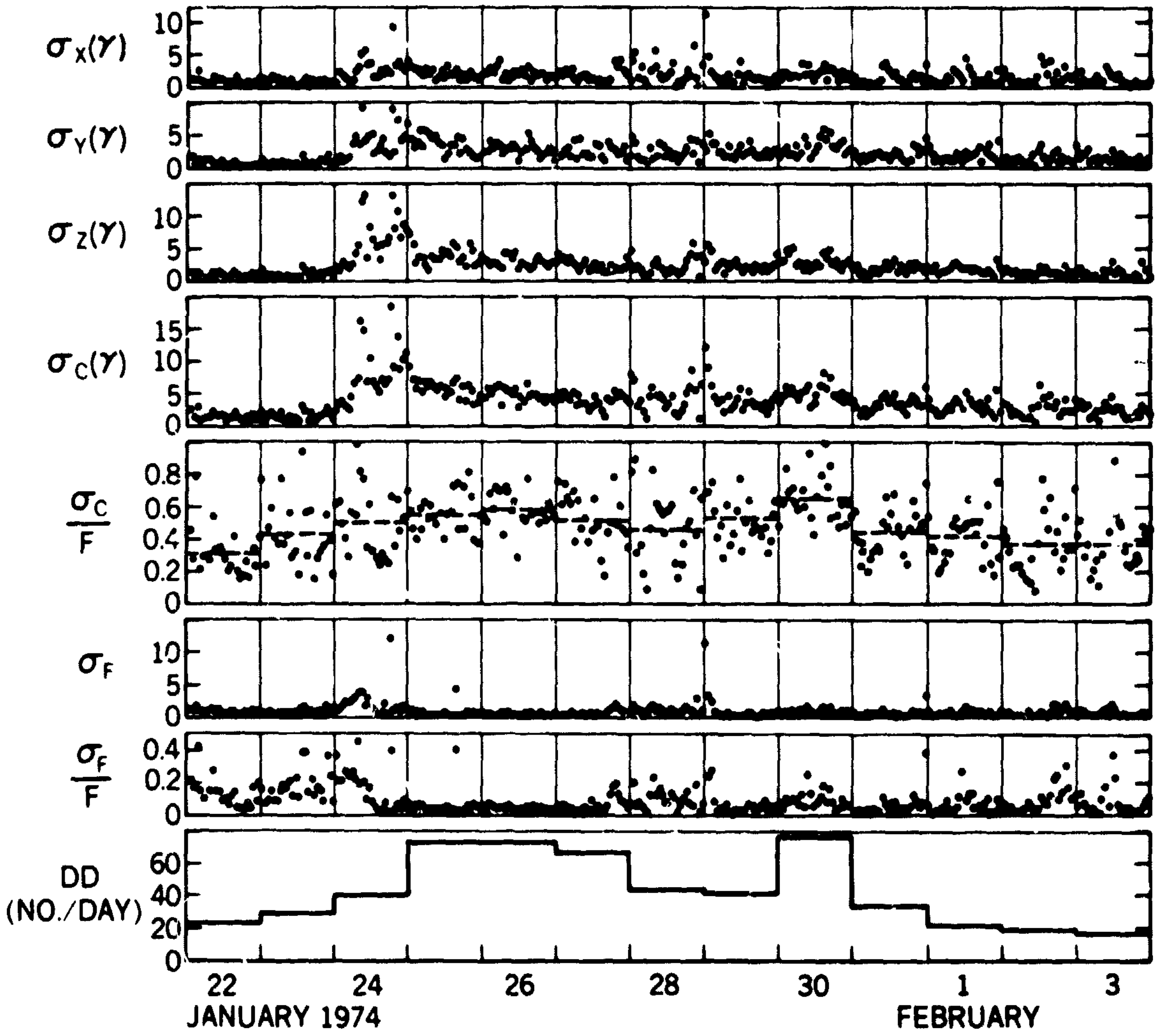

Figure 41. Individual combined and relative component rms deviations and magnitude and relative magnitude deviations corresponding to hourly average fields shown in Fig. 40. Also included in bottom panel is average number of directional discontinuities per day during this period.

After the field compression region had passed, one sees in Figure 40 that large amplitude, low frequency fluctuation in all components continued throughout the period plotted. These fluctuations were mainly in BY and BZ, although occasional large excursions of BX to negative values were seen. At no time between January 24 and February 3 were the BY and BZ hourly averages as steady as they were on January 22 before the stream arrived. The rms deviations, which are measures of fluctuations on a time scale of 42 seconds, all reached high values during January 24, the day of maximum field compression. This is a combination both of the rapid, large-scale changes in the field and its components and enhanced levels of the higher frequency fluctuations. The latter was verified through both the visual inspection of the 6 sec average data and power spectral analysis of 1.2 sec data points.

Again both σ_Y and σ_Z generally showed higher levels of fluctuation than σ_X except on January 28-29 and late in the period. A comparison of σ_C and σ_C/F shows the effects of normalizing by the field magnitude. On January 24 when the field magnitude was high, σ_C was high but σ_C/F did not on average (dashed line) reach a level as high as was seen during several later days. σ_C/F initially peaked during January 25 and 26, which could be the period of highest bulk speed if the 1 AU plasma observation can indeed be extrapolated to Mariner 10. Additional field perturbations were seen on January 28 and 30, roughly corresponding to the days on which two subsequent lesser bulk speed maxima may have occurred (again extrapolating from 1 AU). It is to be noted that the characteristics of the σ_C/F and directional discontinuity occurrence rate variations are similar, with maximum values occurring on the same days.

σ_F also shows somewhat higher values on the days when the bulk speed maxima were probably seen. σ_F/F shows the effects of low values of $\bar{F}$ just ahead of the field compression region, being relatively high through that region, but falling to low values when F becomes large in the compression region. It does show significant variation at the same time that σ_F alone shows enhanced fluctuation, as on January 28 and 30 as well as the days in February that are shown. Thus enhanced fluctuation of both the magnitude of the field and the total vector field were associated not only with the primary high-speed stream in this region, but probably also in association with the subsequent solar wind perturbations in this compound stream structure. It was not possible to make this same association of enhanced fluctuation with the second and third bulk speed maxima in this complex stream in the 1 AU magnetometer data because there was a period during that time when no IMF observations were made by either IMP 8 or HEOS. IMP 8 was in the magnetosheath during most of that time, permitting bulk speed variations to be observed but prohibiting observations of stream-associated magnetic field fluctuations.

At the bottom of Figure 41 one sees the variation of the occurrence rate of directional discontinuities through the complex stream region. A peak number of 77 D.D.'s were counted on January 30, an average of 3.2/hour. This exceeds the count predicted by the best-fit curve in Figure 35 by almost 80%. A peak occurrence rate on January 30 correlated with the maximum average σ_F/F on that day. A broader but slightly lower peak is seen to have been associated with the first region of high bulk speed in the stream.

2. Power Spectral Studies of IMF Fluctuations

As indicated in Chapter I, a substantial number of power spectral studies of the IMF have been conducted to date, particularly at frequencies below 10^{-2} Hz. It is of value to continue investigation at the lower frequencies, especially over a range of heliocentric distance, but the fact that Mariner 10 had a higher data rate than any previous deep-space probe provided the motivation to concentrate on frequencies between 10^{-2} Hz and the experiment cutoff frequency of 12.5 Hz in this first survey study of Mariner 10 IMF data. Later effort will be directed toward studies at lower frequencies.

A small number of spectra were computed using 42 sec average data to provide support for a study of the variation of power spectral density at frequencies from 10^{-4} to 10 Hz with decreasing heliocentric distance. The remaining spectra used in this investigation were computed either from 1.2 sec averages or detail data (25 vector measurements/sec). A total of 241 spectral analysis runs were made, 138 on the 1.2 sec data and 103 on the detail data. These were spread over the range of radial distance from 1 to 0.46 AU and were performed on 40 different days between November 4, 1973 and April 14, 1974, or roughly on 25% of the total number of days in the interval. In most cases at least three separate spectral runs per type of data were made on a given analysis day at widely separated times to test for consistency of the results throughout the day.

In addition to a limited radial distance variation study, which will be discussed in Section 2.1, the spectra were also utilized in a study of waves in the IMF between 10^{-2} and 10 Hz. A computation of polarization parameters confirmed the existence of sinusoidal, highly coherent fluctuations throughout the entire range of heliocentric distance covered during the mission. Since the frequencies ω of the observed coherent fluctuations are such that $\Omega_i \lesssim \omega << \Omega_e$, where Ω_i = ion cyclotron frequency and Ω_e = electron cyclotron frequency, these fluctuations must be considered to be electromagnetic waves rather than hydromagnetic waves, for which $\omega << \Omega_i << \Omega_e$. The wave analysis results will be presented and discussed in Sections 2.2 and 2.3.

2.1 Variation of Power Spectra with Radial Distance

As reviewed in Chapter I, previous investigations of the variation of power spectra with radial distance from the sun have shown that the power in IMF fluctuations of both components and total magnitude generally decreases with increasing heliocentric distance (Coleman, 1968; Coleman et al., 1969; Blake and Belcher, 1974). This is in agreement with other types of fluctuation studies such as those of rms deviation or variance of the field. No other distance dependent characteristics have been found for the power spectra other than the general decrease in power with increasing distance. These previous spectral studies covered the frequency range 10^{-6} to 10^{-2} Hz.

The variation of the power spectral density with radial distance during the Mariner 10 mission is illustrated for the radial component (actually BX_{SEQ}) of the magnetic field in Figure 42. This figure shows composite spectra from separate spectral analyses over 42 sec average data, 1.2 sec average data and detailed, 25 vector samples/sec data at three different distances from the sun: 0.95 AU, 0.6 AU and 0.5 AU. The high data rate of the Mariner 10 instrument extends the observation of this radial distance effect by more than two additional decades of frequency.

Computation of spectra at high frequencies necessitates the use of short time intervals of data and leads to the question of how representative such spectra are of longer term "average" or "typical" conditions. For Figure 42, the 42 sec spectra were computed using 16.6 hours of 42 sec averages. The 1.2 sec spectra are averages of four spectra computed from 30 minute intervals of 1.2 sec averages approximately evenly spaced in time throughout the days indicated. Only half-hour periods were used during which the field as represented by 42 sec averages was relatively uniform throughout the period and free of visually identifiable directional discontinuities and shocks. For each 30 min interval selected for spectral analysis a detail spectrum was also computed from one minute of data approximately at the center of the 30 minute period. Each spectrum has 50 degrees of freedom. The days used in this figure were typical of moderate interplanetary conditions. They were not the quietest days that were observed but were free of the major effects of stream interaction phenomena. Further details of the power spectral analysis procedure are given in Appendix B.

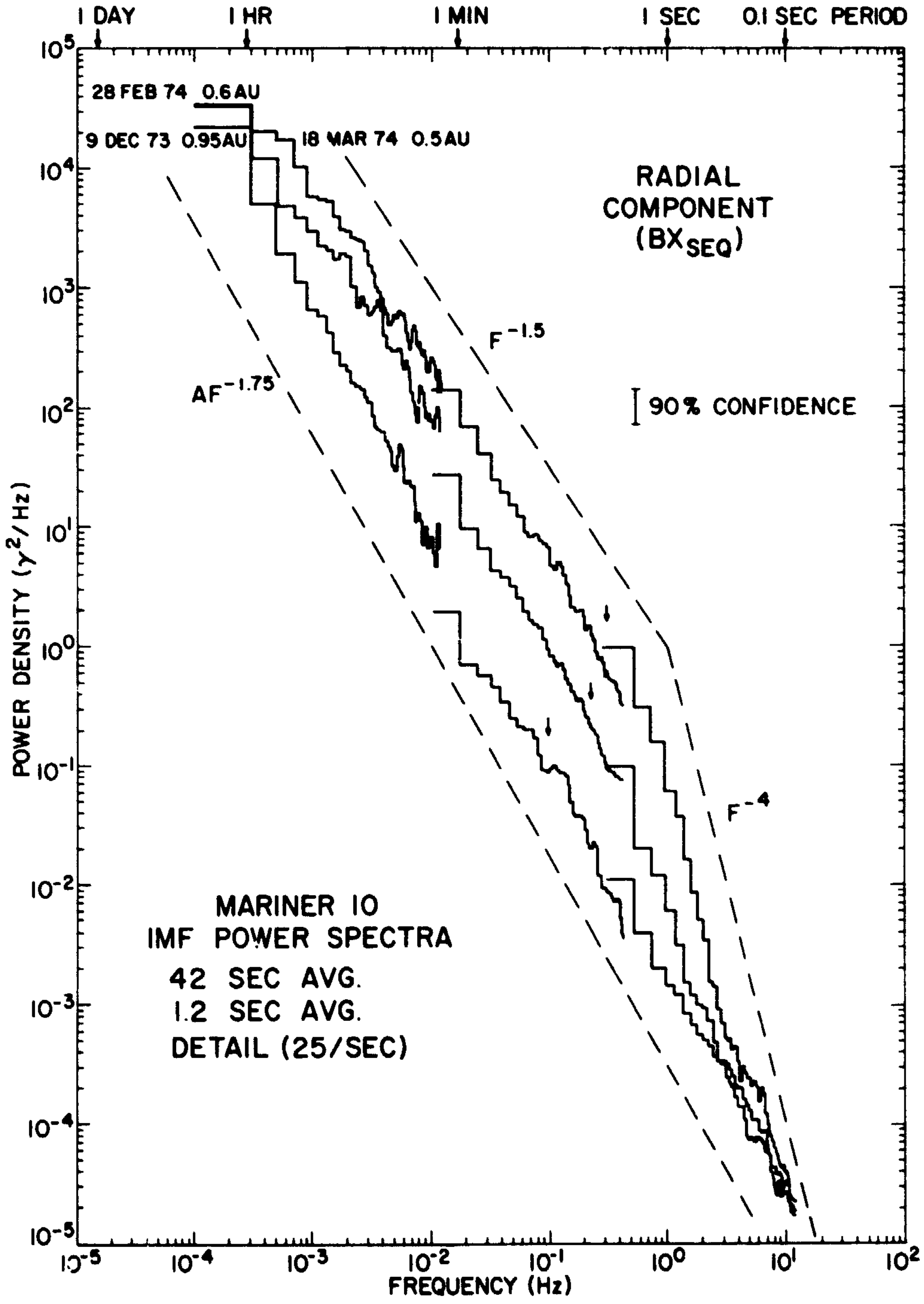

Figure 42. Composite, average radial field component spectra for "typical" days at three heliocentric distances as measured by Mariner 10. The generally increasing power in radial fluctuations with decreasing radial distance is accompanied by a steepening of the high frequency end of the spectrum.

In Figure 42 one sees once again the generally observed increase in power with decreasing radial distance except at the lowest frequency estimate in the case of spectra computed at 0.6 and 0.5 AU and at the highest frequencies observed. In addition, there is a steepening of the spectrum at frequencies above about 0.4 Hz with decreasing distance. Most of the spectra computed in this study tended to support these characteristics of generally increasing power with decreasing distance at all frequencies up to several Hz, accompanied by a steepening fall in the spectrum at higher frequencies. A number of spectra computed under varying disturbance conditions have been examined, and one finds larger variations in power with disturbance state than with distance over the distance range 1 to 0.46 AU. In most cases the power in the field magnitude is roughly an order of magnitude less than that in the components below the frequency at which the steep falloff occurs. Russell (1972) predicted that the slope of the IMF spectrum should be greater than f^{-2} above 1 Hz, and, on the basis of search coil observations by Holzer et al. (1966), Coleman (1968) suggested that between 0.2 and 2 Hz the spectral slope should be $f^{-3.8}$. These results support those predictions at radial distances less than 1 AU.

Two instrumental effects must be taken into consideration in interpreting the results at the high frequency end of the spectrum. The first effect is the rolloff of the magnetometer (illustrated for one axis in Figure 8), which attenuates frequency components of the measured signal above approximately 3 Hz (down 3 db at 5 Hz). This effect tends to steepen the observed spectra. A competing effect is the noise level of a magnetometer sensor (illustrated in Figures 9 and 10). The digitization noise level in the most sensitive ($\pm 16\gamma$) range on Mariner 10 was 6.5×10^{-6} γ^2/Hz, which is below the power range shown in Figure 42. One sees from Figure 10 that a typical Mariner 10 sensor had an intrinsic noise level at frequencies between 3 and 12.5 Hz of between 10^{-5} and 3×10^{-5} γ^2/Hz and thus would also have had little impact on the results shown in Figure 42. The major contribution to the distortion of the spectrum at the higher frequencies must be the effects of rolloff attenuation.

One sees in Figure 42 that even with this attenuation one still has spectra that are sure to be valid up to frequencies of 3 to 4 Hz. Ignoring the portions of the three spectra at frequencies higher than 3 Hz, our previous conclusions (1) that there is an increase in spectral slope with decreasing distance from the sun and (2) that the spectrum becomes steeper than f^{-2} are still valid.

Figure 43 shows roughly the variation with distance of the power in the direction of maximum fluctuation (obtained from the eigenvalue analysis) at 10 selected frequencies. Again the data used were averages for selected days. An attempt was made to use days separated in radial distance by 0.05 AU, but in several cases the candidates turned out to be times of highly disturbed conditions. Thus alternate days shifted by a few hundredths of an AU in radial distance were chosen. Even with these precautions significant structure is seen in the power at all frequencies, and one sees some correlation with the magnetic field sector polarity shown at the bottom of the figure. This supports conclusions discussed in section IV.1.3 that fluctuation power levels are related to the large scale structure of the medium. In fact, one sees large time variations in IMF power density associated with stream structure. On January 24, for example, when Mariner 10 was at 0.78 AU and observed the passage of the field compression region associated with stream B, there was a significant power enhancement. A spectral density of 1.82×10^{-1} γ^2/Hz was computed in the frequency interval centered on 1 Hz, an increase by a factor of $\sim$ 46 over the power level at 0.78 AU (at that frequency) shown in Figure 43. At 0.1 Hz the power density increased to $13\gamma^2$/Hz, an increase by a factor of 32. In contrast, power density levels were lower than those shown in Figure 43 by roughly an order of magnitude on January 22 in the undisturbed IMF ahead of the influence of the stream. Lower amplitude variations of power density at frequencies > 1 Hz were observed during this period. The power density at 5 Hz only increased by a factor of 4 on January 24 over the level shown in Figure 43. In Figure 43 one sees the

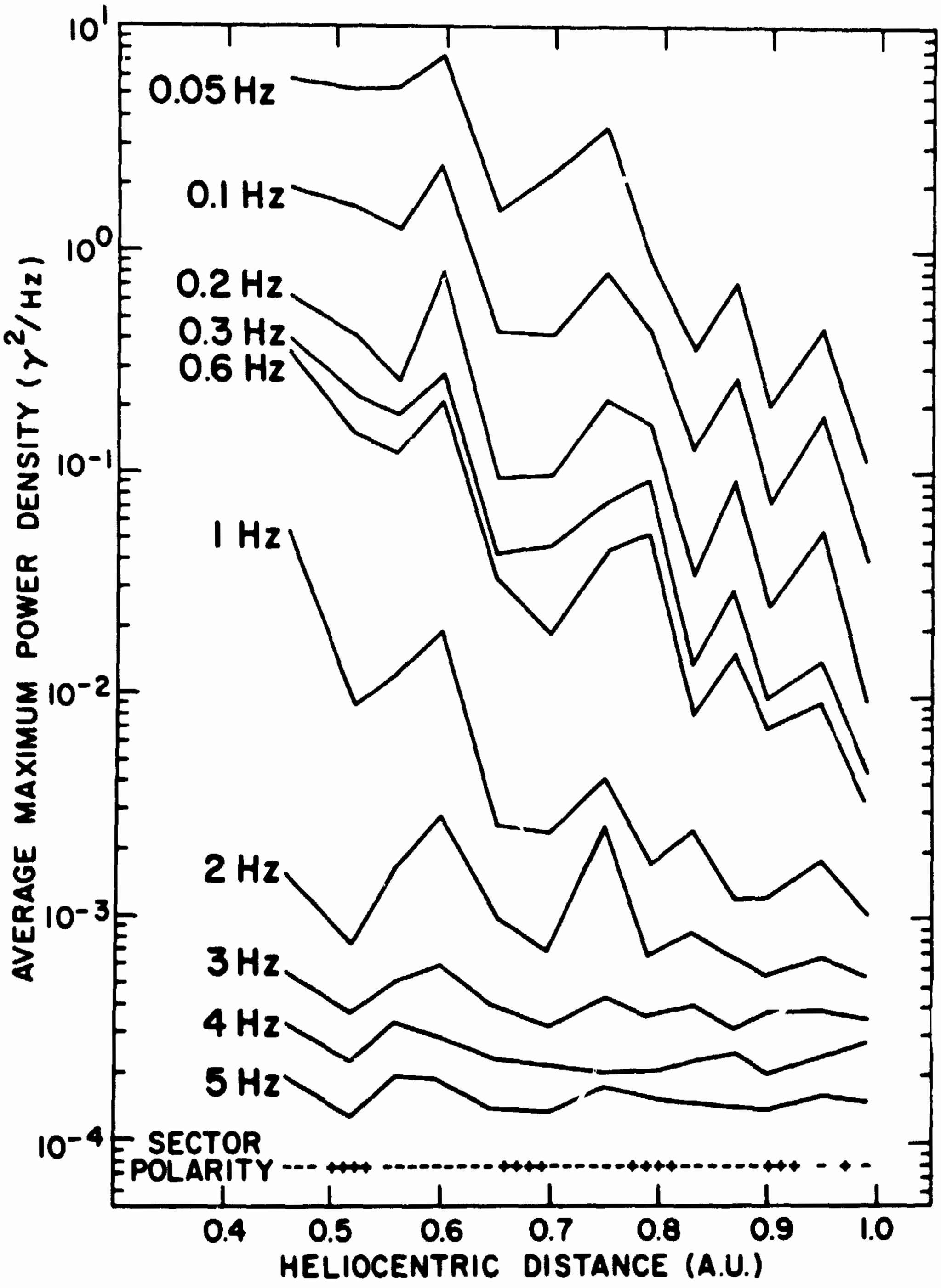

Figure 43. Mariner 10 observation of the radial variation in power with distance from the sun at 10 selected frequencies. Average power in the direction of maximum fluctuation was computed for 13 days which were free of large disturbance variations. The selected days were distributed in distance from the sun between 1 and 0.46 AU. Stream-related time variations are seen in addition to the variation with heliocentric distance.

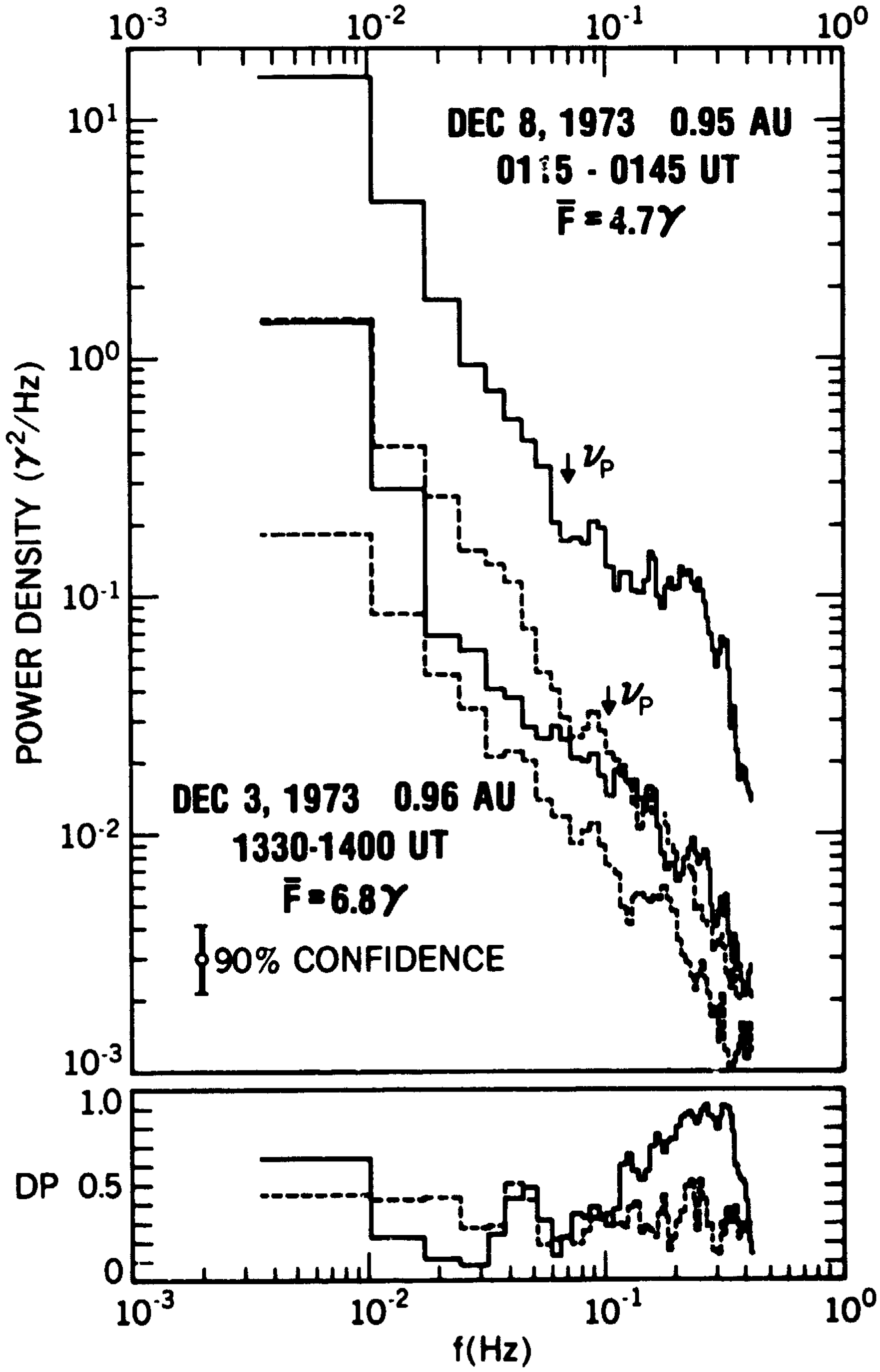

Figure 44. Comparison of power spectra in direction of maximum and minimum field fluctuation and degree of polarization on dates before and after arrival of high-speed stream at Mariner 10. Note order of magnitude higher power density on later date though field magnitude was lower at that time. A large increase in polarized power is also seen. The un-Doppler shifted proton cyclotron frequency ν_p computed from the magnetic field magnitude is indicated by the arrow for comparison.

relatively steep increase in power with decreasing radial distance at frequencies up to 1 Hz, while at higher frequencies there is little overall change with heliocentric distance. This is further evidence of the increased steepening of the spectrum above approximately 1 Hz with decreasing heliocentric distance as illustrated in Figure 42.

Another illustration of time variation in IMF spectra is shown in Figure 44, which includes power spectra computed from 1.2 sec average data taken on two separate days in early December, 1973, when Mariner 10 was at or near 0.95 AU from the sun. The two solid spectra show the power in fluctuations in the directions of maximum fluctuation (upper) and minimum fluctuation (lower) in the IMF during the half-hour period specified on December 3, while the two dashed spectra show the maximum and minimum fluctuation power during a half-hour period on December 3. December 3 was prior to the arrival of a high-speed stream, while the December 8 data were taken within the influence of the stream. In the lower panel are given the variation with frequency of the degree of polarization, DP, defined as the ratio of polarized power to total power in fluctuations (see Appendix B) for the two different time periods. One sees that there was not only an increase overall of approximately an order of magnitude in power density on the later data, but also an even greater increase in power density associated with electromagnetic waves in the frequency range 0.12 to 0.4 Hz. Between 0.25 and 0.35 Hz the degree of polarization exceeds 0.90. At approximately the same time the ellipticity of the waves was near a value of 1, indicating almost circular polarization.

The observation of such waves in the IMF during the Mariner 10 mission will be discussed further in the following section.

2.2 Observations of Electromagnetic Waves in the IMF

Figures 45 and 46 directly illustrate waves which are typical of those detected at various distances from the sun by Mariner 10. The coordinate system

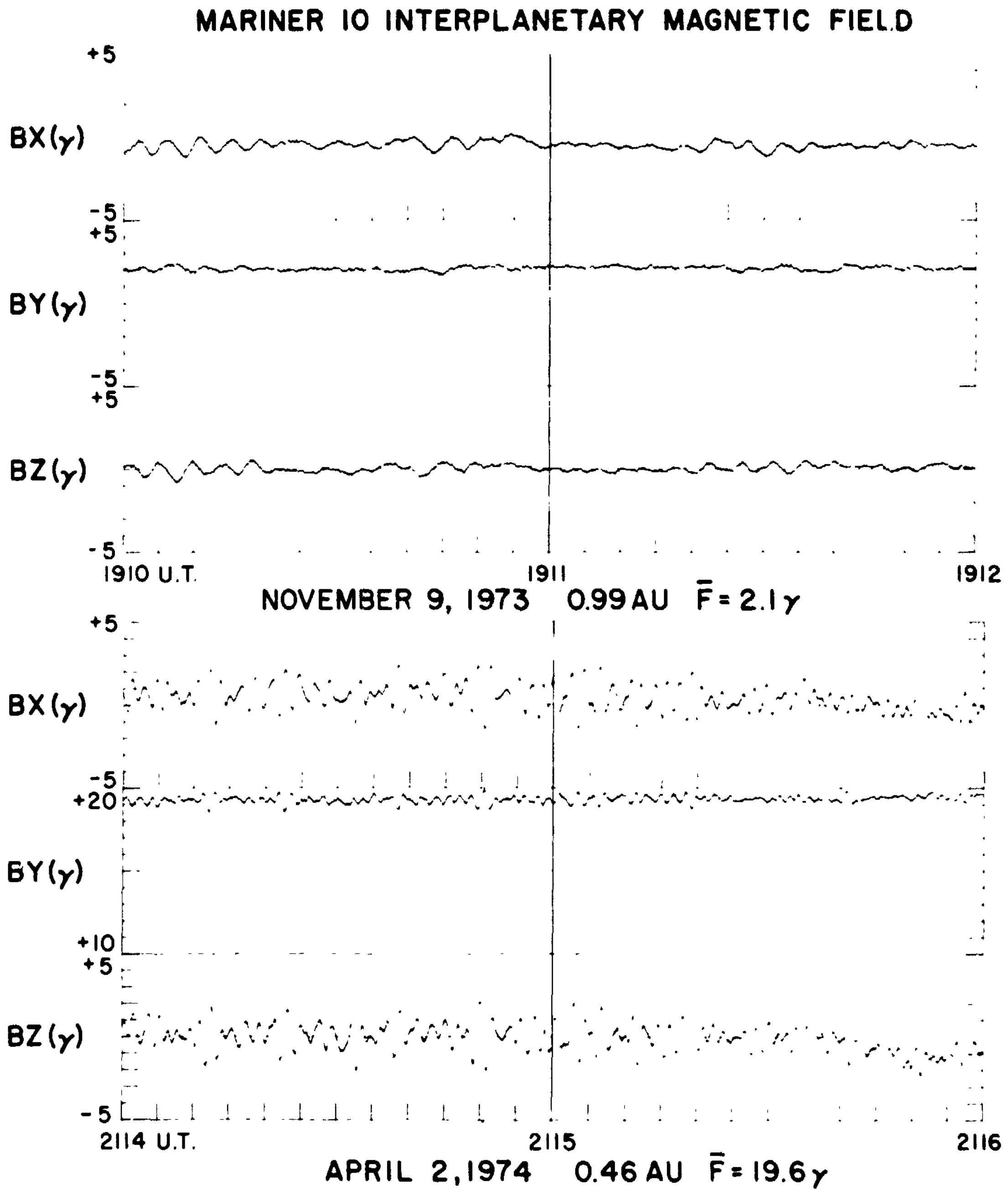

Figure 45. Transverse waves observed in the IMF by Mariner 10 at 0.99 and 0.46 AU. The data plotted are 25 vector samples/sec for intervals of 2 minutes. Five-second marks are given on the time axis. The Y component is along the mean field direction. The higher frequency seen in the lower panel was characteristic of waves observed nearer the sun.

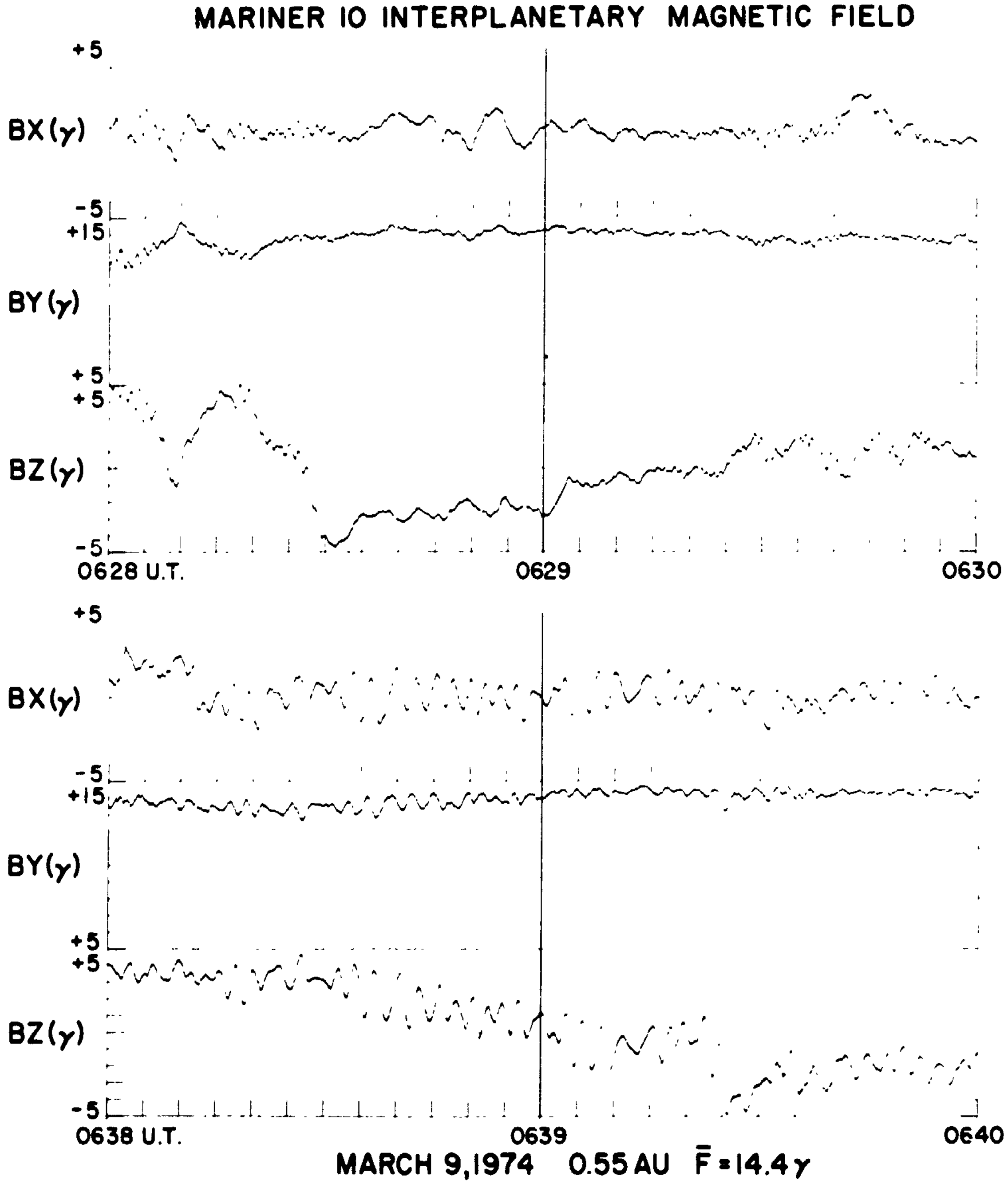

Figure 46. Transverse IMF waves observed on March 9, 1974 when Mariner 10 was at a heliocentric distance of 0.55 AU, plotted in same format as Fig. 45. Note the variety of wave periods observed.

is such that the Y axis is along the mean field direction and the X and Z axes are transverse to the mean field direction. Two minutes of detail data (25/sec) are shown in each panel, with time marks given every 5 sec. As can be seen, in each case almost all of the fluctuation is in the X and Z directions. The wave vector has been found to lie usually at an angle between 5° and 25° from the mean field direction, so for that reason, as well as for the fact that there is always some variation of the actual instantaneous vector field relative to the mean field during the period of the analysis, one would expect to see some fluctuation in the Y component.

In the top panel of Figure 45 one sees a longer period wave typical of those seen nearer 1 AU. There were observations of such waves nearer to the sun but the predominance near 0.46 AU were shorter period, larger amplitude waves such as that illustrated in the lower panel. Note, however, that the relative amplitude of the wave in the upper panel is not small, since the mean field at that time was only 2.1γ and some of the oscillations are $>1\gamma$ peak-to-peak. By contrast, the peak-to-peak amplitude of the wave in the lower panel never exceeds $3.5 - 4\gamma$ in a 19.6γ mean field. The tendency for the waves to occur in discrete packets as seen in the top panel is relatively common among the various Mariner 10 observations.

In Figure 46 are shown two 2-min periods on March 9 (0.55 AU) which were separated in time by 8 minutes. The purpose of Figure 46 is to illustrate the complex array of waves of different frequency that at times can be seen in a relatively short interval of time. Two or more frequencies can sometimes be seen in superposition, and one can at times see abrupt shifts. More characteristically seen are more subtle frequency variations possibly due to fluctuations in the properties of the ambient plasma. One then typically sees a broadened "shoulder" on the spectrum such as that seen in Figure 44. This would be classified as a single wave event. The frequency of the waves seen in the lower panel of Figure 46 is approximately 0.4 Hz. The small amplitude waves superimposed on lower frequency variations in the upper panel are 1 Hz waves. The low frequency component has a period of roughly 7 sec (0.14 Hz). These waves are well separated in frequency and would be seen as discretely different wave "events" in the spectrum.

Figure 47 summarizes the Mariner 10 wave observations. The data have been separated by polarization (LH = left-hand and RH = right-hand) and plotted according to the frequency at which the maximum degree of polarization (DP) occurred in a single wave event, as a function of radial distance from the sun. The error bars are included as a reminder that the power density estimates are computed for an increment Δf rather than at a single frequency, and thus they show the indicated lack of frequency resolution at different points in the spectrum. The points plotted correspond to the central frequency in such a frequency interval. Where points are circled there were two or more different observations at the same frequency at approximately the same heliocentric distance. Also included as dashed lines is the variation in proton cyclotron frequency ν_p associated with the "best-fit" field magnitude variation with radial distance. The actual values of ν_p corresponding to each of the observations plotted have been found to be grouped relatively closely along the curve shown. As can be seen, waves of this type were seen roughly at all distances from the sun, except possibly near $r = 0.6$ AU. Further sampling in that region may find cases that were missed in this first survey.

The wave cases plotted in Figure 47 were those observations which satisfied the following set of criteria:

a) Degree of polarization ≥ 0.5

b) Coherence ≥ 0.5

c) Phase lag in the mean field coordinate system (see Appendix B) equal to either 90° ± 15° (LH polarization) or 270° ± 15° (RH polarization), and the sense of polarization thus obtained must agree with that implied by the polarization parameters.

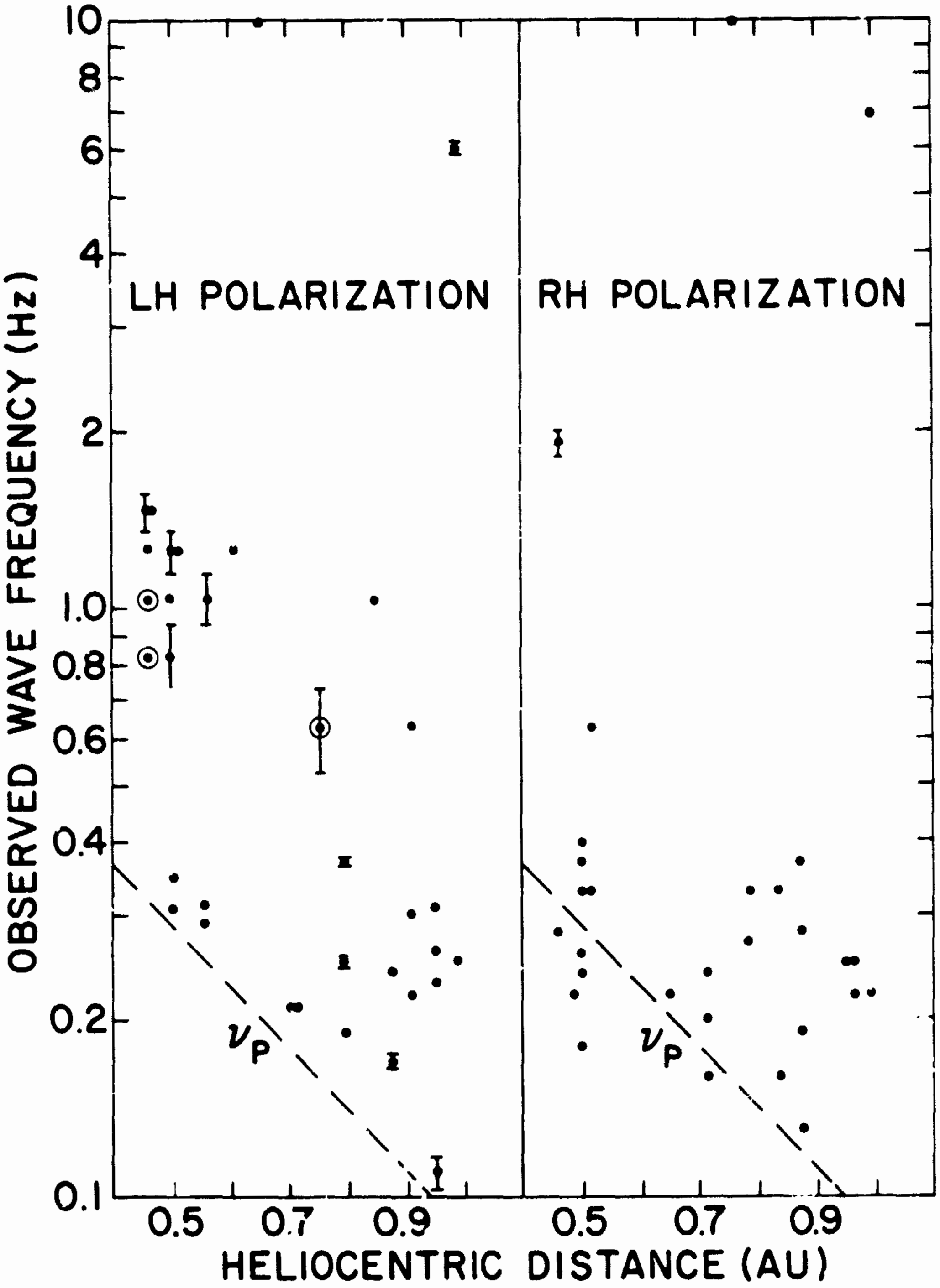

Figure 47. Summary of observed wave cases according to frequency and distance from the sun Cases have also been separated by sense of polarization. Smoothed proton gyrofrequency heliocentric distance dependence is also shown (see text for detailed discussion)

d) Signal to noise ratio (S/N) ≥ 1.5 (see Appendix B)

e) At the same time the angle KK between the two wave vectors computed by independent methods (see Appendix B) should be ≤ 20°. This is utilized as an indicator of the level of confidence associated with the determination of the wave vector direction (Fairfield and Behannon. 1975).

By these five criteria, waves were observed in 25% of the periods in which spectra were computed, as indicated previously. Out of 103 spectral analyses of detail data (0.4 to 12.5 Hz), 24 contained waves by the above criteria and of these, 5 were right-handed (RH) and 19 were left-handed (LH) (21% and 79%, respectively). Of the 138 analyses of 1.2 sec data (0.01 to 0.42 Hz), 45 contained waves. Of these, 26 were RH (58%) and 19 were LH (42%). For the combined data set then there were 31 RH cases (45%) and 38 LH cases (55%). Figure 47 shows that there was a tendency for the frequency at which the waves were observed in the spacecraft frame of reference to increase with decreasing distance from the sun, although there is a great deal of scatter in the data. In the majority of cases the observed frequency was higher than ν_p. Figure 47 also shows that waves observed at frequencies near 1 Hz near a radial distance of 0.5 AU were all LH polarized. Of waves observed at higher frequencies, 3 were RH and 2 were LH polarized. The lower frequency waves observed near 0.5 AU were almost all RH polarized. One sees that there are six RH polarized cases with frequencies below the ν_p curve generated from the field magnitude radial variation. When the actual ν_p values in each individual case are computed, it is found that the observed frequency is lower in only one case (0.18 Hz compared with $\nu_p = 0.22$ Hz), it is higher in two cases (0.24 and 0.26 Hz compared with $\nu_p = 0.20$ Hz), and in three cases it is approximately equal to ν_p.

The wave vector direction which was used in this study was the direction of minimum fluctuation in the field in each case, determined from the real part of the spectral density matrix (see Appendix B). The angle KF between the wave vector direction, given by the unit vector $\hat{k}$, and the mean field direction was computed for each wave observation. KF was found to range between 4° and 27° for both RH and LH polarized waves, except for two cases with frequencies of 10 Hz and KF values of 44° and 71°. These cases will be discussed in more detail later. The mean value and standard deviation for each sense of polarization was found to be (excluding the two cases with KF > 27°):

	$\langle KF \rangle$	σ_{KF}
RH polarized	14.1°	6.5°
LH polarized	13.5°	5.4°

For this limited data set, the differences are probably not significant and thus the average direction will be considered to be 14° for both senses of polarization.

Figure 48 summarizes the statistics on the ellipticity ϵ of the observed waves, both separated by polarization sense and combined. The top panel shows that the observed waves in general tended toward circular polarization ($\epsilon = 1$), but the bottom panel shows that the major contribution was from the LH polarized waves. For the RH waves, 9 of 31 or 29% had $\epsilon \geq 0.8$ while for the LH cases, 26 of 38 or 68% had $\epsilon \geq 0.8$. One also sees that more cases were observed with $0.8 < \epsilon \leq 0.9$ than with $0.9 < \epsilon \leq 1.0$. Figure 49 suggests that there is a possible dependence of observed ellipticity on the KX angle, which is the angle between the wave vector and the SEQ X-axis (approximately the spacecraft-sun line). One sees an increased scatter of the data at large angles. Undoubtedly some of the overall scatter in the data is due to the deviation of the solar wind flow direction from the radial or X-direction at the different observing times.

The average values of ϵ for each 30° interval of KX are shown in Figure 49 as the dashed lines. The distribution in each 30° interval by polarization sense was as follows:

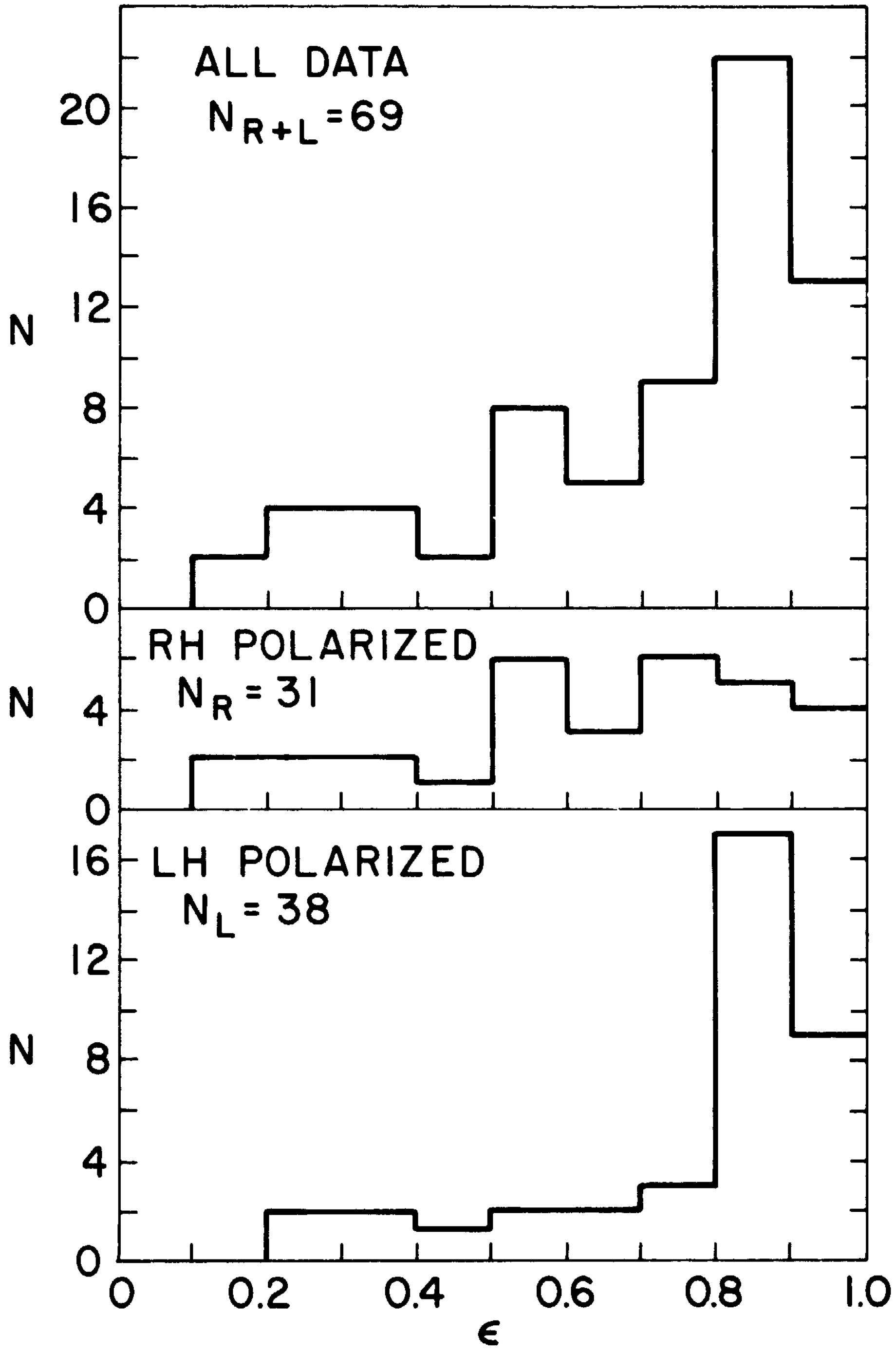

Figure 48. Distribution of observed plane-polarized wave ellipticities for combined cases and separately by sense of polarization.

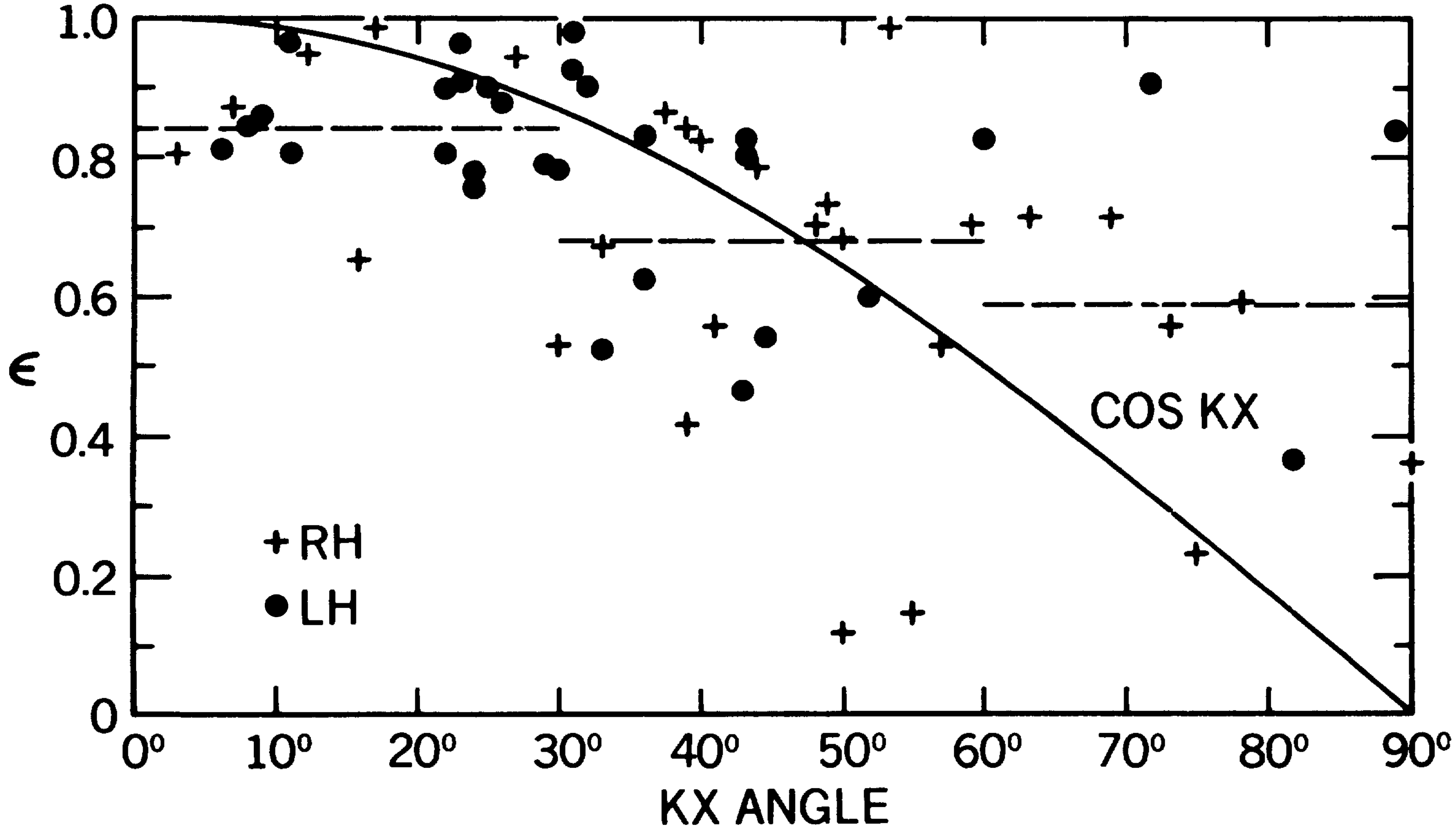

Figure 49. Ellipticity of observed waves as a function of angle KX between wave normal vector and X_{SEQ} axis. Dashed lines show average ϵ within each 30° range of KX. Smooth curve is cos KX for comparison.

	RH	LH
$0^\circ < KX \leq 30^\circ$	9	19
$30^\circ < KX \leq 60^\circ$	16	16
$60^\circ < KX \leq 90^\circ$	6	3

Thus there were twice as many LH polarized waves at small KX angle as RH waves. The average KX angle for all LH polarized waves was 32° with $\sigma^{L}_{KX} = 18^\circ$, and the average for RH waves was 45° with $\sigma^{R}_{KX} = 22^\circ$.

There is also some correlation between the observed wave frequency and the ellipticity, as shown in Figure 50. Here the data have been plotted to illustrate the relationship between the frequency at which the maximum ellipticity was observed and the value of that maximum ellipticity. From this point of the data one can say that (except for the few cases with $f > 5$ Hz) higher frequency corresponds to higher ellipticity, but the converse is not true since there is a relatively large number of observations at high ϵ and low f. Almost all of the high ϵ, high f cases are LH polarized. The distribution breaks down as follows:

		LH	RH
For $f > 0.5$ Hz:	$0.75 < \epsilon \leq 1.0$	15	0
	$0.5 < \epsilon \leq 0.75$	1	2
	$0 < \epsilon \leq 0.5$	2	2
For $f < 0.5$ Hz:	$0.75 < \epsilon \leq 1.0$	15	10
	$0.5 < \epsilon \leq 0.75$	3	14
	$0 < \epsilon \leq 0.5$	2	3

In Figure 50b it is shown that there is a similar relation between the degree of polarization and the observed wave frequency. There is a tendency for the higher frequency fluctuations, again with a few exceptions, to be more highly polarized. There is also a clear division in which most of the cases with high DP are LH polarized. The cases are distributed as follows:

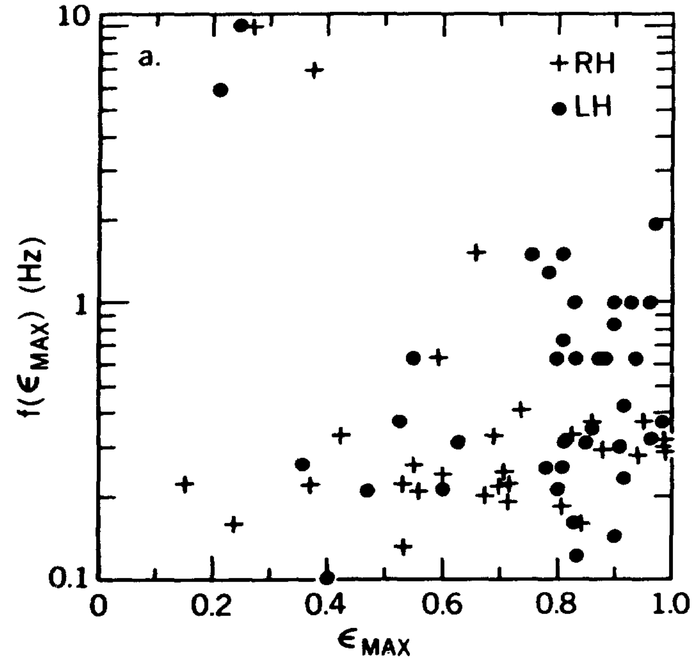

Figure 50a. Frequency at which maximum ellipticity was observed in each wave observation as a function of the maximum ellipticity. Waves with $\epsilon > 0.8$ and $f > 0.4$ Hz were all LH polarized waves.

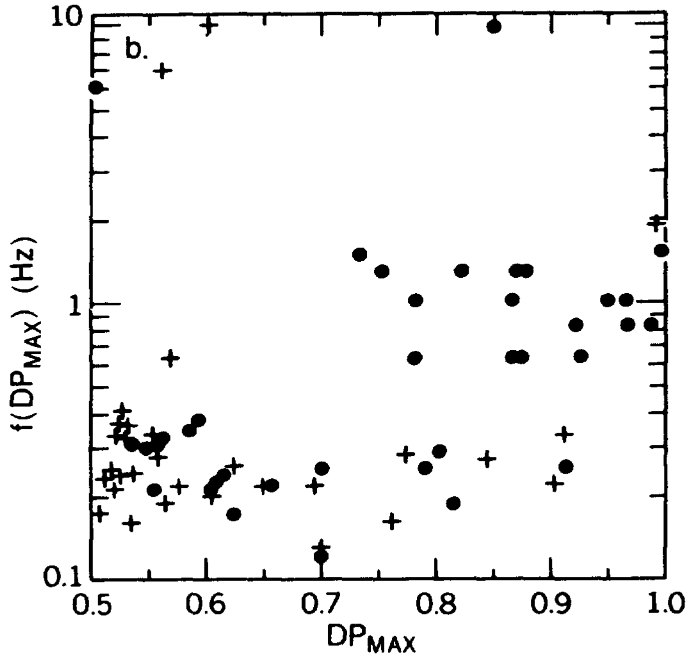

Figure 50b. Frequency at which maximum degree of polarization was observed in fluctuation data as a function of DP_{max}. Fluctuation of the field tended to be less completely polarized when waves with $f < 0.4$ Hz were observed.

	LH	RH
$0.75 < DP \leq 1.0$	23	7
$0.5 < DP \leq 0.75$	15	24

Figure 50 suggests an association between degree of polarization and ellipticity. For any given fraction of total fluctuations that is polarized, one would expect a distribution of ellipticities that resembles the distribution of the total population. However, one sees from the figure that for this limited sample the RH polarized waves tended to be observed mostly in association with low DP, but with a broad range of ellipticities with more concentration at the high ϵ end of the range (see also Figure 48). In contrast, the LH polarized waves tended to have both high ϵ and high DP. Thus for a high degree of polarization in the field fluctuations, there was a strong tendency toward nearly circular polarization, due to the LH wave contribution, whereas a wider range of ellipticities were seen when there was a lower degree of polarization (but still a tendency for ϵ to be > 0.5) due to the RH wave contribution.

We may then summarize the conclusions from Figures 47-50 as follows: a total of 69 cases of coherent, polarized fluctuations were identified in Mariner 10 observations between 1 and 0.46 AU. These waves tended to propagate with their wave vectors 14° from the mean field direction on average, to increase in frequency with decreasing heliocentric distance, and generally to remain above the appropriate proton gyrofrequency. Of the 69 observed cases, 45% were RH polarized and 55% LH polarized. All of the waves with frequencies near 1 Hz but $<$ 2 Hz were LH polarized. Most of these were observed between radial distances of 0.6 and 0.46 AU. These waves were further characterized by high ellipticity, high degree of polarization, and small angle between the wave vector and the radial direction. The RH polarized waves were not observed at frequencies > 0.63 Hz except for a few cases with $f \geq 2$ Hz. The RH polarized waves tended to be observed at large wave vector-radial direction angles ($\sim$ 2/3 of them had KX angle $>$ 30°) and were further characterized by generally a low degree of polarization but a broad range of ellipticities, with the majority in the interval $0.6 \leq \epsilon \leq 0.8$. Many of these characteristics will be discussed further later in connection with wave mode identification. Before we proceed further with that, however, we shall discuss some of the individual cases in more detail.

In Figure 51 are shown the spectra computed from 1.2 sec average data and some of the wave parameters for fluctuations in the frequency range 0.23 to 0.35 Hz observed on March 9, 1974 at a heliocentric distance of 0.55 AU. The power spectra shown correspond to the power in fluctuations along the eigenvector directions. The maximum eigenvalue spectrum gives the power in the direction of maximum fluctuation (solid curve), the minimum eigenvalue spectrum gives the power in the direction of minimum fluctuation (dotted curve) and the third eigenvalue gives the intermediate power level in the direction perpendicular to both of the maximum and minimum fluctuations in a plane whose normal is defined by the minimum fluctuation direction. That is also defined as the wave vector ($\hat{k}$) direction. As indicated earlier, in almost all of the cases studied the angle between $\hat{k}$ and $\langle\vec{B}\rangle$ is relatively small, so that the two upper spectra to a good approximation give the power density in the direction transverse to the field. The dotted spectrum is then the power in fluctuations parallel to $\langle\vec{B}\rangle$.

The ellipticity ϵ, degree of polarization DP, angle KK between two independently determined wave vectors (see Appendix B) and angle KX between the wave vector (from the real part of the spectral density matrix) and the radial direction have all been defined previously. The third angle shown, KF, is that between the $\hat{k}$ used to determine the KX angle and the mean field direction. The range of frequency specified for the observed waves is that range over which the criteria previously listed were satisfied. One sees, for instance, that DP and KK are $>$ 0.5 and $<$ 20°,

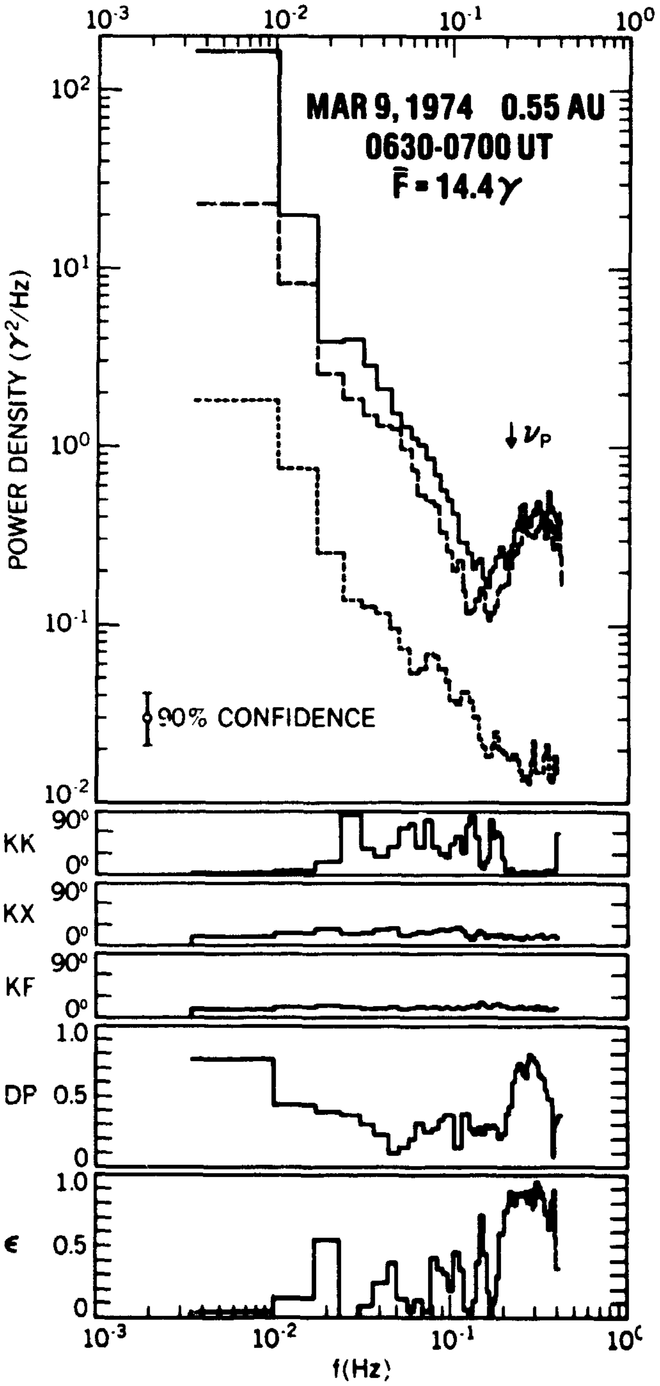

Figure 51. Power density in plane of polarization and perpendicular to that plane (dotted spectrum) for wave of center frequency 0.3 Hz. Also shown in the lower panels are the angle KK between the wave vector directions determined from the real and imaginary parts of the spectral density matrix, the angle KX between the unit wave vector and the ideal solar wind direction, the angle KF between the unit wave vector and the magnetic field vector, and the polarization parameters DP and ϵ. The sign of k has been suppressed in determining KX and KF.

respectively, in that range. Again the frequencies cited are the center frequencies in frequency intervals. For the 1.2 sec data the spectral estimate uncertainties in frequency are ± 0.0035 Hz.

For the case shown in Figure 51, the maximum value of DP = 0.803 occurred at a frequency of 0.29 Hz with corresponding values of ϵ = 0.900, KF = 15° and KX = 11°. The maximum value of ϵ was 0.966 at a frequency of 0.32 Hz. The coherence at DP_{max} was 0.80. This was a LH polarized case and is represented in Figure 47 by the lowest of the points at 0.55 AU in the LH plot. One sees from the spectra that even the lowest power density in the plane perpendicular to the minimum fluctuation direction is generally at least an order of magnitude greater than the minimum fluctuation power density and higher by an even greater amount in the frequency interval in which the enhanced fluctuations are observed.

Figures 52 and 53 illustrate two of the cases of LH polarized waves near 1 Hz. As can be seen, they were observed on two adjacent days, April 1 and 2, when Mariner 10 was at 0.46 AU. In both cases the coherent fluctuations were spread over a broad range of frequencies. On April 1 the degree of polarization and coherency both had maximum values of 0.95 at 1 Hz. The KX angle was 31°. On April 2 a value of 0.99 was observed for both DP_{max} and coherency at 0.83 Hz, with KX = 22°. Ellipticity was equal to 0.90 in both cases. The case in Figure 52 is typical of the majority of the wave observations in that the power density at lower frequencies was relatively high, and consequently the wave contribution to the spectra is seen only as a "shoulder" on the spectral profile. In a few cases, such as that shown in Figure 53, the power density at lower frequencies was low enough so that a spectral peak is seen in the region of the spectrum in which the enhanced, coherent fluctuations contributed almost all of the power. In both cases one sees again the wide separation in power density between that of fluctuations in the minimum fluctuation direction and the power densities in the two transverse directions. Also one sees the very characteristic steeply falling spectrum at the frequency at which the waves cut off.

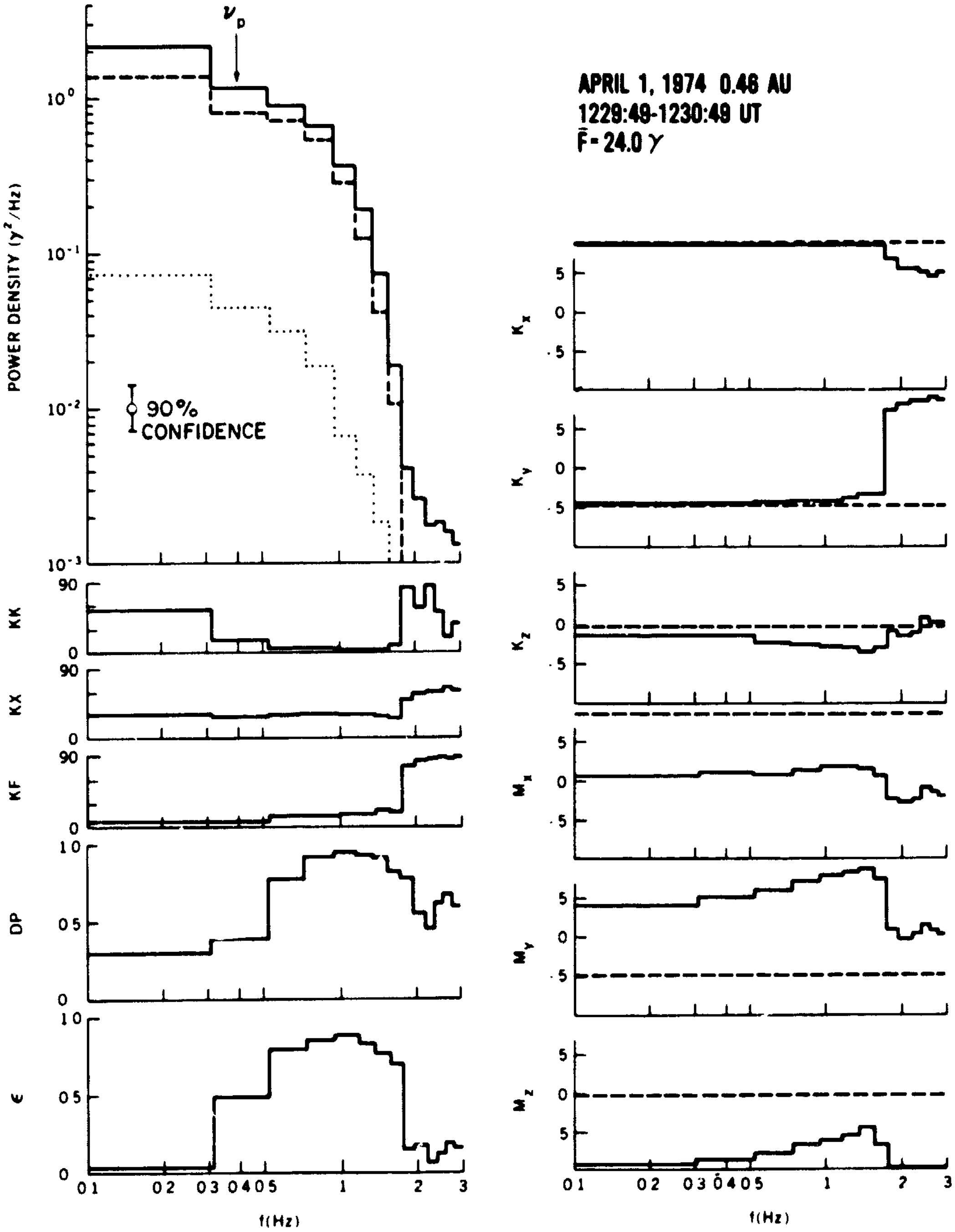

Figure 52. Power spectra, wave vector angles and polarization parameters for wave of center frequency near 1 Hz observed on April 1, 1974. On right-hand side are also shown the components of the unit wave vector k̂ and the unit vector in the direction of maximum fluctuation m̂ as function of frequency. Dashed lines give mean field direction (see text for detailed discussion).

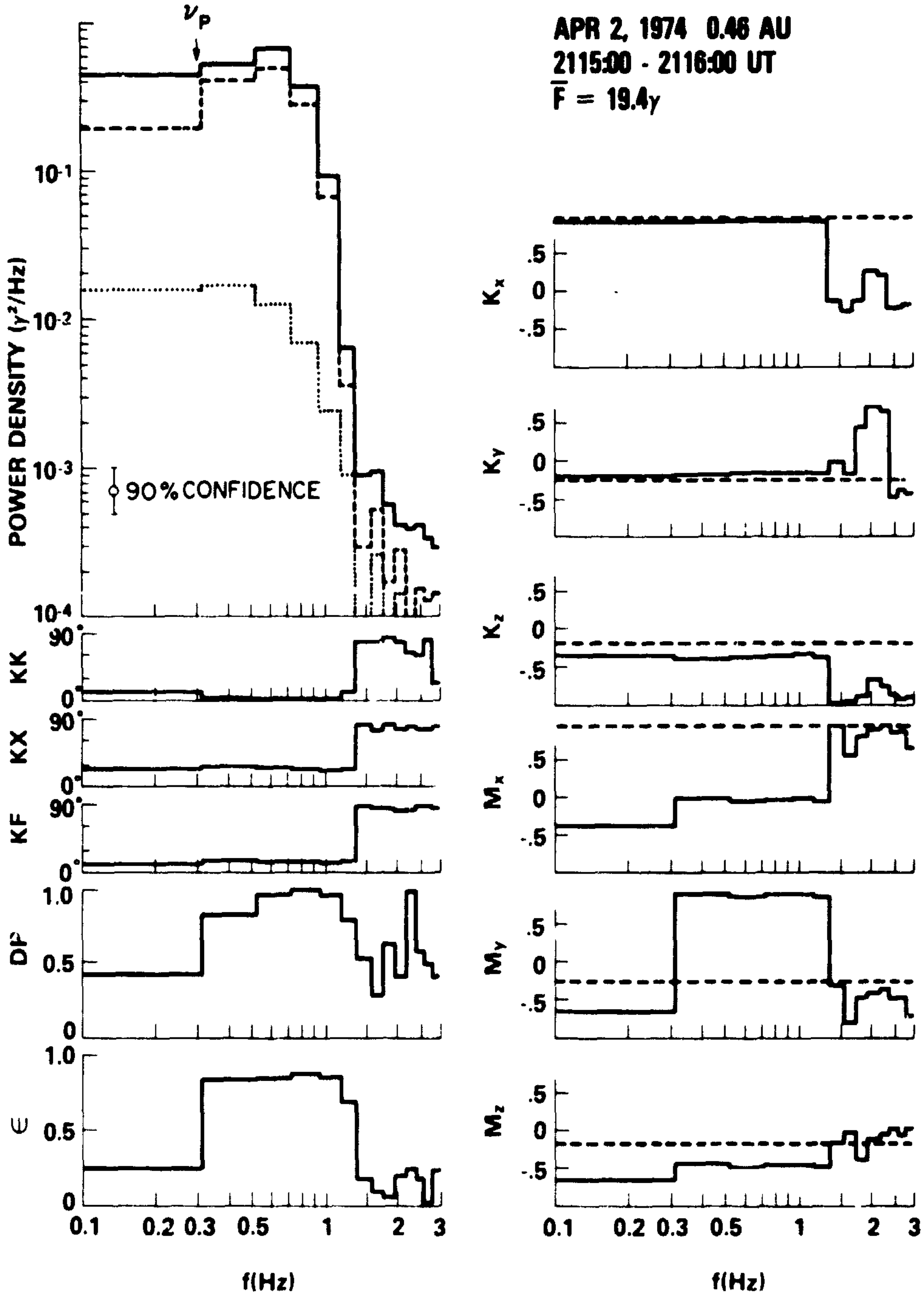

Figure 53. Power spectra, wave vector angles, polarization parameters, and minimum ($\hat{k}$) and maximum ($\hat{m}$) fluctuation direction unit vector components for wave observed on April 2, 1974 (see text).

Also shown in these figures on the right-hand sides are the components of both the unit wave vector $\hat{k}$ and the unit eigenvector $\hat{m}$ in the direction of maximum fluctuation relative to SEQ coordinates. Also shown for comparison with both $\hat{k}$ and $\hat{m}$ are the components of the mean field unit vector (dashed line). One sees that the mean field tends to lie predominantly in the positive SEQ X direction, with a smaller component in the -Y direction and a Z component which is close to or equal to zero. Thus in each case the mean field is roughly in the negative sector spiral direction, in agreement with the large-scale mean field during the period of the observations. One sees the close association of each component of the wave vector with the corresponding mean field components throughout the frequency interval of wave activity. The $\hat{m}$ vector is seen to have components in both the Y and the Z directions.

Figure 54 shows still another case in the same format. This April 11 observation of a RH polarized wave was unique in that the overall power density was so low that the spectral peak due to the waves stood out almost two orders of magnitude above the background power level. The degree of polarization has a maximum value of 0.99 at 1.9 Hz, whereas maximum ellipticity of 0.66 occurred at 1.5 Hz. At 1.9 Hz, KX = 16°. One sees again in the frequency band of the wave that $\hat{k}$ was nearly aligned with the mean field, while the unit vector in the maximum fluctuation direction had its largest component in the SEQ -Z direction.

The actual detail data from which the spectra and wave parameters in Figure 54 were computed are shown in Figure 55. This wave was more nearly monochromatic than many of the other cases studied. The data in Figure 55 have been plotted on an expanded scale relative to the previously shown plots of this type, with a range of 6γ full scale on the ordinate and one minute of time across the abscissa (time marks every 2-1/2 sec). Perhaps the most interesting aspect of the data in Figure 54 is the amplitude-modulated appearance of the fluctuations in the components transverse

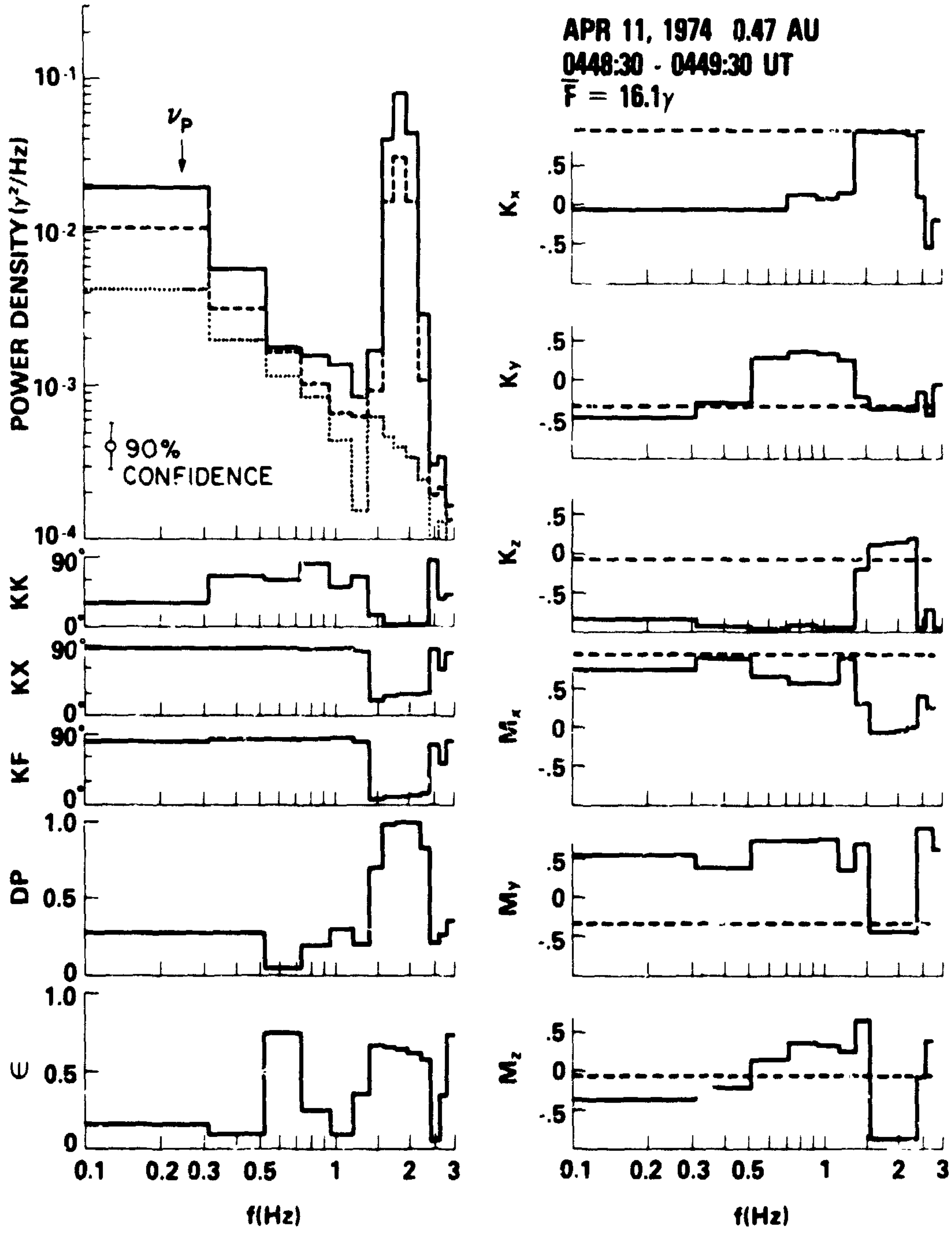

Figure 54. Power spectra, wave vector angles, polarization parameters and components of $\hat{k}$ and $\hat{m}$ for wave observed on April 11, 1974. Note very low level of power density in fluctuation at frequencies not near the wave frequency of 1.9 Hz. Wave had lower ellipticity than was seen in previous cases illustrated.

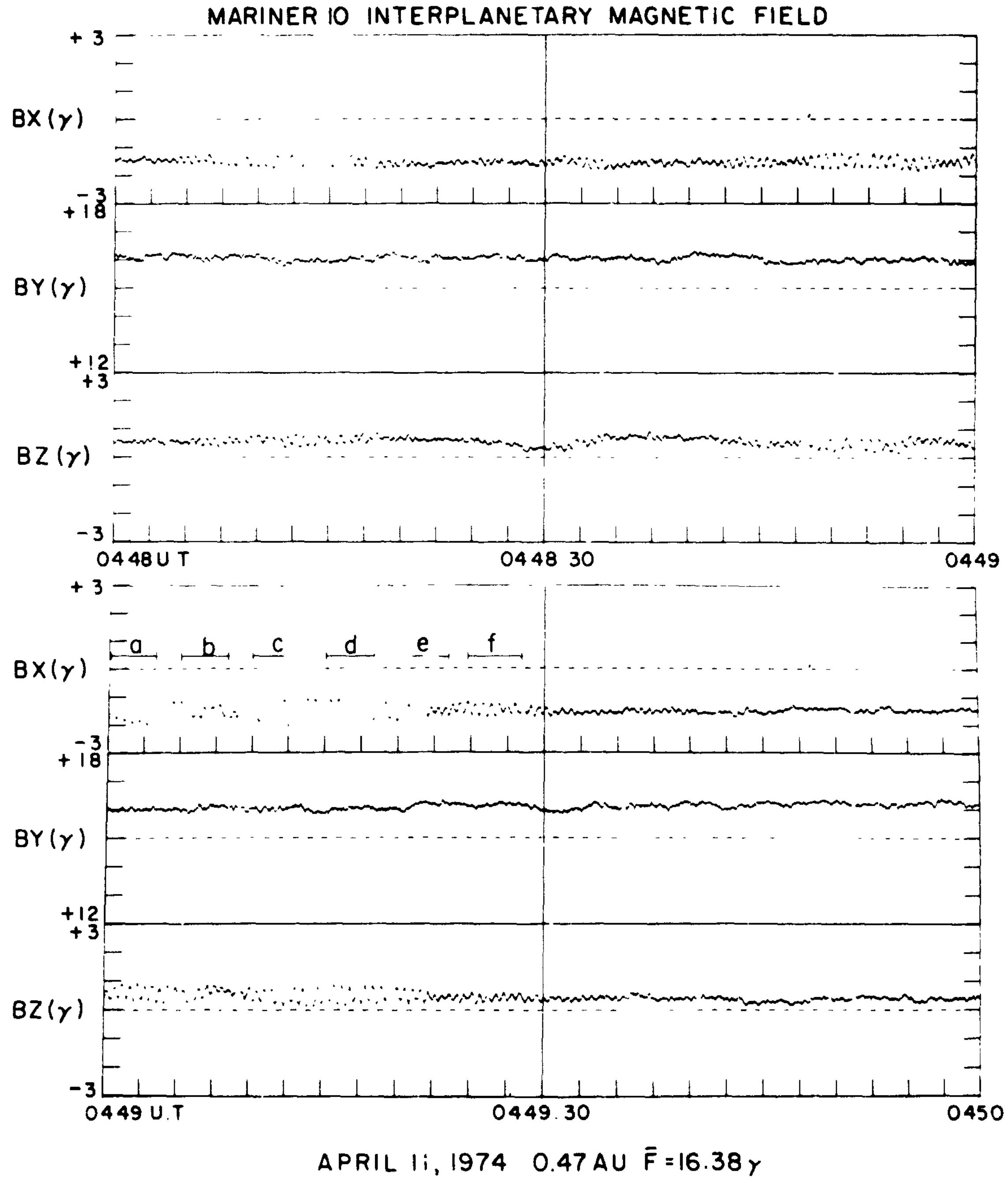

Figure 55. Detail (25/sec) magnetic field component data during observation of wave characterized in Fig. 54, in same format as Figs. 45 and 46 except more sensitive ordinate scale (± 3γ) and only one minute of data is shown in each panel. Note the amplitude-modulated appearance of the wave (see text).

to the mean field direction, reminiscent of "pearls" (Pc1 micropulsations) observed in the terrestrial magnetic field. The most obvious possibility for the cause of the beating appearance is the superposition of a number of signals of different frequencies.

To demonstrate in more detail the characteristics of these fluctuations observed by Mariner 10, polarization diagrams were plotted from the detail BX and BZ component data for the six intervals labeled a through f between 0449:00 and 0449:30 UT. These diagrams are shown in Figure 56. They demonstrate that there was a consistent sense of polarization throughout, which was expected since a clear sense of polarization was obtained from the results of the spectral and polarization analysis which had been performed previously over the entire interval. The diagrams also suggest that there was no rotation of the ellipse axes in the plane of polarization, and that the observed modulation was due more to a time variation in amplitude rather than any variation in ellipticity. These conclusions are supported even by the data in the region of low amplitude (b, e, f) where the pattern is degraded considerably.

2.3 Plausibility Arguments for Wave Mode Identification

Because of the lack of plasma proton measurements onboard the spacecraft during the mission of Mariner 10, there was insufficient data to positively identify the wave mode in each of the various wave observation cases. Plasma parameters are needed not only for dispersion relation computations, but also the solar wind bulk speed is required to determine the degree to which waves have been Doppler-shifted by the solar wind. Such a Doppler-shift can produce not only a significant change in the frequency of the wave as observed by a "stationary" spacecraft but also in some cases a reversal of polarization. In addition, proton and electron thermal anisotropy observations could facilitate the identification of specific plasma instabilities in the solar wind.

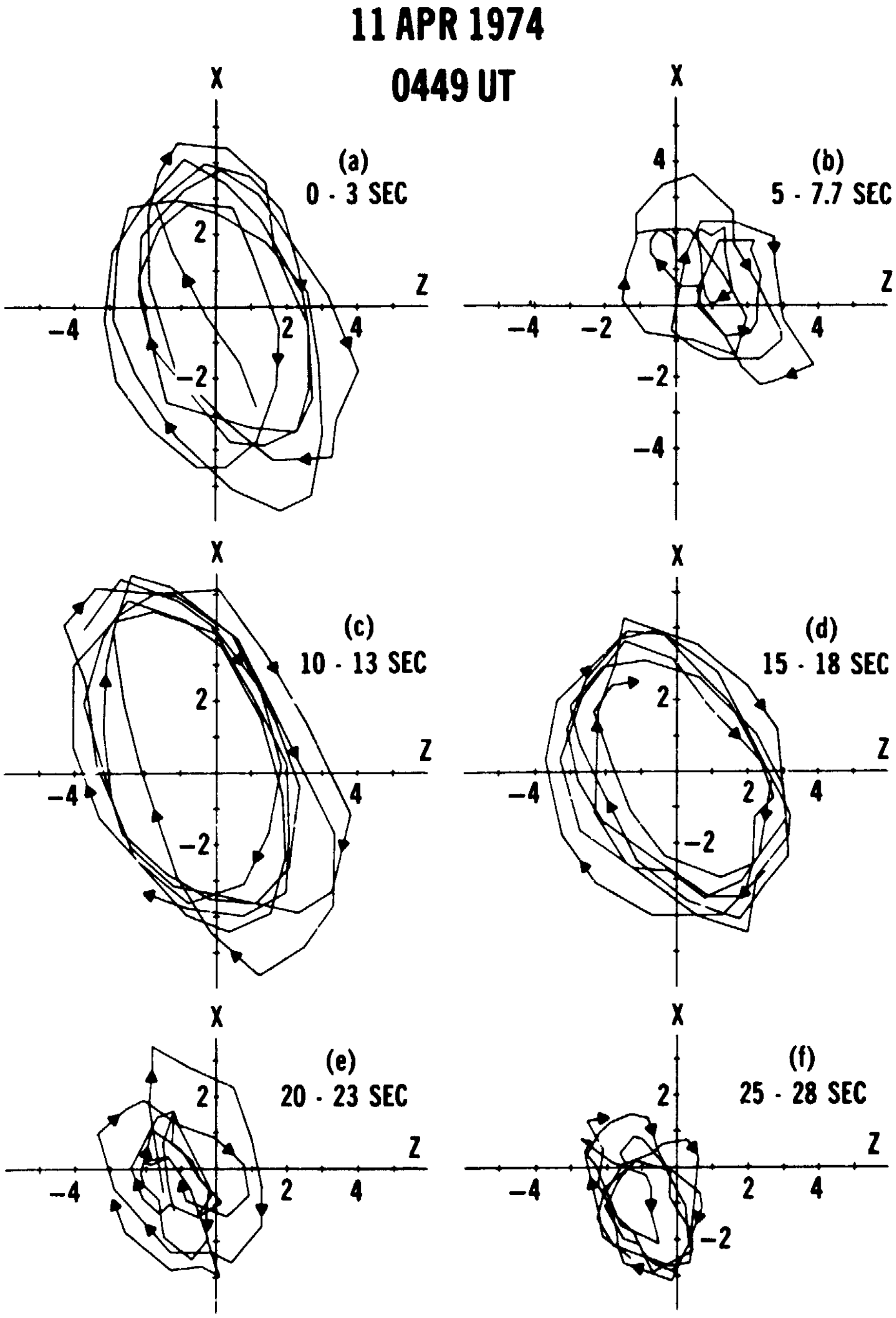

Figure 56. Polarization diagrams for field fluctuations during time intervals labeled a through f in lower panel of Fig. 55. A tendency for the polarization ellipse to maintain its orientation and shape while varying in size is seen.

With the help of some preliminary inferences from the plasma electron detector as well as proton measurements at 1 AU and a knowledge of the basic corotating stream structure as a function of time during the mission, reasonable estimates were made of solar wind parameters corresponding to the magnetic field observations in some of the cases, and these were used to develop arguments to show that a specific mode was at least plausible and perhaps even "most likely" in a given case. In some cases, however, ambient conditions were sufficiently variable so that a more exact set of parameters would be necessary to establish even the most likely identification. Finally, some of the cases may represent modes too complex to be adequately described by the simple theory used in the following arguments.

A likely candidate for the subset of cases with LH nearly circular polarization and frequencies relatively close to the proton gyrofrequency is the ion cyclotron wave. The ion cyclotron wave is LH circularly polarized with a natural frequency lower than the single particle ion cyclotron frequency (Stix, 1962). It is one of two electromagnetic modes which can propagate in the direction of the magnetic field. The dispersion relations (or wave-normal surface equations) for these modes are the two forms of the solution of Maxwell's equation for plane waves for the cold-plas approximation (no zero-order thermal motion) for the $\theta = 0$ (propagation parallel to the field) case. They can be written in the form

$$n_{\pm}^2 = \frac{c^2 k^2}{\omega^2}\begin{pmatrix} R \\ L \end{pmatrix} = 1 - \frac{\omega_{pi}^2}{\omega(\omega \pm \Omega_i)} - \frac{\omega_{pe}^2}{\omega(\omega \mp \Omega_e)} \qquad \text{(IV-3)}$$

where n is the index of refraction of the plasma, k is the wave number (the magnitude of the wave vector), ω_{pi} and ω_{pe} are ion and electron plasma frequencies, respectively, and Ω_i, Ω_e are the ion and electron cyclotron frequencies. R and L represent the right and left-band modes, respectively, and equation (IV-3) shows that the RH and LH modes have resonances ($n = \infty$) at the frequencies $\omega = \Omega_e$, Ω_i and non-propagation bands above those frequencies. The effects of a finite alpha particle content in the solar wind, which introduces additional complexity in that there is an additional resonance at $\omega = \Omega_i\ (H^{++}) = \Omega_i\ (H^{+})/2$ (Scarf and Fredericks, 1968) have not been included in this simple analysis.

The cold plasma treatment allows the wave number k to become infinite at resonance, $\omega = \Omega_i$ (and, equivalently, the wavelength $\lambda = 2\pi/k$ to go to zero) (Stix, 1962). Stix has shown that consideration of finite, nonzero temperatures puts a maximum value on the magnitude of k, thus establishing a minimum wavelength limitation. The expression for maximum k_z, where z is the direction of the static magnetic field, is

$$|k_z|^3 < \frac{\pi^{1/2}\Omega_i\,\omega_{pi}^2}{c^2}\left(\frac{m_i}{2\kappa T_{\parallel i}}\right)^{1/2} \tag{IV-4}$$

where m_i is the ion mass, $T_{\parallel i}$ is the ion temperature parallel to the magnetic field and k is the Boltzmann constant. The ion plasma frequency can be expressed by

$$\omega_{pi}^2 = \frac{4\pi n e^2}{m_i} \tag{IV-5}$$

where n is the ion number density. For simplicity writing $k_z = k$, letting the ion species be protons and evaluating the constants, one may get the expression

$$|k|^3 < 8.029 \times 10^{-23}\,\frac{Bn}{\sqrt{T_{\parallel}}}$$

or

$$\lambda > \left(3.089 \times 10^{9} \frac{\sqrt{T_{\parallel}}}{Bn}\right)^{1/3}, \tag{IV-6}$$

where B is in units of gammas, n is in units of cm^{-3} and T is the temperature in units of 10^5 °K (i.e., for $T_{\parallel} = 8.0 \times 10^4$ °K, $\sqrt{T_{\parallel}} = \sqrt{0.8}$). We note that in (IV-6) λ is only weakly dependent on temperature ($\lambda \propto T_{\parallel}^{1/6}$), so that in the absence of direct measurement of $T_{\parallel}$ it should be sufficiently close to estimate the proton temperature using the empirical T-V relation of Burlaga and Ogilvie (1970, 1973). This relation was established experimentally from solar wind measurements at 1 AU and has the form

$$\sqrt{T} = 0.036\ V_{sw} - 5.548,$$

where in this case T is in kilo °K.

One can use a model of temperature variation with distance from the sun to scale the values valid for various solar wind speeds at 1 AU to other heliocentric distances. The general validity of the T-V relation throughout the inner solar system has not yet been established, but again only a rough estimate of temperature is needed for these calculations, so it will be assumed to give results that are sufficiently close. This approach was also used to discuss the waves observed in Mercury's magnetosheath (Fairfield and Behannon, 1975). Using the one-fluid model curve for temperature as a function of radial distance from the sun (see Figure 38 in Hundhausen, 1972), one can obtain values of $T(r, V_{sw})$ given the heliocentric distance of the observation and the measured or estimated bulk speed of the solar wind during the observation.

Given a value of $T_{\parallel}$ determined according to the above procedure, a measured or estimated value of proton number density n and the measured magnitude of the magnetic field, one then can use equation (IV-6) to compute the minimum possible wavelength, which then provides an estimate of the maximum frequency to which a wave can be Doppler – shifted, through use of the expression.

$$\omega = \Omega_i + \vec{k} \cdot \vec{V}_{sw} \tag{IV-7}$$

which for this case can be written (with frequency in Hz)

$$\nu_{max} = \nu_p + \frac{V_{sw}}{\lambda} \cos \alpha \tag{IV-8}$$

where λ is the λ_{min} value obtained from (IV-6) and α is the angle between $\vec{k}$ and $\vec{V}_{sw}$. In this case we must use the KX angle values determined in the polarization analysis. Since the actual wave frequency in the frame of the solar wind is not known, we use the fact that the frequency of ion cyclotron waves must be near but below the ion cyclotron frequency in the plasma frame. For such a wave to be RH polarized means that $\hat{k}$ must be oriented in the upstream direction and the wave has been Doppler-shifted through a polarization reversal. In this case the $\vec{k}\cdot\vec{V}_{sw}$ term is negative and the plus sign in (IV-8) must be replaced by a minus sign.

To test a particular Mariner 10 wave observation, one first calculates a value for λ_{min} using equation (IV-6). The evaluation of the inequality utilizes the measured magnetic field magnitude, the estimated value of proton number density n, and an estimated value of T. The resulting value of λ is then inserted into equation (IV-8) along with the estimated value of solar wind bulk speed V_{sw} and the best available estimate of the angle α between the direction of propagation and the solar wind flow direction. As already indicated, we must use α = KX. This value of the Doppler-shift term is then added to or subtracted from the appropriate proton gyrofrequency, since it is assumed that the wave frequency in the solar wind frame is less than but near ν_p (= $\Omega_i / 2\pi$). The resulting maximum possible Doppler-shifted frequency is then compared with the observed wave frequency. Using this procedure, some of the cases of LH polarized waves with observed frequency centered between 0.8 and 1.5 Hz were tested and consistency with identification as Doppler-shifted ion cyclotron waves was shown.

Typical of this group was a LH case observed on April 11 at $f_{DP} = 1.5$ Hz. A field magnitude value of $B = 18.7\gamma$ was observed, from which $\nu_p = 0.285$ Hz. The eigenvector analysis yielded KX = 28°. On April 11, Mariner 10 was in a relatively quiet field region preceding a high-speed stream at 0.47 AU. It was estimated that a bulk speed of 400 km/sec and a number density of 20 cm^{-3} would be typical of those conditions (Scudder, private communication). Using an estimated proton temperature of 1.08×10^5 °K, a value of $\lambda_{min} = 208$ km was derived, which leads to a maximum Doppler-shifted frequency $\nu_{max} = 1.98$ Hz. This is greater than the observed f_{DP} and comparable to the frequency at which maximum ellipticity was observed ($f_\epsilon = 1.9$ Hz), and hence it is probable that the observed wave was an ion cyclotron wave. Since this is merely a plausibility argument rather than rigorous mode identification, the data pertaining to the other similar cases have not been tabulated here. We assert again that the case cited was typical.

There was a case of RH polarization observed on April 11, with $f_{DP} = 2.0$ Hz, $\bar{B} = 16.4\gamma$, $\nu_p = 0.25$ Hz, and KX = 23°. If the component of the wave unit vector $\hat{k}$ parallel to the solar wind velocity vector $\vec{V}_{sw}$ was positive in the direction of solar wind flow, then the frequency observed in the spacecraft frame of reference would be higher than that in the plasma frame due to the Doppler-shift, as shown in the previous example, but the sense of polarization would remain the same as in the plasma frame. In this case, then, the polarization would have to have been RH in the plasma frame. If, on the other hand, propagation in the plasma frame was upstream relative to solar wind flow, then the opposite polarization would be observed in the spacecraft frame if the component of the phase velocity $\vec{V}_{ph}$ of the wave along the solar wind bulk velocity direction was less in magnitude than the solar wind speed. However, a lower frequency would be observed in the spacecraft frame than in the plasma frame. On that basis one would conclude that a RH wave at an observed frequency of 2 Hz could not be a Doppler-shifted ion cyclotron wave since the plasma frame frequency of such a wave would have been near to but less than the proton gyrofrequency of 0.25 Hz, and hence in the spacecraft frame one would have observed $f < 0.25$ Hz.

The other possibility for propagation upstream relative to solar wind flow is that both $\vec{V}_{ph}$ and $\vec{V}_g$ components parallel to $\vec{V}_{sw}$ be greater in magnitude than $|\vec{V}_{sw}|$. In this case, however, propagation would also be upstream (toward the sun) in the spacecraft frame and hence no polarization reversal would be observed. A frequency lower than that in the plasma frame would again be observed due to Doppler-shift. Thus in this case there are two counts against the wave being an ion cyclotron wave: the sense of polarization is wrong and again the frequency is greater than ν_p. That leaves the first possibility discussed, that of propagation in the anti-solar direction, as the only viable alternative, but there the sense of polarization in the spacecraft frame must be the same as that in the plasma frame, again ruling out the ion cyclotron mode. One must conclude then that the wave is RH polarized in the plasma as well as the spacecraft frame, which suggests that the electron whistler mode is the appropriate mode identification for this wave. One must, however, demonstrate consistency with whistler mode characteristics.

For an intermediate range of frequency, $\Omega_i << \omega << \Omega_e$, the ion term in equation (IV-3) can be neglected relative to the other two terms, and we can write the cold plasma dispersion relation in the form appropriate for oblique propagation (Stix, 1962):

$$n_{\pm}^2 \approx 1 - \frac{\omega_{pe}^2}{\omega(\omega \pm \Omega_e \cos\theta)} ,$$

where

$$n^2 = \frac{k^2c^2}{\omega^2} \text{ and } \begin{pmatrix} + \\ - \end{pmatrix} = \begin{pmatrix} \text{Lwave} \\ \text{Rwave} \end{pmatrix}$$

In the case of the L wave, the index of refraction turns out to be imaginary, and there is no propagation. The dispersion relation form for the R wave is appropriate for the right-hand polarized whistler mode. The angle θ between the wave normal vector and the magnetic field vector is limited to the range specified by the conditions given in Stix (1962, pp. 39-40). These conditions were investigated and found to be satisfied for the cases treated in this study, even when $\theta \equiv$ KF was as large as 71°. In addition, the cold plasma dispersion relation is assumed to be valid in the cases considered here where in fact $\omega << \theta_e$ is strongly satisfied, since the warm plasma dispersion relation differs from the cold plasma relation only near Ω_e where cyclotron damping absorbs power from the wave (Stix, 1962).

For the whistler mode we then write

$$n^2 \approx 1 - \frac{\omega_{pe}^2}{\omega^2\left(1 - \frac{\Omega_e}{\omega}\cos\theta\right)} \tag{IV-10}$$

or

$$n^2 \approx 1 + \frac{\omega_{pe}^2/\omega^2}{\frac{\Omega_e}{\omega}\cos\theta} \quad \text{if} \quad \frac{\Omega_e}{\omega}\cos\theta >> 1. \tag{IV-11}$$

Further,

$$n^2 \approx \frac{\omega_{pe}^2/\omega^2}{\frac{\Omega_e}{\omega}\cos\theta} \quad \text{if} \quad \frac{\omega_{pe}^2/\omega^2}{\frac{\Omega_e}{\omega}\cos\theta} >> 1. \tag{IV-12}$$

The inequality in (IV-12) reduces to

$$\frac{4\pi n_e e c}{\omega B \cos\theta} >> 1, \qquad \text{(IV-13)}$$

where e = 4.8 × 10^{-10} esu is the unit electron charge, c = 3.00 × 10^{10} cm/sec is the speed of light, n_e is the electron number density and B is the magnetic field magnitude (F in earlier experimental data discussion). Evaluating the constants and taking $\theta = 0$ gives

$$\frac{n_e}{B}\left(\frac{1.8 \times 10^6}{\omega}\right) >> 1, \qquad \text{(IV-14)}$$

where B is in gammas and n_e in cm^{-3}. For typical solar wind conditions n_e/B is of O(1), so we see that for $\omega << 10^6\ sec^{-1}$ the inequality holds. Thus, to a good approximation, we may write for solar wind whistlers

$$\frac{k^2 c^2}{\omega^2} = \frac{4\pi n_e e c}{\omega B \cos\theta} \qquad \text{(IV-15)}$$

or

$$\omega = \frac{c \cos\theta}{4\pi e} \frac{B}{n_e} k^2. \qquad \text{(IV-16)}$$

This can be expressed as

$$f(Hz) = \frac{c \cos\theta}{8\pi^2 e} \frac{B}{n_e} k^2. \qquad \text{(IV-17)}$$

Putting this into a convenient computational form gives

$$f(Hz) = 791.6 \frac{B}{n_e} k^2 \cos\theta, \qquad \text{(IV-18)}$$

where B is in gammas, n_e is in cm^{-3}, and k is in km^{-1}.

Now we wish to apply this to the RH polarized wave observed on April 11 at a frequency f_{DP} = 2 Hz. Evaluating equation (IV-18) using $B = 16\gamma$, $n = 20\ \text{cm}^{-3}$, $\theta = 11°$ and a range of values for k, the solid curve shown in the upper part of the lower panel Figure 57 has been derived. A Doppler-shift term has been evaluated also using V_{sw} = 400 km/sec, α = KX = 23° and the same range of values for k, and that gives the solid curve in the lower part of the lower panel of Figure 57. This Doppler-shift can be added to and subtracted from the dispersion curve, giving the two dashed curves labeled f^+ and f^-. As shown in the figure by the arrows labeled "1" and "2", the observed frequency of 2 Hz could have resulted from a Doppler-shift up in frequency from a lower frequency, or a downward shift in frequency from a frequency in the plasma frame of approximately 9 Hz. The first possibility is not likely, since it suggests that the wave frequency in the plasma frame was very near the proton gyrofrequency (ν_p = 0.25 Hz).

The second possibility is a downward shift in frequency, which, as indicated previously, can occur without a polarization reversal only if both the group and phase velocities of the wave are greater than the plasma velocity. The group velocity of whistler waves, of magnitude $V_g = d\omega/dk$, can be obtained from the dispersion relation and is given by (Fairfield, 1974):

$$V_g = \vec{V}_{ph} \left[\left(2 - \frac{\omega}{\Omega_e \cos\theta} \right) \hat{k} - \tan\theta \hat{\theta} \right], \tag{IV-19}$$

where the components are along $\hat{k}$ and in the direction perpendicular to $\hat{k}$, respectively, and the phase velocity is given by

$$V_{ph} = \omega/k = f\lambda. \tag{IV-20}$$

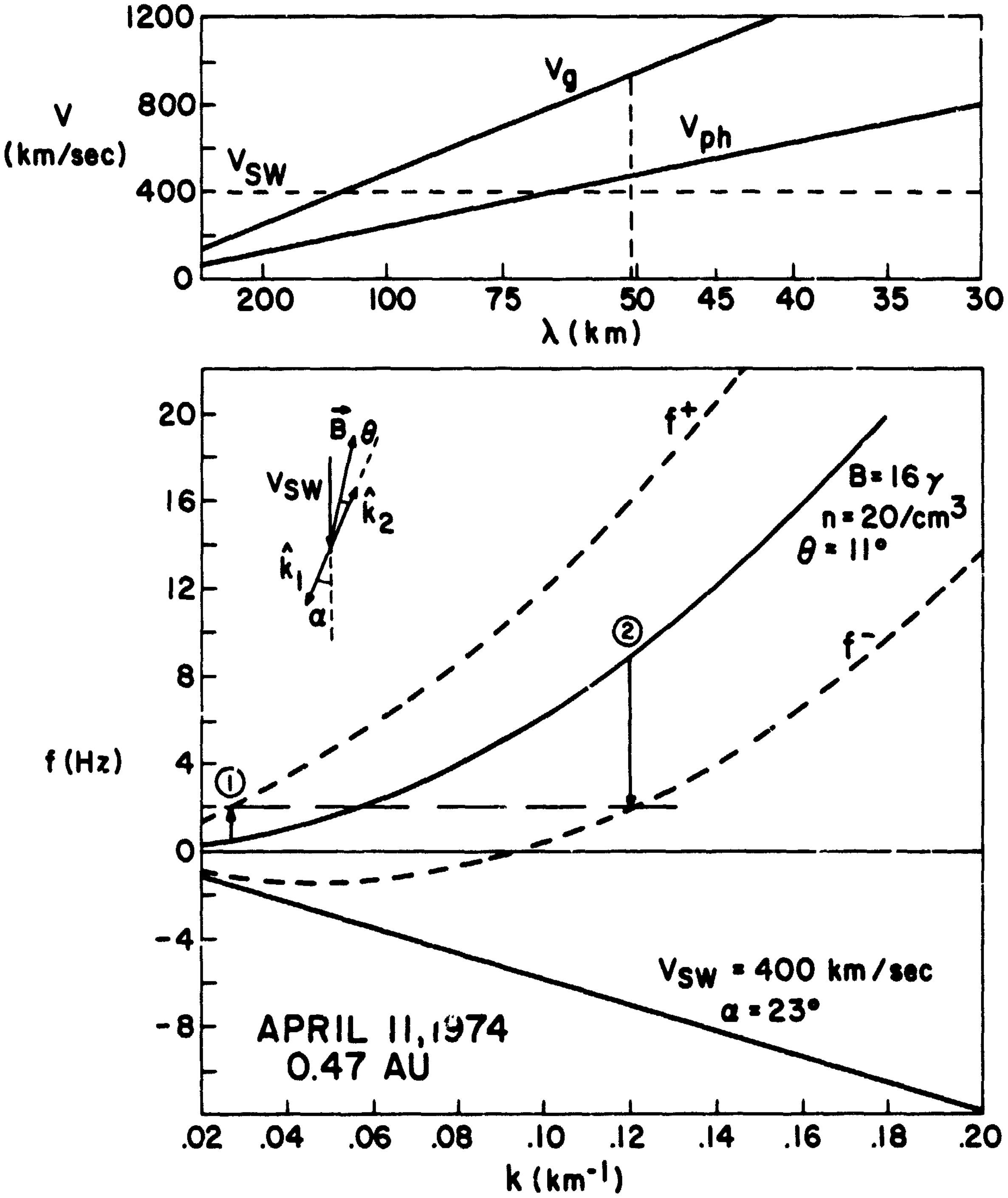

Figure 57. An appropriate Doppler shift (solid curve at negative f) can be both added to and subtracted from the plasma frame frequency derived from the cold plasma whistler dispersion relation (solid curve for positive f) to produce the Doppler shifted frequency curves (dashed curves labeled f^+ and f^-) for the 11 April case. Upper panel shows wave group and phase speeds (solid) as functions of k (or λ), and solar wind bulk speed (dashed). Since both V_g and $V_{ph} > V_{sw}$ for k = 0.12, a shift down to 2 Hz from a higher frequency with no polarization reversal was possible (see text).

For $\omega << \Omega_e$, and for small θ, $\vec{V}_g$ is nearly aligned with the phase velocity direction $\hat{k}$ (Fairfield, 1974). Since this is true for most of the cases considered here, then the θ term can be ignored.

In that case, to a good approximation,

$$|\vec{V}_g| = \frac{\omega}{k}\left(2 - \frac{\omega}{\Omega_e \cos\theta}\right) \tag{IV-21}$$

Using $\Omega_e = eB/m_e c$, where m_e is electron mass = 9.11×10^{-28} gm, and evaluating the constants, we get the expression

$$V_g = \left(4\pi - \frac{0.2244f}{B\cos\theta}\right)\frac{f}{k}, \tag{IV-22}$$

where f is the frequency value computed using equation (IV-18).

The upper panel of Figure 57 shows curves generated using equations (IV-20) and (IV-22) for $B = 16\gamma$, $\theta = 11°$, the given range of values for k and previously computed values of f = f(k). For $V_{sw} = 400$ km/sec, we see that both V_g and V_{ph} were greater than V_{sw} at the value of k corresponding to a Doppler-shift down to 2 Hz from 9 Hz. The corresponding wavelength is seen to have been near 50 km. On the basis of these considerations we conclude that the RH polarized wave observed on April 11 was most likely an electron whistler wave traveling upstream relative to the solar wind.

We have also examined the two cases where the observed frequency was near 10 Hz. These cases were found to be consistent with being whistler waves for solar wind parameter values which were "typical" for the position and time of observation. The RH polarized case observed on January 29 at a heliocentric distance of 0.75 AU is illustrated in Figure 58. The magnetic field magnitude was measured to be $B = 9.6\gamma$. Estimated plasma parameters were electron number density n_e = [illegible] cm^{-3} and

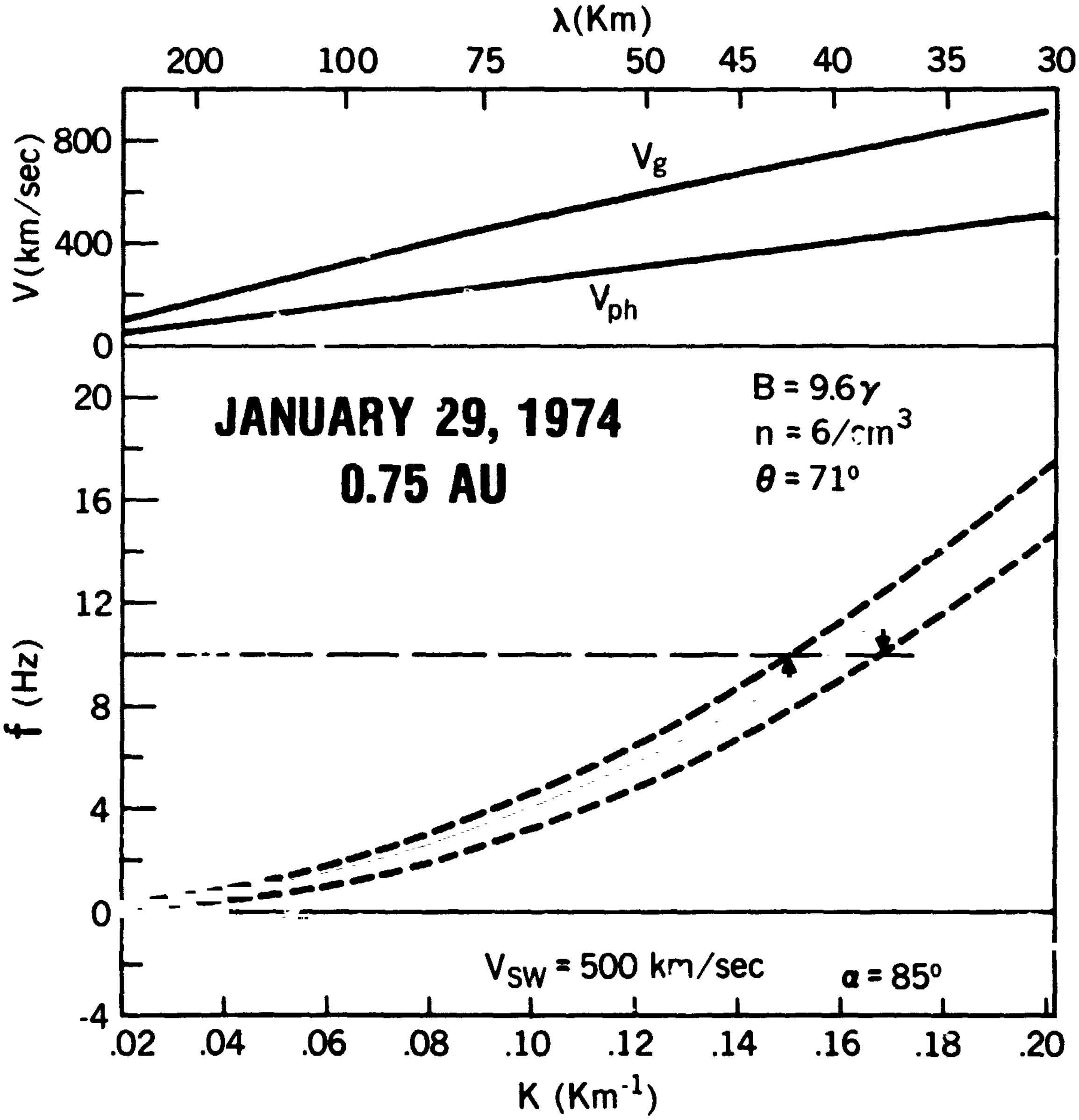

Figure 58. Dispersion relation and Doppler shift curves for 10 Hz RH polarized wave observed on January 29, 1974 in same format as Fig. 57. Only a small Doppler shift was possible, so observed wave frequency must have been near the plasma frame frequency.

solar wind bulk speed V_{sw} = 500 km/sec (Scudder, private communication). At this time the unit wave vector $\hat{k}$ was oriented nearly transverse to a radial solar wind flow direction, i.e., α = KX = 85°, so that little Doppler-shift would have occurred. Thus the plasma frame frequency was probably not very different from the observed frequency of 10 Hz as shown in Figure 58. Although in this case θ = KF = 71°, as indicated earlier the conditions on θ cited in Stix (1962) for applicability of the form of the whistler dispersion relation given as equation (IV-9) were strongly satisfied. The curves in the upper panel of Figure 58 raise the question of whether the wave phase velocity was sufficiently large such that there was no polarization reversal between the plasma and spacecraft reference frames. Since KX = 85°, the component of the solar wind velocity in the $\hat{k}$ direction would have been less than 50 km/sec and polarization reversal would therefore have been impossible. The Doppler-shift in this case is so small that it is not very important to be critically certain about the direction of frequency shift. It is most likely, however, that the wave had a small component of propagation away from the sun in the solar wind frame, and thus that the wavelength was approximately 42 km.

The observation of a LH polarized wave at a frequency of 10 Hz on February 20 at a radial distance from the sun of 0.65 AU has been examined also. The magnetic field magnitude at the time of the measurement was B = 6.3γ (and thus ν_p = 0.10 Hz). In this case α = KX = 29° and θ = 44°. During the first 12 hours of February 20, the most probable bulk speed, based on estimates from the Mariner 10 plasma electron experiment, was approximately 700 km/sec and most probable number density was 13 cm^{-3} (Scudder, private communication). Also, during the five minute period containing the observation, the average bulk speed was V_{sw} = 698 km/sec and average number density was n_e = 10 cm^{-3}. The only possible conclusion in this case is that the wave was propagating in the upstream direction in the plasma frame but with V_{ph} less than V_{sw}, so that LH polarization was observed for the whistler wave. Values for V_g and V_{ph} were calculated and found to be substantially less than 700 km sec, thus supporting this as the only possible interpretation within the framework of the modes under consideration. The dispersion relation curve was generated for $n_e = 10\ \text{cm}^{-3}$ and the Doppler-shift term computed for $V_{sw} = 700$ km/sec. From the observed frequency of 10 Hz one concludes that the wavelength was approximately 37 km.

The lack of highly accurate, continuous and relatively detailed solar wind parameters during the mission precludes an individual analysis of each of the wave cases shown in Figure 47 and included in the statistics. For completeness, however, several of the cases of RH polarization with observed frequencies near the proton gyrofrequency were studied. A case on March 19 at $r = 5.0$ AU and with $f_{DP} = 0.26$ Hz, $B = 13.2\gamma$, $\nu_p = 0.20$ Hz, $\vartheta = 11°$ and $\alpha = 41°$ is representative of that class of events. Using estimated values of $n_e = 20\ \text{cm}^{-3}$ and $V_{sw} = 500$ km/sec it was found that one could compute a spacecraft frame frequency near the proton gyrofrequency for whistler waves with $\lambda \approx 40$ km using the whistler dispersion relation and assuming that the waves propagate upstream with both V_g and V_{ph} greater than 500 km/sec. Calculated values for V_g and V_{ph} supported this interpretation.

In a case where the observed frequency is lower than the computed proton gyrofrequency, there is also the possibility that one is simply observing an ion cyclotron wave propagating upstream in the plasma frame at a speed less than the solar wind speed, so that RH polarization and a frequency somewhat less than ν_p would be detected. In such a case one could compute the phase and group velocities and test for consistency with the whistler interpretation. Failure to achieve consistency with that interpretation would suggest that the ion cyclotron mode is, in that case, the most likely candidate. Estimates of plasma parameters were not available at the time of this study for the time when such a case was observed. Therefore it was not possible to confirm the identification of a wave that was observed to be RH polarized in the spacecraft frame as an ion cyclotron wave propagating toward the sun in the plasma frame.

In considering the interpretation of the observations at the higher frequencies, such as 10 Hz, one must be concerned about the validity of the wave parameters derived from measurements at frequencies sufficiently high that the signal power density is near that due to intrinsic noise in the magnetometers. A maximum power density of $4 \times 10^{-5}\ \gamma^2/\text{Hz}$ was typically observed in association with the 10 Hz wave events. That includes the contribution from sensor noise, but in the same way that the external signal is attenuated by instrument rolloff, sensor noise is attenuated and should have a power density of approximately $10^{-5}\ \gamma^2/\text{Hz}$ at 10 Hz (see Figure 10). Thus the power in coherent fluctuations at that frequency is sufficiently above the noise to be detectable, but the signal to noise ratio is uncertain through undoubtedly relatively low. It is possible that the wave vector directions are not as accurately determined in these cases as at the lower frequencies, and thus the large KF angle values computed for these two cases should perhaps be treated as suspect. There is no way in which the sense of polarization could be detected incorrectly due to instrumental effects since the increasingly larger phase lag of the sensors at high frequencies (see Figure 8) merely delays in time the observation of peak values in the signal but cannot reverse the sense of rotation.

One must also be concerned about the uncertainties in the plasma parameters used in this study. The general validity of the model used to estimate solar wind parameters from the measurements performed by the antisolar -facing electron detector had not been firmly established at the time of this investigation of wave events. However, the overall success in establishing probable mode identification in these calculations using the estimated solar wind parameters in simple relations derived from theory provides a measure of confidence in the electron data analysis. Refined estimates of solar wind flow angles were not available for any of the wave events considered in the study. There are indications from the data that on a short time scale there are at times significant (> 5°) deviations from radial flow (Scudder, private communication). It is not likely that improved α values resulting from such data when available would significantly influence any of the results presented in this section, however.

The Mariner 10 observations of electromagnetic waves in the solar wind are of importance for considerations of instability mechanisms in the solar wind, which in turn are important in studies of both microscale and large scale physical processes in the solar plasma. It is beyond the scape of this investigation to treat plasma instabilities in detail, especially since the lack of measurements of proton temperature anisotropies on Mariner 10 precludes the unambiguous association of the observed waves with particular types of instabilities. We shall, however, return to this topic briefly in the summary of the observations presented in the following chapter.

CHAPTER V

SUMMARY OF RESULTS AND CONCLUSIONS

During the primary mission of the Mariner 10 spacecraft, from launch on November 3, 1973 through first encounter with the planet Mercury on March 29, 1974, almost continuous observation of the IMF at a sampling rate of 25 vectors/sec by the Magnetic Field Experiment onboard Mariner 10 has provided a wealth of new data on both the large-scale structure and the fluctuation characteristics of the IMF over distances from the sun ranging between 0.46 and 1 AU. This initial comprehensive survey of the Mariner 10 magnetic field measurements in interplanetary space has attempted both to characterize the large-scale, corotating IMF during that period of time over the distance range traveled by the spacecraft and to expand our understanding of the radial distance variations of not only the large-scale field but also of the fluctuations of the field. Also the first measurements well away from the environs of Earth of the field fluctuations at frequencies between 0.01 and 12.5 Hz have been performed.

A regular two-sector IMF polarity pattern was clearly discernable in the Mariner 10 observations during the last 3-1/2 months of the period under investigation. It is possible though not conclusively established that the region of space within which this two-sector structure was well-defined was confined in solar latitude to be predominantly below the solar equatorial plane at least to distances from the sun on the order of 1 AU. The sector in which the IMF was directed toward the sun was dominant below the solar equatorial plane, in agreement with previous dominant polarity observations. On the other hand, the observation at this time of a two sector polarity pattern during the approach to solar cycle minimum is atypical relative to what would be predicted in that portion of the cycle on the basis of long term inferences of IMF polarity from polar geomagnetic field measurements.

Variations of the large-scale IMF with heliocentric distance deduced from Mariner 10 measurements are consistent with the zeroth order Parker spiral field model for the variation of the field magnitude and the predicted r^{-2} dependence for the radial component of the field. The azimuthal component of the field was found to have an $r^{-1.3}$ dependence at this time, a somewhat steeper falloff with radial distance than the r^{-1} dependence predicted by the simple model. One must conclude from the consistency in the measurements to date that the radial component of the field is well described on average by the inverse square dependence. However, there are differences between some of the radial distance dependence results for the azimuthal component, although the Mariner 4 and Pioneer 10 results are consistent with the dependence found from Mariner 10 measurements. The question of why the azimuthal component falls off faster with radial distance than r^{-1} has not been as yet explained in a completely satisfactory manner.

Two compound high-speed streams dominated the solar wind flow characteristics near the solar equatorial plane during the period of study, one in each of the two IMF sectors. The enhanced field magnitudes in the high-density regions ahead of the high-velocity solar plasma were found to vary less with heliocentric distance than the fields in less disturbed regions, leading to an increase in the relative enhancement of interaction region fields with increasing radial distance from the sun. Variation in the relative IMF fluctuation amplitudes computed from hourly rms deviations of the field, particularly those associated with fluctuations in direction, were found to be related to the stream structure, in agreement with previous observations. In particular they were found to be highest in the high velocity portions of the high-speed streams.

A number of questions remain concerning the radial gradients in magnetic field fluctuations. Mariner 10 results suggest roughly constant relative magnitude fluctuation levels on average between 1 and 0.46 AU and perhaps a weak decrease in transverse fluctuation with increasing distance, with considerable modulation by solar wind streams. Mariner 4 results suggest relative growth of compressional fluctuations and a weak decrease in transverse fluctuation with increasing distance; Pioneer 10 observations support the view that $\Delta B_r / B_r$ is roughly independent of distance from the sun; and Belcher and Burchsted (1974) have reached the same conclusion for the region between 0.7 and 1.5 AU. The thread of consistency running through these various observations suggests that relative fluctuations of the field are not increasing with radial distances as predicted by Parker and Dessler, except perhaps at frequencies lower than one cycle per day (Rosenberg et al., 1975).

Additional quantitative studies with a self-consistent model of the solar wind are needed to fully understand the observed fluctuation intensity attentuation characteristics as part of the overall energy balance in the flow of the solar wind. Also additional measurements are needed to establish more precisely the nature and degree of relationship of fluctuation levels to large-scale structure in the interplanetary medium as well as to solar cycle variations. The observed average magnitude and radial variation of σ_c / F suggests that the assumption in cosmic ray propagation theory that the relative fluctuations of the field is a "small parameter" is not a very good assumption.

A variation in the occurrence rate of directional discontinuities with heliocentric distance was observed by Mariner 10. A decreasing occurrence rate with increasing radial distance was found, with a power law dependence of $r^{-1.28}$. This variation contributes to the weak decrease in relative directional fluctuations with increasing heliocentric distance that was found in the study of rms deviations of the IMF. A similar dependence has been found by Pioneer 10 (Tsurutani and Smith, 1975). An increase in the "thickness" of directional discontinuities by a factor of 5 to 10 between 1 and 5 AU was also found from the Pioneer 10 measurements. This would be consistent with an apparent decrease in the occurrence rate with increasing radial distance, due to using an identification criterion with a fixed time increment. One may still consider the observed distance dependence of the occurrence rate as being "real" in the sense of being an actual decrease with increasing distance of the occurrence rate of directional discontinuities with thickness equal to or less than a given fixed value. There are large time variations in the discontinuity occurrence rate. Both Mariner 10 and Pioneer 10 have observed the rate to be higher in the high velocity regions of the solar wind.

Receipt on the ground of the full 25 vector sample/sec data from the Mariner 10 Magnetic Field Experiment permitted computation of power spectral density of IMF fluctuations up to the 12.5 Hz Nyquist frequency. In general the power in IMF fluctuations of both field magnitude and individual components was found to decrease with increasing heliocentric distance, in agreement with previous observations over various ranges of radial distance and also in agreement with the variation seen in the un-normalized rms deviation data with distance from the sun. Power density in field component fluctuations was generally an order of magnitude or more greater than that in the magnitude fluctuations, also consistent with other observations. Time variations at times larger than the radial distance variation were seen in the IMF power density in association with stream structure. At frequencies above about 2 Hz, less variation with time and little variation with radial distance was observed. A steepening of the radial component spectral density with decreasing heliocentric distance above approximately 0.4 Hz was also observed.

The high sampling and telemetry data rates for the Magnetic Field Experiment made possible the observation of highly coherent transverse fluctuations at roughly all distances from the sun between 1 and 0.46 AU. The observed waves tended in general toward circular polarization, with the LH polarized waves observed being generally more nearly circularly polarized than the RH polarized waves. In addition to high ellipticity, the fluctuations where LH polarized waves were observed were characterized statistically by a higher degree of polarization and smaller angle between the unit wave vector of the observed waves and the radial direction than was found for the RH polarized fluctuations. For all but two of the cases, an average angle between the wave vector and the mean field vector of 14° was found for both senses of polarization. A selected set of the LH polarized waves were found to be consistent with being ion cyclotron waves that were Doppler shifted to frequencies in the spacecraft frame above the proton gyrofrequency. A number of the RH polarized cases were shown mostly likely to be electron whistler mode waves. The same identification was made for a LH polarized wave observed at 10 Hz. Due to the close proximity of some of the RH polarized wave frequencies to the proton gyrofrequency, it is possible that some of those cases represent ion cyclotron waves propagating toward the sun in the solar wind frame and are thus seen with RH polarization in the spacecraft frame or are possibly proton whistlers Doppler-shifted to low frequencies.

The observations at the higher frequencies together with the preliminary report of evidence of waves in data from the lowest channel (4.7 – 10 Hz) of the Helios A search-coil magnetometer as well as in higher frequency channels (Neubauer and Musmann, 1975) suggest the existence of a continuous spectrum of waves of intermediate frequencies (electromagnetic regime) in the spacecraft reference frame. These waves may be evidence of mode coupling effects at work, in which Alfvén waves moving out from the sun through the interplanetary medium interact with ambient particles and produce higher frequency waves.

The various roles that waves and instabilities may play in determining the thermal and dynamic states of the solar wind have been reviewed recently by Hollweg (1975). Various aspects of the instability conditions have been studied by Soper and Harris (1965), Kennel and Petschek (1966), Scarf et al. (1967), Kennel and Scarf (1968), Hollweg and Völk (1970), Horng (1973), Lakhina and Buti (1975) and others. The ion cyclotron instability is driven by the proton temperature anisotropy $T_{\parallel} > T_{\perp}$, which is not generally thought to be a common state of the solar wind. The dispersion properties of this mode are those of the LH polarized Alfvén mode going to ion cyclotron resonance. Conditions for the occurrence of this instability have been found to be satisfied in interplanetary or counterstreaming solar wind streams. The observation of such streams have been reviewed by Feldman et al. (1974).

Gary et al. (1975) argue that the solar wind proton distribution near 1 AU can be considered composed of a cooler $T_{\perp} > T_{\parallel}$ "core" and a hotter $T_{\parallel} > T_{\perp}$ (halo". For the parameters studied, the firehose and ion cyclotron instabilities were found to the most important modes. Both instabilities have maximum growth rates when $\vec{k} \parallel \vec{B}_0$. Conditions for the occurrence of the firehose instability have been discussed by Kennel and Petschek (1966), Hollweg and Völk (1970), Pilipp and Völk (1971) and Forslund (1972). The firehose instability is driven by the $T_{\parallel} > T_{\perp}$ proton anisotropy. The dispersion properties of this mode are those of the RH magnetosonic mode going into the whistler mode as ω becomes greater than the ion cyclotron frequency. As the phase velocity increases for $\omega > \Omega_i$, the whistler becomes an electron mode. Gary et al. (1975) argue that with the two-component proton distribution, sufficiently large thermal anisotropies and $B_i \sim 1$, where $\omega_i = B/\sqrt{4\pi m_i n_i}$, <u>both</u> the Alfvén-ion cyclotron and the magnetosonic-whistler branches of the dispersion relation become unstable.

It is possible that the electromagnetic waves observed by Mariner 10, if indeed they are ion cyclotron and whistler waves, were associated with the occurrence in the solar wind of these types of instabilities or with other types which may be important in solar wind processes, such as heat flux instabilities. As discussed in Chapter IV, we are unable to make a positive association of the observed waves with specific types of instabilities because of the lack of measured properties of the solar wind protons, including thermal anisotropies. The results do suggest certain associations, however, and future efforts will include the search for more cases to expand the wave data set and improve the statistics. A more definitive study of both the individual and statistical properties of these waves may provide clues as to the most likely instability associations. It will remain for deep space probes with a similar high-rate magnetometer and a plasma experiment measuring a full set of plasma parameters for both protons and electrons to completely close the loop on the remaining questions concerning microscale processes in the solar wind. The fact that the types of waves which have been illustrated in this analysis were observed so frequently by Mariner 10 suggest that they are a common feature of the interplanetary medium at least out to 1 AU and should be readily observable by any magnetometer with the appropriate bandwidth. Previous measurements at the relevant frequencies have been performed near the earth's bow shock where the shock-associated waves tend to dominate the observations. With a finite thermal anisotropy, the solar wind plasma is typically at best in a state of marginal stability. Whereas the "quiescent" thermal anisotropy condition (at least for the halo proton distribution) is $T_{||} > T_{\perp}$, $T_{||} < T_{\perp}$ can also occur in association with disturbed conditions in the solar wind. As already discussed, both types of anisotropy can drive certain instabilities. Since a magnetized collisionless plasma with a significant pressure anisotropy is not generally stable, waves should grow spontaneously (Scarf et al., 196[illegible]). Wave-particle scattering, which tends to make the particle distribution more isotropic, will develop to remove the instability.

The conditions for cyclotron damping have been discussed in detail by Stix (1962). Particles which "feel" field oscillations at their own cyclotron frequency will absorb energy from the field, and if the electromagnetic field is due to a plasma wave, this will cause the wave to damp out with time and/or distance. The range of dissipation by proton cyclotron damping extends upward in frequency from $\sim 10^{-1}$ Hz (Coleman, 1968). Energy in these waves, having reached them by cascading through the spectrum, is dissipated in heating the protons, primarily by increasing $T_{\parallel}$. Brice (1964) analyzed the physical mechanisms that produce the energy exchange. Scarf and Fredricks (1968) showed that the mechanisms of excitation and damping are modified by mode-coupling effects in a multicomponent plasma. In addition to these considerations, when there is a sufficiently large flux of fast or nonthermal electrons present in the plasma, i.e., a significant high energy tail on the electron distribution, Tidman and Jaggi (1962) showed that such fluxs can produce damping of whistler waves while providing negligible damping of hydromagnetic waves.

Thus it is evident that in the anisotropic, time-variable and at times turbulent solar wind, conditions for both the generation and relatively rapid damping of electromagnetic waves such as those observed by Mariner 10 generally should be readily available. This argues in favor of the local generation of such waves throughout the region of observation. These considerations also suggest that such waves should be observable to considerably greater distances from the sun than 1 AU, albeit at somewhat lower frequencies. It will remain for future spacecraft missions into the outer solar system to confirm this conclusion.

Other future studies of the Mariner 10 magnetic field measurements will include a more detailed association of fluctuations in general and polarized waves in particular with particular solar wind stream regions; extended studies of the variation of important properties of field fluctuations, such as the anisotropy ratios and polarization parameters, with frequency and radial distance from the sun; an extension of the spectral studies to lower frequencies; more detailed studies of directional discontinuities and a search for and study of interplanetary shocks; correlative studies between the magnetic field measurements and the observations by the plasma electron and energetic particle experiments and with the measurements on other spacecraft; and of course the analysis of Mariner 10 observations beyond the primary mission time period.

The results of the current and future studies of the Mariner 10 measurements together with those currently being performed by Helios and Pioneers 10 and 11 should provide a more complete understanding of both the large scale structure and the microscale behavior of the IMF. Some of the outstanding problems, such as those pertaining to the radial gradients in both the azimuthal components of the field and the fluctuations of the field and those involving stream interaction phenomena, may be more difficult to resolve completely. It is certain however, that the extensive body of data from recent and current missions together with future measurements by Helios B and Mariner-Jupiter-Saturn will bring a more complete understanding during the next decade of the fundamental characteristics and evolution in both space and time of the interplanetary magnetic field and solar wind plasma throughout the solar system.

APPENDIX A

LEAST SQUARES FITS TO RADIAL DISTANCE VARIATION

One approach to determining the variation with heliocentric distance of the components of the IMF and of IMF fluctuations is to perform a least squares fit of the measured data to a nonlinear power law model Ar^C, where r is the radial distance and A and C are the parameters of the fit which will characterize the radial distance dependence. For a general function f of the magnetic field, we have a set of N measured values $f_i = f(r_i)$, $i = 1, \ldots, N$, and the corresponding set of radial distance values r_i. For given values of A and C, we can also compute $F_i = Ar_i^C$ for each value of r_i, $i = 1, \ldots, N$. Then we can further compute

$$(\mathrm{rms})^2 = g[f(r)] = g\begin{pmatrix} A \\ C \end{pmatrix} = \frac{1}{N} \sum_{i=1}^{N} (f(r_i) - F_i)^2. \tag{A-1}$$

The object of the analysis is to find values of the parameters (A, C) which minimize the rms functional $g\begin{pmatrix} A \\ C \end{pmatrix}$.

We can define the functional G, the gradient of the rms, according to

$$G\begin{pmatrix} A \\ C \end{pmatrix} = \mathrm{grad}\ g\begin{pmatrix} A \\ C \end{pmatrix} = \begin{bmatrix} \partial_A g\begin{pmatrix} A \\ C \end{pmatrix} \\ \partial_C g\begin{pmatrix} A \\ C \end{pmatrix} \end{bmatrix} \tag{A-2}$$

(Ortega and Rheinboldt, 1970).

C.3

The gradient norm is then defined by

$$||G|| = G^TG. \tag{A-3}$$

The computational method that is actually used in this study looks for zeros of the gradient norm $||G||$, which are related to the minima in the rms (Wilde and Beightler, 1967). This offers a more sensitive means of determining the "best fit" values of (A, C) in this problem because the zeros of the gradient are more sharply defined than the minima of the rms functional. Not all critical points are minimizers, however, so the method also looks at the value of the rms functional in each case to establish the minimum.

In the solution of a nonlinear problem one must be concerned about the uniqueness of the solution. In practice the iterative procedure utilized may converge on a minimum which is "local" but not the "least" minimum. This depends on the choice of starting values for the fitting parameters. One can be confident in the solution if convergence to the same solution is achieved for a range of starting values. For the two-parameters fits performed in this investigation, where the model was linear in A and nonlinear in B, care was taken in each case to establish strong convergence to the parameter values cited as "best fit" solutions for A and C.

To compute standard errors for the parameter A and C, we used the parameters

$$\chi^2(A, C) = \sum_{i=1}^{N} [F(A, C, r_i) - f(r_i)]^2, \tag{A-4}$$

where the best fit A*, C* minimized χ^2. For the given data we define the matrix

$$V = \frac{1}{2}\begin{bmatrix} \frac{\partial^2\chi^2}{\partial A^2} & \frac{\partial^2\chi^2}{\partial A\partial C} \\ \frac{\partial^2\chi^2}{\partial A\partial C} & \frac{\partial^2\chi^2}{\partial C^2} \end{bmatrix} = [v_{ij}], \tag{A-5}$$

where the partial derivatives are taken at the best fit point A*, C*. The error (covariance) matrix is then defined by

$$V^{-1} = \frac{1}{v_{11}v_{22} - v_{12}^2} \begin{bmatrix} v_{22} & -v_{12} \\ -v_{12} & v_{11} \end{bmatrix} \qquad \text{(A-6)}$$

The variances and covariances of the estimates A*, C* can be obtained from V^{-1}. Thus to compute these statistical factors, V must be approximated.

A method by Noble (1967) uses the fact that when F is linear in A and C, then χ^2 is quadratic, i.e., there exist unique coefficients a, h, b, f, g, c, such that

$$\chi^2(A, C) = z(x, y) = a\,x^2 + 2h\,xy + by^2 + 2fx + 2gy + c \qquad \text{(A-7)}$$

where

$$X = A - A^*, \quad y = C - C^*.$$

Thus Noble finds a quadratic surface z(x, y) which fits the χ^2 surface in the least squares sense, and makes the approximation

$$V = \frac{1}{2}\begin{bmatrix} \frac{\partial z}{\partial x^2} & \frac{\partial^2 z}{\partial x \partial y} \\ \frac{\partial^2 z}{\partial x \partial y} & \frac{\partial^2 z}{\partial y^2} \end{bmatrix} = \begin{bmatrix} a & h \\ h & b \end{bmatrix}. \qquad \text{(A-8)}$$

This approximation is equivalent to a Taylor's series expansion of χ^2 at (A*, C*), and assumes that in the vicinity of the best fit, the χ^2 surface behaves as though the model F is linear in <u>both</u> A and C.

Hence the covariance matrix is approximated by

$$V^{-1} = \frac{1}{ab - h^2} \begin{bmatrix} b & -h \\ -h & a \end{bmatrix} \qquad \text{(A-9)}$$

If we define $d \equiv a\,b\text{-}h^2$, then for the model Ar^C we have

$$\sigma_A^2 \approx S^2\, b/d \qquad \text{(A-10a)}$$

$$\sigma_C^2 \approx S^2\, a/d \qquad \text{(A-10b)}$$

and

$$\sigma_{A,C}^2 \approx -S^2 \frac{h}{d}, \qquad \text{(A-10c)}$$

where

$$S^2 = \frac{\chi^2}{N - 1}.$$

We also have that $\rho\sigma_A\sigma_C = \sigma_{A,C}^2$ where ρ is the correlation coefficient between A and C. Thus

$$\rho = \frac{-h}{\sqrt{a}\sqrt{b}} \qquad \text{(A-11)}$$

was also computed.

To a 95% confidence level, then, the errors on A and C are given by $E_A = 2\sigma_A$, $E_c = 2\sigma_c$, and the results of the data fitting are given in Chapters III and IV as

$$A \pm E_A$$

$$C \pm E_C.$$

An alternative method for approximating the error matrix V^{-1} was tried (Argentiero, private communication). From equations (A-4) and (A-5) we have that

$$v_{12} = \frac{\partial^2 \chi^2}{2\,\partial A\,\partial C} = \sum_{i=1}^{m} \left[\frac{\partial F_i}{\partial A}\,\frac{\partial F_i}{\partial C} + \frac{\partial^2 F_i}{\partial A \partial B}\,(F_i - f_i)\right]$$

The alternative method simply ignores the second partial derivatives and makes the approximation

$$V = \eta\,[\eta_{ij}] \tag{A-12}$$

where

$$\eta_{12} \equiv \sum_{i=1}^{N} \left[\frac{\partial F_i}{\partial A}\,\frac{\partial F_i}{\partial C}\right]$$

as if F were linear in both A and B. The resulting matrix was found to agree component-wise with that obtained using Noble's method to within 0.8%.

APPENDIX B

POWER SPECTRAL DENSITY AND POLARIZATION ANALYSIS

Power spectral density estimates were computed in this investigation using an existing generalized spectral analysis system based on the mean-lagged-product method of calculating power spectra that was developed by Blackman and Tukey (1958). In this method a series of autocorrelation lags is computed for each of the magnetic field component and magnitude time series which have been normalized to zero mean. The power spectra are then calculated from the finite Fourier transforms of the autocorrelation function. The raw estimates are smoothed using a hanning function. This basic procedure is described in more detail in the PhD Thesis of Sari (1972) and in Otnes and Enochson (1972).

For application to this study, the analysis system was augmented in the following manner.

(i) A trend removal subroutine was written and added to the system. This routine fits a second degree polynomial to a data time series that is passed to it and then subtracts the best-fit polynomial from the time series point by point. This can be applied optionally to any combination of BX, BY, BZ and F.

(ii) A computation of eigenvalues and eigenvectors corresponding to the power density and directions associated with the maximum, intermediate and minimum fluctuations in the magnetic field was added to the system. This was accomplished by diagonalization of the real part of the spectral density matrix using a Givens-Householder technique (Wilkenson, 1965). Three eigenvalues and three eigenvectors are determined for each spectral estimate.

(iii) A subroutine was added to the system to compute various polarization characteristics as functions of frequency for the field fluctuations. This will be discussed further and the parameters defined in the latter part of this appendix.

There are certain fundamental assumptions associated with Fourier transforming sampled data. According to Brigham (1974), there is only one class of waveforms for which the discrete and continuous Fourier transforms are exactly the same to within a scaling constant. Equivalence of the two transforms requires:

(i) The time function b(t) must be periodic;

(ii) b(t) must be band-limited;

(iii) The sampling rate must be at least two times the largest frequency component of b(t); and

(iv) The truncation function must be non-zero over exactly one period (or integral multiple period) of b(t).

In general application to any measured and digitized magnetic field data, one assumes that (i) and (ii) are at least approximately true. It is because of condition (iv) that we apply the trend removal in this analysis in an attempt to prevent spurious contributions to the power from variations of less than one full period in the data. Condition (iii) specifies that, for data points at equispaced intervals Δt, we can only estimate the power spectrum in the frequency range 0 to f_c, where $f_c = 1/2\,\Delta t$ is the cutoff or Nyquist frequency. The cutoff frequency f_c for the Mariner 10 detail data is 12.5 Hz, while that for computation of spectra from 1.2 sec averages is

~0.4 Hz. In a few cases we have also used 42 sec averages to compute spectra, for which $f_c = 0.011$ Hz.

Each spectral estimate computed is a measure of the power in a frequency range that is bounded, for the jth estimate, by the frequencies $(j \pm 1/2)\, f_c/M$ and centered at $j\, f_c/M$, where M is number of spectral estimates calculated. Exceptions to this are the first and last estimates, which sample the power in the range 0 to $1/2\, f_c/M$ and $(M - 1/2)\, f_c/M - f_c$, respectively.

Associated with the computation of power spectral density is the degree of freedom ν, which for moderate to large values is given by

$$\nu = \frac{2N}{M}, \tag{B-1}$$

where N is the number of data points in the given time series. The quantity ν is related to the confidence interval for the estimates (Sentman, 1974). For $\nu \gtrsim 4$, confidence limits can be computed with good accuracy using the confidence factor k_c, where

$$k_c = \exp\left(\frac{2.3b}{10\sqrt{\nu - 1}}\right) \tag{B-2}$$

and for 98% confidence, b = 29; for 96%, b = 25; for 90%, b = 20; and for 80%, b = 16. Using k_c one can calculate the error bar limits from

$$\text{upper limit} = \text{PSD estimate} * \sqrt{k_c}$$
$$\text{lower limit} = \text{PSD estimate} / \sqrt{k_c}.$$

For the spectra computed in this study, N = 1500 samples and M = 60 spectral estimates, giving

$$\nu = \frac{2N}{M} = 50.$$

Thus $k_c = \exp(0.0329b)$ and, for 90% confidence, $\sqrt{k_c} = 1.390$, $1/\sqrt{k_c} = 0.719$.

In the computation of power spectra for the vector magnetic field, a power density and cross spectrum matrix is generated. This matrix is defined by

$$G = \begin{bmatrix} S_x & C_{xy} - iQ_{xy} & C_{xz} - iQ_{xz} \\ C_{yx} - iQ_{yx} & S_y & C_{yz} - iQ_{yz} \\ C_{zx} - iQ_{zx} & C_{zy} - iQ_{zy} & S_z \end{bmatrix} \qquad \text{(B-3)}$$

where S_j is the power density for the jth field component, C_{ij} is the cospectrum and Q_{ij} is the quadrature spectrum. The sample cospectrum measures the covariance between in-phase components (i.e.,between cosine components and sine components separately), and the sample quadrature spectrum measures the covariance between the out-of-phase or quadrature components (i.e., between sine and cosine components) (Jenkins and Watts, 1968).

Now $C_{ij} = C_{ji}$ and $Q_{ij} = - Q_{ji}$ by definition, so that we may write

$$G = \begin{bmatrix} S_x & C_{xy} - iQ_{xy} & C_{xz} - iQ_{xz} \\ C_{xy} + iQ_{xy} & S_y & C_{yz} - iQ_{yz} \\ C_{xz} + iQ_{xz} & C_{yz} + iQ_{yz} & S_z \end{bmatrix}$$

or

$$G = \begin{bmatrix} S_x & C_{xy} & C_{xz} \\ C_{xy} & S_y & C_{yz} \\ C_{xz} & C_{yz} & S_z \end{bmatrix} - i \begin{bmatrix} 0 & Q_{xy} & Q_{xz} \\ -Q_{xy} & 0 & Q_{yz} \\ -Q_{xz} & -Q_{yz} & 0 \end{bmatrix} \qquad \text{(B-4)}$$

Thus the power density matrix is composed of a real, symmetric part and an imaginery, skew- symmetric part, and hence the matrix is hermitian. To obtain eigenvalues and eigenvectors one need only diagonalize the real part of the power density matrix.

Spectra may be computed for data in solar ecliptic or solar equatorial coordinate systems, which in the rotating frame of the sun are at least approximately constant in orientation. A coordinate system which has been more extensively used for spectral computation in this work is the "mean field" coordinate system. This frame of reference is defined such that the Z_{MF} axis is taken along the average direction of the vector magnetic field (over the time period of the analysis or some shorter specified interval of time), the X_{MF} axis is perpendicular to Z_{MF} and lies in the XZ_{SE} or XZ_{SEQ} plane, and Y_{MF} completes the right-handed orthogonal set. Thus the unit vectors of this reference frame are given by

$$\hat{X}_{MF} = \frac{\langle\vec{B}\rangle \times \vec{r}_{xz}}{|\langle\vec{B}\rangle \times \vec{r}_{xz}|} \qquad \text{(B-5a)}$$

$$\hat{Y}_{MF} = \frac{\langle\vec{B}\rangle \times (\langle\vec{B}\rangle \times \vec{r}_{xz})}{|\langle\vec{B}\rangle \times (\langle\vec{B}\rangle \times \vec{r}_{xz})|} \qquad \text{(B-5b)}$$

and

$$\hat{Z}_{MF} = \frac{\langle\vec{B}\rangle}{|\langle\vec{B}\rangle|} \qquad \text{(B-5c)}$$

where $\vec{r}_{xz} = \langle BX_{SEQ}\rangle\,\hat{i} + \langle BZ_{SEQ}\rangle\,\hat{k}$. This coordinate frame facilitates studies of fluctuations parallel and perpendicular to the magnetic field.

In whatever basic coordinate system that is utilized, we compute not only the power spectral density estimates S_i, but also utilize the off-diagonal terms of the power density matrix to compute coherence and phase lag. The coherence function is defined as

$$\gamma_{ij} = \frac{(C_{ij}^2 + Q_{ij}^2)^{1/2}}{(S_i \cdot S_j)^{1/2}} \qquad \text{(B-6)}$$

and phase angle or phase lag in degrees is defined as

$$\phi_{ij} = \frac{180}{\pi} \tan^{-1}\left(\frac{Q_{ij}}{C_{ij}}\right), \tag{B-7}$$

for ij = xy, xz and yz. Some authors define the coherence function as γ^2_{ij} (Bendat and Piersol, 1971; Otnes and Enochson, 1972). Coherence has a value near one for signals which are highly interrelated and a value of zero for signals which are not interrelated (i.e., noise).

For the computation of parameters which characterize the polarization of magnetic field fluctuations, we transform to the coordinate system defined by the eigenvector system. In the new system the z axis is defined by $\hat{z} = \hat{k}$, where $\hat{k}$ gives the wave normal vector direction (taken as the direction of minimum fluctuation, i.e., the direction given by the eigenvector associated with the minimum eigenvalue). We further take $\hat{x}$ to lie in the $\hat{k}\cdot\langle\vec{B}\rangle$ plane and $\hat{y}$ to be oriented perpendicular to that plane. The $\hat{x}$ and $\hat{y}$ unit vectors in the eigenvector system are then given by

$$\hat{x} = \frac{\hat{y} \times \hat{k}}{|\hat{y} \times \hat{k}|} \tag{B-8a}$$

where

$$\hat{y} = \frac{\hat{k} \times \langle\vec{B}\rangle}{|\hat{k} \times \langle\vec{B}\rangle|} \tag{B-8b}$$

and, as given above, $\hat{z} = \hat{k}$.

From these definitions, a matrix R can be derived for transformation from mean field to eigenvector coordinates which is expressed in terms of the components (k_1, k_2, k_3) of $\hat{k}$ only:

$$R = \begin{bmatrix} \frac{-k_1 k_3}{\sqrt{k_1^2 + k_2^2}} & \frac{-k_2 k_3}{\sqrt{k_1^2 + k_2^2}} & \sqrt{k_1^2 + k_2^2} \\ \frac{k_2}{\sqrt{k_1^2 + k_2^2}} & \frac{-k_1}{\sqrt{k_1^2 + k_2^2}} & 0 \\ k_1 & k_2 & k_3 \end{bmatrix} \qquad \text{(B-9)}$$

This matrix is then used to transform both the real and imaginary parts of the power spectral density matrix. To compute polarization parameters (assuming a plane wave) one uses only the components of the resultant spectral density matrix corresponding to the plane perpendicular to the wave vector direction.

For the polarization analysis we have followed the formulations of Fowler et al. (1967) and Rankin and Kurtz (1970). The two-dimensional power spectral matrix is given by

$$J = \begin{bmatrix} J_{xx} & J_{xy} \\ J_{yx} & J_{yy} \end{bmatrix} = \begin{bmatrix} R_{xx} & R_{xy} - i\,I_{xy} \\ R_{yx} - I_{yx} & R_{yy} \end{bmatrix}. \qquad \text{(B-10)}$$

where R and I signify real and imaginary parts, respectively. Now $|J| = R_{xx}\ R_{yy} - [(R_{yx} - I_{yx})(R_{xy} - i\,I_{xy})]$ or, since

$$R_{yx} = R_{xy}, \quad I_{yx} = - I_{xy},$$

$$|J| = R_{xx}R_{yy} - R_{xy}^2 - I_{xy}^2.$$

Computing

$$D = \frac{1}{2}\{(R_{xx} + R_{yy}) - [(R_{xx} + R_{yy})^2 - 4\,|J|]^{1/2}\}$$

from the characteristic root of the matrix J (this derivation will be outlined at the end of this appendix), we can then define a matrix that represents the polarized part of the signal only:

$$P = \begin{bmatrix} P_{xx} & P_{xy} \\ P_{yx} & P_{yy} \end{bmatrix} = \begin{bmatrix} J_{xx} - D & J_{xy} \\ J_{yx} & J_{yy} - D \end{bmatrix} . \qquad \text{(B-12)}$$

We then have that $P_{xx} = R_{xx} - D$ and $P_{yy} = R_{yy} - D$, and we can calculate the degree of polarization DP which is the ratio of polarized power to total power in fluctuations, according to

$$DP = \frac{\mathrm{Tr}\,|P|}{\mathrm{Tr}\,|J|} = \frac{P_{xx} + P_{yy}}{J_{xx} + J_{yy}} . \qquad \text{(B-13)}$$

Further, we can compute, as previously shown, the coherency:

$$\gamma_{xy} = \left(\frac{J_{xy} J_{yx}}{J_{xx} J_{yy}} \right)^{1/2}$$

$$= \frac{(R^2_{xy} + I^2_{xy})^{1/2}}{(R_{xx} R_{yy})^2} . \qquad \text{(B-14)}$$

The angle of polarization θ, defined as the angle between the X axis of the coordinate frame and the major axis of the polarization ellipse, is given by

$$\tan 2\theta = \frac{2\mathrm{Re}(J_{xy})}{J_{xx} - J_{yy}}$$

$$= \frac{2R_{xy}}{J_{xx} - J_{yy}} .$$

where Re = real part.

Thus

$$\theta = \frac{1}{2} \tan^{-1}\left(\frac{2R_{xy}}{J_{xx} - J_{yy}}\right) \tag{B-15}$$

The ellipticity ϵ of the polarization ellipse is the ratio of the minor axis to the major axis of the ellipse. This parameter is computed as follows:

$$\sin 2\beta = \frac{2\,\mathrm{Im}(J_{xy})}{[(J_{xx} + J_{yy})^2 - 4|J|]^{1/2}}$$

$$= \frac{2I_{xy}}{[(R_{xx} + R_{yy})^2 - 4|J|]^{1/2}},$$

where Im = imaginary part. Thus

$$\beta = \frac{1}{2} \sin^{-1}\left\{\frac{2I_{xy}}{[(R_{xx} + R_{yy})^2 - 4\,|J|]^{1/2}}\right\} \tag{B-16}$$

and

$$\epsilon = \tan \beta. \tag{B-17}$$

The sign of β gives the sense of the polarization relative to the magnetic field. This is shown, along with the corresponding phase angle value, in the following table.

	Left-handed Polarization	Right-handed Polarization
Phase lag ϕ_{xy}	90°	270°
$\hat{k}\cdot\vec{B}$ positive	β negative	β positive
$\hat{k}\cdot\vec{B}$ negative	β positive	β negative

From this table we see that we can check results on the sense of polarization relative to the field at a given frequency for consistency between the computed phase angle at that frequency and the sign of β (dependent on the sign of $\hat{k}\cdot\vec{B}$). Such consistency was required in the identification of wave events in this investigation.

Considering now, for completeness, the derivation of the polarized part of the spectral matrix (based on the discussion in Fowler et al., 1967), we have that the polarized part can be written as

$$P = \begin{bmatrix} A & B \\ B^* & C \end{bmatrix},$$

where $A \geq 0$, $C \geq 0$ and $AC - BB^* = 0$ (the latter since det $[J] = 0$ for a totally polarized signal). The matrix for the unpolarized part can be written

$$U = \begin{bmatrix} D & 0 \\ 0 & D \end{bmatrix}, \qquad D \geq 0.$$

Since $J = P + U$ we must have $A + D = J_{xx}$, $B = J_{xy}$, $B^* = J_{yx}$ and $C + D = J_{yy}$. Substituting for A, C, B and B* in $AC - BB^* = 0$, we have

$$(J_{xx} - D)(J_{yy} - D) - J_{xy}J_{yx} = 0$$

or

$$D^2 - (J_{xx} + J_{yy})D + |J| = 0.$$

Thus solving for the eigenvalues or characteristic roots we get

$$D = \frac{1}{2}(J_{xx} + J_{yy}) \pm \frac{1}{2}[(J_{xx} + J_{yy})^2 - 4|J|]^{1/2},$$

which is equivalent to equation (B-11).

In this analysis of magnetic field fluctuations, a second unit wave vector $\hat{k}$ was independently computed using the method described by Means (1972). This technique derives the components of $\hat{k}$ using only the imaginary part of the spectral density matrix. Good agreement between the results from the two methods was taken as an indicator that the wave normal vector was well determined. Also, as one of the selection criteria for wave events (see Section IV.2.2.) we have included the signal-to-noise ratio defined by Means (1972) as

$$S/N = \frac{J_{xx} + J_{yy}}{J_{zz}}, \qquad \text{(B-18)}$$

where $J_{xx} + J_{yy}$ is the trace of the 2-dimensional matrix defined by equation (B-10) and J_{zz} is the additional diagonal element of a 3 × 3 matrix that includes the $\hat{k}$ direction.

The analysis and interpretation of Mariner 10 magnetic field fluctuation observations has assumed that there were no detectable oscillations in the data from spacecraft induced mechanical oscillations. The mounting of the magnetometer sensors on a relatively long (5.8 m) rigid boom to position them at a remote location relative to the main body of the spacecraft produced the possibility that oscillations of the boom driven by the firing of attitude control jets on the spacecraft might be detected by the magnetometer sensors. The mechanical characteristics of the boom have been described by Burdick (1974). The flight boom was found in prelaunch tests to have a natural frequency of 0.61 Hz and weighed 8.1 kg (17.8 pounds). Higher harmonics of the fundamental frequency are 1.22, 1.83, 2.44 and 3.05 Hz. Boom tests in air showed that an initial boom tip deflection of 2 inches double amplitude damped down to 0.1 inch double amplitude in 10 cycles, taking approximately 16 sec.

Since there was a possibility that boom oscillations could be observed in the inflight magnetic field measurements for at least short intervals of time, data taken around the time of onset of a roll calibration maneuver were carefully examined, both by visual inspection of the detail data plotted on a sensitive scale and by spectral analysis. No indication of the fundamental frequency or any of its harmonics was found. Thus at least the firing of attitude control jets to alter the spacecraft state from fixed attitude to a slow roll state did not excite any detectable oscillations of the magnetometer boom.

The absence of observable effects suggests that angular deflections of the boom associated with mechanical oscillations were not large. Table VI summarizes the amplitudes of field variations (for the field component parallel to the boom) that would be produced by boom deflections of various angular sizes. One sees that the deflection angle would have to have been greater than 5° to produce a measurable effect even in strong ambient fields.

REFERENCES

Alfvén, H., Cosmical Electrodynamics, Clarendon Press, Oxford, 1950.

Altschulter, M. D., D. E. Trotter, and F. Q. Orrall, Solar Phys., 26, 354, 1972.

Altschuler, Martin D., Dorothy E. Trotter, and Gordon Newkirk, Jr., Solar Phys., 39, 3, 1974.

Antonucci, Ester and Leif Svalgaard, Solar Phys., 34, 3, 1974.

Babcock, H. D., Astrophys. J., 13, 364, 1959.

Babcock, H. W., Astrophys. J., 118, 387, 1953.

Babcock, H. W., Astrophys. J., 133, 572, 1960.

Babcock, H. W. and Harold D. Babcock, Astrophys. J., 121, 349, 1955.

Ballif, J. R., D. E. Jones, P. J. Coleman, Jr., L. Davis, Jr., and E. J. Smith, J. Geophys. Res., 72, 4357, 1967.

Ballif, J. R., D. E. Jones, and P. J. Coleman, Jr., J. Geophys. Res., 74, 2289, 1969.

Barnes, A., and J. V. Hollweg, J. Geophys. Res., 79, 2302, 1974.

Bartels, J., Terr. Magnetism and Atmos. Elec., 37, 1, 1932.

Bartels, J., Terr. Magnetism and Atmos. Elec., 39, 201, 1934.

Bartels, J., FIAT Review of German Science, 17, part I, Geophysics, 1945.

Bartels, J., Abhandlung, Akad. Wiss. Gottingen, Math-Phys. Kl. Sounderheft, 1951.

Bartels, J., Naturwiss, 45, 181, 1958.

Belcher, J. W., Astrophys. J., 168, 509, 1971.

Belcher, John W., J. Geophys. Res., 78, 6480, 1973.

Belcher, John W., MIT Preprint CSR-P-74-113, Cambridge, Mass.; submitted to J. Geophys. Res., 1974.

Belcher, John W., and Robert Burchsted, J. Geophys. Res., 79, 4765, 1974.

Belcher, J. W., and L. Davis, Jr., J. Geophys. Res., 76, 3534, 1971.

Belcher, John W., and Craig V. Solodyna, J. Geophys. Res., 80, 181, 1975.

Belcher, J. W., L. Davis, Jr., and E. J. Smith, J. Geophys. Res., 74, 2302, 1969.

Bendat, J. S., and A. G. Piersol, Random data: Analysis and Measurement Procedures, John Wiley and Sons, New York, 1971.

Bierman, L., Z. Astrophys., 29, 274, 1951.

Blackman, R. B., and J. W. Tukey, The Measurement of Power Spectra, Dover, New York, 1958.

Blake, David H., and John W. Belcher, J. Geophys. Res., 79, 2891, 1974.

Bobrov, M. S., Planet. Space Sci., 21, 2139, 1973.

Bonetti, A., H. S. Bridge, A. J. Lazarus, B. Rossi, and F. Scherb, J. Geophys. Res., 68, 4017, 1963.

Brice, N., J. Geophys. Res., 69, 4515, 1964.

Bridge, H. S., A. J. Lazarus, J. D. Scudder, K. W. Ogilvie, R. E. Hartle, J. R. Asbridge, S. J. Bame, W. C. Feldman, and G. L. Siscoe, Science, 183, 1293, 1974.

Burdick, Harry F., NASA Technical Memorandum TM X-3274, August 1975.

Burlaga, L. F., Solar Phys., 4, 67, 1968.

Burlaga, Leonard F., Solar Phys., 7, 54, 1969.

Burlaga, Leonard, F., J. Geophys. Res., 76, 4360, 1971a.

Burlaga, L. F., Space Sci, Rev., 12, 600, 1971b.

Burlaga, L. F., Solar Wind, p. 309, Ed. by C. P. Sonett, P. J. Coleman, Jr., and J. M. Wilcox, NASA SP-308, 1972.

Burlaga, L. F., J. Geophys. Res., 79, 3717, 1974.

Burlaga, L. F., Space Sci. Rev., 17, 327, 1975.

Burlaga, L. F., and E. Barouch, To appear in Astrophys. J., Dec. 1975.

Burlaga, L. F., and N. F. Ness, Can. J. Phys., 46, 5962, 1968.

Burlaga, Leonard F., and Norman F. Ness, Solar Phys., 9, 467, 1969.

Burlaga, L. F., and K. W. Ogilvie, J. Geophys. Res., 74, 2815, 1969.

Burlaga, L. F., and K. W. Ogilvie, Astrophys. J., 159, 659, 1970.

Burlaga, L. F., and K. W. Ogilvie, J. Geophys. Res., 78, 2028, 1973.

Burlaga, L. F., and J. M. Turner, NASA-GSFC Preprint X-692-74-329, November 1974.

Burlaga, L. F., K. W. Ogilvie, and D. H. Fairfield, Astrophys. J. 155, L171, 1969.

Burlaga, L. F., K. W. Ogilvie, D. H. Fairfield, M. D. Montgomery, and S. J. Bame, Astrophys. J., 164, 137, 1971.

Chapman, S., p. 371, The Earth's Environment, Eds. C. Dewitt et al., Gordon and Breach, New York, 1963.

Chapman, S., and J. Bartels, Geomagnetism, 2 Vols., Oxford: Clarendon Press, 1940.

Childers, D. D., and C. T. Russell, Solar Wind, p. 375, ibid., 1972.

Chree, C., Phil. Trans. Roy. Soc. (A), 212, 75, 1921; 213, 245, 1913.

Chree, C., and J. M. Stagg, Phil. Trans. Roy. Soc. (A), 227, 21, 1927.

Colburn, D. S., and C. P. Sonnett, Space Sci. Rev., 5, 439, 1966.

Coleman, P. J., Jr., J. Geophys. Res., 69, 3051, 1964.

Coleman, P. J., Jr., J. Geophys. Res., 71, 5509, 1966.

Coleman, P. J., Jr., Planet. Space Sci., 15, 953, 1967.

Coleman, P. J., Jr., Astrophys. J., 153, 371, 1968.

Coleman, P. J., Jr., and Rosenberg, R. L., (Abstract), Trans. Amer. Geophys. Union, 49, 727, 1968.

Coleman, P. J., Jr., and R. L. Rosenberg, J. Geophys. Res., 76, 2917, 1971.

Coleman, P. J., Jr., L. Davis, and C. P. Sonnett, Phys. Rev. Lett. 5, 43, 1960.

Coleman, P. J., Jr., Leverett Davis, Jr., E. J. Smith, and D. E. Jones, J. Geophys. Res., 71, 2831, 1966.

Coleman, Paul J., Jr., Leverett Davis, Jr., Edward J. Smith, and Douglas E. Jones, J. Geophys. Res., 72, 1637, 1967.

Coleman, Paul J., Jr., Edward J. Smith, Leverett Davis, Jr., and Douglas E. Jones, J. Geophys. Res., 74, 2826, 1969.

Cowling, T. G., in The Sun, p. 575, ed. G. P. Kuiper, University of Chicago Press, 1953.

Davis, L., Jr., Stellar and Solar Magnetic Fields, Ed. by R. Lust, North-Holland, Amsterdam, 1965.

Davis, Leverett, Jr., Solar Wind, p. 93, ibid., 1972.

Davis, L., Jr., and E. J. Smith, (Abstract), EOS Trans. AGU, 49, 257, 1968.

Davis, L., E. J. Smith, P. J. Coleman, and C. P. Sonnett, in Solar Wind, p. 35, Ed. R. J. Mackin, Jr. and Marcia Neugebauer, Pergamon Press, New York, 1966.

Dessler, A. J., J. Geophys. Res., 63, 507, 1958.

Dessler, A. J., Rev. Geophys., 5, 1, 1967.

Dulk, G. A., and K. V. Sheridan, Solar Phys., 36, 191, 1974.

Dungey, J. W., Phys. Rev. Lett., 6, 47, 1971.

Fairfield, D. H., J. Geophys. Res., 74, 3541, 1969.

Fairfield, D. H., J. Geophys. Res., 79, 1368, 1974.

Fairfield, D. H., and K. W. Behannon, NASA-GSFC Preprint X-692-75-177, submitted to J. Geophys. Res., 1975.

Fairfield, D. H., and L. J. Cahill, J. Geophys. Res., 71, 155, 1966.

Fairfield, D. H., and N. F. Ness, J. Geophys. Res., 72, 2379, 1967.

Fairfield, D. H., and N. F. Ness, J. Geophys. Res., 79, 5089, 1974.

Feldman, W. C., J. R. Asbridge, S. J. Bame, and M. D. Montgomery, Revs. Geophys. Space Phys., 12, 715, 1974.

Ferraro, V. C. A., Rev. Mod. Phys. 32, 934, 1960.

Fisk, L. A., and J. W. Sari, J. Geophys. Res., 78, 6729, 1973.

Fisk, L. A., and M. VanHollebeke, J. Geophys. Res., 77, 2232, 1972.

Forslund, D. W., Solar Wind, p. 346, ibid., 1972.

Fowler, R. A., B. J. Botick, and R. D. Elliot, J. Geophys. Res., 72, 2871, 1967.

Friis-Christensen, K. Lassen, J. Wilhjelm, J. M. Wilcox, W. Gonzales, and D. S. Colburn, J. Geophys. Res., 77, 3371, 1972.

Garrett, Henry Berry, Ph.D. Thesis, Rice University, Houston, Texas, 1973.

Garrett, H. B., Planet. Space Sci., 22, 111, 1974.

Gary, S. P., M. D. Montgomery, W. C. Feldman, and D. W. Forslund, Los Alamos Scientific Laboratory Reprint, submitted to J. Geophys. Res., 1975.

Goldstein, B., and G. L. Siscoe, Solar Wind, p. 506, ibid, 1972.

Greenstadt, E. W., I. M. Green, G. T. Inouye, D. S. Colburn, J. H. Binsack, and E. F. Lyon, Cosmic Electrodyn., 1, 279, 1970.

Gubbins, D., Rev. Geophys. Space Phys., 12, 137, 1974.

Hale, George E., Astrophys. J., 28, 315, 1908.

Hale, George E., Astrophys. J., 38, 27, 1913.

Hale, G. E., F. H. Seares, A. Van Maanen, and F. Ellerman, Astrophys. J., 47, 206, 1918.

Hansen, Shirley F., C. Sawyer, and Richard T. Hansen, Geophys. Res. Lett., 1, 13, 1974.

Harvey, J., A. S. Krieger, A. F. Timothy, and G. S. Vaiana, Proceedings of the Working Session on the Preliminary Results of the Skylab Solar Experiments and Correlated Ground Observations, Arcetri Astrophysical Observatory, Florence, Italy, 1974.

Hedgecock, P. C., Space Sci. Instrumentation, 1, 61, 1975a.

Hedgecock, P. C., Space Sci. Instrumentation, 1, 83, 1975b.

Hedgecock, P. C., Imperial College Preprint, London; submitted to Solar Phys., 1975c.

Heppner, J. P., N. F. Ness, C. S. Scearce, and T. L. Skillman, J. Geophys. Res., 68, 1, 1963.

Heppner, J. P., M. Sugiura, T. L. Skillman, B. G. Ledley, and M. Campbell, J. Geophys. Res., 72, 5417, 1967.

Hide, R., Phil. Trans. Roy. Soc. (A), 259, 615, 1966.

Hirshberg, J., and D. S. Colburn, Planet. Space Sci., 17, 1183, 1969.

Hollweg, Joseph V., Publ. Astron. Soc. Pacific, 86, 561, 1974.

Hollweg, Joseph V., Rev. Geophys. Space Phys., 13, 263, 1975.

Hollweg, J. V. and H. J. Völk, J. Geophys. Res., 75, 5297, 1970.

Horng, Jiann-Tsorng, Proceedings of the Tenth International Symposium on Space Technology and Science, Tokyo, Japan, 1973.

Holzer, R. E., M. G. McLeod, and E. J. Smith, J. Geophys. Res., 71, 1481, 1966.

Howard, R., Solar Phys. 25, 5, 1972.

Howard, Robert, Solar Phys., 38, 283, 1974.

Howard, Robert, Solar Phys., 38, 59, 1974.

Howard, Robert, Solar Phys., 39, 275, 1974.

Howard, R. A., and M. J. Koomen, Solar Phys., 37, 467, 1974.

Hundhausen, A. J., Coronal Expansion and Solar Wind, Vol. 5, Physics and Chemistry in Space, Springer-Verlag, New York, 1972.

Jenkins, Gwilym M., and Donald G. Watts, Spectral Analysis and its Applications, Holden-Day, San Francisco, 1969.

Jokipii, J. R., Astrophys. J., 146, 480, 1966.

Jokipii, J. R., Astrophys. J., 152, 671, 1968.

Jokipii, J. R., University of Arizona Lunar and Planetary Laboratory preprint 750040, Tucson Arizona, submitted to J. Geophys. Res., 1975.

Jokipii, J. R., and Paul J. Coleman, Jr., J. Geophys. Res., 73, 5495, 1968.

Jones, D. E., J. R. Ballif, and J. G. Melville, J. Geophys. Res., 79, 286, 1974.

Kane, R. P., J. Atmos. Terr. Phys., 34, 1941, 1972.

Kane, R. P., J. Geophys. Res., 79, 64, 1974.

Kennel, C. F., and H. E. Petschek, J. Geophys. Res., 71, 1, 1966.

Kennel, C. F., and F. L. Scarf, J. Geophys. Res., 73, 6149, 1968.

Kiepenheuer, K., Astrophys. J., 117, 447, 1953.

King, Joseph H., NASA-GSFC Preprint X-601-75-136, May 1975a.

King, J. H., Interplanetary Magnetic Field Data Book, NASA-NSSDC 75-64, 1975b.

Krall, Nicholas, A., and Derek A. Tidman, J. Geophys. Res., 74, 6439, 1969.

Krieger, A. S., J. T. Nolte, P. S. McIntosh, J. D. Sullivan, R. E. Gold and E. C. Roelof, Applied Physics Laboratory Preprint, Contributions to the 14th International Cosmic Ray Conference, Munich, W. Germany, Aug. 15-29, 1975.

Lakhina, G. S., and B. Buti, Physical Research Laboratory preprint, Ahmedabad, India, 1975.

Lee, M. A., and I. Lerche, Rev. Geophys. Space Phys., 12, 671, 1974.

Leighton, R. B., Astrophys. J., 140, 1547, 1964.

Leighton, Robert B., Astrophys. J., 156, 1, 1969.

Lepping, R. P., K. W. Behannon, and D. R. Howell, NASA-GSFC Preprint, X-692-75-268, 1975.

Lincoln, J. Virginia, J. Geophys. Res., 79, 3245, 1974a.

Lincoln, J. Virginia, Geomagnetic and Solar Data, J. Geophys. Res., 79, pp. 1134, 1586, 2006, 2555, 2936, 3244; 1974b.

Lincoln, J. Virginia, J. Geophys. Res., 80, 1858, 1975.

Mariani, F., B. Bavassano, U. Villante, and N. F. Ness, J. Geophys. Res., 79, 8011, 1973.

Mariani, F., L. Diodato, and G. Moreno, Laboratorio Plasma Spazio Preprint, CNR Frascati, Italy; submitted to Solar Phys., 1974.

Martin, R. N., J. W. Belcher, and A. J. Lazarus, J. Geophys. Res., 78, 3653, 1973.

Martres, M., M. Pick, and G. K. Park, Solar Phys., 15, 48, 1970.

Matheson, D. N., and L. T. Little, Planet. Space Sci., 19, 1615, 1971.

Matsuda, T., and T. Sakurai, Cosmic Electrodyn. 3, 97, 1972.

Mauder, E. W., Monthly Notices Roy. Astron. Soc., 64, 205, 1904.

Mauder, E. W., Monthly Notices Roy. Astron. Soc., 65, 2, 538, 666, 1905.

Mauder, E. W., Monthly Notices Roy. Astron. Soc., 76, 63, 1916.

McCarthy, Dennis K., NASA-GSFC Preprint X-723-70-166, April 1970.

McCracken, K. G., Nuovo Cimento (10), 13, 1074, 1959.

McCracken, K. G., J. Geophys. Res., 67, 447, 1962.

Means, Joseph D., J. Geophys. Res., 77, 5551, 1972.

Moyer, C. V., NASA-GSFC Preprint X-616-68-455, 1968.

Munro, R. H., and G. L. Withbroe, Astrophys. J., 176, 511, 1972.

Mustel, E. R., Astron. Zurnal (USSR), 39, 28, 1961, also Soviet Astron., 5, 19, 1961.

Nakagawa, Y., and R. E. Wellck, Solar Phys., 32, 257, 1973.

Nerney, S. F., and S. T. Suess, Astrophys. J., 200, 503, 1975.

Ness, Norman F., Space Sci. Rev., 11, 459, 1970.

Ness, N. F., and K. H. Schatten, J. Geophys. Res., 74, 6425, 1969.

Ness, N. F., and J. M. Wilcox, Phys. Rev. Lett., 13, 461, 1964.

Ness, N. F., and J. M. Wilcox, Astrophys. J., 143, 23, 1966.

Ness, Norman F., and John M. Wilcox, Solar Phys., 2, 351, 1967.

Ness, N. F., S. C. Scearce, and J. B. Seek, J. Geophys. Res., 69, 3531, 1964.

Ness, N. F., C. S. Scearce, and S. Cantarano, J. Geophys. Res., 71, 3305, 1966.

Ness, N. F., A. J. Hundhausen, and S. J. Bame, J. Geophys. Res., 76, 6643, 1971a.

Ness, N. F., K. W. Behannon, R. P. Lepping, and K. H. Schatten, J. Geophys. Res., 76, 3564, 1971b.

Ness, N. F., K. W. Behannon, R. P. Lepping, Y. C. Whang, and K. H. Schatten, Science, 183, 1301, 1974a.

Ness, N. F., K. W. Behannon, R. P. Lepping, Y. C. Whang, and K. H. Schatten, Science, 185, 151, 1974b.

Ness, N. F., K. W. Behannon, R. P. Lepping, and Y. C. Whang, J. Geophys. Res., 80, 2708, 1975a.

Ness, N. F., K. W. Behannon, R. P. Lepping, and Y. C. Whang, Nature, 255, 204, 1975b.

Neubauer, F. M., J. Geophys. Res., 80, 3235, 1975.

Neubauer, F. M., and G. Musmann, Presented at XVI IAGA-IUGG General Assembly, Grenoble, France. 1975.

Neugebauer, M., Solar Wind Three, p. 373, Ed. C. T. Russell, Institute of Geophysics and Planetary Physics, U. of California, Los Angeles, 1974b.

Neugebauer, Marcia, Space Sci. Rev., 17, 221, 1975a.

Neugebauer, M., J. Geophys. Res., 80, 998, 1975b.

Neugebauer, M., and C. W. Snyder, J. Geophys. Res., 71, 4469, 1966.

Neupert, W. M., and V. Pizzo, J Geophys. Res., 79, 3701, 1974.

Newkirk, Gordon, Jr., in Solar Wind, p. 11, ibid, 1972.

NOAA Solar-Geophysical Data, Prompt Reports, No. 353-Part I, Jan. 1974 through No. 358-Part I, June 1974, National Geophysical and Solar Terrestrial Data Center, Boulder, Colorado.

NOAA Solar-Geophysical Data, Explanation of Data Reports No. 366 (Suppl.) Feb. 1975, ibid.

Nolte, J. T., A. S. Krieger, R. E. Gold, E. C. Roelof, J. D. Sullivan, A. J. Lazarus, A. F. Timothy, P. S. McIntosh, and G. S. Vaiana, submitted to Solar Phys, 1975.

Ogilvie, K. W., J. D. Scudder, R. E. Hartle, G. L. Siscoe, H. S. Bridge, A. J. Lazarus, J. R. Asbridge, S. J. Bame, and C. M. Yeates, Science, 185, 145, 1974.

Ortega, J. U., and W. C. Rheinboldt, Interactive solution of nonlinear equations in several variables, Academic Press, New York, N. Y., 1970.

Otnes, Robert K. and Loren Enochson, Digital Time Series Analysis, J. Wiley and Sons, New York, 1972.

Parker, E. N., Astrophys. J., 121, 491, 1955.

Parker, E. N., Astrophys. J., 128, 664, 1958.

Parker, E. N., Interplanetary Dynamical Processes, Interscience, New York, 1963.

Parker, E. N., Space Sci. Rev. 4, 666, 1965.

Parker, E. N., Astrophys. J., 198, 205, 1975.

Pilipp, W., and H. J. Võlk, J. Plasma Phys., 6, 1, 1971.

Rankin, D., and R. Kurtz, J. Geophys. Res., 75, 5444, 1970.

Rhodes, Edward J., Jr., and Edward J. Smith, Jet Propulsion Laboratory Preprint, Pasadena California, 26 August 1975.

Roberts, P. H., and M. Stix, Astron. & Astrophys., 18, 453, 1972.

Rosenberg, Ronald L., J. Geophys. Res., 75, 5310, 1970.

Rosenberg, Ronald L., J. Geophys. Res., 80, 1339, 1975.

Rosenberg, Ronald L., and Paul J. Coleman, Jr., J. Geophys. Res., 74, 5611, 1969.

Rosenberg, R. L., and P. J. Coleman, Jr., Inst. Geophys. and Planet. Phys. Publ. No. 1196-26, U. of California, Los Angeles, 1973.

Rosenberg, R. L., P. J. Coleman, Jr., and D. S. Colburn, J. Geophys. Res., 76, 6661, 1971.

Rosenberg, R. L., P. J. Coleman, Jr., and N. F. Ness, J. Geophys. Res., 78, 51, 1973.

Rosenberg, Ronald L., Margaret G. Kivelson, Shao C. Chang, and E. J. Smith, Inst. Geophys. and Planet. Phys. Publ. No. 1500, U. of California, Los Angeles, 1975.

Russell, Christopher T., Solar Wind, p. 365, ibid, 1972.

Russell, C. T. and R. L. McPherron, J. Geophys. Res., 78, 92, 1973.

Russell, C. T., D. D. Childers, and P. J. Coleman, J. Geophys., Res., 76, 845, 1971.

Sakurai, T., Cosmic Electrodyn. 1, 460, 1971.

Sari, James W., Ph.D. Thesis, U. of Maryland, 1972 NASA-GSFC Preprint X-692-72-309, August 1972.

Sari, James W., J. Geophys. Res., 80, 457, 1975.

Sari, James W., and Norman F. Ness, Solar Phys., 8, 155, 1969.

Sari, J. W., and N. F. Ness, in Proc. 11th Int. Conf. on Cosmic Rays 2, Acta Physica Academiae Scientiarum Hungaricae, 29, suppl. 373, 1970.

Scarf, Frederick L., Space Sci. Rev., 11, 234, 1970.

Scarf, F. L., and R. W. Fredricks, J. Geophys. Res., 73, 1747, 1968.

Scarf, F. L., J. H. Wolfe, and R. W. Silva, J. Geophys. Res., 72, 993, 1967.

Scearce, C. S., C. V. Moyer, R. P. Lepping, and N. F. Ness, in preparation, 1975.

Schatten, K. H., Ph.D. Thesis, Univ. California, Berkeley, 1968.

Schatten, Kenneth H., Solar Wind, p. 65, ibid, 1972.

Schatten, Kenneth H., Solar Phys., 33, 305, 1973.

Schatten, K. H., and J. M. Wilcox, J. Geophys. Res., 72, 5185, 1967.

Schatten, Kenneth H., John M. Wilcox, and Norman F. Ness, Solar Phys. 6, 442, 1969.

Schulz, Michael, Astrophys. Space Sci., 24, 371, 1973.

Scudder, J. D., Presented at XVI IAGA/IUGG General Assembly, Grenoble, France, 1975.

Seek, J. B., J. L. Scheifele, and N. F. Ness, NASA-GSFC Preprint X-692-75-267, 1975.

Sentman, Davis, D., U. of Iowa Preprint 74-5, The University of Iowa, Iowa City, Iowa 52242, January 1974.

Severny, A. B., in Solar Magnetic Fields, p. 675, Ed. by Robert Howard, D. Reidel, 1971.

Siscoe, G. L., J. Geophys. Res., 77, 27, 1972.

Siscoe, G. L., L. Davis, P. J. Coleman, Jr., E. J. Smith, and D. E. Jones, J. Geophys. Res., 73, 61, 1968.

Smith, Edward J., J. Geophys. Res., 78, 2054, 1973a.

Smith, Edward J., ibid, p. 2088, 1873b.

Smith, E. J., Solar Wind Three, p. 257, ibid, 1974.

Sonett, C. P., Phys. Rev. Lett., 5, 46, 1960.

Sonnett, C. P., D. L. Judge, A. R. Sims, and J. M. Kelso, J. Geophys. Res., 65, 55, 1960a.

Sonett, C. P., E. J. Smith, D. L. Judge, and P. J. Coleman, Jr., Phys. Rev. Lett., 4, 161, 1960b.

Soper, G. K., and E. G. Harris, Phys. Fluid, 8, 984, 1965.

Stix, M., Astron. & Astrophys., 37, 121, 1974.

Stix, T. H., The Theory of Plasma Waves, McGraw-Hill, New York, 1962.

Suess, S., AIAA J., in press, 1975.

Svalgaard, L., Geophys. Papers R-29, Danish Meteorol. Int., Copenhagen, 1968.

Svalgaard, L., J. Geophys. Res., 77, 4027, 1972.

Svalgaard, L., J. Geophys. Res., 78, 2064, 1973.

Svalgaard, Leif, and John M. Wilcox, Solar Phys., 41, 461, 1975.

Svalgaard, Leif, John M. Wilcox, and Thomas L. Duvall, Solar Phys., 37, 157, 1974.

Sykora, J., Solar Phys., 18, 72, 1971.

Taylor, H. E., Solar Phys., 6, 320, 1969.

Tidman, D. A., and R. K. Jaggi, J. Geophys. Res., 67, 2215, 1962.

Timothy, A. F., A. S. Krieger, and G. S. Vaiana, Solar Phys., 42, 135, 1975.

Tsurutani, B. T., and E. J. Smith, (Abstract), EOS Trans. AGU, 56, 438, 1975.

Turner, J. M., and G. L. Siscoe, J. Geophys. Res., 76, 1816, 1971.

Unti, T. W. J., and M. Neugebauer, Phys. Fluids, 11, 563, 1968.

Unti, T. W. J., M. Neugebauer, and B. E. Goldstein, Astrophys. J., 180, 591, 1973.

Urch, I. H., Cosmic Electrodyn., 3, 316, 1972.

Vaiana, G. S., A. S. Krieger and A. F. Timothy, Solar Phys., 32, 81, 1973a.

Vaiana, G. S., J. M. Davis, R. Giacconi, A. S. Krieger, J. K. Silk, A. F. Timothy and M. Zombeck, Astrophys. J., 185, L47, 1973b.

Villante, U., and F. Mariani, Geophys. Res. Ltrs. 2, 73, 1975.

Völk, Heinrich, J., Space Sci. Rev., 17, 255, 1975.

Völk, H. J., and W. Alpers, Astrophys. Space Sci., 20, 267, 1973.

Whang, Y. C., J. Geophys. Res., 78, 7221, 1973.

Whang, Y. C., and C. C. Chang, J. Geophys. Res., 70, 4175, 1965.

Whang, Y. C., and N. F. Ness, J. Geophys. Res., 75, 6002, 1970.

Wilcox, J. M., Space Sci. Rev., 8, 258, 1968.

Wilcox, J. M., and D. S. Colburn, J. Geophys. Res., 74, 2388, 1969.

Wilcox, J. M., and D. S. Colburn, J. Geophys. Res., 75, 6366, 1970.

Wilcox, John M., and David S. Colburn, J. Geophys. Res., 77, 751, 1972.

Wilcox, J. M., and R. Howard, Solar Phys., 5, 564, 1968.

Wilcox, John M., and Norman F. Ness, J. Geophys. Res., 70, 5793, 1965.

Wilcox, J. M., and N. F. Ness, Solar Phys., 1, 437, 1967.

Wilcox, John M., and Philip H. Scherrer, J. Geophys. Res., 77, 5385, 1972.

Wilcox, J. M., and L. Svalgaard, Solar Phys., 34, 461, 1974.

Wilde, D. J., and C. S. Beightler, Foundations of Optimization, Prentice-Hall, Englewood Cliffs, New Jersey, 1967.

Wilkinson, J. H., The Algebraic Eigenvalue Problem, Clarendon Press, Oxford, 1965.

Winters, John B., Jae R. Ballif, and Douglas E. Jones, Solar Phys., 7, 478, 1969.

Wolff, Charles L., Astrophys. J., 194, 489, 1974.

Table I

Summary of Hourly Average Field Magnitude F Distribution Data

	IMP 8/HEOS		Mariner 10	
S.R.	$\langle \bar{F} \rangle$	σ_F	$\langle \bar{F} \rangle$	σ_F
1918	5.64	1.93	5.69	2.13
1919	6.04	3.07	5.95	2.93
1920	6.03	2.32	7.42	2.80
1921	5.91	3.22	8.78	3.51
1922	5.74	1.88	12.78	4.10
1923	6.64	2.29	19.05	4.66

at 1 AU: $\langle \bar{F} \rangle = 6.00\gamma$ $\bar{\sigma}_F = 2.45\gamma$

$\sigma_{\langle \bar{F} \rangle} = 0.35\gamma$ $\sigma_\sigma = 0.57\gamma$

IMP 8/HEOS by sector:

S.R.	$\langle \bar{F} \rangle$	σ_F	S.R.	$\langle \bar{F} \rangle$	σ_F
1918	+5.54	1.90	1921	+6.18	2.68
	-5.79	1.82		-5.99	3.52
1919	+5.64	2.97	1922	+5.75	2.49
	-6.64	3.18		-5.80	1.48
1920	+6.62	2.69	1923	+6.74	2.61
	-6.02	2.10		-6.66	2.06

	$\langle \bar{F} \rangle$	$\bar{\sigma}_F$
Total sector means	+6.08 γ	2.56 γ
	-6.15 γ	2.36 γ

Table II

Values of the exponent C in the power law model r^C for the radial distance dependence of the radial and azimuthal (or tranverse) magnetic field components.

	B_r		B_ϕ		
Spacecraft	Measured Quantity	Result	Measured Quantity	Result	Comments
Theory		-2		-1	Parker spiral model dependence for field in equatorial plane.
Mariner 4	$\langle \lvert B_r \rvert \rangle$	Quiet: -1.23 ± 0.02 All: -1.46 ± 0.02	$\langle B_\phi \rangle$	Quiet: -1.22 ± 0.02 All: -1.29 ± 0.02	Overlapping 27-day averages. Least squares fit.
Mariner 5	$\langle \lvert B_r \rvert \rangle$	-1.78 ± 0.02	$\langle B_\phi \rangle$	-1.85 ± 0.02	Same as M4 analysis.
Pioneer 6	$\langle \lvert B_x \rvert \rangle$	~ -2	$\langle \sqrt{B_y^2 + B_z^2} \rangle$	~ -1	Solar rotation aves. "Consistency" with theory demonstrated (Burlaga & Ness, 1968).
Pioneer 6	$\langle \lvert B_r \rvert \rangle$	-2.0 ± 0.2	$\langle B_\phi \rangle$	-2.5 ± 0.2	Solar rotation averages. Least squares fit. (Villante & Mariani, 1975)
Pioneer 10	$\hat{B}_r$	~ -2	$\hat{B}_\phi$	~ -1	Solar rotation most probable values. "Reasonable agreement" w/theory demonstrated (Smith, 1974).
Pioneer 10	$\langle B_r \rangle_p$	-2.1 ± 0.30	$\langle B_\phi \rangle_p$	-1.29 ± 0.06	Least squares fit to polarity weighted averages (Rosenberg et al., 1975)
Mariner 10	$\lvert B_x \rvert$	-1.95 ± 0.31	$\sqrt{B_y^2 + B_z^2}$ $\lvert B_\phi \rvert \equiv \lvert B_y \rvert$	-1.40 ± 0.30 -1.30 ± 0.36	Daily ave. data. Least squares fit.

Table III

Percentages of Observation Time in Each Sector Polarity During Each Solar Rotation

SR	Sector Polarity	Total Hours		Hours in Each Polarity		% Hrs in Each Polarity	
		M10	IMP 8/HEOS	M10	IMP 8/HEOS	M10	IMP 8/HEOS
1918	+	406	376	171	154	42	41
	-			235	222	48	59
1919	+	649	522	312	266	48	51
	-			337	256	52	49
1920	+	539	487	216	136	40	28
	-			323	351	60	72
1921	+	635	474	241	137	38	29
	-			394	337	62	71
1922	+	679	475	251	162	37	34
	-			428	313	63	66
1923	+	752	509	248	229	33	45
	-			504	280	67	55

Table IV

Summary of Solar Rotation Statistics of Vector Field Fluctuations

	Mariner 10			IMP 8/HEOS	
SR	$\langle \sigma_c/F \rangle$	σ_D^*	$\sigma_H^\dagger$	$\langle \sigma_c/F \rangle$	σ_D^*
1918	0.438	0.086	0.22	0.495	0.100
1919	0.398	0.113	0.22	0.440	0.137
1920	0.423	0.108	0.20	0.522	0.122
1921	0.453	0.098	0.25	0.525	0.127
1922	0.483	0.102	0.22	0.542	0.128
1923	0.496	0.094	0.20	0.487	0.168
Average	0.448	0.100	0.22	0.502	0.130
σ	0.037	0.010	0.02	0.037	0.022
	IMP 8 only			HEOS only	
1918	0.461	0.092	0.20	0.530	0.114
1919	0.355	0.075	0.19	0.493	0.128
1920	0.495	0.089	0.20	0.575	0.131
1921	0.454	0.089	0.20	0.563	0.124
1922	0.487	0.092	0.20	0.582	0.144
1923	0.397	0.121	0.19	0.552	0.172
Average	0.441	0.093	0.20	0.549	0.135
σ	0.055	0.015	0.005	0.033	0.020

[*] σ_D = rms deviation of hourly average values of σ_c/F over one day

[†] σ_H = rms deviation of fine time scale values of σ_c/F over one hour

Table V

Summary of Solar Rotation Statistics of Field Magnitude Fluctuations

	Mariner 10			IMP 8/HEOS		
SR	$\langle\sigma_F/F\rangle$	σ_D	σ_H	$\langle\sigma_F/F\rangle$	σ_D	σ_H
1918	0.108	0.033	0.11	0.111	0.022	0.07
1919	0.096	0.040	0.10	0.102	0.028	0.08
1920	0.080	0.044	0.10	0.106	0.029	0.06
1921	0.097	0.038	0.20	0.115	0.039	0.10
1922	0.094	0.042	0.13	0.118	0.044	0.11
1923	0.090	0.034	0.10	0.082	0.028	0.05
Average	0.094	0.039	0.12	0.106	0.033	0.08
σ	0.009	0.004	0.04	0.013	0.007	0.02
	IMP 8 only			HEOS Only		
1918	0.108	0.029	0.07	0.112	0.030	0.07
1919	0.096	0.028	0.08	0.112	0.029	0.07
1920	0.120	0.046	0.08	0.106	0.029	0.06
1921	0.114	0.047	0.12	0.114	0.028	0.06
1922	0.103	0.033	0.07	0.123	0.045	0.12
1923	0.074	0.026	0.05	0.094	0.030	0.06
Average	0.102	0.035	0.08	0.110	0.032	0.07
σ	0.016	0.009	0.02	0.010	0.006	0.02

Table VI

Error in Field Component Parallel to Magnetometer Boom Due to Boom Deflection

Boom Deflection Angle β (deg)	Boom Tip Displacement		$\frac{\Delta B}{B_0} = 1 - \cos \beta$	ΔB ($B_0 = 5\gamma$) gammas	ΔB ($B_0 = 20\gamma$) gammas
	cm	in.			
1°	10.1	4.0	0.0002	0.001	0.004
5°	50.7	20.0	0.0038	0.019	0.076
10°	102.3	40.3	0.0152	0.076	0.304